technische universität
dortmund

CERN

Doctoral thesis

Characterisation of Silicon Detectors Using the Two Photon Absorption – Transient Current Technique

Sebastian Pape
aus Dortmund

2023

AG Kröninger
Fakultät Physik
TU Dortmund

SSD team
EP-DT-DD
CERN

RD50

This dissertation was submitted to the department of physics of TU Dortmund University in partial fulfillment of the requirements for the degree of *Doctor rerum naturalium*.

First corrector:	Prof. Dr. Kevin Kröninger
Second corrector:	Prof. Dr. Iván Vila Álvarez
Head of commission:	Prof. Dr. Heinrich Päs
Further member of the examination board:	Prof. Dr. Edvardas Narevicius
Date of submission:	15.11.2023
Date of disputation:	29.01.2024

Abstract

Modern high energy physics experiments have increasing demands on particle detectors in terms of their spatial and temporal resolution, as well as their ability to withstand higher radiation levels. To meet these demands, increasingly complex detectors with ever smaller device segmentations are being developed that require precise device characterisation. This work is dedicated to a newly developed characterisation technique: the two photon absorption - transient current technique (TPA-TCT); a method to characterise particle detectors with micrometer-scale three-dimensional spatial resolution. Femtosecond laser light with a wavelength in the quadratic absorption regime is focused to generate excess charge by two photon absorption in a volume of about $75\,\mu m^3$ around the focal point. The drift of the excess charge carriers is studied to obtain information about the device under test. In this work, silicon detectors are used to explore and further develop the TPA-TCT. The technique is applied to pad detectors in order to study the technique and to strip and monolithic detectors to demonstrate the potential of TPA-TCT for the characterisation of state-of-the-art detector technologies. The applicability of the TPA-TCT in neutron, proton, and gamma irradiated devices is shown and radiation damage related effects on the technique are systematically studied. The reduction of charge multiplication in a low gain avalanche detector for increasing excess charge densities is observed and the role of diffusion to partially recover the gain is investigated. New techniques to investigate the electric field in complex segmented devices are developed and applied to strip and monolithic detectors. This work paves the way for the TPA-TCT as a tool to characterise detectors with three-dimensional micrometer-scale spatial resolution.

Kurzfassung

Heutige und zukünftige Experimente der Hochenergiephysik stellen immer höhere Anforderungen an Teilchendetektoren in Bezug auf ihre räumliche und zeitliche Auflösung sowie ihre Fähigkeit, steigenden Strahlungswerten standzuhalten. Um diese Anforderungen zu erfüllen, werden immer komplexere Detektoren mit immer kleineren Segmentierungen entwickelt, die eine präzise Charakterisierung erfordern. Diese Arbeit widmet sich einer neuen Charakterisierungstechnik: der *Two Photon Absorption - Transient Current Technique* (TPA-TCT); einer Methode zur Charakterisierung von Teilchendetektoren mit dreidimensionaler Auflösung im Mikrometerbereich. Femtosekunden-Laserlicht mit einer Wellenlänge im quadratischen Absorptionsbereich wird fokussiert, um durch Zwei-Photonen-Absorption in einem Volumen von etwa $75\,\mu m^3$ um den Brennpunkt herum Überschussladung zu erzeugen. Die Bewegung der Ladungsträger wird untersucht, um Informationen über den Detektor zu erhalten. Im Rahmen dieser Arbeit werden Detektoren aus Silizium verwendet, um die TPA-TCT zu untersuchen und weiterzuentwickeln. Pad-Detektoren werden untersucht, um grundlegende Studien bezüglich der TPA-TCT durchzuführen. Das Potenzial der TPA-TCT für die Charakterisierung moderner Detektortechnologien wird anhand von Streifen- und monolithische Detektoren demonstriert. Die Anwendbarkeit der TPA-TCT in Neutronen, Protonen und Gamma bestrahlten Detektoren wird gezeigt, und die Auswirkungen von Strahlenschäden auf die Technik werden systematisch untersucht. Die Verringerung der Ladungsvervielfachung in einem *Low Gain Avalanche Detector* bei zunehmender Ladungsträgerdichte wird beobachtet und die Rolle der Ladungsträgerdiffusion zur teilweisen Wiederherstellung der Verstärkung wird untersucht. Neue Techniken zur Untersuchung des elektrischen Feldes in komplexen, segmentierten Detektoren werden entwickelt und auf Streifen- und monolithische Detektoren angewandt. Diese Arbeit ebnet den Weg für die TPA-TCT als Methode für die Charakterisierung von Detektoren mit dreidimensionaler räumlicher Auflösung im Mikrometerbereich.

Publications

In the following, articles and conference contributions prepared in the course of this thesis are listed.

Articles

1. S. Pape, M. Fernández García, M. Moll, R. Montero, F. R. Palomo, I. Vila, M. Wiehe. "Characterisation of irradiated and non-irradiated silicon sensors with a table-top two photon absorption TCT system." In: *Journal of Instrumentation* (2022). DOI: 10.1088/1748-0221/17/08/C08011.

2. S. Pape, E. Currás, M. Fernández García, M. Moll, R. Montero, F. R. Palomo, C. Quintana, I. Vila, M. Wiehe. "First observation of the charge carrier density related gain reduction mechanism in LGADs with the Two Photon Absorption-Transient Current Technique." In: *Nucl. Instrum. Methods Phys. Res. A: Accel., Spectrom., Detect. Assoc. Equip.* (2022). DOI: 10.1016/j.nima.2022.167190.

3. A. Almagro-Ruiz, S. Pape, H. Muñoz-Marco, M. Wiehe, E. Currás, M. Fernández-García, M. Moll, R. Montero, F. R. Palomo, C. Quintana, I. Vila, P. Pérez-Millán. "Fiber laser system of 1550 nm femtosecond pulses with configurable properties for the two-photon excitation of transient currents in semiconductor detectors." In: *Applied Optics* (2022). DOI: 10.1364/AO.470780.

4. S. Pape, E. Currás, M. Fernández García, M. Moll. "Techniques for the Investigation of Segmented Sensors Using the Two Photon Absorption-Transient Current Technique." In: *Sensors* (2023). DOI: 10.3390/s23020962.

5. A. Almagro-Ruiz, M. Fernández-García, M. Moll, H. Muñoz-Marco, S. Pape, P. Pérez-Millán, C. Quintana, I. Vila, M. Wiehe. "Commissioning of a complete TPA-TCT system." In: *Zenodo* (2023). DOI: 10.5281/zenodo.8027092.

6. S. Pape, E. Currás, M. Fernández García, M. Moll, M. Wiehe. "Influence of temperature on measurements of the Two Photon Absorption - Transient Current Technique in silicon planar detectors using a 1550 nm femtosecond fibre laser." In: *Nucl. Instrum. Methods Phys. Res. A: Accel., Spectrom., Detect. Assoc. Equip.* (2023). DOI: 10.1016/j.nima.2023.168387.

7. S. Pape, M. Fernández García, M. Moll, M. Wiehe. "Influence of neutron, proton, or gamma irradiation damage on the Two Photon Absorption - Transient Current Technique." (In preparation)

Conference contributions

1. S. Pape, M. Fernández García, M. Moll, R. Montero, F. R. Palomo, I. Vila, M. Wiehe. "A table-top Two Photon Absorption - TCT system: experimental results." In: *38th RD50 Workshop* (June 23, 2021). Online (talk).
   URL: https://indico.cern.ch/event/1029124/contributions/4411336.

2. S. Pape, M. Fernández García, M. Moll, R. Montero, F. R. Palomo, I. Vila, M. Wiehe. "A table-top Two Photon Absorption - TCT system: measurements of irradiated and non-irradiated silicon sensors." In: *PSD12: The 12th International Conference on Position Sensitive Detectors* (Sept. 17, 2021). Online (poster).
   URL: https://indico.cern.ch/event/797047/contributions/4455936.

3. S. Pape, E. Currás, M. Fernández García, M. Moll, R. Montero, F. R. Palomo, I. Vila, M. Wiehe. "Gain suppression mechanism in LGADs and SEE studies in a RD53B chip measured with the TPA-TCT method." In: *39th RD50 Workshop* (Nov. 17, 2021). Valencia, Spain (talk).
   URL: https://indico.cern.ch/event/1074989/contributions/4601951.

4. S. Pape, E. Currás, M. Fernández García, A. Himmerlich, M. Moll, R. Montero, F. R. Palomo, I. Vila, M. Wiehe. "Characterisation of the charge collection in LGAD sensors with a newly developed table-top TPA-TCT system." In: *VCI2022 - The 16th Vienna Conference on Instrumentation* (Feb. 21-25, 2022). Online (recorded presentation).
   URL: https://indico.cern.ch/event/1044975/contributions/4663778.

5. S. Pape, E. Currás, M. Fernández García, M. Moll, R. Montero, F. R. Palomo, C. Quintana, I. Vila, M. Wiehe. "Two Photon Absorption - TCT: Characterisation of LGAD and other silicon sensors with a newly developed table-top TPA-TCT system." In: *DPG Spring Meeting Heidelberg 2022* (March 24, 2022). Online (talk).
   URL: https://dpg-verhandlungen.de/year/2022/conference/heidelberg/part/st/session/9/contribution/3.

6. S. Pape, E. Currás, M. Fernández García, M. Moll, R. Montero, F. R. Palomo, C. Quintana, I. Vila. "The gain reduction mechanism in Low Gain Avalanche Detectors investigated with the TPA-TCT." In: *40th RD50 Workshop* (June 23, 2022). CERN, Switzerland (talk).
   URL: https://indico.cern.ch/event/1157463/contributions/4922748.

7. S. Pape, E. Currás, M. Fernández García, M. Moll, R. Montero, F. R. Palomo, C. Quintana, I. Vila, M. Wiehe. "Two Photon Absorption - Transient Current Technique: Techniques for the investigation of segmented sensors and the influence of temperature." In: *41st RD50 Workshop* (Nov. 30, 2022). Seville, Spain (talk).
   URL: https://indico.cern.ch/event/1132520/contributions/5140040.

8. S. Pape, E. Currás, M. Fernández García, M. Moll, R. Montero, F. R. Palomo, C. Quintana, I. Vila, M. Wiehe. "Two Photon Absorption - Transient Current Technique: Recent results on segmented sensors and improved measurement methods." In: *18th Trento Workshop on Advanced Silicon Radiation Detectors* (March 2, 2023). Trento, Italy (talk).
URL: https://indico.cern.ch/event/1223972/contributions/5262011.

9. S. Pape, E. Currás, M. Fernández García, M. Moll. "Techniques for the investigation of segmented sensors using the Two Photon Absorption - Transient Current Technique." In: *DPG Spring Meeting Dresden 2022* (March 23, 2023). Dresden, Germany (talk).
URL: https://dpg-verhandlungen.de/year/2023/conference/smuk/part/t/session/146/contribution/3.

10. S. Pape, E. Currás, M. Fernández García, M. Moll, R. Montero, F. R. Palomo, C. Quintana, I. Vila, M. Wiehe. "Investigation of neutron, proton, and gamma irradiated planar sensors using the Two Photon Absorption - Transient Current Technique." In: *42nd RD50 Workshop* (June 20, 2023). Tivat, Montenegro (talk).
URL: https://indico.cern.ch/event/1270076/contributions/5450168.

11. S. Pape, M. Fernández García, M. Moll, M. Wiehe. "Two Photon Absorption - Transient Current Technique: TCAD Simulation of a PIN & Influence of Radiation Damage on the TPA-TCT." In: *43rd RD50 Workshop* (Nov. 29, 2023). CERN, Switzerland (talk).
URL: https://indico.cern.ch/event/1334364/contributions/5668792/.

Contents

1 Introduction

In order to detect the wide spectrum of particles and their properties, modern high energy particle detector systems consist of a variety of detector technologies. Silicon detectors are nowadays the leading particle tracking technology and the heart piece of almost every detector system. The European committee for future accelerators (ECFA) emphasises the need of research and development (R&D) in the field of silicon detector to meet the demanding requirements of future high energy experiments, i.e. to withstand radiation levels beyond 10^{16} neutrons per cm^2, spatial resolution of few micrometers, and temporal resolution of few tenths of picoseconds [1]. Detector R&D goes hand in hand with developments in device characterisation techniques to satisfy the need for increasing measurement precision.

This work is dedicated to the investigation of the two photon absorption - transient current technique (TPA-TCT) to characterise silicon detectors with high three-dimensional spatial resolution. High spatial resolution is needed to precisely study micrometer-scale device segmentation and features of present and future detector technologies. The fundament of the TPA-TCT is the transient current technique (TCT), which is a central tool for detector R&D and especially the characterisation of silicon detectors [2]. Conventional TCT employs red and near infrared lasers to generate excess charge and study the induced transient current of the drifting carriers. Red light has a shallow charge generation depth and is ideal to separately study the drift of electrons or holes in silicon [3], while light in the near infrared penetrates the full silicon volume and generates excess charge carriers along the full device depth. Near infrared light is used to mimic the charge generation of ionising particles in order to provide comparable measurements to beam tests [4]. Illumination from the edge (edge-TCT) with near infrared light enables resolution along the device depth [5]. Single photon absorption (SPA) based techniques reach lateral spatial resolutions of 6 to 10 µm, but are limited to two-dimensional resolution. In contrast, the TPA-TCT uses light with a wavelength beyond the linear and within the quadratic absorption regime of silicon ($1100\,\text{nm} < \lambda < 2300\,\text{nm}$). Charge generation by two photon absorption (TPA) depends quadratically on the laser intensity, so that focused light dominantly generates excess charge in a small volume around the focal point. The confined volume of excess charge enables device characterisation with three-dimensional spatial resolution, where a lateral resolution of 2.5 µm and an in-depth resolution of 20 µm is typically reached. The idea of the TPA-TCT developed from single event effect investigation in electric circuits, where TPA is used to simulate the charge deposition of heavy ions [6–8]. The proof-of-concept of the TPA-TCT was demonstrated in a prototype experiment at the laser facility of the University of the Basque Country (UPV/EHU) [9–11]. To lower the cost and complexity of the laser setup, a table-top TPA-TCT laser source was developed [12] and a table-top TPA-TCT setup was commissioned [13].

Besides TPA-TCT, the ion beam induced charge (IBIC) method also offers three-dimensional spatial resolution for the device characterisation [14, 15]. Excess charge is generated by ions and the method's spatial resolution is defined by the ionisation profile of the used ion that is spatially localised due to the Bragg-peak. Time resolved IBIC (TRIBIC) studies the drift of the excess charge to obtain similar results like TCT [16, 17]. Advantages of TRIBIC compared to TCT are the possibility to measure through metal and the potentially increased spatial resolution. On the other hand, TRIBIC has the following three disadvantages compared to TCT. First, accelerators are needed to obtain tunable ion beams,

which increases the cost of operation and significantly enlarges the setup. Second, TRIBIC is more complex in terms of the charge generation profile, where elaborate calibration of the setup is needed. In-depth measurements are more challenging, because the depth is adjusted via the used ion, angle of incidence, or kinetic energy, which influences the excess charge profile and leads to a changing excess charge along the device depth [18]. Third, ions that are used to characterise the device simultaneously damage the silicon bulk [17], which limits the reproducibility of such measurements. The TPA-TCT produces comparable results to TRIBIC at a lower setup and operation cost, simpler execution and interpretation of measurements, and in a non-destructive manner.

This work was performed in the framework of the RD50 collaboration [19] and contributed within AIDAinnova [20] to the work package WP4. Task 4.4 of WP4 is dedicated to the design and development of a new sensor characterisation system based on the TPA-TCT technique. It includes the milestone M16 [21] and the deliverable D4.4 [22]. M16 covers the commissioning of a TPA-TCT system and was achieved during the course of this work [23]. Deliverable D4.4 tackles supporting other groups towards the implementation of TPA-TCT systems and to make a contribution to the evaluation of newly developed sensor technologies. D4.4 is already far progressed due to the development of a commercial laser source [12], the further development of the TPA-TCT [24], discussion of the TPA-TCT in RD50 workshops [25–37] and other conferences, and discussions with interested institutes. TPA-TCT setups are already commissioned at the University of the Basque Country (UPV/EHU) [9–11], the Institute of physics in Cantabria (IFCA) [23], Nikef [38], the ELI beamlines facility [39], the Jožef Stefan Institute (JSI) [40], the University of Manchester [41], and CERN [42]. Due to the success of the TPA-TCT, the commissioning of TPA-TCT setups at further institutes is planned.

The thesis is structured as follows. Chapter 2 contains a brief introduction to silicon detectors. A section about the TPA in silicon detectors is added due to its relevance to this work. Further, the influence of radiation damage on the performance of silicon detectors is discussed. In chapter 3 the focus is set to the devices and experimental methods used in the course of this work. A current-voltage (IV) and capacitance-voltage (CV) setup, a ^{90}Sr setup, and a TPA-TCT setup are introduced and the TCT method is discussed in detail. Investigations on the TPA-TCT with respect to the spatial resolution, the influence of the pulse energy, the temperature dependence of the TPA charge generation, the influence of laser beam clipping, and the influence of laser reflections are presented. Neutron, proton, and gamma irradiated pad detectors are systematically studied in chapter 4, where the influence on the TPA charge generation, the influence of the device thickness, and the influence on the refractive index are discussed. The gain reduction mechanism in low gain avalanche detectors (LGADs) is subject of chapter 5. The mechanism is part of the current scientific discourse [43–45] and here studied with respect to the influence on the electric field and the role of charge carrier diffusion. Techniques dedicated to segmented devices are developed in chapter 6 and the application of these techniques to state-of-the-art strip and monolithic devices is presented. In the course of the application, the passive CMOS strip detector [46], the HV-CMOS [47], the RD50-MPW2 [48], and the Monolith picoAD [49] are investigated. In chapter 7 single event effect studies in the lower analogue circuitry of the RD53B chip from the preproduction are carried out [50]. Finally, this thesis is summarised and concluded in chapter 8 and an outlook on the TPA-TCT setup and the technique is presented.

2 Silicon detectors

Silicon is, after oxygen, the most abundant element in the earth's crust. Due to its vast availability, its favourable properties, the possibility to fabricate structures of high purity, and low fabrication cost, it is widely used in high energy physics experiments. So far it offers the best balance between spatial resolution and fabrication cost, which makes it suitable for position tracking detectors like inner trackers. This chapter discusses the silicon for the application in particle detection. First, the characteristics of silicon are presented and the requirements for detector grade silicon are introduced. Then, the working principle of a silicon detector is explained, where the ideal electric behaviour is discussed; followed by a review on the principle of particle detection and the various mechanisms of interaction between particles with silicon. An extra section about the two photon absorption in silicon detectors is given, as it is especially relevant to this work. Finally, an overview on the influence of radiation damage in silicon detectors is presented, and its consequences are discussed in detail.

2.1 Silicon

Silicon is a chemical element from the carbon group (group 14). For the crystallisation it requires four neighbouring atoms to satisfy the octet configuration and forms covalent bonds with a strength of 1.8 eV by sp^3 hybridisation. The resulting lattice is face-centered diamond-cubic [51]. A sketch of the covalent bonding and a three-dimensional representation of the silicon lattice is shown in figures 2.1a and 2.1b, respectively. Silicon is a semiconductor with a band gap energy of $E_g \approx 1.12\,\text{eV}$ at 300 K. The band scheme is shown in figure 2.2a, where the band gap, the valence, and the conduction band are indicated. The valence band is formed by the highest filled energy states at 0 K, while the conduction band is formed by the lowest unfilled energy states. Contrary to metals, the valance and conduction band are non-overlapping, thus forming the band gap. Silicon is an indirect semiconductor, i.e. the maximum of the valence band and the minimum of the conduction band lie at different crystal momentum $\vec{k}$, which is relevant to the absorption process of

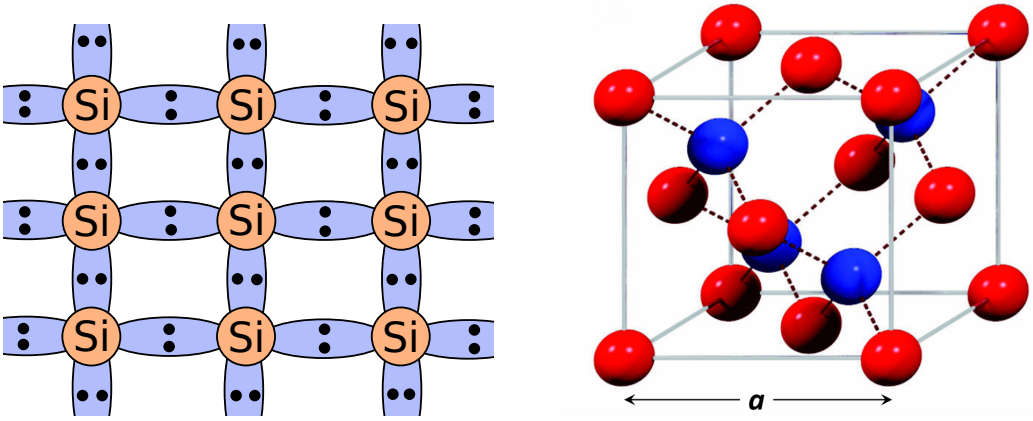

Figure 2.1: (a) Sketch of the covalent bonding in silicon (after [52]). (b) Three-dimensional lattice structure of silicon [53]. The two base atoms are indicated by different colours and a denotes the lattice constant that is about 5.431 Å at 300 K [54].

photons. Direct optical absorption is possible for energies $\geq 3.4\,\mathrm{eV}$ at $300\,\mathrm{K}$ [53]. The value becomes smaller for increasing temperatures, because the band gap energy is temperature dependent. The temperature dependence of E_g is well described by the semi-empirical Varshni equation [55]:

$$E_\mathrm{g}(T) = 1.1692\,\mathrm{eV} - \frac{(4.9 \pm 0.2) \cdot 10^{-4}\,\mathrm{eV/K} \cdot T^2}{T + (655 \pm 40)\,\mathrm{K}}. \tag{2.1}$$

Figure 2.2b shows the band gap energy of silicon for temperatures up to $750\,\mathrm{K}$ ($\approx 477\,^\circ\mathrm{C}$). Further, the temperature determines the band filling and therefore the conductivity of silicon. The filling follows the Fermi-Dirac distribution, wherefore silicon becomes conductive at elevated temperatures or fully insulating at low temperatures. However, silicon is semiconducting for the temperature range relevant to this thesis ($-20\,^\circ\mathrm{C}$ to about $25\,^\circ\mathrm{C}$).

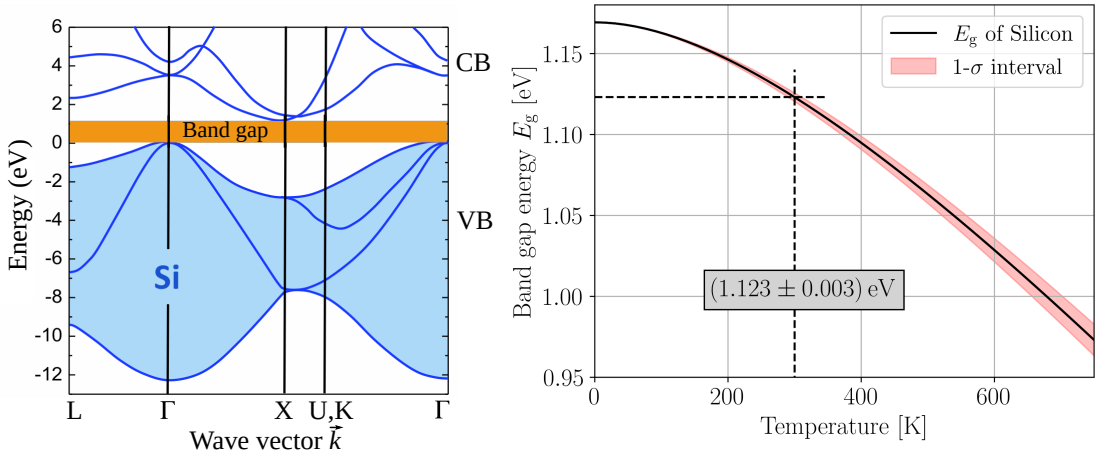

Figure 2.2: (a) Band scheme of silicon with the most important symmetry points (after [52]). The valence band (VB) is below the band gap and the conduction band (CB) above. (b) Temperature dependence of the band gap energy of silicon using data from [55].

2.1.1 Detector grade silicon

Silicon provides beneficial mechanical and electrical properties that make it suitable as a detector material. It is rigid and allows thin self-supporting structures [56], its small band gap offers a high energy resolution (3.6 eV compared to $\approx 30\,\mathrm{eV}$ for gaseous detectors), and its charge carrier mobilities allow charge collection in the nanosecond regime. The material is widely used in industrial application. Thus, material research is far progressed, and commercial fabrication is cheap compared to many other materials. In nature, silicon does not occur as a pure element, but appears in the form of silicon dioxide or silicate minerals. Detector grade silicon is obtained by different growing techniques: the float zone method (FZ), the epitaxial method (Epi), the Czochalski method (Cz), and the magnetic Czochalski method (MCz). All of them allow fabricating silicon detectors with high resistivity ($\rho > 1\,\mathrm{k\Omega\,cm}$), thicknesses of about $50\,\mu\mathrm{m}$ to $300\,\mu\mathrm{m}$, and minority carrier lifetimes long enough for the use in particle detection [57, 58]. Detailed information about

the growth techniques is given in [59, 60]. The silicon lattice can be grown with different orientation, which is denoted by Miller indices [53]. Crystal orientations of ⟨100⟩ and ⟨111⟩ are mainly used for detector grade material, because they tend to push lattice impurities towards the outside boundary of the silicon crystal and thus increase the achievable resistivity. The crystal orientation influences mechanical and electrical properties of the detector, but the impact on the device performance is for practical purposes usually negligible [61].

2.2 Working principle

The idea of a silicon detector is similar to an ionisation chamber: ionising particles generate excess charge carriers inside an active volume and the excess carriers drift towards their corresponding collection electrodes. During the drift, the charge carriers induce a current at the electrodes, which is used for the particle detection. In analogy to ionisation chambers, where gas is used as an active medium, silicon detectors have the silicon bulk that serves as a conversion medium. The mechanisms of energy conversion and particle detection are explained in detail in section 2.3 and first principles for the operation of silicon detectors are motivated.

Intrinsic silicon has a charge carrier density of about $1.45 \cdot 10^{10}\,\mathrm{cm}^{-3}$ (resistivity $\rho = 235\,\mathrm{k\Omega\,cm}$) at room temperature and therefore about $2.7 \cdot 10^{7}$ free charge carriers (under the assumption of a 300 µm thick silicon detector with an active area of 2.5 mm × 2.5 mm) [62]. A minimum ionising particle (MIP) generates $\approx 3 \cdot 10^{4}$ excess charge carriers inside such a detector, which is three orders of magnitude less than the amount of free charge carriers of intrinsic silicon. To allow detection with a reasonable signal-to-noise ratio (SNR), the free charge carriers need to be removed from the silicon, i.e. the active volume needs to be depleted. This is done by tailoring the electric properties through adding impurity atoms. The process is known as doping and the impurity atoms can either act as donors or acceptors that add or bind lattice electrons, respectively. The function of doping is explained in the following and the question of how it helps to deplete the active volume is addressed in sections 2.2.1 and 2.2.2. A functional representation of donor and acceptor doping is depicted in figure 2.3, where the integration in the silicon lattice and the corresponding band scheme is visualised. Figure 2.3a shows the integration of phosphorus, a group 15 element, in silicon. Impurity atoms add additional energy levels close to the conduction band, because phosphorous has five outer shell electrons, but only four electrons are used for the covalent bonding in the silicon lattice. The additional electron is loosely bound, i.e. its orbit is wider spread across the lattice. The delocalisation of the electron creates a positively charged region in the lattice and thereby changes locally the electric properties. The counterpart of the donor doping is the acceptor doping, where an impurity element that binds an additional electron is brought into the lattice. Such doping introduces shallow energy levels close to the valence band. For example boron can be used as an acceptor in silicon. It is a group 13 element and only has three electrons in its outer shell. It uses an electron from the surrounding silicon lattice for the covalent bonding and leaves behind a hole that can migrate through the lattice. Figure 2.3b shows the bonding of boron in silicon schematically.

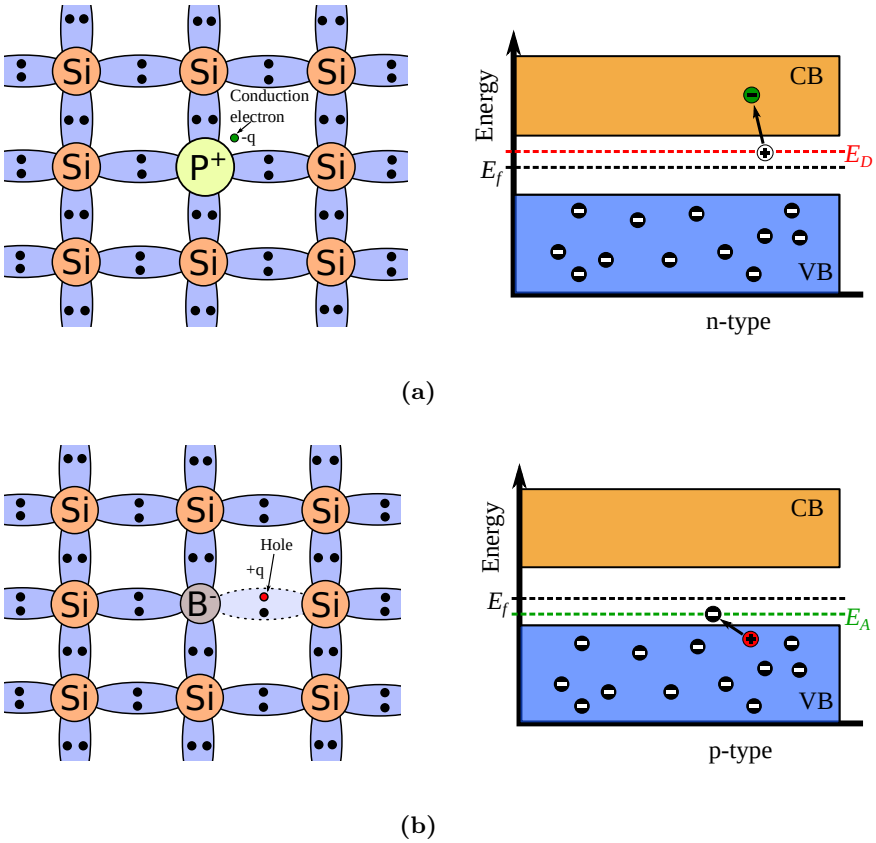

Figure 2.3: Two-dimensional representation of the bonding scheme of a phosphorous (a) and a boron (b) impurity atom in a silicon lattice. The energy bands of the donor and acceptor states are shown on the right-hand side (after [53, 60]).

2.2.1 The pn-junction

Silicon is referred to as n- or p-type doped, when the majority carriers are electron or holes, respectively. In pristine silicon the majority carrier is defined by the implanted dopant atoms, where donors are related to electrons as majority carriers and acceptors to holes. The transition between n- and p-type silicon is called pn-junction. At the junction, electrons from the n-type region and holes from the p-type region diffuse into each other and recombine. The diffusion process can be described as a current, called diffusion current. The formed region is depleted from free charge carriers and called depletion region or space charge region (SCR). The latter refers to the space charge ρ_0 that origins from the recombined charge carriers that introduce negative or positive space charge for electrons and holes, respectively. Following the Poisson equation, ρ_0 introduces a change of potential φ and an electric field E that are given by

$$-\frac{\partial^2 \varphi}{\partial z^2} = \frac{\partial E}{\partial z} = \frac{\rho_0(z)}{\epsilon_0 \epsilon_\mathrm{r}} \,. \tag{2.2}$$

The potential difference in the SCR is called built-in voltage V_bi and the resulting electric field is maximum at the junction and falls off linearly to both sides. It generates a drift current that compensates the diffusion current and thus prevents further carrier diffusion,

as the charge carriers are hindered from migration beyond the SCR. Depending on the doping concentration, values of $V_{\mathrm{bi}} = 0.6$ to $0.8\,\mathrm{V}$ are typical at room temperature. The width of the depletion region w is given in thermal equilibrium by

$$w = \sqrt{\frac{2\epsilon_0\epsilon_{\mathrm{r}}(N_{\mathrm{D}} + N_{\mathrm{A}})}{e_0 N_{\mathrm{D}} N_{\mathrm{A}}} V_{\mathrm{bi}}}\,, \tag{2.3}$$

with the electric constant ϵ_0, the susceptibility ϵ_{r}, and the donor (acceptor) concentration N_{D} (N_{A}) [52]. The doping in particle detectors is usually highly asymmetric, meaning that the concentration of one dopant is significantly higher than the other. Nowadays, silicon detectors have mainly a shallow high n-type doping at the top side electrode, a low p-type doped bulk, and a shallow high p-type doping at the back side electrode. This configuration showed to be especially radiation hard for reasons discussed in section 2.5. Such asymmetric doping simplifies equation (2.3), with a bulk doping of N_{A} and $N_{\mathrm{D}} \gg N_{\mathrm{A}}$ at the top side, to

$$w \approx \sqrt{\frac{2\epsilon_0\epsilon_{\mathrm{r}}}{e_0 N_{\mathrm{A}}} V_{\mathrm{bi}}}\,. \tag{2.4}$$

To maintain electrical neutrality, the total positive and negative charge in the depleted region needs to be equal, which reflects as

$$\frac{x_{\mathrm{n}}}{x_{\mathrm{p}}} \approx \frac{N_{\mathrm{A}}}{N_{\mathrm{D}}}\,, \tag{2.5}$$

with $x_{\mathrm{n/p}}$ being the penetration depth of the depletion region inside the n-type and p-type doped area. Thus, asymmetric doping leads to depletion that spreads mainly into the lower doped bulk region. Moreover, the doping concentration defines the resistivity ρ of a pn-junction, which is defined as the inverse conductance

$$\sigma = \frac{1}{\rho} = e_0(\mu_{\mathrm{e}} N_{\mathrm{D}} + \mu_{\mathrm{h}} N_{\mathrm{A}})\,, \tag{2.6}$$

with the charge carrier mobility $\mu_{\mathrm{e/h}}$ [52]. The mobility is discussed along the charge transport in section 2.3.3.

2.2.2 The pn-junction under bias voltage

For the operation of a particle detector, the depletion of the active volume is desired in order to increase the sensitive detector volume. The application of an external bias voltage V helps to enlarge the SCR of a particle detector, where a bias voltage with a similar polarity to the built-in voltage, called reverse bias, is applied. Opposite polarity narrows the depletion region and for $|-V| > V_{\mathrm{bi}}$ the device becomes conductive. Bias voltages that narrow the depletion region are referred to as forward bias. The width of the depletion region is described by

$$w(V) \approx \sqrt{\frac{2\epsilon_0\epsilon_{\mathrm{r}}}{e_0 N_{\mathrm{A}}}(V_{\mathrm{bi}} + V)} \propto \sqrt{V}. \tag{2.7}$$

The bias voltage that fully depletes the active volume is called depletion voltage V_{dep}. Hence, the full depletion voltage of a detector with active thickness d is given by

$$V_{\mathrm{dep}} \approx \frac{e_0}{2\epsilon_0\epsilon_{\mathrm{r}}} N_{\mathrm{A}} d^2 - V_{\mathrm{bi}} \propto N_{\mathrm{A}} d^2 \,. \tag{2.8}$$

The external voltage is usually much higher than the built-in voltage, wherefore V_{bi} is often neglected. From the depletion voltage it can be seen that higher resistivity corresponds to lower depletion voltages and vice versa. This is the reason why high resistive bulk material is favourable for the particle detection.

2.2.3 Electrical characteristics of a pn-junction

This section discusses the expected characteristics of a pad detector with active area A and the depletion width w. A pad detector, a single detecting cell, is the simplest realisation of a pn-junction. Such a detector is well modelled by a plate capacitor, which has a capacitance of

$$C(w) = \epsilon_0\epsilon_{\mathrm{r}} \frac{A}{w} \,. \tag{2.9}$$

The capacitance translates to the capacitance-voltage (CV) characteristic using equation (2.7)

$$C(V) = A\sqrt{\frac{\epsilon_0\epsilon_{\mathrm{r}} e_0 N_{\mathrm{A}}}{2V}} \,. \tag{2.10}$$

It should be noted that the description via the plate capacitor becomes less satisfactory for a non-abrupt junction or when lattice imperfections have a notable influence on the space charge. Equation (2.10) can be rearranged to extract the bulk doping concentration from the CV characteristic against the bias voltage

$$N_{\mathrm{A}}(V) = \frac{2}{\epsilon_0\epsilon_{\mathrm{r}} e_0 A^2} \left(\frac{\mathrm{d}}{\mathrm{d}V} \frac{1}{C^2(V)} \right)^{-1} \,. \tag{2.11}$$

Further, the bulk doping can be extracted against the depletion depth w using equation (2.9) and therefore provides the doping profile of the detector. In thermal equilibrium, the diffusion and drift current fully compensate each other and no current flows. When a bias voltage is applied, the total current does not vanish, but a characteristic following

$$I(V) = I_{\mathrm{S}} \left(\exp\left(-\frac{e_0 V}{k_{\mathrm{B}} T} \right) - 1 \right) \,, \tag{2.12}$$

is found [58]. Here, k_{B} is the Boltzmann constant and T the temperature. I_{S} is the saturation current and has the same sign as the drift current. A derivation and explanation of this value is given in [53, 63]. Note that reverse bias is considered as voltages with positive polarity compared to negative polarity for forward bias. This current-voltage (IV) characteristic is valid for a negligible current generation in the SCR, which is generally true for forward bias voltage and ideal detectors. Real detectors have additional contributions to the current due to surface and volume current generation. This additional current is called leakage current and not desired for operation as it is the dominating reason for the power dissipation. The leakage current in pristine devices is usually in the order of $\mathrm{nA/mm^2}$, but damage due to device handling, defects introduced in the fabrication process, or radiation

damage can dramatically increase the leakage current by several µA/mm^2. Surface current generation mainly origins from fabrication and scratches introduced during the device handling, while volume current is mainly generated by thermal carrier generation in the SCR that is strongly influenced by defects. When a reverse bias voltage is applied, the SCR broadens and such generation becomes more relevant. Thermal carrier generation depends significantly on the temperature, wherefore the leakage current can be parametrised as

$$I \propto T^2 \exp\left(\frac{-E_{\text{eff}}}{2k_{\text{B}}T}\right). \tag{2.13}$$

The effective band gap energy E_{eff} is experimentally found to be $(1.214 \pm 0.014)\,\text{eV}$ at 20 °C [64]. The contribution of surface and volume generated current can be discriminated by their corresponding voltage dependence, as the latter grows with the width of the SCR, hence $\propto \sqrt{V}$. Deviations from this relation are likely related to surface current generation, which is typically linear with the bias voltage. The behaviour depends as well on the surface geometry, which needs to be considered for the interpretation of the leakage current [58].

2.3 Particle detection

Ionising particles generate electron-hole pairs in silicon and the amount of pairs is proportional to the deposited energy. The excess charge carriers do not recombine in the depleted volume and induce a signal at the collecting electrodes during their drift. The mechanisms that lead to the charge carrier creation and the signal formation are discussed in this section for silicon detectors.

2.3.1 Charged particles

When a charged particle traverses a silicon detector, it continuously looses energy due to ionising and non-ionising processes. The process of energy loss is, due to the large number of atoms involved, of probabilistic nature. It can be understood as the occurrence of many random individual collisions, where in each of which an arbitrary amount of energy is lost, i.e. transferred to the traversed medium [65]. The average energy loss in a medium, i.e. the linear stopping power, is described by the Bethe-Bloch equation. The resulting linear stopping power of low energetic electrons is shown in figure 2.4a. The energy loss is first dominated by collision effects, while radiative effects start to arise for increasing energies. At a certain energy, radiative effects start to dominate the linear stopping power. However, this energy regime is beyond the region of interest for this thesis. Details about radiative effects can be found in [66, 67]. When energy is lost by ionisation, excess electron-hole pairs are generated, where the amount is proportional to the deposited energy. If the particles of a mono-energetic source are fully stopped within the active volume, their deposited energy, i.e. generated amount of electron-hole pairs, follows a Gaussian distribution. For thin detectors this is usually not the case, because the traversing particle passes through the active volume and exits with a given amount of remaining energy. Due to the probabilistic nature of the deposition mechanism, the amount of generated charge carriers fluctuates and the distribution is well described by a

Landau distribution [68]. Further, the finite resolution of the experimental apparatus is typically Gaussian distributed, which is why the measured amount of generated charge carriers is generally best described by a convolution of a Landau distribution with a Gauss distribution. Such a distribution is called Landau-Gauss distribution and is depicted in figure 2.4b for the charge generation of a minimum ionsing particle (MIP) in a 300 µm thick silicon detector. The most probable value (MPV) is about 3.6 fC, which is about 70 % of the mean value.

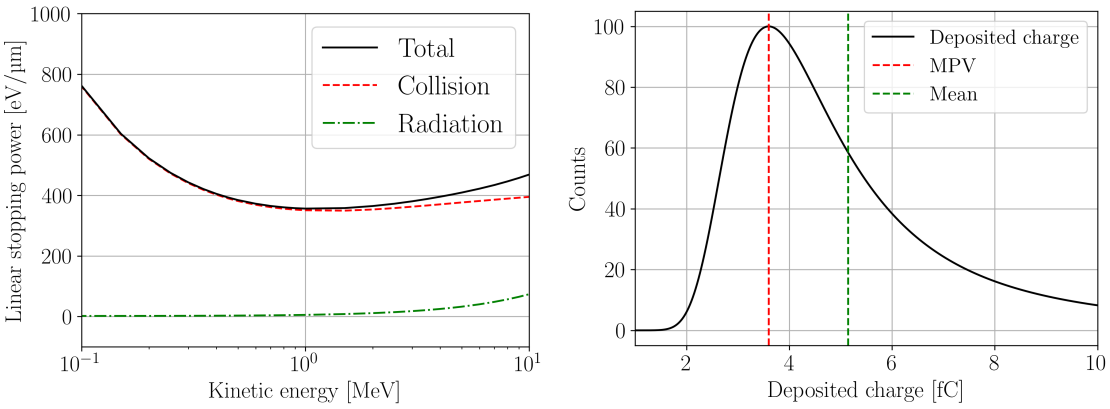

(a) **(b)**

Figure 2.4: (a) Linear stopping power of low energetic electrons in silicon (data taken from [69] and converted to stopping power in silicon with parameters from [58]). (b) Schematic distribution of the charge deposited by a MIP in a 300 µm thick silicon detector. The mean and the most probable value (MPV) are shown.

2.3.2 Photons

The interaction between silicon and photons is performed by three different processes: Compton scattering, pair production, and photoelectric/photovoltaic effect. The prior two are relevant for energies beyond several 100 keV, which are reached in high energy collider experiments [58], but irrelevant to the energies discussed within this thesis (several electronvolts). The photoelectric and the photovoltaic effect describe the mechanism of excess charge generation from light. The difference is that for the photoelectric effect the generated charge carriers are ejected from the material, while they remain within the material for the photovoltaic effect. For this thesis only the photovoltaic effect is relevant. Compared to a charged particle, a photon at the relevant energy range can not deposit only part of its energy; it is either fully absorbed or not absorbed at all. The likelihood of interaction strongly depends on the wavelength, and the process is quantified by the absorption coefficient α [53]. The ionisation due to photons is discussed in more detail in section 2.4, as it appears natural to discuss the photon absorption in the framework of two photon absorption.

2.3.3 Charge carrier transport

When excess charge carriers are generated, they start to move within the detector. Here, only charge transport in fully depleted silicon detector is considered. The charge transport

origins from two distinct process: the diffusion by Brownian motion and the drift due to the electric field. Diffusion is a slow transport mechanism compared to the drift, as will be discussed in the following. Both mechanisms are discussed separately, but for charge transport both appear superimposed.

Drift occurs in the presence of an electric field E and the motion of drift follows the electric field lines. The charge carrier's velocity due to drift is described by

$$\vec{v}_{\mathrm{D,e/h}} = \mu_{\mathrm{e/h}} \vec{E} \,, \tag{2.14}$$

with the mobility of electrons/holes $\mu_{\mathrm{e/h}}$. The mobility itself depends on the electric field, the temperature, and the doping concentration [63]. The dependence on temperature and doping concentration can be neglected for the temperature range and the investigated devices relevant to this work and only the dependence on the electric field needs to be considered. The mobility is approximately linear with the electric field until about $\approx 1\,\mathrm{V/\mu m}$ for electrons and $\approx 3\,\mathrm{V/\mu m}$ for holes and approaches saturation beyond these electric fields. The Caughey-Thomas parametrisation is so far most commonly used to model the mobility

$$\mu_{\mathrm{e/h}}(E) = \mu_{0,\mathrm{e/h}} \left(1 + \left(\frac{\mu_{0,\mathrm{e/h}} E}{v_{\mathrm{sat,e/h}}} \right)^{\beta_{\mathrm{e/h}}} \right)^{-1/\beta_{\mathrm{e/h}}} , \tag{2.15}$$

with the low field mobility $\mu_{0,\mathrm{e/h}}$, the saturated drift velocity $v_{\mathrm{sat,e/h}}$, and the phenomenological parameter $\beta_{\mathrm{e/h}}$ [70]. A detailed review on the Caughey-Thomas parametrisation can be found in [71]. The saturation of the mobility at high electric fields infers as well saturation of the drift velocity. Beyond saturation, v_{D} reaches the saturation value $v_{\mathrm{sat,e/h}} \approx 100\,\mathrm{\mu m/ns}$, which is the same for electrons and holes. Electrons reach saturation after $> 6\,\mathrm{V/\mu m}$ and holes after $> 11\,\mathrm{V/\mu m}$. Note that electrons are before saturation about three times faster than holes for the same electric field. The crystal orientation is also found to impact the drift velocity, however for experimental purposes the difference is usually negligible [61].

Diffusion occurs when a concentration gradient is present, and it is described by the Fick's law

$$\frac{\mathrm{d}n_{\mathrm{e/h}}}{\mathrm{d}t} = D_{\mathrm{e/h}} \triangle n_{\mathrm{e/h}} \,, \tag{2.16}$$

with the electron or hole density $n_{\mathrm{e/h}}$ and the corresponding diffusion constant $D_{\mathrm{e/h}}$ that is given by the Einstein equation

$$D_{\mathrm{e/h}} = \frac{k_{\mathrm{B}} T}{e_0} \mu_{\mathrm{e/h}} \,. \tag{2.17}$$

The broadening of the charge carrier density by diffusion evolves in a Gaussian manner with a standard deviation $\sigma(t) = \sqrt{2 D_{\mathrm{e/h}} t}$, until spatial uniformity of the charge carrier density is reached [58]. An example of diffusion on a charge carrier density is presented in figure 2.5. The shown charge carrier density corresponds to the typical charge carrier density generated by TPA-TCT, which will be developed in section 2.4.2.

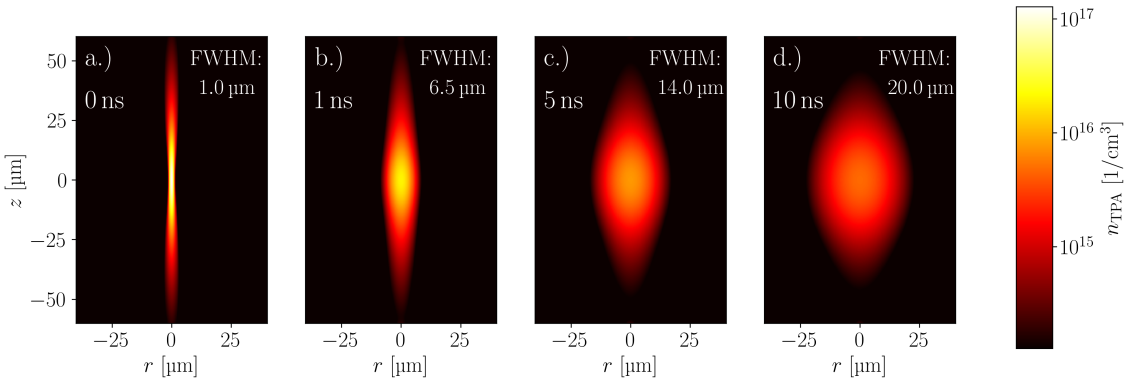

Figure 2.5: Simulation of the evolution of the charge carrier density of TPA-TCT at different timestamps. The charge carrier density is calculated using the beam parameters $E_\mathrm{p} = 100\,\mathrm{pJ}$, $\tau = 430\,\mathrm{fs}$, $w_0 = 1.3\,\mu\mathrm{m}$, and $z_{\mathrm{R,Si}} = 11.9\,\mu\mathrm{m}$. The meaning of these parameters is introduced in section 2.4.1. Diffusion leads to a broadening of the distribution. The approximate full width at half maximum (FWHM) at the waist ($z = 0\,\mu\mathrm{m}$) is stated in the pictures. The bin size in r and z is $0.5\,\mu\mathrm{m}$.

2.3.4 Signal formation

When N charge carriers move relative to an electrode, they induce a current according to the Shockley-Ramo theorem

$$I = N e_0 \mu_{\mathrm{e/h}} \vec{E} \vec{E}_\mathrm{W}\,, \tag{2.18}$$

with the total charge $Q = N e_0$, the electric field E, and the weighting field E_W [72, 73]. The weighting field accounts for the coupling of the charge carriers to the electrode, depends on the electrode geometry, and is in general position dependent [74].

An example of the weighting field in a strip detector is shown in figure 2.6a. In strip detectors, E_W has its maximum close to the readout strip and decreases towards the back side. Pad detectors with thickness d are a special case, as their weighting field is position independent and given by the constant $E_{\mathrm{W,pad}} = 1/d$. In high electric fields, the drift velocity reaches saturation and equation (2.18) becomes constant with the saturated induced current $I_\mathrm{sat} = Q\vec{E}_\mathrm{W}\vec{v}_\mathrm{sat}$. Further details on the Shockley-Ramo theorem can be found in [75, 76]. In principle, equation (2.18) can be used to extract the electric field when the induced current for a known charge deposition is recorded against time. However, this approach is usually not practical, as energy depositing processes generate charge in pairs of electrons and holes that have an opposite polarity and drift towards opposite collection electrodes. Thus, the measured induced current is the superposition of the electron and hole current, which complicates the direct extraction of the electric field. Further, diffusion smears out the distributions, which is why the correlation between drift time and position becomes less reliable. To avoid these difficulties, the electric field can be spatially investigated by using the current directly after charge generation, when the excess charge did not drift a meaningful distance. As the measurement electronics have a finite response, only the current at a short time after the charge generation t_pc is observable and the assumption of a linear response of the electronics is used to approximate $I_\mathrm{m}(t_\mathrm{pc}) \approx I(0)$, with the measured current I_m. The method is known as the prompt current (PC) method and PC times of $t_\mathrm{pc} = 600\,\mathrm{ps}$ are typical [5]. A comparison of the influence of different t_pc is shown in figure 2.6b, where the PC measured in a thick p-type pad detector using the

TPA-TCT is given against the device depth. Increasing t_{pc} lead to less steep edges in the PC profile, but similar results in the bulk and a decreasing t_{pc} lowers the SNR. No further details about the TPA-TCT and interpretations of this plot are given here, because this matter is discussed in detail in section 3.5 and 6.2, respectively. It should be noted that t_{pc} can not be selected arbitrarily short, because PC times that do not comply with the bandwidth of the readout electronics do not add additional information. This is a result of the damping of frequency components beyond the bandwidth of the readout electronics. In figure 2.6b this is visible for $t_{pc} = 200\,\text{ps}$ and 300 ps, as both yield about the same information. The bandwidth of the used readout electronics is not high enough for such short t_{pc}.

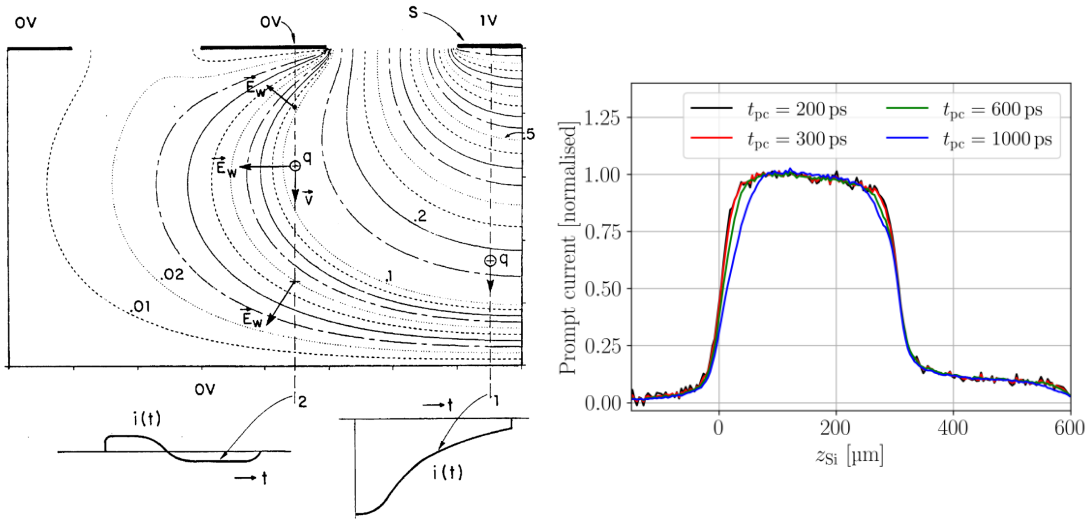

(a) **(b)**

Figure 2.6: (a) The weighting field in a strip detector. The sensing electrode is the right-most strip and labelled *S*. The induced current is shown for a charge terminating on the measurement electrode (lower right) and the neighbour electrode (lower left), showing the change in polarity. The caption is after [74] and the original figure is from [77]. (b) The prompt current measured with the TPA-TCT in the 300 µm thick CIS16 25-DS-66 p-type pad detector for different prompt current times t_{pc}.

2.4 Two photon absorption in silicon detectors

The process of two photon absorption (TPA) describes the excitation process of an atom by the simultaneous absorption of two photons [78]. It was predicted more than 90 years ago in 1931 [79] and experimentally proven in 1961 [80]. TPA allows absorption for photon energies below the band gap energy, which becomes relevant in silicon for wavelengths above 1100 nm and below 2300 nm. For wavelength below 1100 nm, linear absorption is the dominant contribution at room temperature. Figure 2.7a shows the single photon absorption (SPA) coefficient, i.e. linear absorption coefficient, of intrinsic silicon at 300 K, where it can be seen that the absorption for wavelength above 1100 nm is negligible in thin silicon samples (about 300 µm). The process of TPA is schematically shown in figure 2.7b. A single photon of the given wavelength does not provide enough energy to excite a valence electron to the conduction band, but simultaneous absorption of two such photons does.

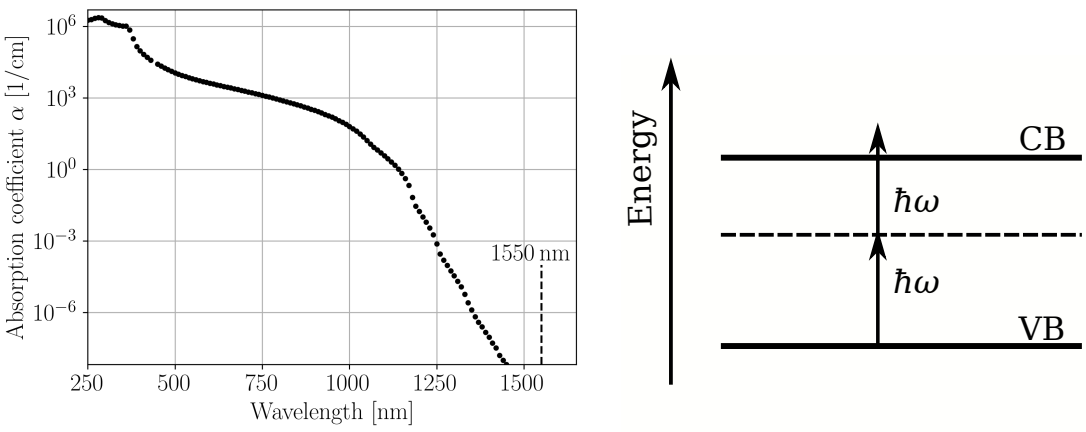

(a) **(b)**

Figure 2.7: (a) Linear absorption coefficient of silicon at 300 K in intrinsic silicon. The data is taken from [81]. (b) Sketch of the excitation process via two photons in a semiconductor.

The laser intensity decreases due to absorption in a medium along the propagation direction z. This process is described, up to the second order, by

$$\frac{\mathrm{d}I(r,z',t)}{\mathrm{d}z} = -\overbrace{\alpha I(r,z',t)}^{\text{SPA}} - \overbrace{\beta_2 I^2(r,z',t)}^{\text{TPA}} - \overbrace{\sigma_{\text{ex}} N I(r,z',t)}^{\text{FCA}} + \mathcal{O}\left(I^3\right) , \tag{2.19}$$

with the single photon absorption (SPA) coefficient α, the two photon absorption (TPA) coefficient β_2, the cross-section for free carrier absorption (FCA) σ_{ex}, and the amount of free charge carriers N [7]. Note that the intensity I has a distribution along the propagation direction. The centre of that distribution, i.e. the focal point is at the position z and additional movement along the distribution for a fixed z value is marked as z'. The two coordinate systems are visualised below in figure 2.8a. The first term in equation (2.19) corresponds to SPA, the second to TPA, and the third to FCA. With respect to TPA in silicon detectors, it is well justified to neglect the first and third contribution, because the linear absorption is negligible for the relevant wavelength regime (see figure 2.7a) and silicon has a negligible free charge carrier density. The TPA term yields the following solution to equation (2.19)

$$I(z,z') = \frac{I_0(r,z',t)}{1+\beta_2 \cdot (z+z') \cdot I_0(r,z',t)} , \tag{2.20}$$

with the initial intensity $I_0(r,z',t)$. In section 2.4.2 it will be shown that the absorption due to TPA is negligible and that the intensity is in good approximation constant over the whole depth.

2.4.1 Gaussian beams

Lasers can be operated with a variety of different transverse field distributions. The most relevant to this work is the Gaussian distribution for the so-called Gaussian beams, as it is the typical transverse field distribution of fibre lasers. In this section, the intensity profile of a Gaussian beam is discussed. Such a beam is described by the following intensity

distribution

$$I(r,z',t) = \frac{E_\mathrm{p} 4\sqrt{\ln 2}}{\tau\pi^{3/2}} \overbrace{\frac{1}{w^2(z')} \exp\left(-2\frac{r^2}{w^2(z')}\right)}^{R(r,z')} \overbrace{\exp\left(-4\ln 2 \frac{t^2}{\tau^2}\right)}^{T(t)}, \tag{2.21}$$

with the distance from the focal plane along the z-axis z', the pulse energy E_p, the temporal width τ, and the beam radius $w(z')$. $R(r,z')$ and $T(t)$ denote the spatial and temporal distribution, respectively [82]. The intensity I is given in units of $\mathrm{J/m^2 s}$. Figure 2.8a shows the relation between z and z'. The beam radius is a function of z' and given by

$$w(z') = w_0 \sqrt{1 + \left(\frac{z'}{z_\mathrm{R}}\right)^2}, \tag{2.22}$$

with the beam waist w_0 that is defined as the radius where the intensity drops to $1/\exp(2)$ of its maximum value at $z' = 0$ and the Rayleigh length z_R. $w(z')$ can be converted to the standard deviation of the Gaussian distribution of the intensity as $\sigma(z') = w(z')/2$. The course of the beam radius is schematically shown in figure 2.8b. Beam parameters of a Gaussian beam can not be selected independently, because the Rayleigh length is defined as the z'-value where the beam radius is $\sqrt{2}$-times larger than w_0 [78], which is in a medium with refractive index n given by

$$z_\mathrm{R} = \frac{\pi n w_0^2}{\lambda}. \tag{2.23}$$

Further, the opening angle θ can be approximated for large distances, i.e. $z' \gg z_\mathrm{R}$, as

$$\lim_{z'\to\infty} \theta = \frac{w(z')}{z'} = \frac{w_0}{z_\mathrm{R}} = \frac{\lambda}{\pi n w_0}. \tag{2.24}$$

Returning to the intensity profile in equation (2.21), the profile is normalised so that the integral over polar coordinates and time yields the pulse energy

$$\int_0^\infty \int_0^{2\pi} \int_0^\infty I(r,z,t) r \mathrm{d}r \mathrm{d}\varphi \mathrm{d}t = E_\mathrm{p}. \tag{2.25}$$

From this it can be seen that the pulse energy is the same for all depth z. This is only valid as long as absorption is neglected.

2.4.2 Excess charge carrier density

In the following, the excess charge carrier generation by SPA and TPA in a silicon detector will be derived. For normal incidence in a homogeneous medium with relative permittivity ϵ_r and relative permeability μ_r, the depth dependence in equation (2.19) can be substituted by the propagation of light

$$\mathrm{d}z = \frac{c}{\sqrt{\epsilon_\mathrm{r}\mu_\mathrm{r}}} \mathrm{d}t. \tag{2.26}$$

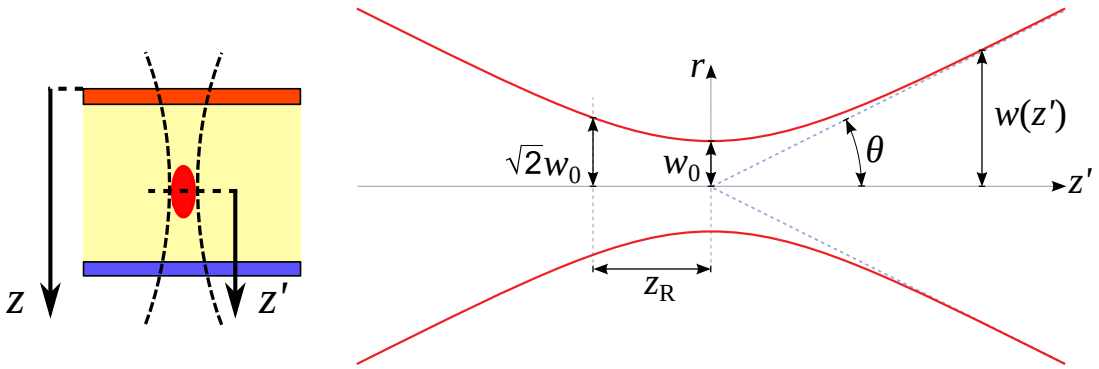

Figure 2.8: (a) Sketch of the coordinate system. The coordinate system marked z has its origin at the detectors surface and z' has its origin at the centre of the intensity profile. (b) Schematic intensity profile of a Gaussian beam with the usual notation of the beam parameters: the beam radius $w(z')$, the beam waist w_0, the Rayleigh length z_R, and the divergence angle θ.

This yields in silicon ($\mu_{\mathrm{r,Si}} \approx 1$) with negligible free carrier absorption

$$\frac{\mathrm{d}I}{\mathrm{d}t} = -\frac{c}{\sqrt{\epsilon_{\mathrm{r,Si}}}} \left(\alpha I + \beta_2 I^2\right) . \tag{2.27}$$

The intensity I has the photon density N_Ph and can be noted as the composition of the energy density $\hbar\omega N_\mathrm{Ph}$ and the propagation velocity $c/\sqrt{\epsilon_{\mathrm{r,Si}}}$

$$I = \frac{c}{\sqrt{\epsilon_{\mathrm{r,Si}}}} \hbar\omega N_\mathrm{Ph} . \tag{2.28}$$

Due to absorption, the photon density will be lowered with time due to SPA and TPA. However, the sum of the photon density and generated excess charge carriers must be constant to conserve the particle number. This can be written as a rate equation between the decreasing amount of photons and the increasing amount of excess charge carriers

$$\frac{\mathrm{d}N_\mathrm{Ph}}{\mathrm{d}t} = -\frac{\mathrm{d}n_\mathrm{SPA}}{\mathrm{d}t} - 2\frac{\mathrm{d}n_\mathrm{TPA}}{\mathrm{d}t} , \tag{2.29}$$

with the excess charge carrier density due to SPA n_SPA and TPA n_TPA. Combining equations (2.27) and (2.28), and comparing this to equation (2.29) yields the charge carrier generation of SPA and TPA

$$\frac{\mathrm{d}n_\mathrm{SPA}}{\mathrm{d}t} = \frac{\alpha}{\hbar\omega} I , \tag{2.30a}$$

$$\frac{\mathrm{d}n_\mathrm{TPA}}{\mathrm{d}t} = \frac{\beta_2}{2\hbar\omega} I^2 . \tag{2.30b}$$

Solving equation (2.19) for the SPA contribution yields the Lambert-Beer law

$$I(z, z') = I_0(r, z', t) \exp\left(-\alpha(z + z')\right), \tag{2.31}$$

with the initial intensity $I_0(r, z', t)$. The process of charge generation is in the order of several femtoseconds, which is fast relative to the observation time (several nanoseconds). Therefore,

the act of charge generation can be assumed as instantaneous and equation (2.30a) can be integrated over time. When equation (2.31) is inserted for the intensity, the excess charge carrier density generated by SPA is obtained

$$n_{\mathrm{SPA}}(r,z,z') = \frac{\alpha}{\hbar\omega}\frac{2E_{\mathrm{p}}}{\pi}R(r,z')\exp\left(-\alpha\cdot(z+z')\right). \tag{2.32}$$

The charge carrier density can be further integrated over polar coordinates to obtain the amount of charge carriers generated for a certain depth $z+z'$ along the light propagation direction

$$N_{\mathrm{SPA}}(z,z') = \int_0^{2\pi}\int_0^{\infty} n_{\mathrm{SPA}}(r,z,z')\,r\,\mathrm{d}r\mathrm{d}\varphi = \frac{\alpha}{\hbar\omega}E_{\mathrm{p}}\exp\left(-\alpha\cdot(z+z')\right). \tag{2.33}$$

It can be seen that the amount of excess charge carrier generation is a function of the device depth and a continuous ionisation occurs along the light propagation direction.

Neglecting absorption, analogous calculation for the TPA charge carrier generation of equation (2.30b) yields the TPA excess charge carrier density

$$n_{\mathrm{TPA}}(r,z') = \frac{E_{\mathrm{p}}^2\beta_2 4\ln 2}{\tau\hbar\omega\pi^{5/2}\sqrt{\ln 4}}\frac{1}{w^4(z')}\exp\left(-\frac{4r^2}{w^2(z')}\right). \tag{2.34}$$

Contrary to n_{SPA}, n_{TPA} is independent of the central position of the intensity z and proportional to the inverse of the temporal width τ. Hence, shorter pulses are in general beneficial for the process of TPA, until the dispersion limit of silicon is reached [83]. Pulses $\geq 60\,\mathrm{fs}$ comply with the dispersion limit [42]. It should be mentioned that the z dependence only disappears because absorption is neglected. The assumption of negligible beam depletion by TPA is investigated in the following. Equation (2.20) can be evaluated numerically for increasing depth of silicon. For the numerical evaluation, the centre position of the focal point is positioned at the top surface of a silicon bulk. Intensity loss due to absorption is calculated iteratively in steps of $1\,\mu\mathrm{m}$ for increasing depth inside the silicon. At each depth, the intensity after absorption is calculated and compared to the initial intensity. Figure 2.9a shows the result of the numerical evaluation, where the beam depletion due to TPA is presented as a function of the device thickness for different values of β_2. Typical laser beam parameters ($w_0 = 1.3\,\mu\mathrm{m}$, $\lambda = 1550\,\mu\mathrm{m}$, and $\tau = 430\,\mathrm{fs}$) are used for the calculation. Less than $1.5\,\%$ of the initial laser intensity is absorbed for all used β_2 after traversing $500\,\mu\mathrm{m}$ of silicon. This justifies the neglect of absorption for TPA in silicon. Further, in figure 2.9a it can be seen that absorption only occurs within the first few tenths of microns, as there is only one focal plane where the intensity is high enough for meaningful TPA. After the initial absorption, the transmission becomes constant, which is related to a negligible absorption. This reassures that TPA only generates charge carriers in a small volume around the focal spot and that the charge generation before and behind this small volume can be neglected. The absorption coefficient only moderately effects the absorption, which indicates that the precise value is not critical. In the literature β_2 is given with a large uncertainty as $\beta_2 = (0.79 \pm 0.39)\,\mathrm{cm/GW}$ [84]. In conclusion, it is a well justified to approximate equation (2.20) to $I(z,z') = I(z')$, which legitimises the TPA excess charge carrier density of equation (2.34).

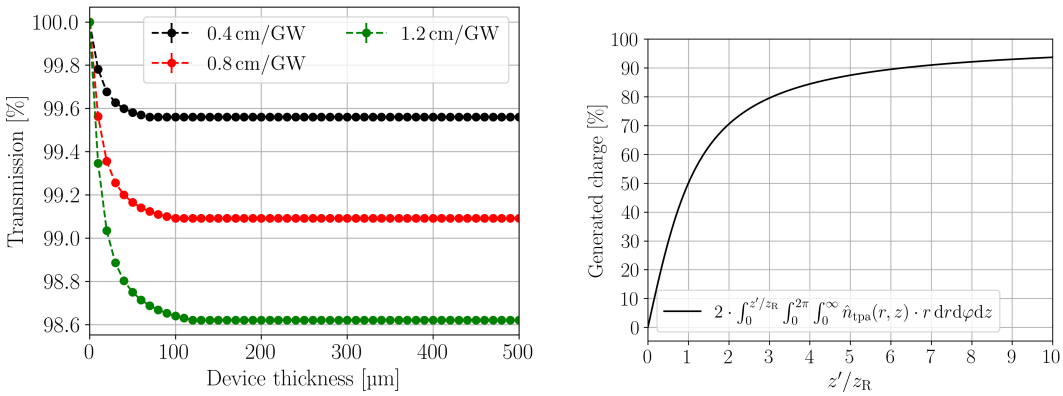

(a) **(b)**

Figure 2.9: (a) Simulated intensity loss due to two photon absorption as a function of the device thickness for different β_2. (b) Cumulative charge generation as a function of the distance from the focal point in units of the Rayleigh length.

The cumulative generated charge as a function of the distance from the focal point is shown in figure 2.9b. 50 % of the charge is generated within the first Rayleigh length and the increase in generated charge becomes less steep for increasing z'. The further away from the focal spot, the less charge is generated and the less relevant it is to the charge generation. The first Rayleigh length dominates the charge generation, which makes it a suitable parameter to quantify the spatial resolution of the TPA. Compared to TPA, SPA does not offer spatial resolution along the propagation direction. A comparison between the excess charge carrier densities generated by a red laser with $\lambda = 660\,\text{nm}$ (left), an infrared laser with $\lambda = 1060\,\text{nm}$ (middle), and a TPA infrared laser with $\lambda = 1550\,\text{nm}$ (right) is shown in figure 2.10. The beam waist of the SPA lasers is $w_0 = 10\,\mu\text{m}$, the beam waist of the TPA laser is $w_0 = 1.3\,\mu\text{m}$ and the focal plane is at $z = 50\,\mu\text{m}$. It can be seen that the

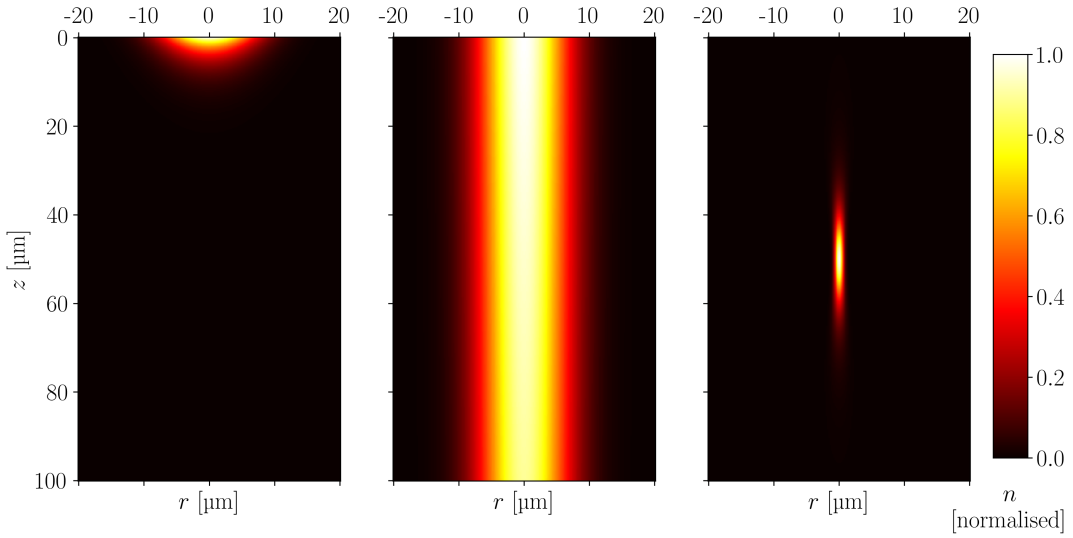

Figure 2.10: Calculated excess charge carrier densities in 100 µm silicon generated by a red laser with $\lambda = 660\,\text{nm}$ (left), an infrared laser with $\lambda = 1060\,\text{nm}$ (middle), and a TPA infrared laser with $\lambda = 1550\,\text{nm}$ (right). The focal point is in the centre at $z = 50\,\mu\text{m}$.

red laser is absorbed within the first few micrometers due to its high absorption coefficient (see figure 2.7a). The infrared laser is much less affected by absorption and generates charge carriers throughout the whole depth. Typical application of infrared SPA-TCT is the mimicking of the ionisation profile of a charged particle [4]. The Rayleigh length is chosen of comparable length as the device thickness, to approximate the ionisation profile to a pseudo track across the full device depth. The TPA infrared laser generates charge only in a small volume that is concentric around the focal point. Negligible charge generation above and below that volume is observed. The volume of charge generation is usually quantified by $\frac{4}{3}\pi w_0^2 z_\mathrm{R}$, because the most charge is generated within the first Rayleigh length, as discussed for figure 2.9b. It should be noted that the absorption, and hence the charge carrier generation can differ at very high doping concentrations [85].

2.4.3 Refraction in silicon

Refraction of light occurs when the refractive index of the traversed media changes. It is described by Snell's law and relevant to TPA-TCT, because silicon has a higher refractive index than air $n_\mathrm{Si}(293\,\mathrm{K}) = 3.4757 > n_\mathrm{air} \approx 1$ [86]. The refraction leads to an elongation in the propagation direction of the laser beam and enlarges the Rayleigh length (see equation (2.23)). The movement of the focal point in air and in silicon is related by a scaling factor that is derived in [42] to

$$\frac{z_\mathrm{Si}}{z} = \sqrt{\frac{\pi n_\mathrm{Si}^3 z_\mathrm{R,Si}}{\pi n_\mathrm{Si} z_\mathrm{R,Si} - \lambda n_\mathrm{Si}^2 + \lambda}}\,, \tag{2.35}$$

with the Rayleigh length in silicon $z_\mathrm{R,Si}$, which is defined by $z_\mathrm{R,Si} := z_\mathrm{R}\,(n_\mathrm{Si})$. The factor is constant with the depth and strongly depends on the used optical components, like the objective. The influence of the objective is discussed later in section 3.5.4. Here it is just mentioned that the scaling factor for an objective with NA = 0.5 (NA = 0.7) is found to be about 3.77 (4.12). The values are extracted from the Rayleigh length that is measured by in-depth scans with the TPA-TCT. The refraction needs to be taken into account for applications where the absolute position is of interest, for example when the active thickness is extracted. The lateral coordinates x and y are not affected by refraction.

2.5 Radiation damage

The limiting factor in the lifetime of silicon detectors in high energy physics experiments, is the loss in performance with increasing particle fluence. When high energetic particles traverse a silicon device, some energy is lost via non-ionising processes that can damage the silicon crystal by displacing lattice atoms. A sketch of displacement in a silicon lattice is shown in figure 2.11. They occur, when a recoil energy $\gtrapprox 25\,\mathrm{eV}$ is transferred to the lattice [57]. If even more energy is transferred by the primary knock on atom, the displaced silicon can displace consecutive lattice atoms, in compliance with the displacement threshold energy. The displacement damage is called point damage when only single silicon atoms are affected, in contrast to cluster damage where many neighbouring atoms are displaced. The impinging particle can knock the atom from its lattice position to form a vacancy and the displaced atom can come to a halt in-between lattice position to form an interstitial.

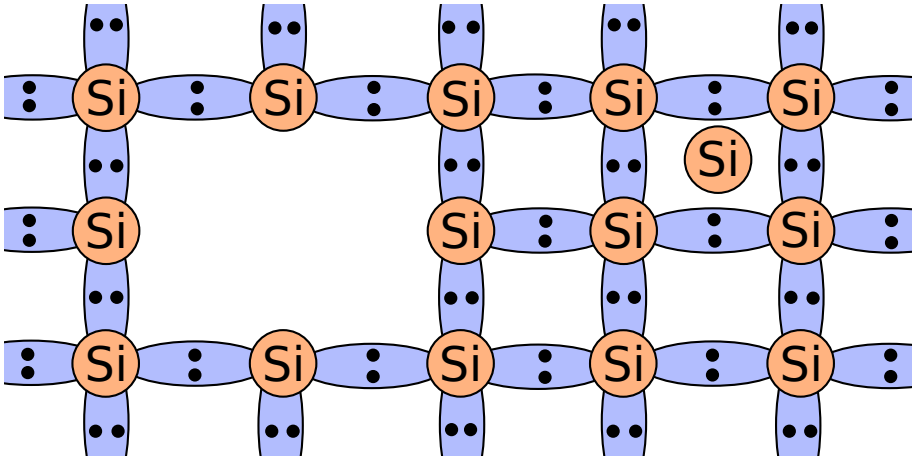

Figure 2.11: Schematic representation of the displacement damage in a silicon lattice. Radiation damage can lead to vacancies and interstitial atoms. These defects can occur in forms of multiples.

Vacancies and interstitials can appear in multiples, where multiple neighbouring atoms are displaced within the same event. Impurity atoms from the doping or the fabrication process may also be displaced, but as their concentration is usually orders of magnitudes less than silicon, their displacement is typically negligible. However, the impurity atoms can become mobile by interacting with migrating interstitials or vacancies. They can fill the vacancies (see figure 2.3), end up themselves as interstitials, or form more complex defects.

The amount of displacement damage a given particle introduces strongly depends on its kinetic energy and charge, as can be seen in figure 2.12. The damage functions of various particles normalised with the displacement damage of 1 MeV neutrons is shown against the particle energy. This damage functions are used to uniformise the damage from various particle species and energies. This kind of scaling underlies the non-ionising energy loss hypothesis (NIEL), which assumes that radiation damage reflects similar on the device performance, regardless its spatial distribution [87]. Following the NIEL hypothesis, radiation damage for all type of particles and particle energies should scale linear with the amount of transferred recoil energy. NIEL is a very successful concept to describe bulk-damage parameters, like the increase in generation current, but deviations are found for e.g. radiation induced changes in the space charge [88]. The deviations are related to the spatial distribution of displacement damage for different irradiations. Simulations from [89] are presented in figure 2.13, where the resulting damage distributions due to different irradiations is shown. For example, neutrons tend to introduce spatially confined damage in clusters with only few point defects, while low energetic protons lead to a more homogeneous distribution of point defects. The classification between cluster and point defects is non-trivial, because defects can have multiple bi-stable configurations, change their formation depending on their charge state and temperature, they can diffuse, recombine, or combine to defect complexes. For simulation purposes, the recoil energy is often used to distinguish the occurrence of cluster defects, where recoil energies $< 5\,\mathrm{keV}$ are related to exclusively point displacements, while higher recoil energies are related to point and cluster defects [87]. The maximum energy $E_{\mathrm{T,max}}$ a particle with mass m and kinetic energy E_{kin} transfers to a silicon lattice atom by elastic scattering is given in the

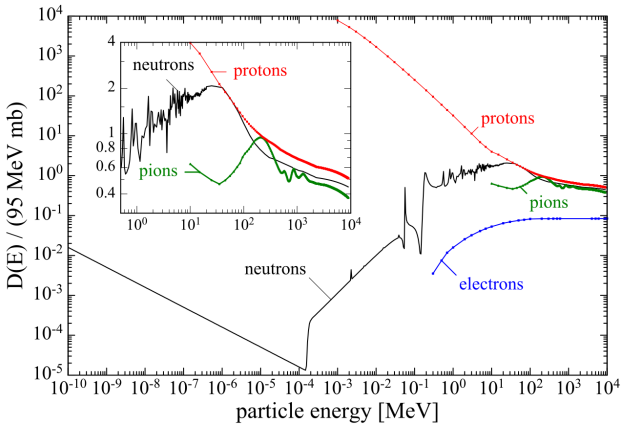

Figure 2.12: The displacement damage due to NIEL normalised with the displacement assumed damage of 1 MeV neutrons: $D_n(1\,\mathrm{MeV}) = 95\,\mathrm{MeV\,mb}$. The inset shows the high energy range with a linear scale for the ordinate. The figure is taken from [88] with data collected by [90].

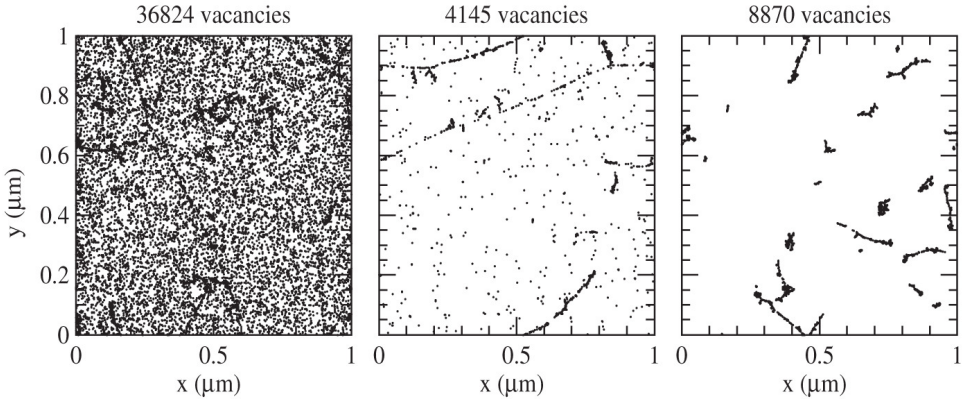

Figure 2.13: Initial distribution of vacancies produced by 10 MeV protons (left), 24 GeV/c protons (middle) and 1 MeV neutrons (right). The plots are projections over 1 µm of depth (z) and correspond to a fluence of $10^{14}\,\mathrm{cm}^{-2}$. The figure and the caption are taken from [89].

non-relativistic approach as

$$E_{\mathrm{T,max}} = 4E_{\mathrm{kin}}\frac{mm_{\mathrm{Si}}}{(m+m_{\mathrm{Si}})^2}\,. \tag{2.36}$$

When obeying the above-mentioned thresholds for displacement (25 eV) and the threshold for cluster damage production ($> 5\,\mathrm{keV}$), one can calculate the point and cluster damage thresholds for various particles [57]. Neutrons for example create point defects for $E_{\mathrm{kin}} > 185\,\mathrm{eV}$ and clusters for $> 35\,\mathrm{keV}$. Even for lower kinetic energies damage is observed as shown in figure 2.12. This damage is related to high energetic gamma ray emission after neutron capture. On the other hand, electrons need, due to their lower mass, much higher energies $E_{\mathrm{kin}} > 255\,\mathrm{keV}$ and $> 8\,\mathrm{MeV}$ for point and cluster damage, respectively. Compared to hadron irradiation, gamma rays do not directly damage the silicon crystal. By the mechanisms of the photoelectric/photovoltaic effect, pair production, and Compton scattering (see 2.3.2), they can produce high energetic electrons that may interact non-ionising with the silicon lattice. Gamma irradiation is typically performed with a ^{60}Co

source. ^{60}Co provides gamma rays of 1.17 MeV and 1.33 MeV. At such gamma ray energies, Compton scattering is the dominant effect [91] and the electrons that are produced have a maximum energy in the order of ≈ 1 MeV [92]. Using equation (2.36) and the displacement thresholds from above, it can be concluded that gamma irradiation with a ^{60}Co source creates, similar to low energetic electron irradiation, exclusively point defects, while neutrons produce dominantly cluster defects for typical irradiation energies. Hence, a comparison between identical devices irradiated with neutrons and ^{60}Co gamma rays (or low energetic electrons) allows drawing conclusions on cluster and point defects [93].

Following the NIEL hypothesis, the displacement damage from different irradiation facilities, i.e. different particle types and energy spectra, is aligned using the hardness factor κ. It is defined as the amount of displacement damage a particle with given energy spectrum introduces, with respect to the damage of a 1 MeV neutron. κ allows to calculate the NIEL fluence or equivalent fluence $\Phi_{\mathrm{eq}} = \kappa\Phi$ that is used to align NIEL damage parameters. It should be noted that the concept of the hardness factor is usually not applied to gamma irradiation, due to the completely different damaging mechanism involved [57].

2.5.1 Impact on the electrical characteristics

Defects can introduce energy levels within the band gap of silicon and thereby vary the electrical device characteristic. Figure 2.14 shows a schematic overview of additional energy levels within the band gap. Defects that introduce energy levels at or close to the middle of the band gap (I.) are efficient current generation centres and mainly responsible for the increase of the leakage current. When the levels are shallow, they act as donors or acceptors (II.) comparable to doping atoms, and thus contribute to the space charge. Deeper levels can capture charge carriers (III.), which are released after a defect specific trapping time. If the trapping time exceeds the collection time, the captured charge carrier does not contribute to the collected charge (CC) and becomes apparent as a decrease in the charge collection efficiency (CCE). Note that the categories are a simplification, as the effects are not exclusive. For example deep levels can also influence the SCR (e.g. $B_iO_i^+$ [94]) and shallow levels can also trap charge carriers (with typically short trapping times). In the following, the consequences of these three categories are explained in more detail.

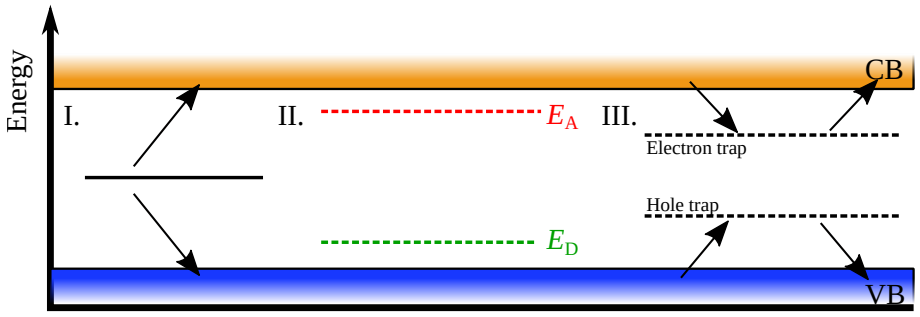

Figure 2.14: Schematic representation of energy levels introduced by impurities, defects, or radiation damage. Energy levels are efficient current generation centres when they are located close to or at the middle of the band gap (I.). Shallow levels act as donors or acceptors (II.) and deeper levels predominantly trap charge carriers (III.).

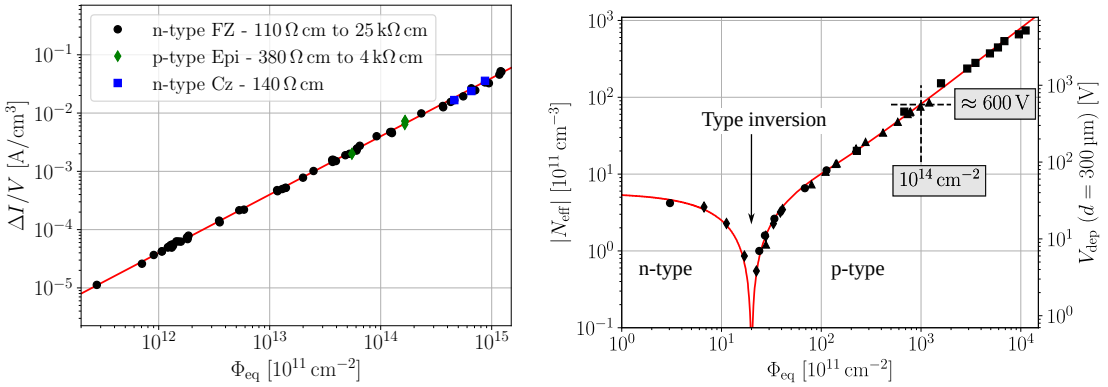

(a) **(b)**

Figure 2.15: (a) Volume current as a function of the equivalent fluence measured in silicon detectors of different resistivity and growth technique. The measurements are performed at 20 °C and the fit yields a slope of $\alpha_R(80\,\text{min}, 60\,°\text{C}) = (3.99 \pm 0.03) \cdot 10^{-17}\,\text{A/cm}$. The figure is adapted from [88] and shows data from [57]. (b) Effective space charge and depletion voltage as a function of the equivalent fluence in an n-type detector. The figure is adapted from [88] and shows data from [95].

The increase of leakage current is the most striking effect of irradiation. The volume current increases due to additional current generation centres in the SCR. From the Shockley-Read-Hall [96, 97] statistics it follows that energy levels at or close to the middle of the band gap are the most efficient current generators. A derivation of the above stated argument can be found in [57]. Figure 2.15a shows the volume current measured in various silicon devices versus the equivalent fluence. A linear relation is found in a log-log plot, where the slope yields the current-related damage factor α_R that is itself a function of the temperature and annealing state. Note that in literature the symbol α is used for the current-related damage factor and to avoid the ambiguity with the linear absorption coefficient, the index R is added. The increasing leakage current is for practical terms undesirable, as it increases the power consumption and can lead to additional noise in the readout electronics. Due to the strong temperature dependence of the leakage current (see equation (2.13)), an effective means to counteract leakage current is to lower the operation temperature. Highly irradiated devices are typically measured and operated at temperatures of about −20 °C. Defects with shallow energy levels contribute to the space charge, wherefore the bulk doping may not be exclusive from the initial acceptor or donor dopants. To cope with the presence of overlapping doping concentrations, the concept of effective doping is used. The bulk doping is then written as an effective doping

$$N_{\text{eff}} = |N_D - N_A|\,, \tag{2.37}$$

where N_D and N_A represent the donor and acceptor concentration in the SCR, respectively. Equations (2.4), (2.7), (2.8), (2.10), and (2.11) of section 2.2 can be rewritten, where N_A is replaced by N_{eff}. The concept is especially useful to quantify the bulk resistivity, where equation (2.6) is rewritten to

$$\rho = \frac{1}{e_0 \mu N_{\text{eff}}}\,, \tag{2.38}$$

with the mobility μ of the majority carrier. Holes (electrons) are the majority carrier in p-type (n-type) material. Changes in the space charge reflect especially on the depletion

voltage ($V_{\text{dep}} \propto N_{\text{eff}}$). Depending on the defect type and the specific device, the space charge can be increased or decreased and thus even be inverted. Figure 2.15b shows the evolution of the effective space charge and the depletion voltage with increasing neutron fluence in FZ n-type detectors. The depletion voltage decreases until a device specific equivalent fluence is reached and then starts to increase again with increasing fluence [95]. This is related to a build up of negative space charge due to the neutron irradiation that transforms the bulk flavour from n- to p-type. This process is called type inversion or space charge sign inversion (SCSI) and was first observed [98] and systematically studied [95] in n-type FZ detectors. It was observed that the SCSI occurs at higher fluences for oxygen rich silicon [99, 100], which was the main argument to use oxygenated n-type detectors to improve the radiation hardness. Type inversion finally lead to the use of p-type bulks for high energy particle experiments, as they are intrinsically radiation harder compared to the former used n-type bulks. It should be noted that even for p-type bulk SCSI was reported in Epi [101] and MCz [102] silicon, but at fluences and doses significantly higher than for n-type bulk. Besides the generation of additional donors or acceptors, radiation damage can also electrically deactivate present bulk dopants. Such mechanisms are called acceptor or donor removal [103] and an overview about the recent field of study is given in [104]. It is shown that these processes violate the NIEL hypothesis, because they differ with the type of irradiation, e.g. a higher acceptor removal is found for protons than for neutron irradiation [88]. A recent example for the NIEL violation by acceptor removal are so-called low gain avalanche detectors (LGADs), where protons remove about 2.5 times more acceptors than neutrons at the same equivalent fluence [105]. LGADs are discussed in more detail in chapter 5.

Defects with deep energy levels can capture charge carriers that are released after a defect specific trapping time. These trapping times and the occurrence of capture, i.e. the defect's trapping cross-section, are different for electrons and holes. For practical reasons, the trapping time of all individual defects is usually described with an effective trapping time approach, which is the mean of all individual trapping times of electrons and holes together. With the presence of trapping, the charge collected by drifting excess charge carriers is written as

$$Q(t) = Q_0(t) \cdot \exp\left(\frac{-t}{\tau_{\text{eff}}}\right), \tag{2.39}$$

where $Q_0(t)$ notes the charge transient without the presence of trapping and τ_{eff} the effective trapping time [107]. When the trapping time exceeds the charge collection time, the trapped carrier does not contribute to the signal and the CCE decreases. Section 4.5 contains CCE measurements of hadron irradiated pad detectors, where it is found that an equivalent fluence of about $5 \cdot 10^{15}\,\text{cm}^{-2}$ decreases the CCE to about 50 %. Hence, charge loss due to trapping is significant for the device performance and approaches to decrease the loss are essential to increase the radiation tolerance. Besides loss in the collected charge, deep level traps can influence the electric field shape. The so-called double junction is observed in hadron irradiated devices [108], which is related to polarisation due to trapping of deep level defects at the highly doped electrode contacts [106]. The effect is schematically shown in figure 2.16, where it is illustrated how trapping of charge carrier leads to the formation of a double peak electric field structure. The trapped charge carriers originate from the leakage current that continuously fills the traps. Contrary to type inversion, the double junction effect is independent of the bulk flavour and becomes always present after a given fluence of hadron irradiation.

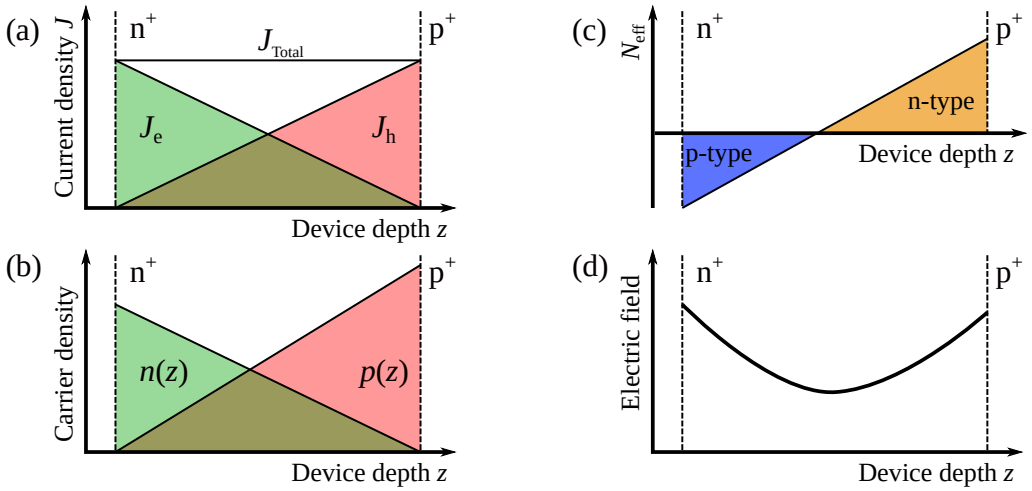

Figure 2.16: The diagrams illustrate the polarisation effect leading to a double-peak electric field distribution in sensors with high defect concentration. (a) Current density distribution due to the generation of leakage current. (b) Carrier density distribution with higher hole concentration due to lower hole mobility. (c) Distribution of space charge due to predominant trapping of electrons close to the n^+-contact and holes close to the p^+-contact. (d) Distribution of electric field strength arising out of space charge distribution given in (c). The caption and figure are adapted from [88] and the model behind the diagrams was developed in [106].

2.5.2 Impact on the optical absorption

Besides electrical properties, the optical properties of silicon detectors are as well influenced by radiation damage. The additional energy levels of the defects can introduce absorption bands further in the infrared that give rise to infrared absorption even with $\hbar\omega < E_g$ [109, 110]. Additional absorption occurs when the energy levels lie within the band gap so that a single photon can provide enough energy to excite a charge carrier. The sketch in figure 2.17 visualises the introduction of linear absorption by defect levels for photon energies below the band gap energy. It is ensured that the band gap energy E_g is constant for up to at least $\Phi_{eq} = 10^{17}\,\mathrm{cm}^{-2}$ [111]. Further, it is found in section 4.8 that hadron or gamma irradiation does not significantly influence the refractive index, which means

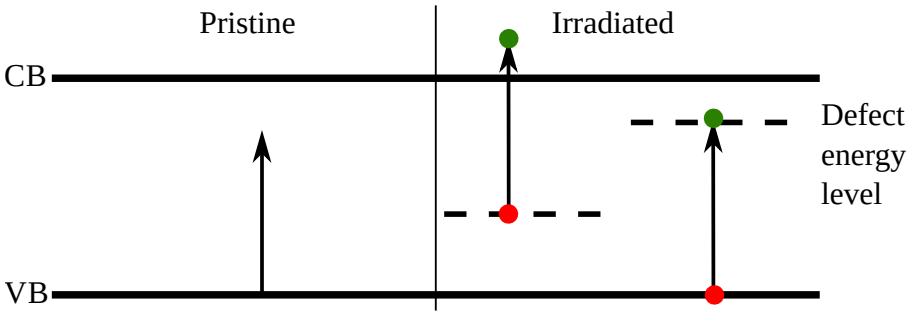

Figure 2.17: Schematic representation of additional linear due to defect energy levels. On the left-hand side a pristine sample is shown, where a single photon does not provide enough energy to a charge carrier in the valence band. On the right-hand side the same situation is shown in an irradiated sample. A single photon provides enough energy to excite a charge carrier from or into a defect level, which is than available for conduction. Holes are sketched as red and electrons as green dots.

that the reflectivity of silicon is not changed by fluences relevant to high energy particle detectors. However, it should be noted that the refractive index increases with heavy ion irradiation, which is already significant at fluences of $10^{14}\,\mathrm{cm}^{-2}$ [112].

2.5.3 Annealing

When damaged silicon is treated with heat, a partial curing of the crystal is observed, where the concentrations of some defects tend to shrink significantly. This process is called annealing, and it strongly depends on the temperature and time the damaged silicon is exposed to a selected temperature. Thereby, the temperature defines how fast the annealing process takes place, where elevated temperatures increase the speed of annealing, while lower temperatures can practically stop it. The naive picture of the process is that defects, e.g. vacancies and interstitials, migrate through the lattice and recombine with their counterpart. Elevated temperatures accelerate the migration and thus the annealing process. However, measurements show that this picture oversimplifies the process, as aside of the curing effect also disadvantageous effects are observed [57, 113]. Figure 2.18 shows the influence of annealing on the effective space charge (a) and the charge carrier trapping (b), where annealing can be beneficial or disadvantageous for the device parameters. Concerning the effective space charge, two distinct annealing regions are observed. The first region occurs within the first $\approx 100\,\mathrm{min}$, where the effective space charge is reduced and part of the radiation damage is cured. This region is called beneficial annealing, to distinct it from the second region, the reverse annealing, where the effective space charge increases up to a given saturation. Annealing is very important with respect to the detector operation, because short term annealing is often exploited to extend the detector's operation lifetime. Regarding the charge carrier trapping shown in figure 2.18b, differences between electrons and holes are found, which shows that the defects responsible for the corresponding trapping are treated differently by annealing. As the annealing state has a strong impact on the device parameters, a standard heat treatment of 10 min at 60 °C is typically applied to make the device history negligible and ensure that all devices are in the same annealing state.

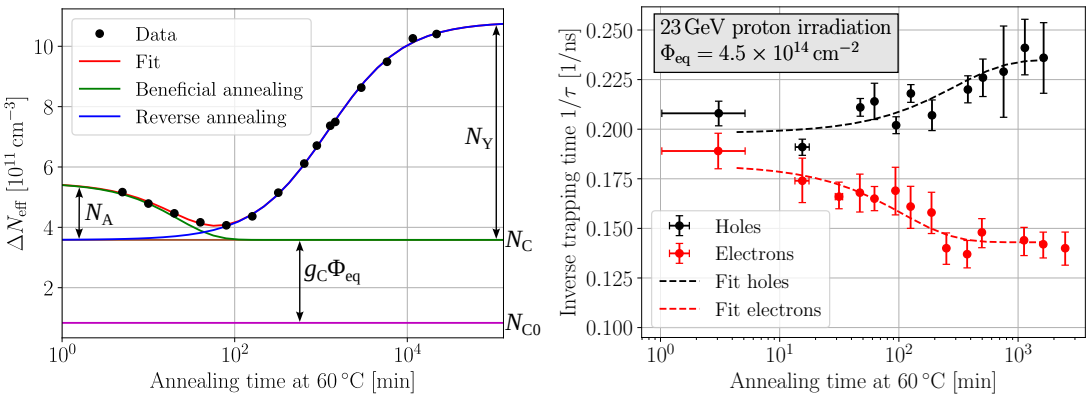

(a) **(b)**

Figure 2.18: (a) Effective doping concentration at different annealing times. $g_C \cdot \Phi_{eq}$ is the stable damage, N_A the beneficial annealing component and N_Y the reverse annealing component. (b) Inverse trapping time at different annealing states for electrons and holes. The figures are adapted from [88] and show data from [57] and [113].

3 Experimental methods

This chapter introduces the devices, methods, and corresponding experimental setups for the device characterisation. To this work three different kinds of techniques are the most relevant: electrical characterisation, source measurement with a ^{90}Sr source, and laser based charge injection, i.e. the TPA-TCT. This chapter first introduces the used devices and then describes the methods and setups.

3.1 Devices

This section gives a tabulated overview about the devices used within this thesis. A distinction between pad and segmented detectors is made.

3.1.1 Pad detectors

Pad detectors are the simplest realisation of pn-junction based detectors and hence widely used for the device research. Table 3.1 summarises the used pristine pad detectors. Note that one low gain avalanche detector (W5-D8-LGAD2) is included in the table as well. This device is subject of section 5.

Table 3.1: Details of the pristine pad sensors. The active thicknesses are extracted using the TPA-TCT.

Name	Campaign	Producer	Bulk type	Resistivity [kΩ cm]	Active thickness [µm]
WL-A63-PIN4	7859	CNM	FZ p	≈ 3.7	290
W5-J6-PIN2	8622				286
W5-D8-LGAD2	8622				286
25-DS-66	CiS16	CiS	FZ p	>10	300
21-DS-79					156
04-DiodeL-5	Deep diffused	HPK	FZ n	N/A	304
02-DiodeL-8			FZ p		304
05-DiodeL-3			FZ n		204
09-DiodeL-1			FZ n		150
05-DiodeL-2			Epi p		103
12-DiodeL-2			Epi n		67
07-DiodeL-3			Epi n		54

Pad detectors fabricated by CiS [114] in the CiS16 campaign were used to investigate the effects of irradiation. Neutron irradiation was performed at the TRIGA reactor at the Jožef Stefan Institute [115], proton irradiation at the PS-IRRAD proton facility at CERN [116], and gamma irradiation at the Ruđer Bošković Institute [117]. The neutron irradiation in the TRIGA reactor has a broad energy spectrum and in order to obtain the equivalent fluences the hardness factor $\kappa_n = 1.00 \pm 0.05$ is used. It should be noted that the fluences obtained from the TRIGA reactor facility are already the 1 MeV equivalent fluences, which is why $n/cm^2 = n_{eq}/cm^2$ within this work. The notation n/cm^2 is still used to distinguish the type of irradiation from the proton irradiation, where p/cm^2 states the fluence. The

PS-IRRAD proton facility uses 23 GeV protons for the irradiation and the hardness factor of the facility is $\kappa_{23\,\mathrm{GeV\ p}} = 0.62 \pm 0.01$. The gamma irradiation was performed with a ^{60}Co source. No hardness factor can be given for the gamma irradiation due to the completely different damage mechanism. Table 3.2 summarises the fluences/doses and annealing states of the used devices. Measurements performed on the devices can be found in section 4.

Table 3.2: Details of the irradiated pad sensors. All devices are fabricated by CiS in the CiS16 campaign and have a FZ p-type bulk with a pre-irradiation resistivity $> 10\,\mathrm{k\Omega\,cm}$. The active thickness is extracted from the corresponding pristine device.

Name	Active thickness [µm]	Fluence/ Dose	Annealing state
Neutron [n/cm^2]			
21-DS-78	156 µm	$7.80 \cdot 10^{12}$	10 min at 60 °C and 6600 min at 20 °C
21-DS-84		$3.86 \cdot 10^{13}$	
21-DS-98		$7.80 \cdot 10^{13}$	
21-DS-99		$3.32 \cdot 10^{14}$	
21-DS-101		$5.00 \cdot 10^{15}$	
21-DS-102		$7.02 \cdot 10^{15}$	
25-DS-104	300 µm	$3.32 \cdot 10^{14}$	
25-DS-87		$5.00 \cdot 10^{15}$	
25-DS-88		$7.02 \cdot 10^{15}$	
Proton [p/cm^2]			
21-DS-97	156 µm	$1.3 \cdot 10^{13}$	10 min at 60 °C and 6600 min at 20 °C
21-DS-96		$6.44 \cdot 10^{13}$	
21-DS-94		$5.54 \cdot 10^{14}$	
21-DS-92		$1.17 \cdot 10^{16}$	
Gamma [Mrad]			
19-DS-97	156 µm	92.4	None
19-DS-99		186.1	

3.1.2 Segmented detectors

Within this work, several segmented devices were investigated, which are summarised in table 3.3. All devices are pristine, and their measurement results are mainly presented within section 6.

Table 3.3: Details of the segmented devices used within this work.

Name	Device type	Project	Producer	Bulk type	Pitch [µm]	Active thickness [µm]
2328-11	Strip	N/A	Micron	FZ p	80	300
F2-S1	Strip	passive CMOS	LFoundry	p	75.5	156
HV-CMOS	CCPD v3	HV-CMOS	LFoundry	p	N/A	30
MPW2-04	Monolithic	RD50-MPW2	LFoundry	p	N/A	94
W6417A	Monolithic	Monolith picoAD	IHP	p	100	15

3.2 Electrical characterisation techniques

The power consumption and the operational voltage range are key parameters for particle detectors. They are defined by the leakage current and the effective doping concentration, which are characterised by current-voltage (IV) and capacitance-voltage (CV) measurements. Section 2.2 discussed the electrical behaviour of an ideal particle detector, where the IV and the CV characteristic was determined in equations (2.12) and (2.10), respectively. Here, IV and CV characterisation is performed in a probe station, where the device under test (DUT) is fixed with vacuum to a thermally controlled chuck. The chuck supplies the high voltage to the back side of the DUT and the top side is contacted with a needle probe. It is advantageous to apply the high voltage to the back side for two reasons. First, the pad and the guard ring (GR) are usually contacted separately. To avoid separate biasing of the GR, which requires an additional power supply, the ground is set to the top surface. The decoupling of the pad from the total current is needed, because the total current is typically dominated by currents from the edges that originate from the dicing that are collected by the GR. Second, sparks occur more likely when the high potential is applied via a needle, because of the small diameter at the needle tip. The risk is significantly lower if the high potential is applied by a large area, which is here the chuck. The chuck is cooled by an Unichiller from Huber [118] and temperatures of $-25\,°C$ are stably reached ($\sigma < 0.1\,°C$). Condensation at temperatures below the dew point is avoided by continuos dry air flushing. A picture of the chuck is presented in figure 3.1. A pad detector is positioned above a small hole that provides a vacuum to hold the DUT in place. The needle probes contact the pad and the GR. A metal box encloses probe station that serves as a Faraday cage to shield external electromagnetic noise. The Faraday cage was opened for the picture in figure 3.1 and is thus not visible. Two configurations of the setup are available to measure IV or CV characteristics. The configuration can be interchanged by an electrical switch. Figure 3.2 shows a scheme of the IV (a) and the CV (b) configuration. Precise current measurement is performed through a Keithley 6487 pA-meter. The bias voltage is provided using a Keithley 2410 source-meter, which also records the total current. An

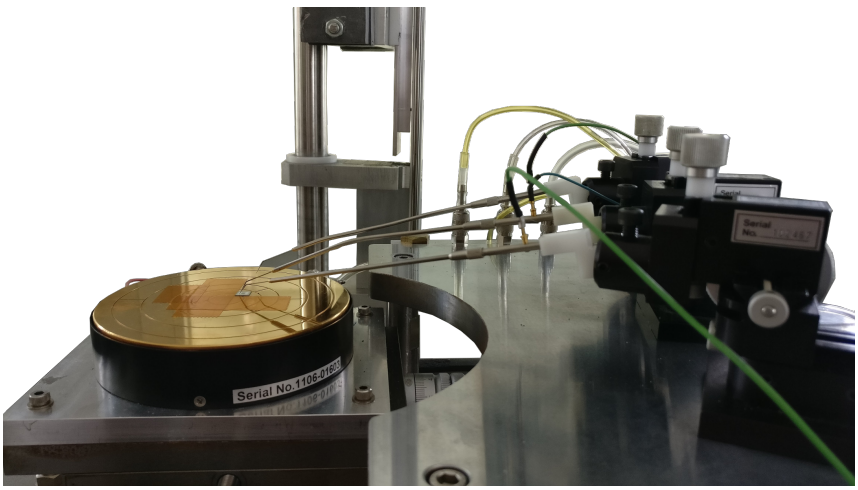

Figure 3.1: Picture of the probe station used for the electrical characterisation. The DUT is fixed by vacuum to a chuck. The high voltage is applied from the chuck and the ground connection is done by probing needles. Multiple needles are available to probe the pad and guard ring individually. The figure is taken with modification from [119].

Agilent E4980A LCR meter is used for the capacitance measurement. The bias voltage is set by a Keithley 2410 source-meter, which defines a fixed depletion width, e.g. the capacitance. This capacitance is probed by the LCR meter through the application of a small alternating voltage ($\delta V \ll V_{\text{bias}}$) with frequency f. The LCR meter has a frequency range between $20\,\text{Hz} \leq f \leq 2\,\text{MHz}$ and an operational voltage range of $\pm 42\,\text{V}$. Usual particle detectors require higher bias voltages, wherefore the LCR meter is decoupled from the DC voltage by an isolation box that extends the operation range to the maximum range of the voltage supply ($\pm 1.1\,\text{kV}$).

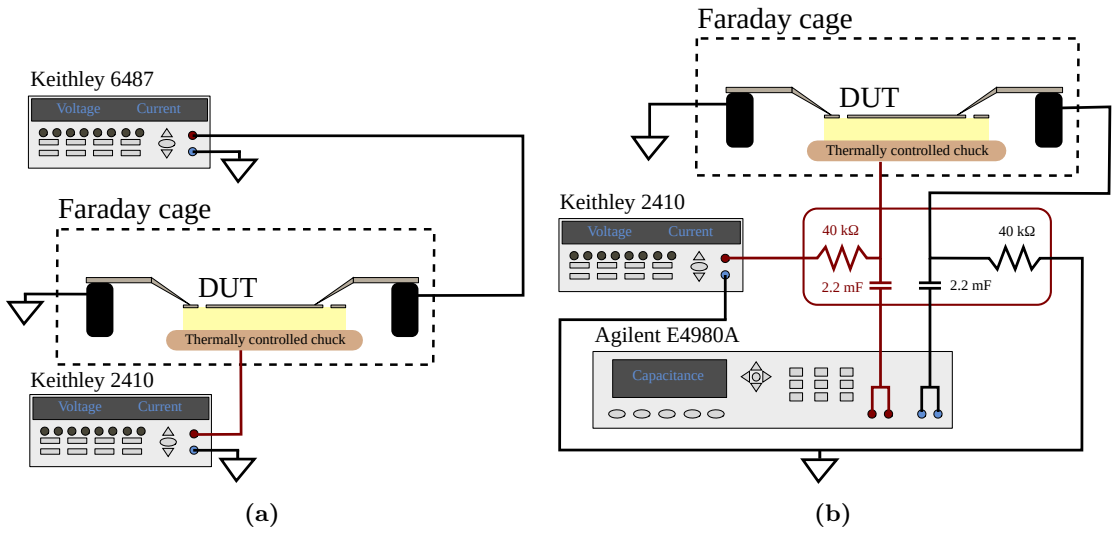

Figure 3.2: Sketch of the IV (a) and the CV (b) setup (after [120]). The setup can be changed between configuration (a) and (b) via an electrical switch.

3.3 ^{90}Sr setup

Measurements with radioactive sources are a valuable tool for the detector characterisation. The source emits particles that generate excess charge carriers via energy deposition. α-, β-, and γ-particles can be used, where ^{241}Am, ^{90}Sr, and ^{55}Fe are used as a source, respectively. There are three main benefits of source measurements, which are discussed in the following. First, source measurements allow to study the influence of a probabilistic excess charge generation, which is not feasible with light. Second, compared to charge generation via light, particles do not require an opening window in the electrode, because they penetrate metals. Third, source setups can be lightweight setups, which makes the application widely available. Their main drawbacks are the hazard due to the radioactive source material and lower SNR compared to laser measurements. Laser measurements generate pulse-per-pulse a reproducible excess charge, which is why signal averaging can be applied to increase the SNR. The SNR of laser setups is typically higher, because the amount of excess charge can be tuned to much larger values than available with typical sources. In the framework of this work, a ^{90}Sr source setup was used. The charge generation profile of a ^{90}Sr source is assumed as a 1 µm wide cylinder that extends over the full traversing path, i.e. the full device depth. The here used ^{90}Sr setup is depicted in figure 3.3 as a photography (a) and a sketch (b). Three devices are stacked on top of each other, whereby

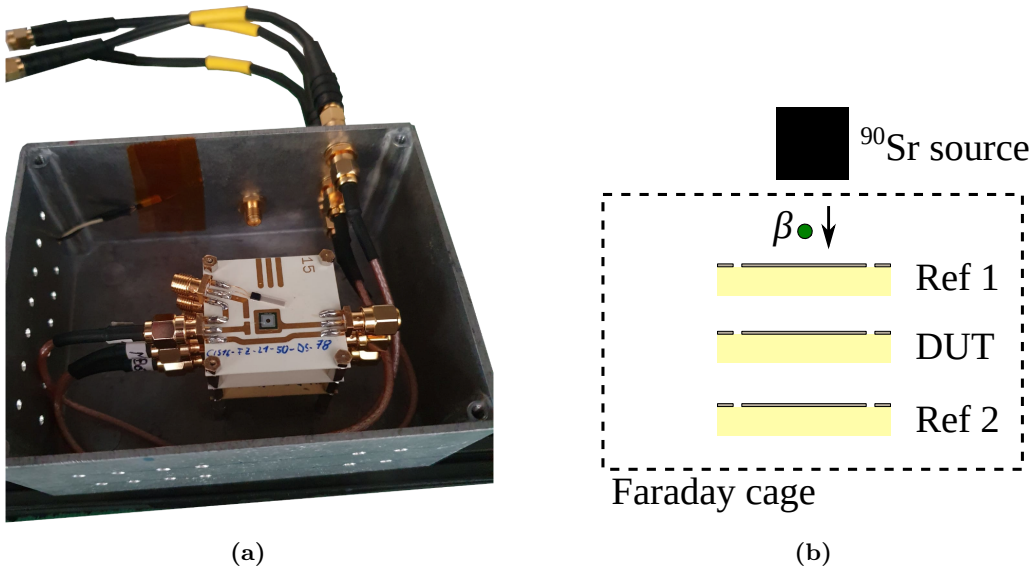

Figure 3.3: Picture (a) and sketch (b) of the ^{90}Sr setup. The top plate of the Faraday cage was removed for the picture. The DUT is stacked in between two reference sensors inside a Faraday cage and the Pt1000 at the upper wall serves as a temperature reference. The source is placed central above the stack of sensors on top of the top plate of the Faraday cage.

the middle device is the DUT and the other two devices serve as references. Coincidence between the two references is used to trigger the data acquisition. The data acquisition is done by the Keysight MXR254A that provides a bandwidth of 2.5 GHz with a sampling rate of 16 GSa/s. The stacked configuration is selected to lower the acceptance angle, to avoid heavily inclined β-particles. The devices are operated under high voltage supplied by an ISEG SHQ 222M. The signals require amplification to be in a suitable voltage range. Therefore, two different amplifier versions are available: the C2HV and the Cx-L amplifier from CIVIDEC [121], which serve as a transimpedance and a charge sensitive amplifier, respectively. Both versions provide an amplification of about 40 dB with a bandwidth of 10 kHz to 2 GHz. Charge sensitive amplifiers (CSA) are used for precise charge collection (CC) measurements, while transimpedance amplifiers allow studying induced current transients and enable the study of timing properties. The source has an activity of about 18.55 MBq and is encapsulated in a stainless steel capsule with a ceramic window. For the safe handling of the source it is further enclosed in a poly-carbonate encasing with an opening at the bottom that serves as a collimator. The Faraday cage is positioned inside a climate chamber that allows to control the temperature. Temperatures between 20 °C and −20 °C are stably reached by the setup ($\sigma < 0.1$ °C). The setup is used for CC measurements in section 4.5 and 5.3.

3.4 Transient current technique

The transient current technique (TCT) is a detector characterisation method that studies the drift of excess charge carriers. It emerged as an alternative to electrical techniques, e.g. CV- and IV-measurements, with the aim to extract the effective doping concentration of irradiated devices [2] and developed into an essential tool for the device characterisation

before and after irradiation for all kind of device parameters. When excess charge carriers are generated in a depleted volume, they begin to drift and induce a current at the readout electrode according to the Shockley-Ramo theorem (see section 2.3.4). This current contains information about the generated charge and more importantly about the DUT itself. An example of an induced current transient is shown in figure 3.4 measured in a thick pad detector. Figure 3.4a is based on a charge generation close to the top side and shows the extraction of the prompt current $I_{\mathrm{m}}(t_{\mathrm{pc}})$ and the collected charge Q_{coll}. For the prompt current (PC), first the starting time t_0 of the signal is found by a linear fit towards the rising edge. A region $\pm 500\,\mathrm{ps}$ around the 20 % threshold of the maximum signal amplitude is used for the fit. The intersection between the rising edge fit and the baseline yields t_0. The starting time serves as a reference to the PC time t_{pc}. The baseline of the pulse is extracted as the mean before the illumination, e.g. the mean between $-10\,\mathrm{ns} \leq t \leq -2\,\mathrm{ns}$. The CC is extracted as the integral of the induced current

$$Q_{\mathrm{coll}} = \int_{t_0}^{t_{\mathrm{coll}}} I_{\mathrm{m}}(t)\mathrm{d}t\,, \tag{3.1}$$

for a collection time t_{coll}. The collection time needs to be selected long enough to allow full charge collection in waveforms from all depth. Usually, a t_{coll} of about 25 ns is used for a 300 µm thick device. Figure 3.4b shows the extraction of the time over threshold (ToT) and rise time (RT) from an induced current transient taken at the back side of a thick pad detector. The ToT is defined as the time the current transient is above a given threshold relative to the maximum amplitude (here 20 %). The RT is defined as the time in which the induced current rises from 20 % to 80 % of its maximum amplitude.

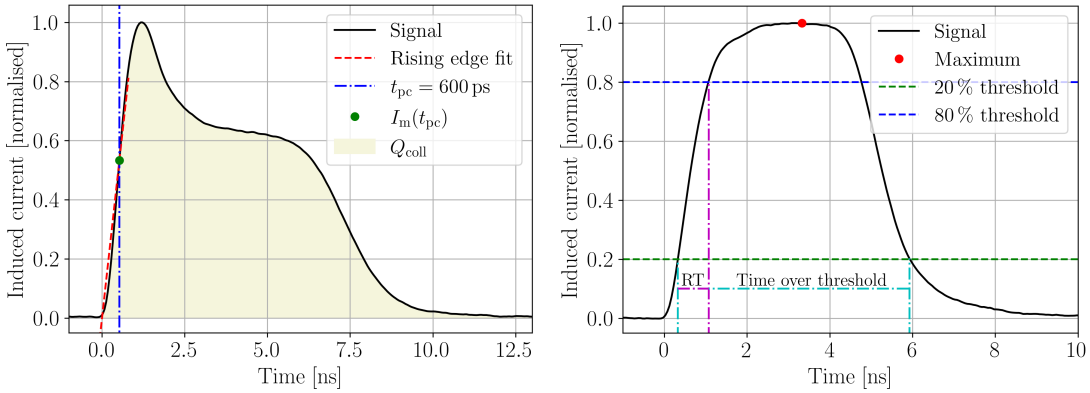

(a) **(b)**

Figure 3.4: Induced current waveforms recorded with the TPA-TCT in the CiS16 25-DS-66 pad detector. Methods to extract the start time, the prompt current, and collected charge are shown in (a). The extraction of the time over threshold, the signal maximum, and the rise time (RT) is shown in (b).

Transient excess charge can be generated via ionising particles or pulsed light sources. Both mechanisms are widely spread, but for this work the latter is of specific interest. Pulsed light sources are well suited for the device characterisation, because they generate charge in a non-destructive manner and provide a well-defined and reproducible charge generation. Further, such setups are, compared to beam test facilities, cheap and thus widely used. Lasers are mainly used due to their small spectral bandwidth and short temporal profiles

down to the fs-regime. For the TCT in silicon mainly lasers with red $\lambda_{\mathrm{red}} \approx 700\,\mathrm{nm}$ and infrared $\lambda_{\mathrm{IR}} \approx 1060\,\mathrm{nm}$ wavelength are used. Developments in commercial fs-pulse infrared laser systems boost the usage of central wavelength in the quadratic absorption regime, e.g. $\lambda_{\mathrm{TPA}} \approx 1550\,\mathrm{nm}$ to exploit the charge generation by TPA. Contrary to SPA, the TPA generates excess charge in a confined volume that allows measurements with three-dimensional spatial resolution. A comparison of the different excess charge carrier densities is presented in section 2.4.2 and visualised in figure 2.10. It should be noted that resolution along the device depth can also be achieved with λ_{IR}, when the illumination is applied from the edge (edge-TCT) [5]. Compared to TPA-TCT, edge-TCT requires careful sample preparation, which is not suitable for every device. Further, for high spatial resolution, the edge-TCT can not be applied if the active volume is not reasonably close to the device edge, because of the laser beam divergence. This can be relevant to pad detectors, because most devices have a width $> 1\,\mathrm{mm}$ where the laser opening cone for focused lasers might exceed the device dimensions. However, edge-TCT is a valuable tool for the device characterisation and contributed especially to the characterisation of strip detectors. The mentioned difficulties of edge-TCT do not apply to TPA-TCT, as resolution along the device depth is already obtained by illumination from the top side.

In the framework of this work an SPA-TCT setup is available, which employs red and infrared lasers. Both lasers can be either applied from the top or bottom. For the red lasers this is ideal to study the drift of electrons or holes independently depending on the illumination direction. Additional to top and bottom illumination, the SPA infrared lasers can as well be applied from the edge to enable edge-TCT. The setup is not central to this work, which is why the reader is referred to [122] for a detailed description of the setup.

3.5 Two photon absorption – transient current technique

The TPA-TCT was developed to obtain spatial resolution along the device depth and profits from the profound experience available from the SPA-TCT. This section focuses on the experimental implementation of the technique and discusses topics relevant to the application. First, a description of the TPA-TCT setup from the CERN EP-DT-DD SSD group is given. Second, the calibration of the setup regarding the laser pulse energy and its energy stability are shown and the influence of the objective is discussed, where recommendations for an adequate choice are given. Finally, setup parameters like the spatial resolution and noise are investigated, a description of the alignment procedure and sample preparation is given, and studies of high laser intensities, influence of temperature, clipping and reflection are presented.

3.5.1 TPA-TCT setup

The setup was commissioned within the work of [13]. It is shown as a sketch in figure 3.5 and as a photography in figure 3.6. Femtosecond laser pulses with a central wavelength of $\lambda = 1550\,\mathrm{nm}$ are provided by the FYLA LFC1500X fibre laser module that is used as a laser source. It provides a $\tau = 430\,\mathrm{fs}$ long laser pulse with a repetition rate of 8.2 MHz and a pulse energy of $E_{\mathrm{p}} = 10\,\mathrm{nJ}$. Downstream the laser source, the light is guided into the

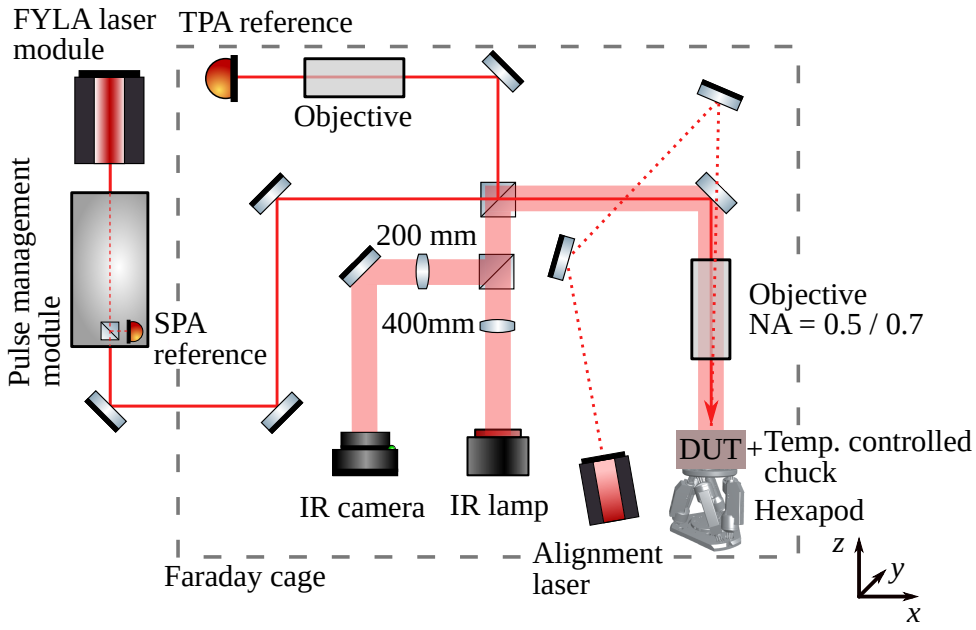

Figure 3.5: Schematic drawing of the TPA-TCT setup.

pulse management module, where the repetition rate can be adjusted by an acusto-optic modulator and the pulse energy can be lowered to a given value by a neutral density filter (NDF). Further, an SPA reference and a diode that produces a trigger signal are included inside the pulse management module. Repetition rates of 1 kHz are typically used, and for irradiated devices the repetition rate is lowered to 200 Hz to decrease potential accumulation of trapped charge carriers. The NDF is a circular disc with decreasing transparency for increasing angles, i.e. higher angles correspond to lower pulse energies. The laser system is commercially available and was developed in a collaboration between FYLA [123], IFCA [124], and CERN [125]. A detailed description of the laser system can be found in [12]. Downstream the pulse management module, the beam traverses through open space inside a Faraday cage that shields from external electromagnetic noise. Mirrors designed for the used wavelength are used to guide the light through an objective onto the DUT. The choice of objective is delicate and discussed in detail in section 3.5.4. The DUT itself is typically glued to a printed circuit board (PCB), which provides a stable mount and electrical contact. For a measurement, the PCB is screwed to a copper chuck for two reasons. First, it serves as a mount for the PCB and second, it is thermally coupled to a Peltier element, so that it allows to temperature control the DUT. The hot side of the Peltier element is cooled by a chiller from Huber [118]. The copper chuck is mounted on a six axis hexapod stage that has a step size precision of 200 nm. Beyond precise movement in xyz-direction, it allows rotation around all three axes, which is useful for a precise sample alignment. The sample alignment is discussed in section 3.5.5. Fifty percent of the laser beam is coupled out from the primary beam to a second arm, which is guided towards a reference silicon pad detector that serves as a TPA reference. Calibration measurements of the SPA and TPA reference are presented in section 3.5.2 and the energy stability obtained with the references is shown in section 3.5.3. As the central wavelength of the TPA laser is not visible by the human eye, a red laser diode is used to perform the coarse alignment of the DUT. The path of the alignment laser is emphasised by the red dotted line in figure 3.5. Precise alignment is performed using an infrared microscope. The infrared microscope

consists of a camera and a lamp, where each of which operates at a wavelength of 1550 nm. A thick transparent red line shows the beam path of the microscope in figure 3.5 and example pictures of it are depicted in figure 3.7. The microscope is especially useful to find small regions of interest, e.g. in segmented devices and as it allows measuring through silicon, the microscope is even useful when illumination is applied from the back side of a DUT.

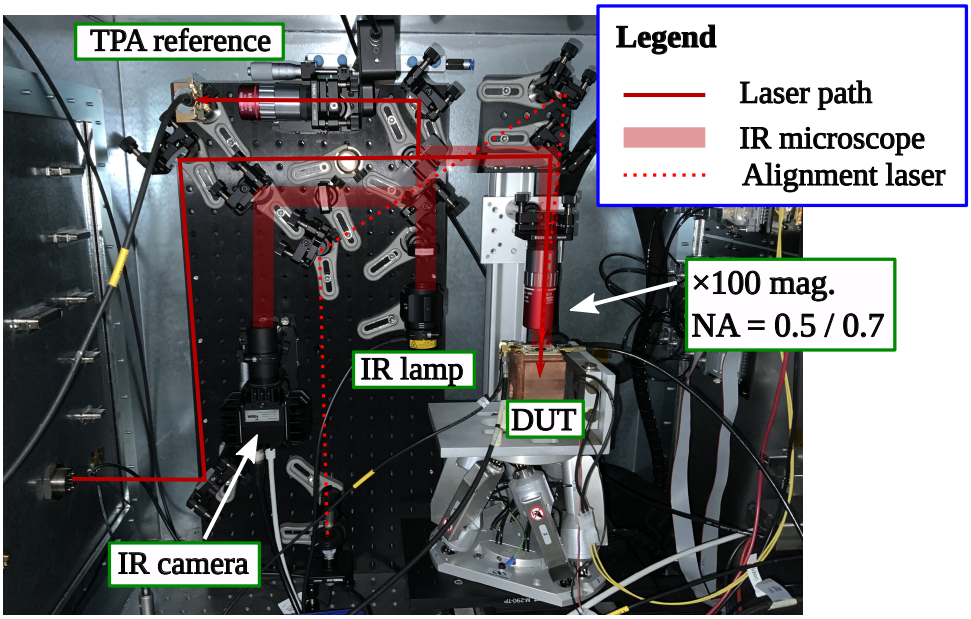

Figure 3.6: Photography of the TPA-TCT setup, showing the inside of the Faraday cage. The laser source is outside the Faraday cage towards the left side.

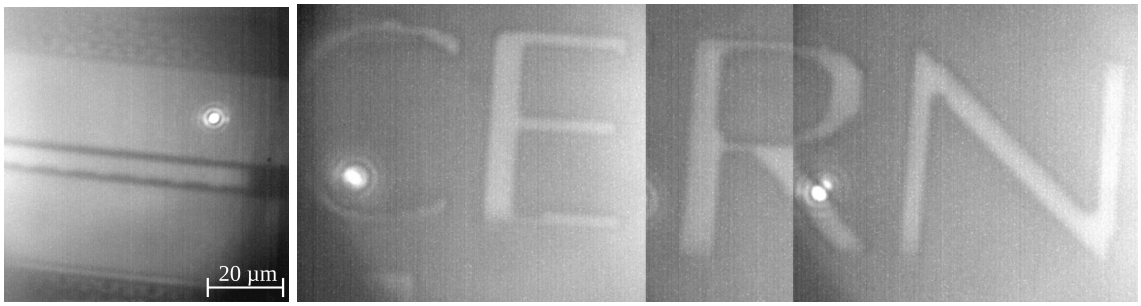

(a) **(b)**

Figure 3.7: Example pictures of the infrared microscope. (a) Picture of the top surface of the CMOS-Do-F2-S12 strip detector. The laser spot is visible as a bright dot and positioned close to the strip metal. (b) CERN logo imprinted on a test structure of a silicon optical link. It is cropped together from multiple picture to show the full imprint. The magnification of the objective is ×100 and the given scale is valid for both pictures.

The data acquisition is handled by a LabVIEW [126] program that coordinates the laser operation, bias voltage control, stage motion, temperature control, and data recording. A Keithley 2410 source-meter is used to supply bias voltage to the DUT, while the temperature control is done using the Laird PR-59 PID controller [127]. The data recording is triggered by the trigger signal from the pulse management module and performed by

an Agilent DSO9254 oscilloscope. Depending on the application, the C2HV or the Cx-L amplifier from CIVIDEC [121] is used to obtain signals amplitudes in a suitable voltage regime. The oscilloscope has a high bandwidth limit at 2.5 GHz and a sampling rate of 20 GSa/s $\hat{=}$ 50 ps/pt, while the amplifiers provide an amplification of about 40 dB with a bandwidth from 10 kHz to 2 GHz. The impedances of the DUT and the electronic readout are not matched, which is why signal reflections occur. Long labels are used in order to delay the reflection and shift reflections beyond the time window of interest. Moreover, the used cables are coaxial to minimise pickup of electromagnetic noise. The electronic readout chain is further discussed in the appendix A.1, where the influence of the bandwidth, the sampling rate, and the transfer function is discussed.

3.5.2 Setup calibration

In order to obtain an energy reference, a PDA05CF2 photodiode from Thorlabs [128] and the 02-DiodeL-8 pad detector are calibrated. The PDA05CF2 photodiode is made of InGaAs, which absorbs light at 1550 nm linearly and is thus suitable to reference the pulse energy. It yields an output voltage that can be converted to a power using the calibration factor $\approx 386.75\,\mu W/V$. Note that the calibration factor is sensitive to the wavelength, which is obtained from the device's manual. On the other hand, the 02-DiodeL-8 pad detector is made out of silicon and thus uses TPA for charge generation at 1550 nm. This makes the silicon detector, contrary to the InGaAs detector, sensitive to fluctuations in the temporal profile. The silicon detector is amplified using a C2HV from CIVIDEC and the acquired signal is converted to femtocoulomb by integration over the collection time and normalising by the amplifier specific gain factor. In the following, the PDA05CF2 photodiode is referred to as the SPA reference and the 02-DiodeL-8 pad detector as the TPA reference. Reference [13] showed that the TPA reference is required in order to achieve a proper correction of laser instabilities. For the calibration, both reference detectors are calibrated against the S401C thermal power sensor from Thorlabs that measures the pulse energy in units of power. The output of the S401C is converted to the pulse energy by division with the used laser repetition rate. A repetition rate of 4 MHz is used for the calibration in order to receive a reliable output from the S401C. For the calibration, the S401C is mounted at the DUT position and the intensity is varied using the NDF. Figure 3.8 shows the calibration of the SPA (a) and TPA (b) reference against the laser's pulse energy. The relation between the SPA (TPA) reference is linear (quadratic) with the pulse energy. The maximum available energy depends on the used optics and varies with the manual alignment of the optical path. In the here present configuration, the laser provides energies above 700 pJ to the DUT position. The output pulse energy of the laser (10 nJ) is not reached at the DUT position, as part of the light is lost by absorption in the optical components and about half of the light is guided towards the TPA reference via a 50/50 beam splitter. The beam splitter is mounted on a flip mount and can be easily moved out of the beam line to double the available pulse energy at the DUT position if needed. When the beam splitter is outside the beam line, the TPA reference and the infrared microscope can not be operated (compare to figure 3.5). Calibration scans are performed before every campaign of measurements as the alignment of the setup potentially changes slightly over time. Further, a calibration needs to be performed every time optical components are moved or changed.

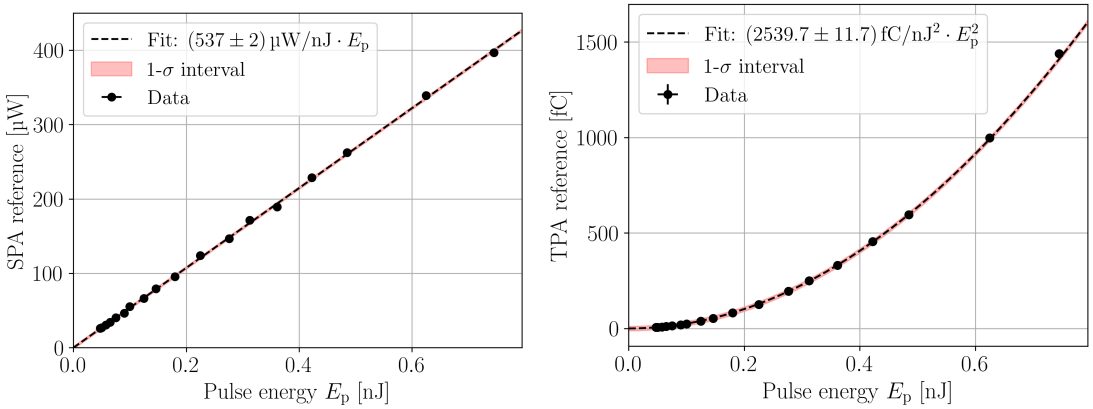

(a) **(b)**

Figure 3.8: Responses of the SPA (a) and the TPA (b) reference to different laser intensities. The SPA and TPA reference follows a linear and quadratic function, respectively. Fitting parameters to the corresponding fit function are included in the legend.

3.5.3 Laser and temperature stability

The reproducibility of measurements requires a stable laser intensity. Long term measurements are presented in figure 3.9, where figures 3.9a and 3.9b show the response of the SPA and TPA reference, respectively. From figures 3.9a and 3.9b it can be seen that the SPA reference has a stable response, while the TPA reference shows a more volatile response, which is not correlated to fluctuation seen by the SPA reference. The stable response of the SPA reference confirms that the laser source provides a stable pulse energy. Therefore, it can be concluded that the temporal profile of the laser source is not constant, which leads to fluctuations that are only probed by the TPA reference. The origin of the fluctuations in the temporal profile are unknown, but it is observed that they are caused by the laser source itself. Figures 3.9c and 3.9d show a long term scan of the TPA reference and the DUT response. In figure 3.9c the DUT and the TPA signal are separated and in figure 3.9d the DUT response is normalised with the TPA reference in order to compensate fluctuations in the charge generation. In order to correct for these fluctuations, the TPA reference is used. The correlation between the TPA reference (black) and the DUT signal (red) is clearly visible in figure 3.9c, while figure 3.9d shows that the DUT signal can be corrected through normalisation with the TPA reference to achieve a stability within $\leq 2\,\%$. Hence, it is possible to reach a satisfactory laser stability in order to achieve reproducible measurements.

The setup has the availability to temperature control the DUT. The mount of the DUT is made out of copper to provide a sufficient heat transfer. Stable operation of the DUT at $-20\,°\mathrm{C}$ with a standard deviation of $\pm 0.1\,°\mathrm{C}$ is achieved, as can be seen from figure 3.10a. The reference detectors are not actively temperature controlled, wherefore they are subject to fluctuations in the ambient temperature. A long term temperature measurement at the position of the TPA reference is shown in figure 3.10b, where fluctuations in the order of 1 K are observed within a day. In section 3.5.9 it will be shown that fluctuations of 1 K yield an error of $\approx 0.2\,\%$ and thus can be considered as negligible. It should be noted that the air conditioning of the laboratory was upgraded in the spring of 2023, which is why temperature fluctuations in the TPA reference are now significantly lower.

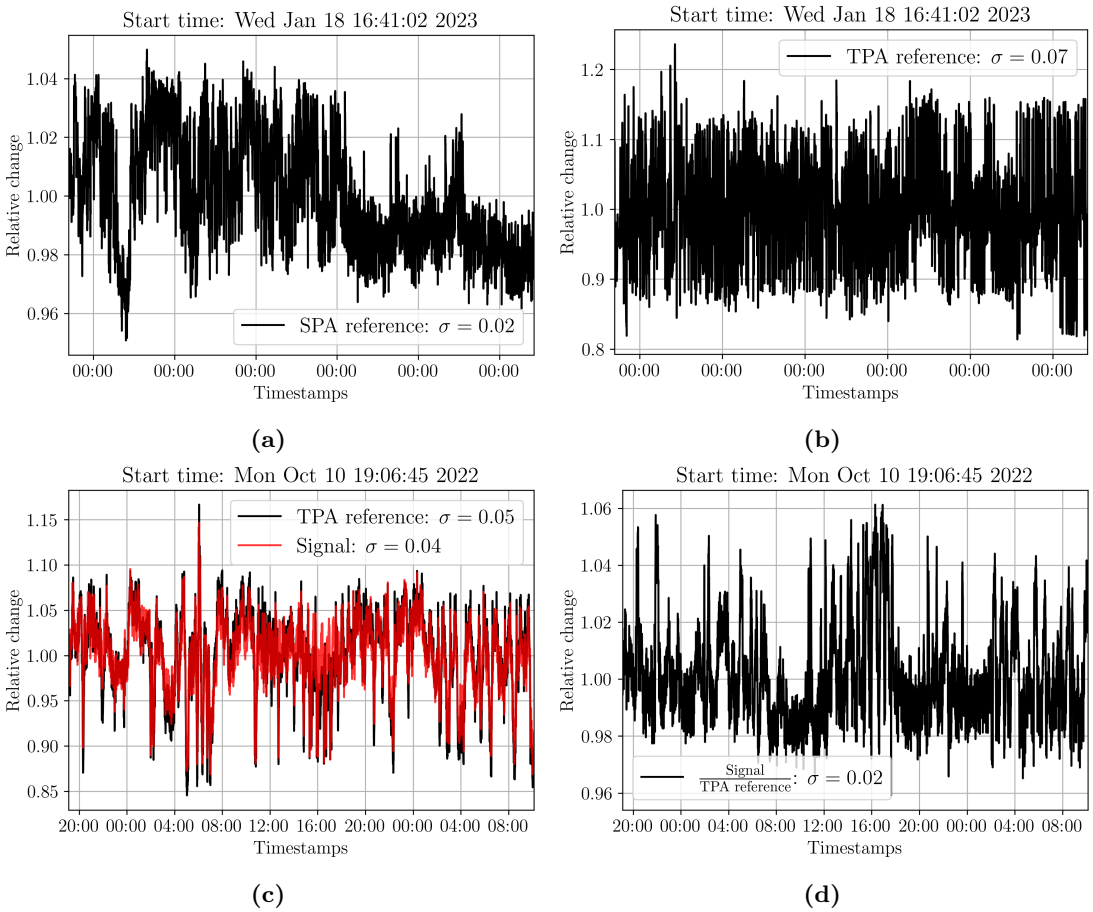

Figure 3.9: Long term stability measurement of the SPA (a) and TPA (b) reference. Every 120 s a measurement point is acquired averaging over 256 signals in order to increase the SNR. One division on the x-axis equals 24 h. Note the different y-scales in both plots. (c) Stability measurement of the TPA reference and the DUT signal, taking a measurement point every 30 s. They are well correlated, wherefore the TPA reference can be used to correct fluctuations from the laser source. (d) Correction of the DUT signal with the TPA reference.

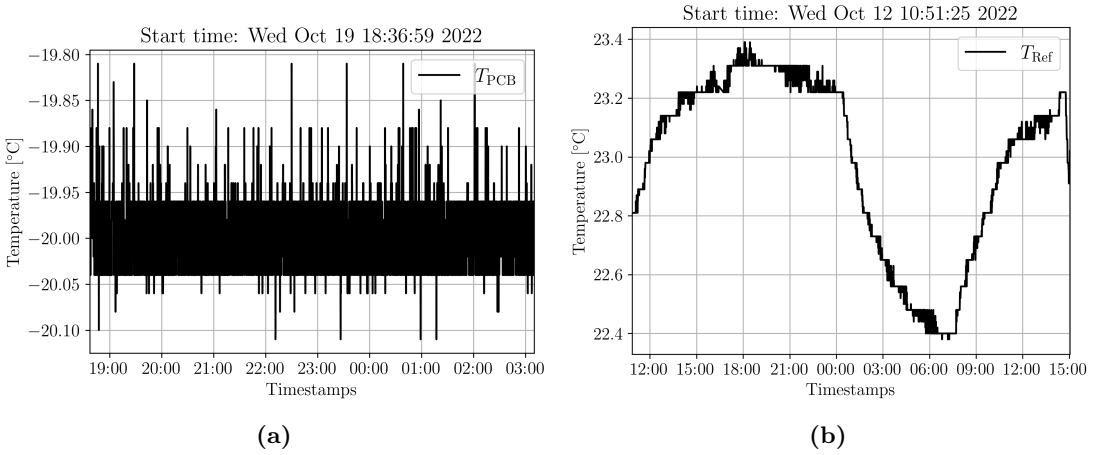

Figure 3.10: Temperature stability at the DUT (a) and TPA reference (b). The DUT is actively temperature controlled and reaches a stability of $\sigma_T < 0.1\,\mathrm{K}$. The TPA reference is floating in temperature, wherefore it is affected by changes in the room temperature.

3.5.4 Choice of objective

To this work Gaussian beams are most relevant, due to the advantageous focusing of such beam profiles. The beam waist w_0 and the Rayleigh length z_R define the intensity profile, i.e. the density of excess charge carrier generation. A definition of these parameters was given in section 2.4.1. The beam parameters can be measured by a knife edge or an in-depth scan, which is described in detail in [42]. Setup-wise the beam parameters are defined by the objective. The typical parameter quantifying objectives is the numerical aperture (NA) that is defined as

$$\mathrm{NA} = n \sin(\theta)\,, \tag{3.2}$$

with the refractive index between the objective and the DUT n and the opening angle of the light cone θ. As the interstitial space is air, it follows $n = n_{\mathrm{air}} \approx 1$. Here, objectives with NAs of 0.5 and 0.7 are available. In general, a higher NA corresponds to a higher focusing, hence smaller volumes of charge generation and higher spatial resolution. The spatial resolution is influenced, because measurements of the TPA-TCT can be understood as a convolution of the investigated structure with the charge carrier density of equation (2.34). Figure 3.11 shows a simulation of the expected spatial resolution in a thick pad detector for the two available objectives (a) and an experimental in-depth scan with NA = 0.5 of a pad detector with the deconvoluted charge collection profile (b). It can be seen that the measurement is in good agreement with the expectation and the mechanism that defines the spatial resolution of the TPA-TCT is well understood.

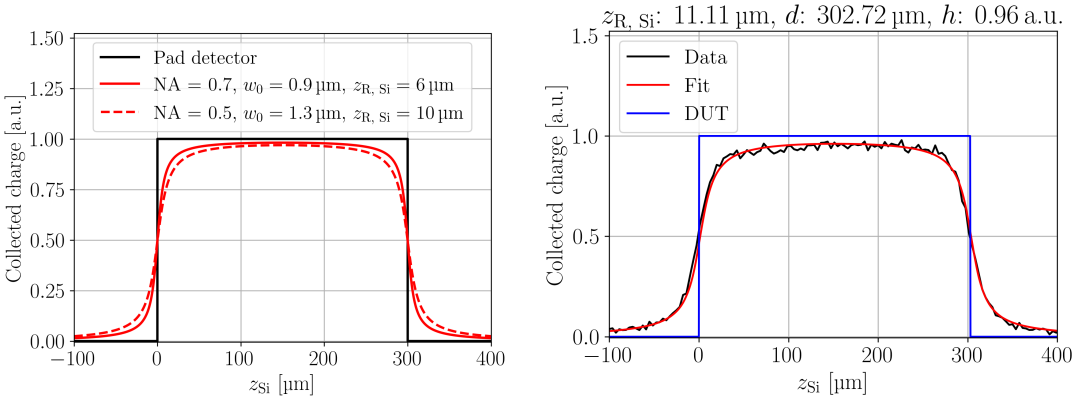

(a) **(b)**

Figure 3.11: (a) Simulated convolution of the charge collection of a pad sensor (black) with a TPA charge carrier density generated by an objective with NA = 0.5 and NA = 0.7. (b) In-depth measurement of the HPK 04-DiodeL-5 deep diffused pad detector (black), with a fitted charge collection profile (red) and the extracted DUT charge collection profile that is corrected by the charge generation volume of the laser (blue). An objective with NA = 0.5 was used and the extracted Rayleigh length $z_{R,Si}$, device thickness d, and height of the charge collection profile h are shown in the figure title.

On the one hand, higher focussing is beneficial as it increases the spatial resolution, but on the other hand, it is related to higher refraction that increases spherical aberration [129]. Spherical aberration elongates the volume of charge generation asymmetrically towards the light propagation direction and thereby decreases the total generated charge. The effect

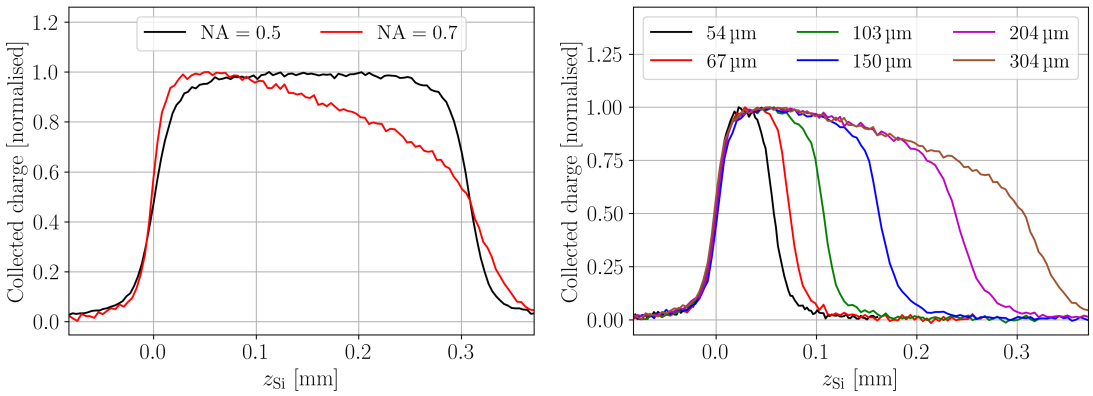

(a) **(b)**

Figure 3.12: (a) Charge collection measured in the HPK 04-DiodeL-5 deep diffused pad diodes measured with different objectives. (b) Charge collection measured with an objective with NA = 0.7 of pad detectors from the HPK deep diffused campaign with different active thicknesses. Spherical aberration becomes visible after about 70 µm as a loss in the collected charge.

is always present and becomes more pronounced with deeper positions of the focal point in the silicon sample. Figure 3.12a shows a comparison between both objectives using the example of a charge collection measurement of a thick pad detector. It can be seen that the objective with NA = 0.5 yields the expected box-like shape of a pad detector, while NA = 0.7 measures a CC that decreases with depth. The decrease is related to spherical aberration that has a noticeable influence after $\approx 70\,\mu m$ of silicon. Spherical aberration increases the volume of charge generation linearly. The linear increasing volume leads to a linear decrease of the laser intensity, which in turn decreases the charge generation quadratically. Further, the falling edge at the back side is less steep compared to the rising edge at the top side, because the increased volume of charge generation lowers the spatial resolution at the back side. The influence of spherical aberration is not observed for NA = 0.5 up to a device thickness of 300 µm. Thicker devices are usually not relevant for particle detection, but in case thicker devices are investigated, the objective should be selected carefully to allow the highest spatial resolution without noticeable spherical aberration. The smaller Rayleigh length provided by NA = 0.7 leads to the steeper rising edge in figure 3.12. From the measurements it can be concluded that spherical aberration is an unwanted effect so that the objective with NA = 0.7 is suitable up to a device thickness of $\leq 70\,\mu m$, while thicker devices are reliably measured with an objective with NA = 0.5. Experimentally, beam parameters of $w_0 = 1.3\,\mu m$ and $z_{R,Si} = 10\,\mu m$ are achievable with the NA = 0.5 objective and the NA = 0.7 objective enables beam parameters of $w_0 = 0.9\,\mu m$ and $z_{R,Si} = 6\,\mu m$. It should be noted that the spherical aberration can be counteracted with a spatial light modulator (SLM). SLMs are already used in the field of optical microscopy [130, 131] and laser direct writing [132]. Besides the correction of the spherical aberration, SLMs can be used to modify the shape of the focal spot to make it e.g. more spherical. In general, SLMs offer great potential for the TPA-TCT, but their main disadvantage is the added complexity to the setup. The implementation of an SLM in the TPA-TCT setup is foreseen in the future.

3.5.5 Sample alignment

The red alignment laser of the setup is used for the coarse alignment of the DUT with respect to the laser spot. After the coarse alignment, features of the DUT can be found using the infrared microscope. When the region of interest is found, an alignment to level the focal plane and the DUT needs to be established. Already small tilt angles of 1° can result in a 6 µm difference in the deposition depth for a scan range of 100 µm. Further, it was observed that tilt can lead to artefacts in the CC profile, wherefore an orthogonal illumination is necessary to ensure meaningful observations. A procedure to correct the tilt was developed, which is referred to as tilt correction [13]. Details about the tilt correction method are given in the appendix A.2. In general, scans presented within this work are performed in the central position of the DUT's opening window if not stated else wise.

3.5.6 Noise evaluation

Multiple setup components introduce electromagnetic noise to the measurements. The two most relevant are the amplifier and the high voltage supply. The lowest noise achievable is dictated by the intrinsic noise of the amplifier which is for the CIVIDEC C2HV around 3.3 mV. A Keithley 2410 source-meter is used for the high voltage supply, which introduces a baseline root-mean-square (RMS) of < 1 mV. This noise is introduced before the amplification, which is why the noise is amplified according to the gain factor of the amplifier that can add up to multiple 10 mV RMS of noise. This contribution is avoided by the use of a low pass filter that filters high frequency noise from the high voltage. Typically, the minimum baseline RMS of 3.3 mV is reached within the measurements. It should be mentioned that the infrared microscope was found to introduce a large electromagnetic noise (6.5 mV RMS) to the measurement, wherefore it is powered off during all measurements. The SNR is further increased by averaging of single acquired current transients. Averaging of the current transients is possible, because the charge generation is sufficiently reproducible pulse per pulse, so that the baseline RMS can be brought to an arbitrarily small value. For N acquisitions the noise RMS scales with $1/\sqrt{N}$ and for a typical measurement 128 to 256 averages are sufficient to balance of measurement speed with the noise RMS. Note that averaging is not possible for techniques that use ionising particles to generate excess charge, due to the probabilistic nature of the energy conversion process.

3.5.7 Sample preparation

The only sample preparation needed to conduct TPA-TCT measurements is to mount the DUT to a support and connect it via wire bonds in order to read out the current transients. Compared to edge-TCT, polishing of the sample is not required to achieve resolution along the device depth. Polishing is only needed when illumination is applied from the edge. TPA-TCT can also be applied from the edge, but the application is usually limited to DUTs where the region of interest is close to the edge (few 10 µm). The limitation originates from the large laser opening angle required for the high spatial resolution in the TPA-TCT that can lead to clipping at the DUT boundaries. Clipping is further discussed in section 3.5.10. Devices that do not require complex readout schemes (typically pad and

strip detectors) are glued to a PCB using conductive silver epoxy. The PCB is equipped with SubMiniature version A (SMA) connectors for the bias voltage, signal readout, and a Pt1000 that serves as a thermistor. Electrical contact to the top side of a DUT is established using wire bonds. An example of the used PCB with a glued and wire bonded pad detector from the CiS16 campaign is shown in figure 3.13a. The guard ring (GR) of a DUT, if present, is left floating for the measurement. Hence, high voltage can be applied either from the top or the back side without the need to change wire bonds. To verify that the GR connection does not significantly influence the device performance, a comparative measurement of a pad sensor was performed. The used pad detector has a large active area (about 2.5 mm × 2.5 mm) and the measurement is performed in the central region of the pad. For the measurements the GR was once grounded and once floating. The charge collection was measured for increasing bias voltages, which is presented in figure 3.13b. It can be seen that the GR connection does not influence the depletion behaviour of the tested device. However, it should be noted that the GR connection is important when it comes to the electrical characterisation of the DUT [133].

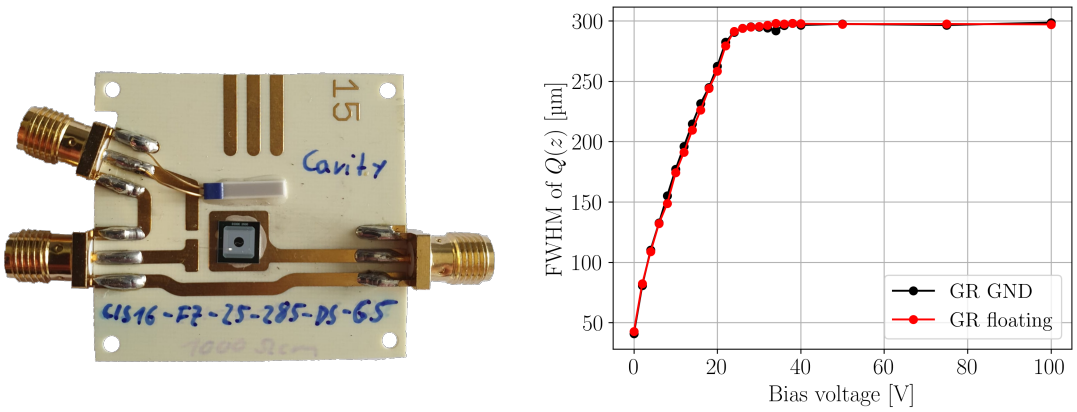

(a) **(b)**

Figure 3.13: (a) Photography of a typical PCB. A pad sensor from the CiS16 campaign is mounted. The Pt1000 is mounted < 4 mm close to the DUT. The PCB is about 38 mm wide, 35 mm long and 0.8 mm high. (b) Study of the influence of the guard ring (GR) connection on the depletion behaviour in the CNM WL-A63-PIN4 detector. The FWHM of the collected charge profiles measured with TPA-TCT for a grounded (GND) GR and a floating GR is shown.

3.5.8 High laser intensities

The excess charge carrier generation depends quadratically on the laser intensity, which makes it a crucial parameter for the TPA-TCT. At a certain intensity, the charge carrier density becomes high enough to form an electron-hole plasma. The plasma builds up an internal electrical field that shields charge carriers in the plasma against the outer electric field. The shielding prolongs the beginning of the charge carrier drift and results in a longer collection time [134]. Plasma can be described by the Tove-Seibt model, which predicts that the collection time increases due to the formation of plasma with an $E_p^{4/3}$-depepdence [11, 135]. Measurements with increasing pulse energies were performed, where the ToT was used as a representative of the collection time. Figure 3.14 shows current transients (a)

at a bias voltage of 300 V, next to the ToT profiles (b) taken at different bias voltages. Both figures show data measured at the back side of a p-type pad detector. Prolongation effects due to plasma can be seen from the current transients in figure 3.14a, as the peaking time is delayed for increasing pulse energies and the transients last longer. Concerning the ToT, it can be seen that it is constant up to a given energy threshold after which the ToT increases. After the threshold, the profiles are fitted with the predicted $E_{\mathrm{p}}^{4/3}$-dependence and a good description of the measured data is found. The threshold corresponds to the plasma onset energy and increases with the bias voltage, because the plasma shielding strength decreases with the external electric field. It can not be excluded that electron-hole plasma is formed even below the threshold energy, however the influence may not be visible with the used method and is considered as negligible. The absolute value of the threshold strongly depends on the optical parameters, as it is related to the excess charge carrier density. Here, values of the 140 pJ, 170 pJ, and 260 pJ were measured for the plasma onset for the bias voltages 300 V, 500 V, and 900 V, respectively. The measurement was performed at 20 °C with the beam parameters $w_0 = 1.2\,\mu\mathrm{m}$ and $z_{\mathrm{R,Si}} = 10.4\,\mu\mathrm{m}$. For the usual TPA-TCT application and especially device characterisation, plasma formation is an unwanted effect and avoided whenever possible. Examples for the applications of the high intensity regime are the study of electron-hole plasma and direct laser writing. The latter is the process of material modification using laser light. Various examples of this application are demonstrated in [136, 137]. It was experimentally verified that direct laser writing is not feasible with the present configuration of the TPA-TCT setup.

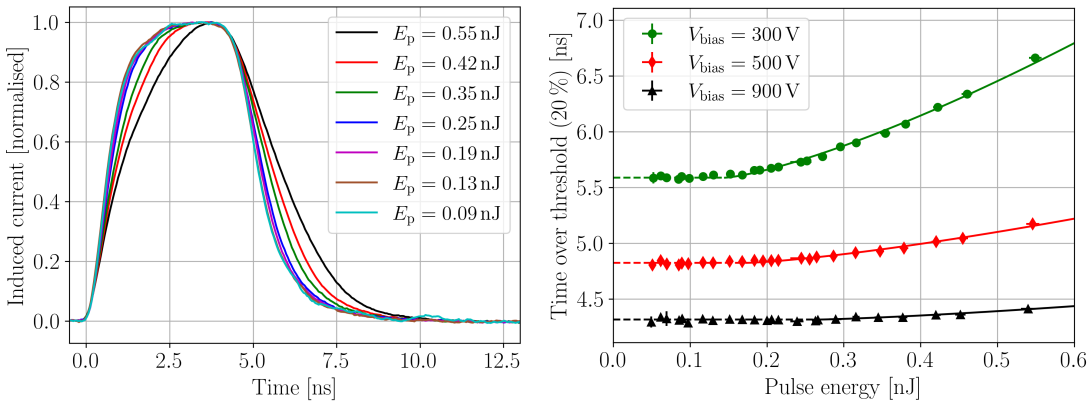

(a) **(b)**

Figure 3.14: (a) Current transients for different laser intensities measured at the back side of the CNM W5-J6-2 pad detector for a bias voltage of 300 V. The transients are normalised by their amplitude. (b) Time over threshold measured at the back side of the CNM W5-J6-2 pad detector for different bias voltages versus the pulse energy. The increase is caused by the onset of electron hole plasma. The dashed lines are a constant fit before the plasma onset and the solid lines fit the plasma model described in [11].

3.5.9 Influence of temperature

The influence of temperature on the TPA-TCT is of particular interest as irradiated silicon detectors require cooling to −20 °C during the measurements. Material parameters of silicon change with temperature. The most important material parameters to TPA-TCT are: the

band gap energy [138], the refractive index [86], the charge carrier mobility [139], the linear absorption [140], and the quadratic absorption [141]. A dedicated study on a pad detector was performed to investigate the influence of temperature on the TPA-TCT [142].

The influence on the charge carrier mobility is emphasised in figure 3.15a, where the ToT profile is shown at various temperatures. The ToT decreases with temperature, because the charge carrier mobility increases. Scattering between charge carriers and phonons becomes fewer with temperature due to the shrinking phonon population, which in turn increases the mobility [139]. Further, it can be seen that at the used bias voltage and temperature range, the temperature dependence of the hole mobility is stronger than for electrons, as the ToT at the front side ($z_{\mathrm{Si}} \approx 290\,\mu\mathrm{m}$) decreases more with temperature than at the back side ($z_{\mathrm{Si}} \approx 0\,\mu\mathrm{m}$). The mobility of holes (electrons) can be studied independently, when current transients from the top (back) side are evaluated. Selected current transients from this measurement at the top and back side are presented in the appendix A.6 in figure A.7. When the drift times of electrons and holes are extracted at different temperatures, a scaling with temperature is found that agrees with the models of [61, 71].

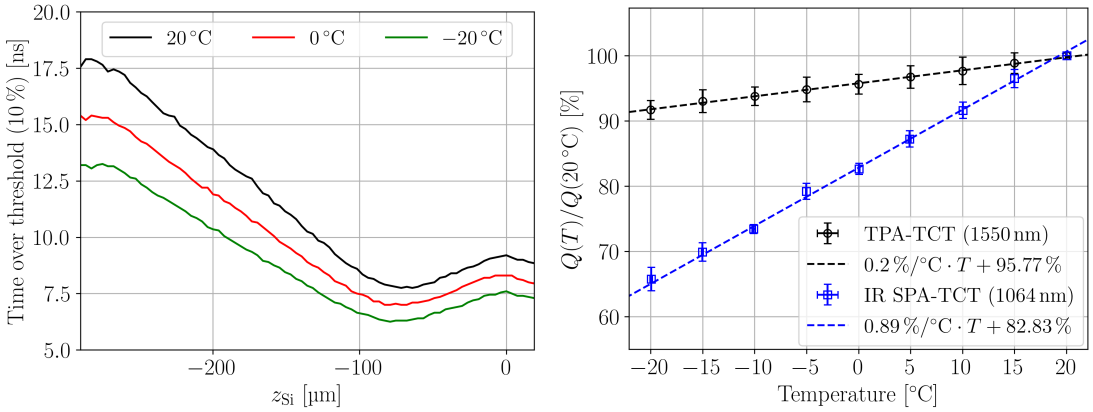

Figure 3.15: (a) Time over threshold profile measured in the CNM WL-A63-PIN4 pad detector at various temperatures. The time over threshold decreases with temperature as the mobility increases [142]. (b) Charge collection efficiency measured with SPA- and TPA-TCT at different temperatures in the same detector. The charge collected at 20 °C serves as the nominal charge collection [142].

Light absorption in silicon strongly correlates to the phonon population, because silicon is an indirect semiconductor [53]. Therefore, the charge generation is affected by temperature. Long term charge measurements were carried out in order to investigate the temperature dependence of the charge generation. The focal point was positioned in the middle of the DUT and a charge sensitive amplifier (CIVIDEC Cx-L) was used to measure the CC as precise as possible. Five thousand waveforms were recorded per temperature step to obtain enough statistics. Instabilities of the temporal profile of the laser lead to incomparable charge generations between different measurements. Therefore, only data with a comparable charge generation was considered for the measurement, where the CC measured by the TPA reference is used as a reference. Figure 3.15b shows the result, where the charge normalised with the CC at 20 °C is shown versus the temperature. A similar measurement with an IR SPA laser is shown for comparison. It can be seen that the charge collection decreases linearly with temperature for both techniques and the

influence on the shown SPA is stronger than the influence on the TPA. It should be noted that the temperature dependence is sensitive to the wavelength, wherefore the difference between the TPA and SPA measurements is not necessarily related to the difference in the charge generation mechanisms. A similar temperature dependence to the used TPA laser is found for a $\approx 750\,\mathrm{nm}$ laser [140]. This indicates that the temperature dependence might not be influenced by the absorption mechanism, but is driven by the phonon population. Further, it should be noted that the temperature dependence is in general not linear and only appears linear in the investigated temperature range. Charge collection is influenced by two variables: the generated charge and the process of charge collection. The latter could be influenced by e.g. ballistic deficit, but it is ensured that all generated charge is collected at all investigated temperatures. Thus, the changes in the CC directly reflect on the generated charge. In the following, the process of charge generation is discussed with respect to the temperature. The charge generation for SPA and TPA is affected by

$$Q_{\mathrm{SPA}}(T) \propto (1 - \exp(-\alpha(T) \cdot d)), \tag{3.3}$$

$$Q_{\mathrm{TPA}}(T) \propto n_{\mathrm{Si}}(T)\beta_2(T), \tag{3.4}$$

where the charge generation of TPA is, in contrast to SPA, independent of the device thickness d. Only the refractive index and the corresponding absorption coefficient potentially change with temperature. The refractive index decreases within the investigated temperature by 0.2 % and can not fully explain the decrease in charge generation. Therefore, the dominant contribution must originate from the absorption coefficient, which is correlated to the band gap energy and the phonon population. As the change in band gap energy (see figure 2.2b) is in the order of 1 meV, it can be concluded that the dominating effect that drives the temperature dependence of the charge generation is the phonon population, which agrees with results presented in [141]. It is found that the TPA charge generation decreases by $(8.3 \pm 1.4)\,\%$ from $20\,^{\circ}\mathrm{C}$ to $-20\,^{\circ}\mathrm{C}$, which agrees within the errors with the $(12.0 \pm 2.6)\,\%$ decrease from $23\,^{\circ}\mathrm{C}$ to $-17\,^{\circ}\mathrm{C}$ reported in [141]. Concerning the SPA-TCT, when values from [140] are used and reflection at the back and top surface are included, a decrease in CC by $(40.4 \pm 2.8)\,\%$ is calculated for a decrease in temperature from $20\,^{\circ}\mathrm{C}$ to $-20\,^{\circ}\mathrm{C}$. On the other hand, a decrease of $(35.0 \pm 0.4)\,\%$ is measured, which is $(5.4 \pm 2.8)\,\%$ less than the calculated value. The cause of this difference is so far unknown.

3.5.10 Laser beam clipping

As discussed in section 3.5.4, the TPA-TCT typically uses large opening angles to achieve high focusing. The dimensions of the light cone can exceed the dimensions of the opening at the top surface, especially in segmented devices. Figure 3.16a shows the beam radius for given beam parameters versus the distance from the focal spot, which can be used to estimate the geometries for which clipping is expected. Figure 3.16a can be used to estimate the appearance of clipping. In the following, a strip detector with a pitch size of 80 µm, 30 µm wide metal strip, and a device thickness of 300 µm is used as an example. The opening window between two strips is 50 µm. This distance is exceeded by the beam diameter after about 65 µm for NA = 0.5, which corresponds to a depth of only $\approx 240\,\mu\mathrm{m}$ in silicon. Note that the beam radius is shown in 3.16a and for the example the beam diameter needs to be taken $2 \cdot w(65\,\mu\mathrm{m}) > 50\,\mu\mathrm{m}$. Figure 3.16b shows a simplified simulation of clipping. The amount of laser intensity that enters the device's opening window for a

given xy-position is colour-coded. The opening window's area is 50 µm × 100 µm and the focusing depth is set to 65 µm (≈ 240 µm in silicon). Clipping is not present in the central region, but appears at the edges and especially at the corners. Further, it can be seen that light enters even regions below the metal that are near the opening window. At these positions, the light cone partially enters the opening window to allow charge generation even below the metal. The available distance from the opening increases for deeper focusing depth. Methods to handle clipping in segmented devices are discussed in section 6. With respect to edge illumination, clipping is highly relevant because the active volume can be buried several 100 µm away from the edge and thus clipping can not be avoided. Clipping is the main reason why illumination is preferably applied from the top or back side.

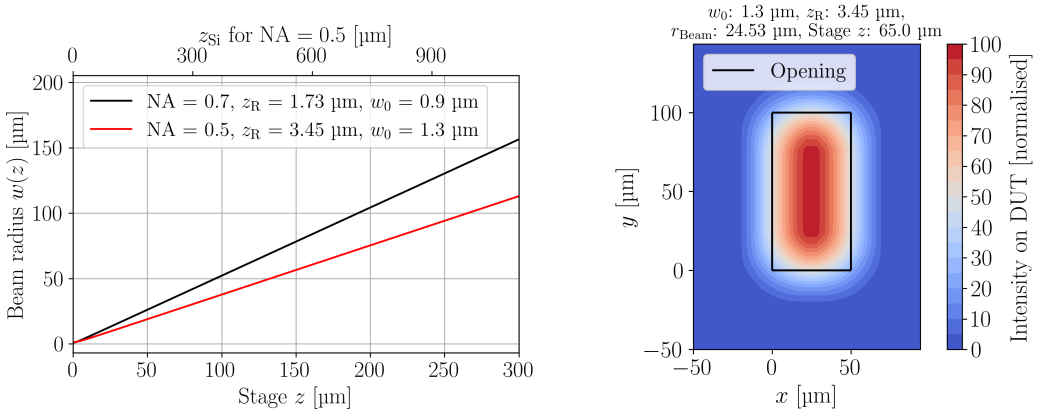

(a) **(b)**

Figure 3.16: (a) Beam radius $w(z)$ against the distance from the focal point for NA = 0.7 and 0.5. Note that the shown z_{Si}-axis is only valid for NA = 0.5. (b) Modelled distribution of clipping at a 50 µm × 100 µm rectangular opening. The encircled region is considered as the opening window and everything outside the opening is considered as metal. The percentage of intensity that reaches the DUT's active volume, i.e. that is not clipped at the opening is colour-coded. The beam parameters and the focusing depth (Stage z) are stated above the figure.

3.5.11 Influence of reflection

Whenever the refractive index changes, e.g. at a back side silicon-air interface, a part of the light intensity is reflected. The reflectivity depends on the angle of incidence and the refractive indices. For orthogonal incidence at an interface, where light traverses from a medium with n_1 to a medium with n_2, the reflectance is given by

$$R = \left| \frac{n_1 - n_2}{n_1 + n_2} \right|^2 . \tag{3.5}$$

As reflection can usually not be avoided, the understanding of its influence is key. Figure 3.17 shows schematically the process of reflection (a) and the effect it has on the measured CC in a pad detector (b). The latter shows charge collection beyond the DUT boundaries that is caused by a reflection at the back side silicon-air interface. Using the refractive index of silicon $n_{Si} = 3.4757$ [86] and air $n_{air} = 1$, equation (3.5) yields $R \approx 0.3$. As TPA scales quadratically with the light intensity, the reflection leads to 10 % of the ordinary charge

collection. The fit in figure 3.17b is performed after a model from [42], with additions to include the reflection. A model to include reflection in the fit function was developed within this work and is discussed in the appendix A.3. The reflection corrected graph reveals that the full width at half maximum (FWHM) of the original CC profile is about 7 µm larger than the actual active thickness of the DUT. Hence, the FWHM is not suitable to extract the device depth when reflection is present. A direct application of reflection is derived in section 6. There, the reflection at a back side metal is exploited to investigate regions below a top side metal using top side illumination.

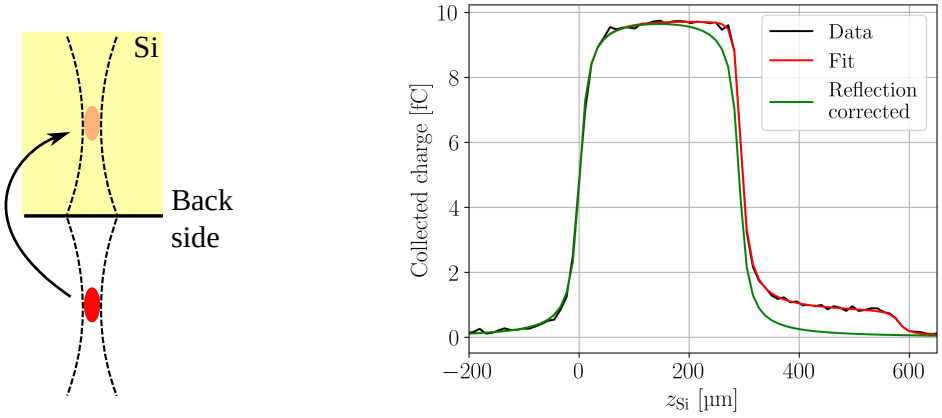

(a) **(b)**

Figure 3.17: (a) Sketch of reflection at a back side interface. The slightly transparent focal spot marks the reflection from the ordinary beam that is located below the back side interface. (b) Charge collection in the CNM WL-A63-PIN4 detector with a fit that models the reflection and the reflection corrected charge collection profile. Reflection at the back side silicon-air interface leads to charge collection beyond the DUT's back side.

3.5.12 Detector characterisation techniques

In this section, useful concepts for the device characterisation with TPA-TCT are discussed using pad detectors. Before it was shown that the FWHM is not suitable to extract the device thickness reliably, as it can be elongated by reflection or impacted by potential laser beam clipping. Hence, an intensity independent quantity is best suited to appropriately extract the device thickness. A suitable candidate is found by the ToT [143], because it is independent of the laser intensity. Figure 3.18a shows the CC profile of a thick pad detector and the ToT profile in the same figure. The half maxima of the CC profile are indicated and charge collected beyond $z_{\mathrm{Si}} = 300\,\mu\mathrm{m}$ is associated to reflection at the back side silicon-air interface. The ToT profile appears symmetric, with the back side as the symmetry axis. This is a result of the reflection that mirrors the focal spot movement and thus the ToT profile. Deviations from a perfect symmetry are observed due to the decreased SNR in the reflected region, which leads to uncertainties in the ToT extraction. The shape of the ToT profile yields insight to the collection time of the charge carriers. When charge is generated close to or at the top side, electrons are, for practical reasons, instantly collected at the top side n-electrode, while the holes drift the full thickness to reach the back side p-electrode. Thus, holes dominate the induced current recorded close to or at the top side. On the other hand, induced current transients recorded close to

or at the back side are dominated by the electron collection. Therefore, the maxima at and close to the half maximum positions are a result of the hole and electron collection that are maximum at the device's boundaries. The back side maximum aligns with the position of the back side surface and can be used to extract the back side boundary's position. The second half maximum position of the CC does not align with the maximum due to reflection, which makes the FWHM unsuitable for the extraction of the device thickness. For the top side, a maximum is observed as well. Naively expected, the collection time of the charge carriers should always be maximal e.g. constant in front of the top surface, because when the focal spot is at or above the top side ($z_{\mathrm{Si}} \leq 0\,\mu\mathrm{m}$) and thus at its maximum position. The decrease in ToT in front of the detector is related to the change in the weighting of the excess charge carrier density. When the focal point exits the active volume, the median of the excess charge carrier density moves away from the top surface, inside the bulk region. Thus, the contribution of charge carriers created in the bulk region is more pronounced in the current transient, which lowers the ToT. The median of the excess charge carrier density is discussed in more detail in the appendix A.4. Hence, the position of the first maximum can be used to extract the top surface position, when the half maximum is not reliably extracted from the CC. Here, a discrepancy of about 7 µm between the position of the first half maximum and the first ToT maximum is observed, which is related to the used laser intensity. To obtain a suitable SNR in the reflection region, the scan was recorded with a laser intensity of about 300 pJ and beam parameters of $w_0 = 1.2\,\mu\mathrm{m}$ and $z_{\mathrm{R,Si}} = 9.7\,\mu\mathrm{m}$. Plasma formation is present at such parameters, which leads to an increasing ToT when a critical amount of excess charge is generated. The discrepancy disappears if the same scan is performed at a lower laser intensity, and the discrepancy increases if a higher laser intensity is used. Appendix A.7 shows technology computer-aided design (TCAD) simulation of a thick pad detector, where the ToT profile is simulated among others. It is found that all observed features are reproduced, which gives confidence in the profound understanding of the measurement. Figure 3.18b shows the ToT profile in the same DUT for various thresholds. The ToT strictly increases with decreasing thresholds and the shape starts to differ for thresholds above 50 %. The current transients

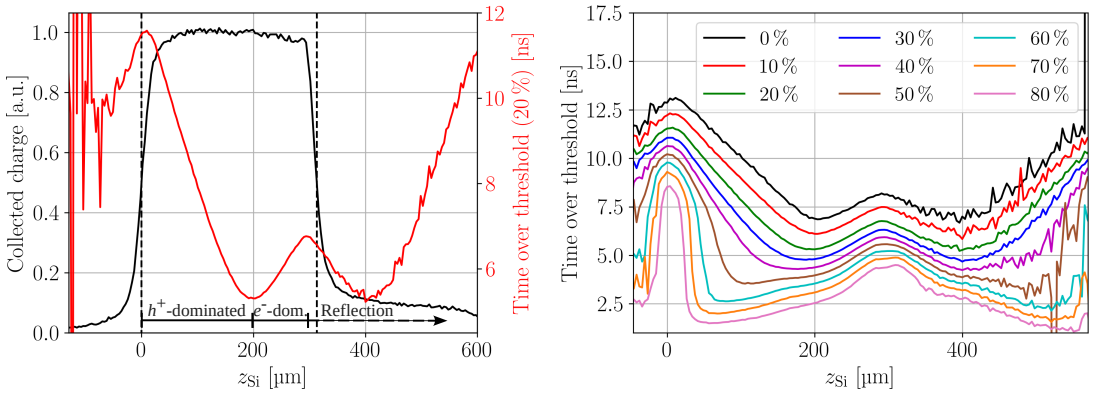

Figure 3.18: (a) Collected charge and time over threshold profile of the 300 µm thick CiS16 25-DS-66 pad detector. The half maxima of the collected charge profile are indicated by the dashed lines. (b) Time over threshold profiles for various thresholds measured in the same pad detector. Artefacts occur if the threshold is selected to high (here $\geq 50\,\%$). The bias voltage is 300 V.

recorded near the top surface have a steep peak due to fast collection of electrons, which leads to the differences in the ToT at the top side. The waveforms recorded directly at the top surface do not have such a steep peak, because the electrons are collected faster than resolvable with the used readout electronics. It should be mentioned that low thresholds lead to difficulties for low SNR, because the method to extract the ToT is sensitive to noise. Hence, the threshold for the ToT is usually selected between 15 % and 50 % to avoid the demonstrated effects.

The resolution along the device depth can be exploited to study the depletion behaviour of a detector. A device can be considered as fully depleted, when an electric field is present everywhere in the sensor, meaning that all generated charge should be collected independent of its generation position. Various TCT parameters, like the ToT, RT, CC or PC allow the study of the depletion behaviour. Figure 3.19 shows the CC (a) and PC (b) for increasing bias voltages in a thick pad detector. The CC profile grows with depth and more charge is collected for increasing bias voltages. However, even after the CC reached the full thickness at about 14 V, the CC still not reaches its maximum, meaning that part of the generated charge is not collected. This is related to the selected t_{coll}, as charge collection in regions with low electric field can exceed the collection time and thus not contribute to the CC. This effect is known as ballistic deficit and can be minimised by selecting sufficiently long collection times. Here $t_{\text{coll}} = 50\,\text{ns}$ was selected, which leads to ballistic deficit for bias voltages below 35 V. The PC is not influenced by ballistic deficit, as it is extracted from the rising edge of the current transient. Therefore, the PC gives a clear picture of the depletion behaviour and the bias voltage for which the PC is above zero across the whole device thickness is found to be about 14 V. This is in good agreement with the $V_{\text{dep}} = (14.2 \pm 0.5)\,\text{V}$ extracted from CV measurements.

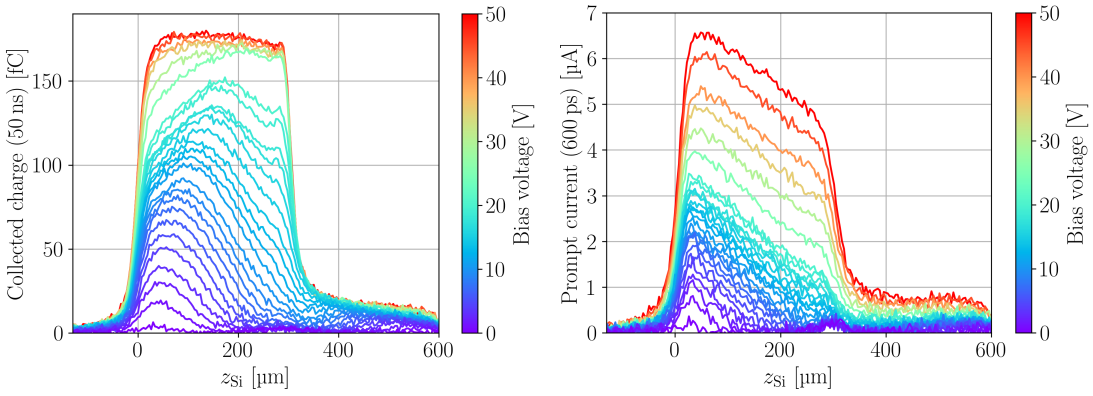

(a) **(b)**

Figure 3.19: Depletion of the 300 µm thick CiS16 25-DS-66 p-type pad detector. The charge collected in $t_{\text{coll}} = 50\,\text{ns}$ is shown in (a) and the prompt current for $t_{\text{pc}} = 600\,\text{ps}$ is shown in (b). The collected charge is impacted by ballistic deficit for $V_{\text{bias}} < 35\,\text{V}$, wherefore the collected charge profile is not saturated even after full depletion at about $V_{\text{fd}} \approx 14\,\text{V}$.

4 Influence of radiation damage on the TPA-TCT

Radiation damage does not only affect the device performance, but also the characterisation technique. To disentangle technique and device related effects, a precise knowledge about the influence on the characterisation technique is needed. The aim of this chapter is to investigate the influence of radiation damage on the TPA-TCT. Studies on p-type pad sensors from the CiS16 campaign irradiated with neutrons, protons, or gamma particles were carried out. Details about the used devices can be found in section 3.1. All measurements were performed at a temperature of $-20\,°\mathrm{C}$ and a relative humidity of $\approx 0\,\%$. Only the averaged current transients of 256 single acquisitions were recorded. The laser was operated at a pulse frequency of 200 Hz and the beam parameters $w_0 = 1.2\,\mu\mathrm{m}$ and $z_{\mathrm{R,Si}} = 9.7\,\mu\mathrm{m}$ were present.

4.1 Correction of the SPA offset

Defects introduce energy levels within the band gap of silicon, so that linear absorption is observed for wavelengths that were originally above the linear absorption regime [109]. This additional single photon contribution is called SPA background or SPA offset, because light is continuously absorbed along the propagation direction and thus yields a constant contribution independent of the focal point's position. Three different methods to correct the SPA offset were developed: correction by constant subtraction [143], correction by intensity [13], and correction by waveform subtraction [9]. The prior is the simplest method, where a constant is fitted to the offset and subtracted from the profile. It does not provide a correction on the waveform level, which means that is does not correct the influence of the SPA contribution towards the shape of the current transient. Due to its simplicity it is useful to correct charge collection (CC) profiles, but it is not appropriate to correct e.g. the prompt current (PC) or the time over threshold (ToT). The intensity method is the most elaborated of all three methods. A measurement is recorded twice at different intensities, and the different scaling of the SPA and the TPA contribution to the laser intensity is exploited for correction. The measurements taken at different laser intensities are compared to yield the SPA and the TPA contribution separately. The method was developed to cope with intensity variation due to clipping or reflection, as it compares two measurements and thus intrinsically corrects such effects. Appendix A.5 contains more information about the method and derives the relevant formulas. The third method is the waveform subtraction method. A waveform is recorded with the focal spot above the active volume, so that the volume of TPA charge generation is well outside the active volume. This waveform contains a negligible amount of TPA and is dominated by the SPA contribution. As the SPA contribution is independent of the focal spot's position, this waveform is subtracted from all other waveforms to cancel out the SPA contribution. The method is valid as long as the laser light intensity within the DUT is constant throughout the measurement, i.e. no clipping or reflection is present. Concerning the laser system it was reported that significant fluctuations in the temporal pulse width τ are observed. These fluctuations are irrelevant to the waveform subtraction method, as the SPA contribution is independent of the temporal pulse width and thus properly corrected even for a fluctuating τ. Therefore, the TPA reference can be used to correct for fluctuations of the temporal pulse width after the SPA correction was applied. Figure 4.1 shows a comparison between the three methods using a neutron irradiated pad detector as an example. The correction of the CC

profile is shown in (a) and the correction of the ToT profile in (b). Most striking in the CC profiles is the increased noise for the intensity correction method in comparison to the other methods. The origin of the increased noise in the intensity correction method lies in the need to take two measurements at different intensities. One measurement is performed at a low intensity (65 pJ) and the other at a higher intensity (320 pJ). The low intensity measurement has a lower SNR, which is propagated by the correction method and leads to an increased noise. It is necessary to perform the two measurements at significantly different intensities, because too equal intensities lead to numerical instability in the method. The constant subtraction method does not appear in figure 4.1b, because it does not provide a correction on the waveform level and thus can not be used to correct the ToT.

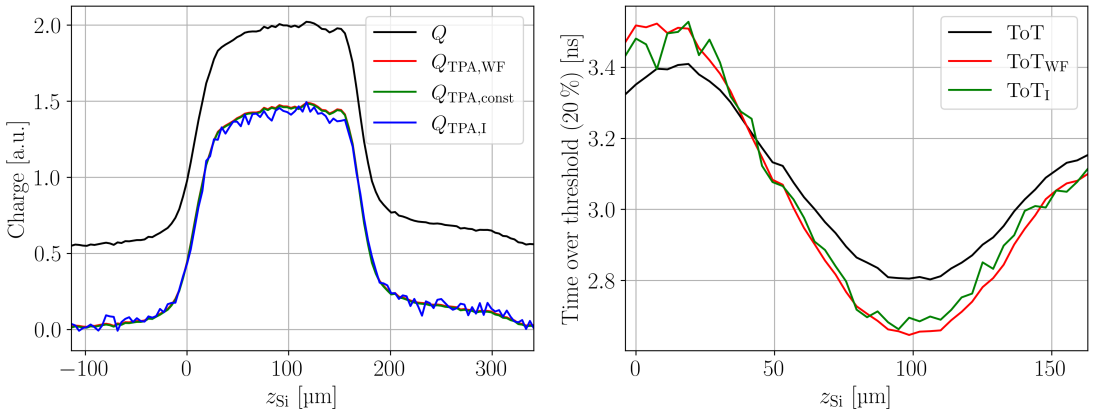

(a) **(b)**

Figure 4.1: (a) Collected charge versus depth profile of an irradiated ($3.32 \cdot 10^{14}$ n/cm) 156 µm thick p-type planar pad detector. The bias voltage is 300 V. A comparison of the three different SPA correction methods is shown. The non-corrected waveform is labelled Q, the waveform subtraction method is indicated by the index WF, the constant subtraction method by the index *const*, and the correction by intensity method by the index I. (b) Time over threshold measurement in the same pad detector, including a comparison of the waveform subtraction and the intensity correction method.

In conclusion, the waveform subtraction method is the recommended method to correct the SPA contribution whenever it is applicable. It is simple to apply and offers correction on the waveform level. However, for applications under the presence of clipping or reflection, the intensity correction method is recommended. In the following, the waveform subtraction method is used for the SPA correction if not stated otherwise.

4.2 Neutron and proton irradiation

This section presents the investigation of the influence of neutron and proton irradiation on the TPA-TCT. CC profiles of neutron and proton irradiated samples are shown in figures 4.2 (a) and (b), respectively. It can be seen that neutron and proton irradiation leads to an SPA offset that increases with fluence. Figures 4.2 (c) and (d) show the SPA corrected in-depth scans, where the decreasing CC becomes evident. Further, the inhomogeneity of the CC profile over the device depth for increasing irradiation is clearly

visible. The inhomogeneity is linked to charge carrier dependent trapping. Depending on the excess charge deposition depth, electrons or holes need to drift a longer distance, so that their probability of trapping changes with the deposition depth.

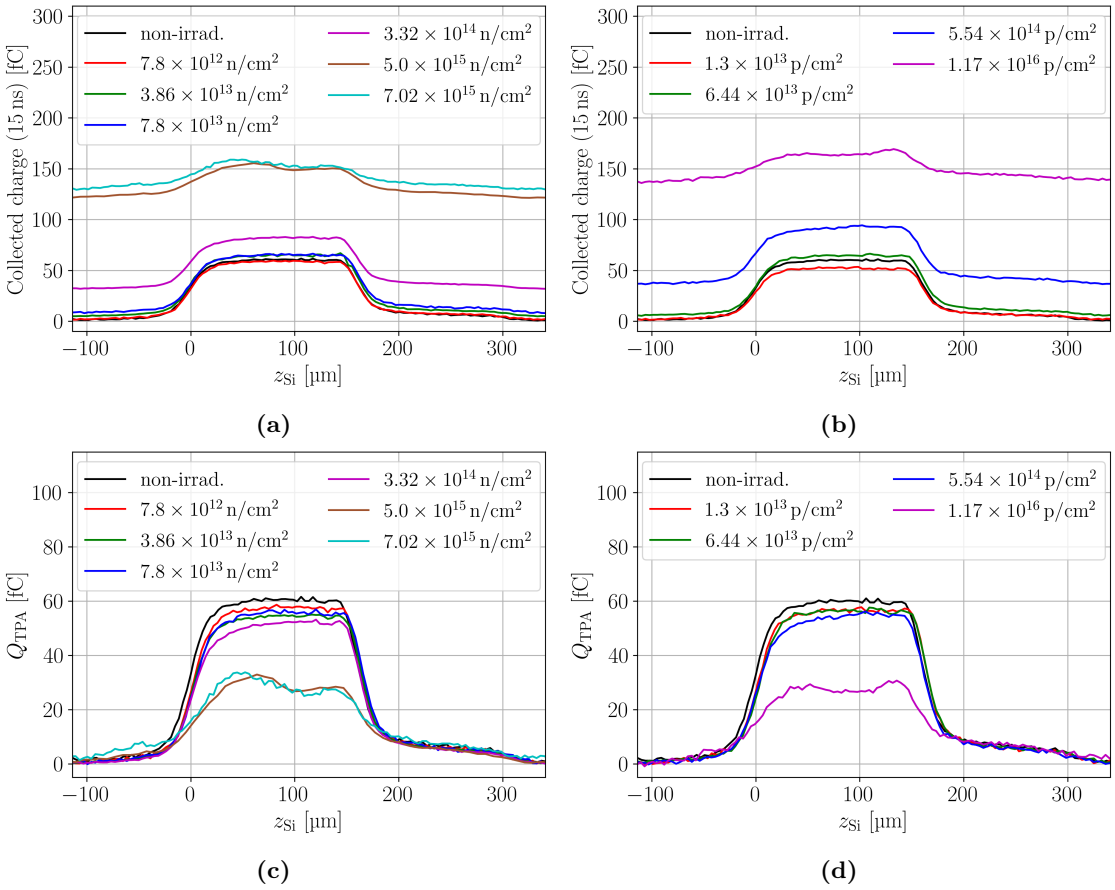

Figure 4.2: In-depth scans of the charge collection in pad detectors (CiS16) for neutron (a) and proton (b) irradiated samples. Figures (c) and (d) show the SPA corrected in-depth scans for neutrons and protons, respectively. The bias voltage is 300 V.

In-depth scans are performed for various laser intensities, to exploit the linear and quadratic dependence of the SPA and the TPA contribution, respectively. The SPA contribution to the collected charge Q_{SPA} is extracted as the mean CC in a range between $-265\,\mu\mathrm{m} \leq z_{\mathrm{Si}} \leq -130\,\mu\mathrm{m}$ in front of the device. In this range the TPA contribution is negligible and thus suitable to obtain the pure SPA contribution. On the other hand, the TPA charge Q_{TPA} is extracted from the SPA corrected CC profiles as the mean between the FWHM and is thus an average over the full device depth. It should be noted that the analysis procedure of Q_{TPA} can also be performed for a given depth of the device to investigate the CC along the device depth. Here, the average over the full device depth is used to ease the procedure. Figures 4.3a and 4.3c show the CC in the neutron irradiated devices from SPA (a) and TPA (c) as a function of the laser intensity. In accordance with the expectations, the SPA contribution scales linear and the TPA contribution quadratic with the intensity. Both, the CC and the pulse energy E_{p} have an error. The presented error on the CC is the standard deviation of the averaged SPA and TPA contribution over the full active thickness, while the error on the laser intensity propagates from the setup calibration that was performed before the measurement campaign. The measurement procedure was repeated at different

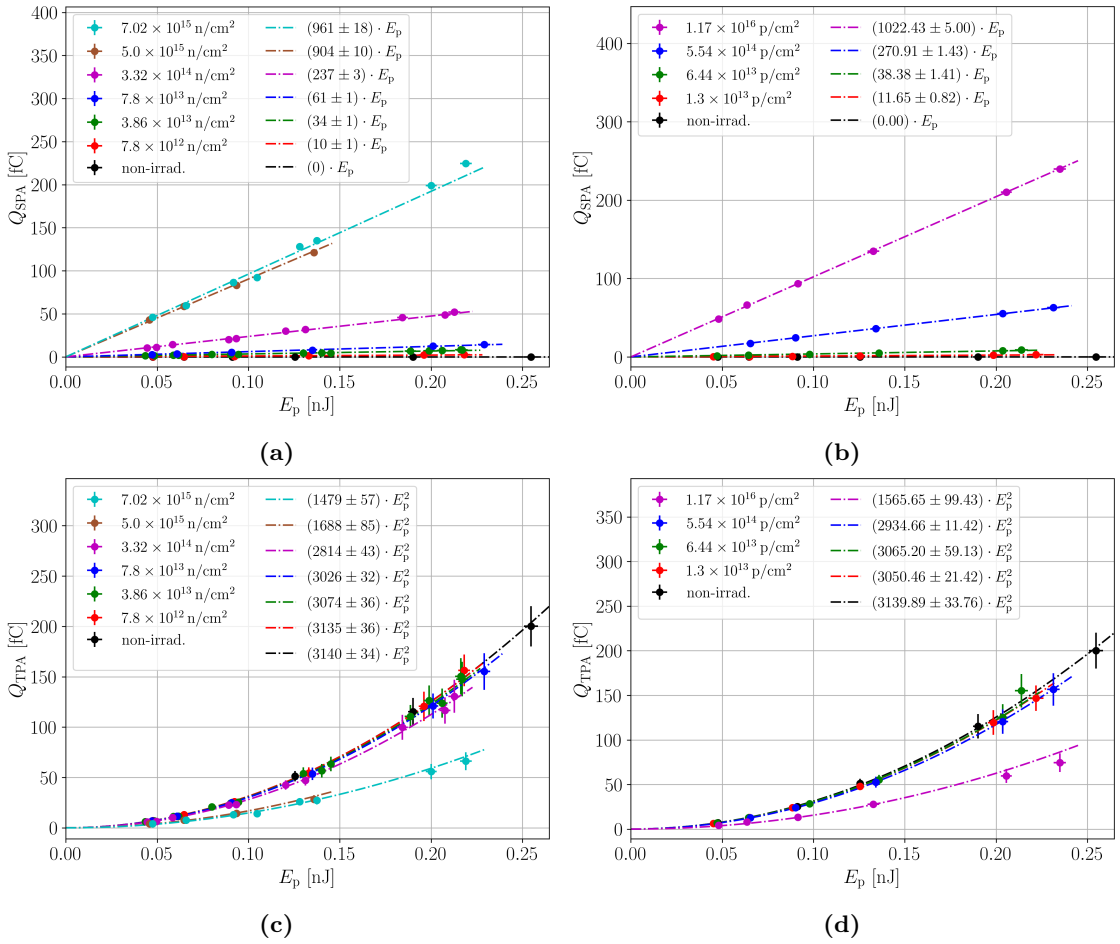

Figure 4.3: Charge collected by SPA in neutron (a) and proton (b) irradiated pad sensors from the CiS16 campaign. Charge collected by TPA for the same neutron (c) and proton (d) irradiated devices. The TPA charge is extracted as the mean of the collected charge between the FWHM of the in-depth scans. The bias voltage for all scans is 300 V.

bias voltages, but here only measurements at 300 V are presented. Figures 4.3b and 4.3d show the CC from SPA (b) and TPA (d) against the laser intensity in the proton irradiated devices. It can be seen that the proton irradiated samples show the similar behaviour as the neutron irradiated samples. A dedicated comparison between the neutron and proton irradiated samples is performed in section 4.4.

The PC of the highest neutron and proton irradiated sample is shown in figures 4.4 (a) and (b), respectively. Different bias voltages are shown to emphasise the evolution of the electric field. Both samples show a clear double junction for increasing bias voltages, where the electric field has maxima at the top and back side. The double junction indicates that there is negative space charge at the n-type electrode (top side), while the space charge is positive at the p-type electrode (back side) Further, the direction of electric field evolution is opposite for neutron and proton irradiated devices at the given fluence. While the electric field grows from the top towards the back side in the neutron irradiated device, the direction of electric field evolution is opposite in the proton irradiated device. The evolution of electric field from the top towards the back is the typical direction of electric field in a p-type device, while the opposite is the case for n-type devices. Thus, the space charge

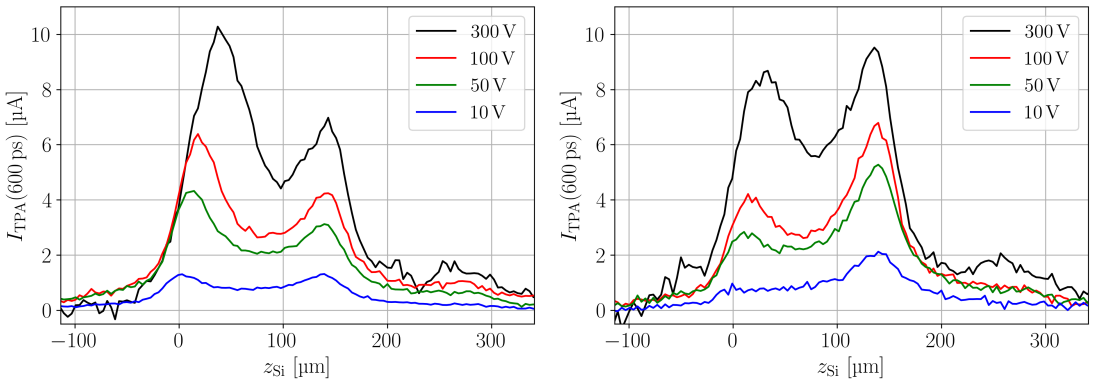

Figure 4.4: Prompt current at $t_{\mathrm{pc}} = 600\,\mathrm{ps}$ for different bias voltages measured for a neutron fluence of $7.02 \cdot 10^{15}\,\mathrm{n/cm^2}$ (a) and a proton fluence of $1.17 \cdot 10^{16}\,\mathrm{p/cm^2}$ (b). The equivalent fluences are comparable. The double junction is visible in both plots and the proton irradiated sample is inverted.

of the proton irradiated device appears sign inverted compared to the neutron irradiated device. This is particularly interesting because space charge sign inversion (SCSI) in a p-type FZ detector was so far never reported. However, the situation is complex because of the double junction. Not a typical SCSI is present where the flavour of the bulk is fully transitioned, but for the neutron irradiated device the negative space charge at the n-type electrode is higher than the positive space charge at the p-type electrode, while the ratio is inverted in the proton irradiated device. Selected current transients of this measurement are presented in the appendix A.6 in figure A.8b. For pad detectors this proton irradiation induced SCSI is not critical, because the weighting field is constant so that excess charge independent of its position contributes equally to the current transient. On the other hand, this effect could be highly relevant to p-type strip detectors, where the weighting field is much higher at the top side compared to the back side. Excess charge in the vicinity of the strip contributes to the majority of the current transient, which is why the highest electric field is desired to be in that region. Thus, the CCE of proton irradiated p-type strip detectors might be decreased compared to similar neutron irradiated devices at high fluences.

Besides, from the PC profile in figure 4.4 it can be seen that depletion as defined for a pristine detector is not a useful concept anymore. Already at the lowest shown bias voltage an electric field is present across the full DUT's active volume and thus full depletion in that sense is already reached, even though the CC will still increase with increasing bias voltage. To define the operational voltage the CC is potentially a better indicator. The operational voltage could be found as the voltage where the CC reaches a given threshold. This threshold needs to comply with the specifications of the intended use case.

4.3 Gamma irradiation

The gamma irradiation was performed with a ^{60}Co source at IRB in Zagreb [117]. Gamma photons from a ^{60}Co source do not create defect clusters, but exclusively point defects. This is in contrast to hadron irradiation that creates both defect types (compare to section 2.5).

Two pad sensors from the CiS16 campaign irradiated to 92.4 Mrad and 186.1 Mrad are studied. In-depth CC scans are shown in figure 4.5a, where a non-irradiated device is shown for comparison. It is observed that the gamma irradiation, in contrast to neutron and proton irradiation, does not introduce an SPA background. A comparison between the CC in neutron, proton, and gamma irradiated devices can be seen in figure 4.5b. The gamma irradiated samples show also a decrease in CC with respect to the non-irradiated device, which indicates that trapping is present. Further, the charge loss is constant throughout the device, contrary to the neutron and proton irradiated device. Hence, the trapping is equal for all excess charge deposition positions, which suggests that the trapping cross-section of electrons and holes is the same in the gamma irradiated samples.

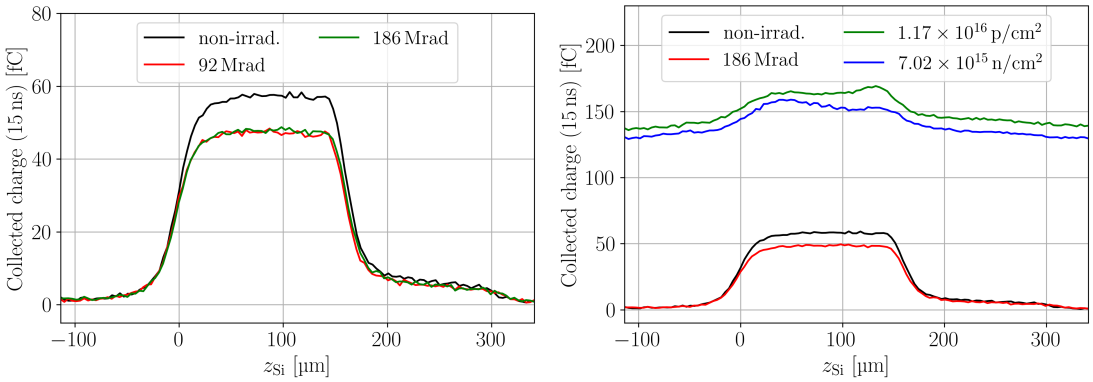

(a) **(b)**

Figure 4.5: (a) In-depth scans of the charge collection in pad detectors (CiS16). Gamma irradiated samples and a non-irradiated sample are shown. (b) Comparison between the in-depth scans of a non-irradiated, a neutron, a proton, and a gamma irradiated pad sensor. The bias voltage in all scans is 300 V.

4.4 Comparison of neutron, proton, and gamma irradiation

As presented above, neutron, proton, and gamma irradiation have different influences within TPA-TCT measurements. The most striking difference between hadron and gamma irradiated samples is the SPA background in hadron irradiated devices, as shown in figure 4.5b. In the following, it will be argued that the SPA offset is related to cluster defects. Concentrations of point defects introduced by neutron and gamma irradiation can be calculated using introduction rates from [57]. The most common point defects introduced by neutron and ^{60}Co-gamma irradiation are $VO^{-/0} + C_iC_s^{-/0}$ and $C_iO_i^{+/0}$. Neutron irradiation introduces both defects approximately proportional to the fluence. After a neutron fluence of $3.9 \cdot 10^{13}$ n/cm^2 SPA offset is visible, which corresponds to a concentration of approximately $3.9 \cdot 10^{13}$ cm^2 for the $VO^{-/0} + C_iC_s^{-/0}$ and $C_iO_i^{+/0}$ defects. On the other hand, gamma irradiation at the highest investigated dose introduces about $1.2 \cdot 10^{14}$ cm^2 and $0.8 \cdot 10^{14}$ cm^2 of these two defects, respectively and thus a comparable concentration of both defects is present. As the defect concentrations of the neutron and gamma irradiation are comparable, while the SPA offset is absent in the gamma irradiated devices, it can be concluded that the SPA offset is not caused by the discussed point defects. Compared to the $VO^{-/0} + C_iC_s^{-/0}$ and $C_iO_i^{+/0}$ defect, other point defects are present in smaller concentration and thus assumed to be less significant. This gives indication that the linear

light absorption found in neutron and proton irradiated devices originates from cluster defects that are not introduced by gamma irradiation. In [110] linear absorption of 1550 nm light in neutron irradiated silicon is linked to the electrically neutral divacancy V_2^0 defect state, which is introduced by neutron irradiation within cluster defects [144]. This is in agreement with the hypothesis that the SPA background originates from cluster defects, which explains the absence of the SPA background for gamma irradiated devices.

Figure 4.6 shows a comparison between the different irradiations for the highest fluence/dose available, where the SPA corrected CC (a) and PC (b) are shown. It can be seen that independent of the particle type, a decrease in the CC is present. Only the neutron and proton irradiated samples show variation along the device depth that is related to different trapping cross-section of electrons and holes. Further, all particle types decrease the PC, i.e. the electric field in the device. Neutron and proton irradiation at the presented fluences leads to a double junction in the DUT and the proton irradiated device shows additionally an inverted space charge sign. The PC profiles of the hadron irradiated devices were previously discussed in section 4.2. Both, the non-irradiated and the gamma irradiated sample show a roundish shaped PC profile, which does not agree with the expected linear behaviour in a pad detector. It is found that the roundish shape is an effect of CC during the PC time t_{pc}, which is discussed in more detail in section 6.2. Here it is just mentioned that smaller t_{pc} or lower bias voltages decrease the roundish shape and reveal the expected linear electric field shape throughout the device depth. The effect is here especially visible as the charge is collected quickly at the used bias voltages that correspond to about 2 V/µm. The PC time of $t_{pc} = 600$ ps is here used for a sufficient SNR that allows an easy qualitative comparison among all samples.

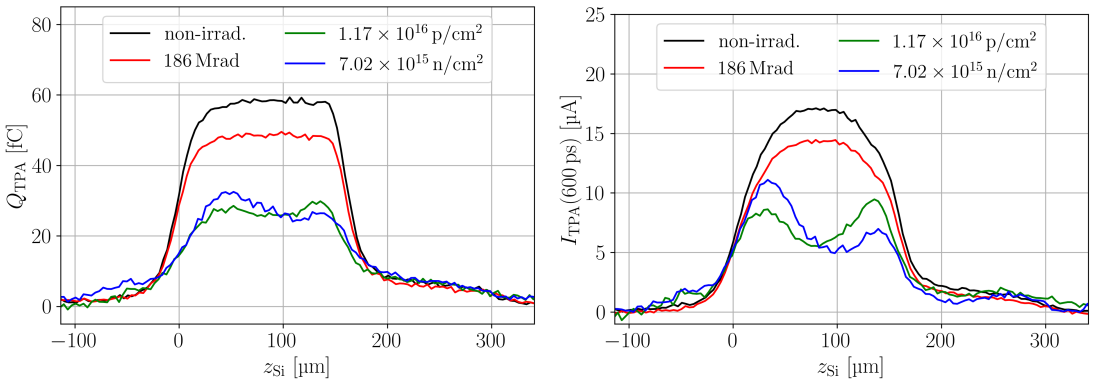

Figure 4.6: (a) SPA corrected in-depth scans of the charge collection in pad detectors (CiS16). A non-irradiated sample is shown together with a neutron, a proton, and a gamma irradiated sample. (b) Prompt current of the same SPA corrected in-depth scans. The bias voltage is 300 V.

Figure 4.7 shows the normalised SPA (a) and TPA (b) contribution against the equivalent fluence and dose. The SPA and TPA parameters are extracted from in-depth scans with the analysis procedure described in section 4.2. To account for the device thickness dependence of the SPA, the SPA contribution is normalised with the bias voltage over the device thickness. Thicker devices collect more SPA charge due to the higher charge generation in the increased active thickness, and they collect less TPA charge due to the longer drift

times, as more charge is trapped. It can be seen that the SPA and TPA contribution of neutron and proton irradiated samples scales similarly with the 1 MeV neutron equivalent fluence, which indicates that both quantities scale with NIEL. The scaling with NIEL supports the hypothesis that the SPA background originates from cluster damage.

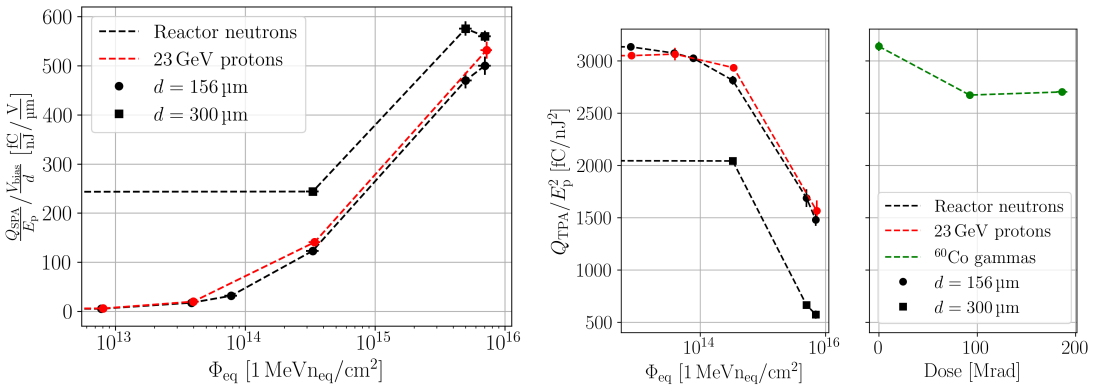

(a) **(b)**

Figure 4.7: (a) SPA charge collection normalised with the average electric field versus the equivalent fluence for neutron and proton irradiated FZ p-type pad detectors from the CiS16 campaign. (b) TPA charge collection versus the equivalent fluence and dose for the same DUTs measured at a bias voltage of 300 V.

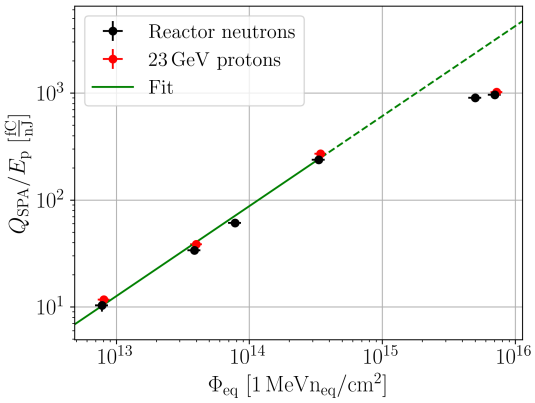

Figure 4.8: Charge collected by SPA normalised with the pulse energy for proton and neutron irradiated CiS16 samples at a bias voltage of 300 V. The fit function is of the form $C \cdot \Phi_{eq}^{a}$, with $C = 14.3 \cdot 10^{-11}\,\mathrm{cm}^{2\cdot a}\mathrm{fC/nJ}$ and $a = 0.84$. The highest fluences are excluded from the fit due to significant charge trapping.

Figure 4.8 shows the SPA background against the 1 MeV neutron equivalent fluence. The SPA contribution follows a function $C \cdot \Phi_{eq}^{a}$ for fluences $< 10^{15}\,\mathrm{n_{eq}/cm^2}$. For higher fluences an SPA contribution below this functionality is found, where it is observed that increasing bias voltages reduce the deviations. The bias dependence indicates that the deviations are related to charge trapping that becomes apparent at the highest fluences.

When the laser focus is driven across the opening window's metal edge of hadron irradiated pad detectors, a strong increase in the charge generation is observed. Figure 4.9a shows the experimental findings, where the opening window's edge is positioned at $x = 0\,\mu m$. Scans of the bias voltage confirm that this effect is not related to some kind of charge multiplication, which is observed in strip detectors at the strip metal [5, 145]. As the gamma irradiated and the non-irradiated device do not show this kind of behaviour, it is concluded that the increased CC is related to the presence of the SPA absorption. The effect appears for all hadron irradiated devices, and it's extend is affected by the deposition

depth. The differences seen between the neutron and proton irradiated device are most likely related to different deposition depth, as for the measurement the deposition depth was arbitrarily selected. The sketch in figure 4.9b shows a possible explanation of the large increase of SPA charge generation. When the laser is driven across the metal edge, some light rays are potentially reflected under a shallow angle. The reflected light would have a long traversing distance in the active volume, which leads to significant SPA. This effect could be relevant to devices with large active volumes comparable to pad detectors. For segmented devices, where only a single strip or pixel is read out, the effect is not observed, which is most likely related to the pitch sizes that are typically in the order of 80 µm or less. The small active area that contributes to the readout strip might not lead to sufficient SPA increase and the effect is negligible in such structures.

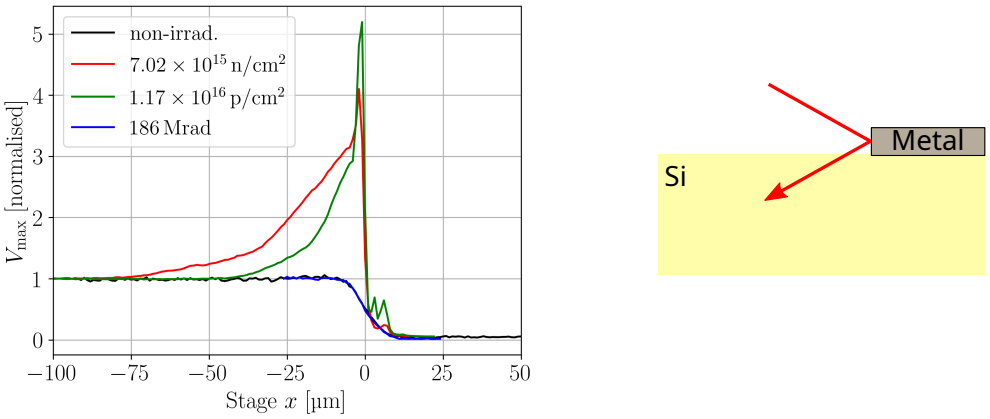

Figure 4.9: (a) Scans across the opening window's metal edge of pad sensors (CiS16) irradiated with different particles. The signal amplitude is shown, which is normalised with a value observed in the central position of the opening window. A strong increase in charge generation is found for neutron and proton irradiated samples, when the focal point is positioned at the edge. The additional charge generation is not present in gamma irradiated or non-irradiated samples. (b) Sketch of a possible explanation for the strong increase in SPA signal. Light rays (red) might are reflected at the opening window's metal edge so that they traverse the silicon bulk under a shallow angle. The long travel distance through the bulk increases the SPA charge.

4.5 Influence on the two photon absorption coefficient

In the above presented measurements, it is observed that irradiation decreases the CC. However, it is not given that the charge generation mechanism of TPA is not impacted by the irradiation, meaning that the absorption coefficient β_2 could be a function of fluence. To investigate the fluence dependence of β_2, a comparative CC study was performed using the ^{90}Sr setup described in section 3.3. Charge sensitive amplifiers are used to increase the SNR. The 156 µm thick, neutron irradiated subset of the CiS16 samples is used for this study and the non-irradiated detector from the same wafer serves as a reference. An example for the CC measurement in a non-irradiated device shown in figure 4.10a. It can be seen that the CC resembles the expected Landau-Gauss distribution as discussed in section 2.3.1 and an additional noise peak for a charge < 1 fC is measured. The signal of the

CC distribution is fitted with a Landau-Gauss distribution and the noise peak is fitted by a Gaussian distribution [146]. The fit is performed in a single function, where the Landau-Gauss and Gaussian distribution are added together and a satisfactory agreement with the data is found. The found MPV corresponds to the generated charge of a minimum ionising particle (MIP). For the non-irradiated detector the MPV is measured as 1.92 fC $\hat{=}$ 12 k electron-hole pairs, which is in good agreement with the expected $\approx$ 11.9 k electron-hole pairs from literature [62]. Figure 4.10b shows the evolution of the CC with increasing neutron irradiation. To suppress noise as efficient as possible, the distributions are filtered, where data is rejected if the peaking time of the DUT is not around the peaking time of the reference within a time frame of $\pm$50 ns. When the CC of the non-irradiated device in figure 4.10b is compared to figure 4.10a, it is evident that the used criteria suppresses noise efficiently. Some noise remains after filtering, because the noise is randomly distributed in time. It is observed that the CC decreases with fluence due to the increasing charge trapping. At a certain fluence, the signal and noise distribution begin to overlap, which hinders the extraction of the MPV. Here, for fluences $\geq 5 \cdot 10^{15}$ n/cm^2 the extraction of the MPV is no longer possible.

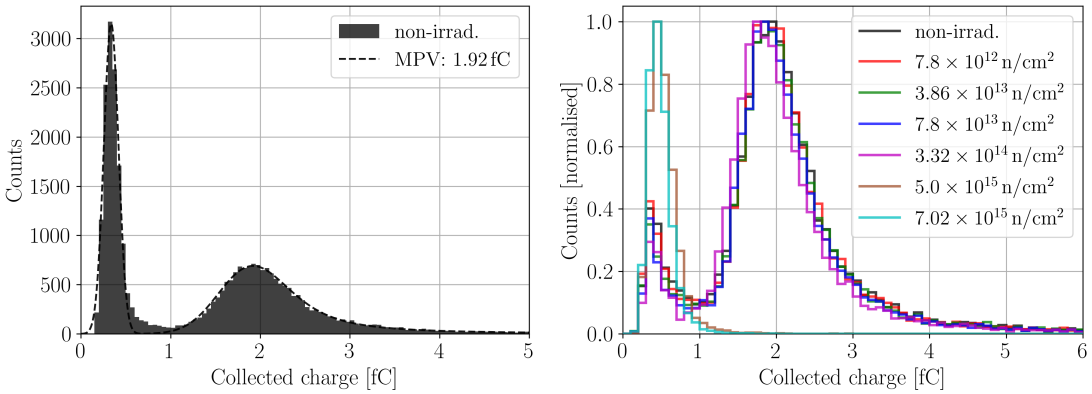

(a) **(b)**

Figure 4.10: (a) Charge collection of a non-irradiated 156 µm thick p-type pad sensor measured in a ^{90}Sr setup. (b) Charge collection in neutron irradiated pad sensors for different fluences. The histograms are normalised with their maximum amount of counts to ease the comparison. The bias voltage in all measurements is 300 V and the used sensors are from the CiS16 campaign.

Figure 4.11 shows charge collection efficiency (CCE) against the equivalent fluence measured with the TPA-TCT setup and the ^{90}Sr setup. The CCE is defined as the percentage of charge that is collected in comparison to the non-irradiated device. For the ^{90}Sr setup this means the normalisation of the MPV with the MPV of the non-irradiated device and for the TPA-TCT the fitting parameters for Q_{TPA} described in section 4.2 are normalised with the fitting parameter from the non-irradiated device. The data from the proton irradiated devices is included even though they were only measured with the TPA-TCT. It can be seen that both techniques yield, within the measurement uncertainty, a compatible CCE. The compatibility of both techniques indicates that the charge generation mechanism of TPA and the β-particle of the ^{90}Sr source scales similar with fluence up to at least $3.32 \cdot 10^{14}$ n/cm^2. As the excess charge generation by the two processes is very different, the similarity of the CCE measurements strongly hints that the charge generation mechanism of TPA, i.e. the absorption coefficient β_2, is constant with fluence: $\frac{\mathrm{d}}{\mathrm{d}\Phi}\beta_2(\Phi) = 0$. Contrary to β_2,

the SPA coefficient α is fluence dependent as discussed in section 2.5.2. Besides the investigation of β_2, it can be seen that the TPA-TCT provides CCE values even for fluences $\geq 5 \cdot 10^{15}\,\mathrm{n/cm^2}$ that are not accessible with the used ^{90}Sr setup. This is caused by two reasons. First, the intensity of the laser can be increased to much more than one MIP equivalent of charge. Second, averages for multiple acquisitions are available, as the charge generation of the laser is reproducible pulse-per-pulse. Both reasons significantly increase the SNR and thus the measurement range. In contrast, the ^{90}Sr setup relies on single acquisition, because the charge generation is a stochastic process and the events are uncorrelated. Further, the setup triggers on the coincidence of the two reference detectors and in order to mitigate influences on the DUT's signal acquisition, the DUT is not included in the trigger. Hence, it is not ensured that the DUT records a particle hit for every acquisition, which leads to the noise floor. In conclusion, it was demonstrated that the TPA-TCT allows performing CCE measurements similar to a ^{90}Sr setup and the TPA-TCT offers an extended measurement range of CCE measurements.

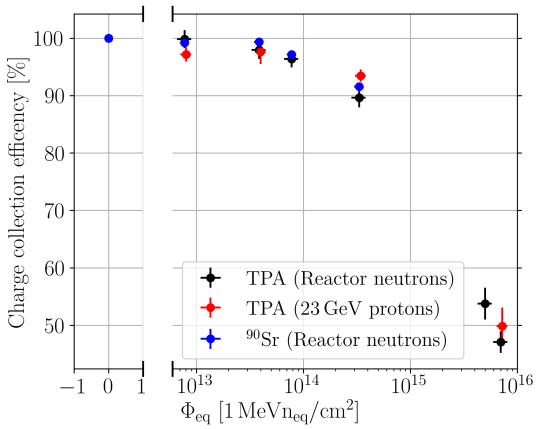

Figure 4.11: Charge collection efficiency of pad detectors from the CiS16 campaign measured with the TPA-TCT and a ^{90}Sr setup against the equivalent fluence. The particle type used for irradiation is mentioned in the legend.

4.6 Influence of the device thickness

Neutron irradiated samples of two thicknesses (156 µm and 300 µm) are investigated in order to compare the influence of thickness. The SPA and TPA contribution is extracted from in-depth measurement, similar to the analysis procedure described in section 4.2. Figure 4.12 depicts the results, where the fitting parameters of the SPA (a) and TPA (b) contribution are shown versus the bias voltage. The bias voltage is normalised by the device thickness to ease the comparison between the two thicknesses. With increasing bias voltage, an increase in the collected SPA charge is observed, which results from the increase of the depletion region and the increasing drift velocity. The increase of the depletion region is only applicable to the fluences below $< 5 \cdot 10^{15}\,\mathrm{n/cm^2}$ and the increase of drift velocities lead to lower collection times and hence reduces the trapping. Saturation of the SPA charge is reached up to fluences of at least $3.32 \cdot 10^{14}\,\mathrm{n/cm^2}$, which means that further increasing electric fields do not decrease the amount of charge loss. Higher fluences do not reach saturation within the investigated bias voltage range, but it is expected that higher bias voltages would still reduce the charge loss until the drift velocities are saturated. Thicker devices collect more SPA charge than the thinner devices, which originates from the thickness dependence of the SPA contribution. However, trapping is more pronounced in

thick devices due to longer drift times, which balances off against the thickness dependence. The influence of the longer drift times can be seen in figure 4.12a, where the SPA charge for the fluence $3.32 \cdot 10^{14}\,\mathrm{n/cm^2}$ (purple curve) of the thicker device saturates later than for the thinner device. The collected TPA charge increases with bias voltage due to the same two mechanisms discussed above for the SPA charge. Similar to the SPA charge collection, all devices for fluences $< 5 \cdot 10^{15}\,\mathrm{n/cm^2}$ reach a saturated CC and the TPA charge of the fluence $3.32 \cdot 10^{14}\,\mathrm{n/cm^2}$ (purple curve) saturates for higher bias voltages for the thicker device than for the thinner device. For higher fluences, the thicker devices collect significantly less TPA charge than the thinner devices, which is caused by more trapping during the longer drift time.

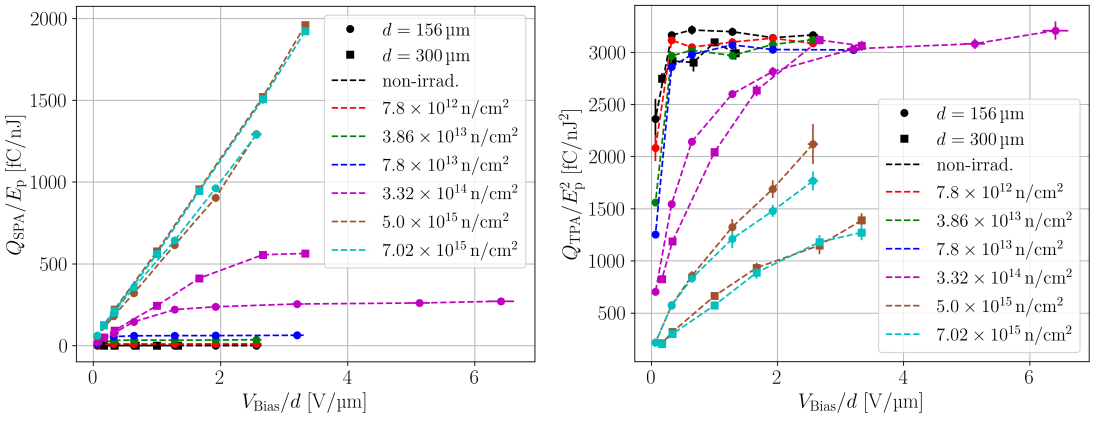

(a) **(b)**

Figure 4.12: SPA (a) and TPA (b) charge versus the bias voltage normalised by the device thickness for neutron irradiated pad detectors from the CiS16 campaign.

4.7 Beam depletion due to SPA

The additional SPA contribution in irradiated devices might lead to beam depletion, which in turn would lead to a decreasing TPA charge generation along the device depth. For fluences up to $3.32 \cdot 10^{14}\,\mathrm{n_{eq}/cm^2}$, no variations of the TPA charge over the device depth is observed, which suggests that potential beam depletion is negligible for these fluences. However, higher fluences lead to inhomogeneities in the CC profile (compare to figure 4.3c and 4.3d). These inhomogeneities potentially originate from beam depletion and are not only a result of deposition dependent trapping or changes of the effective doping concentration. To estimate the beam depletion due to linear absorption, an effective absorption coefficient can be defined by integrating the SPA charge generation of equation (2.33) over the full device depth d. The result can be rewritten using $Q_{\mathrm{SPA}} = e_0 N_{\mathrm{SPA}}$ and rearranged for the absorption coefficient

$$\alpha_{\mathrm{eff}} = -\frac{1}{d} \ln\left(1 - Q_{\mathrm{SPA}} \frac{\hbar\omega}{e_0 E_{\mathrm{p}}}\right). \tag{4.1}$$

$Q_{\mathrm{SPA}}/E_{\mathrm{p}}$ is obtained from the fitting of the SPA contribution (see figure 4.3a and 4.3b). The absorption coefficient is called effective, because only absorbed light that generates charge, which is measured as CC and not the total amount of absorbed light. Hence, the inequality $Q_{\mathrm{SPA,coll}} \leq Q_{\mathrm{SPA,gen}}$ applies, where equality is only reached if all SPA light

contributes to the charge generation and charge loss is fully absent. When charge loss is present, the inequality yields

$$\alpha_{\text{eff}} \leq \alpha_{\text{irrad}} \,, \tag{4.2}$$

with α_{irrad} being the linear absorption coefficient due to irradiation, which is defined as

$$\alpha_{\text{irrad}} = \alpha(\Phi_{\text{eq}}) - \alpha(0) \,. \tag{4.3}$$

Figure 4.13a shows the effective linear absorption coefficient versus the bias voltage for neutron irradiated pad sensors with different thicknesses. α_{eff} increases with the bias voltage and saturates within the investigated voltage range for fluences up to $3.32 \cdot 10^{14}\,\text{n/cm}^2$. The maximum absorption coefficient for these fluences is below $0.2\,\text{cm}^{-1}$, which leads to a beam depletion below 0.6 % in a 300 µm thick silicon detector. Such low intensity loss can be neglected. Thicker devices yield lower α_{eff}, because the charge loss is more pronounced, which increases the inequality of equation (4.2). Higher fluences do not reach saturation within the used bias voltage range, because the charge loss does not saturate within the observed bias voltage range. Figure 4.13b shows the effective absorption coefficient for neutron and proton irradiated pad detectors versus the equivalent fluence. As the SPA charge collection does not saturate for the highest fluences, only a lower limit for α_{eff} is stated. From the measured data it is ensured that the beam is not depleted by the SPA absorption for fluences up to at least $3.32 \cdot 10^{14}\,\text{n/cm}^2$. The effective absorption coefficient does not saturate for higher fluences, which hinders to investigate the absolute beam depletion. Reference [110] measures $\alpha_{\text{irrad}} < 1\,\text{cm}^{-1}$ for a fluence of $10^{16}\,\text{n/cm}^2$ in non-biased detector grade silicon, which corresponds to less than 3 % absorption in a 300 µm thick device. In conclusion, beam depletion in irradiated devices due to SPA for fluences up to at least $10^{16}\,\text{n/cm}^2$ is assumed to be negligible.

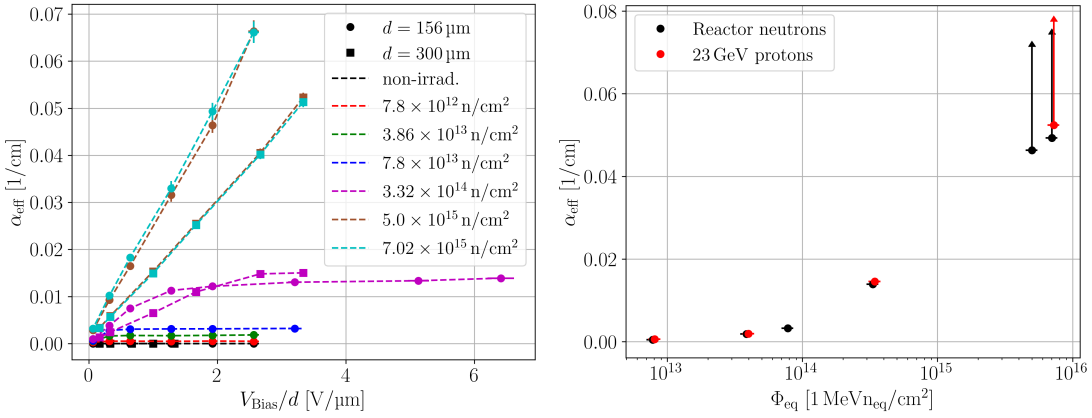

(a) **(b)**

Figure 4.13: (a) Effective linear absorption coefficient of neutron irradiated pad detectors versus the bias voltage, which is normalised with the device thickness. (b) Effective linear absorption coefficient for 156 µm thick neutron and proton irradiated pad detectors versus the equivalent fluence. The value for the maximum bias voltage is used. The absorption coefficient does not saturate for the highest fluences and the highest applied bias voltage is different for the proton and neutron irradiated devices. In order to show comparable α_{eff}, a bias voltage of 300 V is selected. The arrows indicate that the α_{eff} did not reach saturation for the used bias voltage. The devices are from the CiS16 campaign.

4.8 Influence on the refractive index

Irradiation potentially changes the refractive index of silicon, as is observed for heavy ion irradiation [112]. A changing refractive index influences the reflectance of the material and thus the amount of generated charge. In this section, the refractive index is studied indirectly from TPA-TCT in-depth scans, by exploiting the refraction at the top air-silicon interface. Refraction is described by equation (2.35), where the scaling factor $s = z_{\mathrm{Si}}/z$ depends on the refractive index. The equation can be rearranged to the squared refractive index

$$n^2 = -\frac{\gamma - s^2}{2} + \sqrt{\frac{(\gamma - s^2)^2}{4} + \gamma}, \tag{4.4}$$

with $\gamma = (\lambda s^2)/(\pi z_{\mathrm{R}})$. Therefore, a study of the scaling allows drawing conclusions on the refractive index. If irradiation changes the refractive index, the scaling factor would depend on the fluence and dose, so that the boundary interfaces of the devices would appear at different positions in the uncorrected coordinate system. As all devices are from the same wafer, the assumption of the same thicknesses is reasonable. The position of the boundaries is extracted from in-depth scans, following the procedure described in section 6.1. The back side surface is found from symmetries in the ToT profile, which is why such plots are well suited to qualitatively compare the devices thicknesses. Figure 4.14a shows ToT profiles in uncorrected z-coordinates, where the position of the top and back side surface, extracted from the non-irradiated device, is indicated. In the figure it can be seen that the devices have, independent of their irradiation, the interfaces at the same position, which indicates that the potential changes in the refractive index are small. Aside the boundary positions, the hadron irradiated devices show differences in the ToT at the top side and only slight differences at the back side. The difference at the top side is related to hole trapping, which is more severe than the electron trapping, thus a less significant difference is present at the back side.

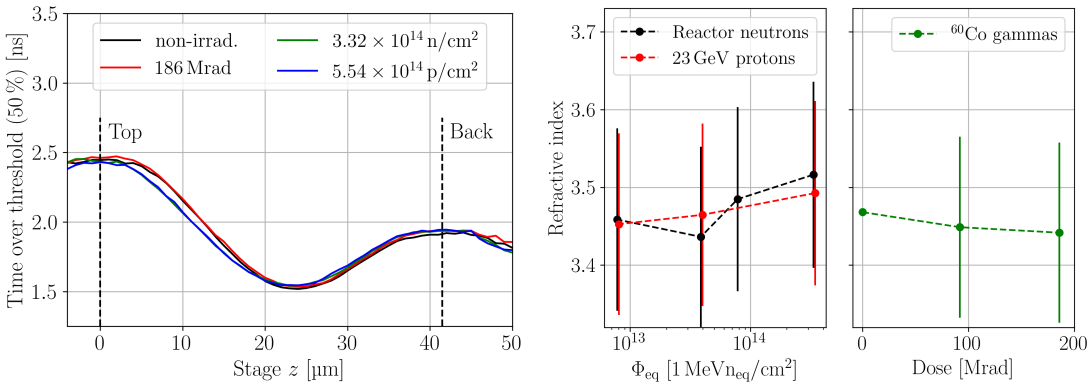

(a) **(b)**

Figure 4.14: (a) Time over threshold profiles of the non-irradiated and the irradiated CiS16 pad detectors. The highest fluences, while avoiding the double junction effect, are used to allow the comparison. The refraction from the air-silicon interface is not corrected in the z-axis. The location of the top and back interface is extracted from the non-irradiated device and indicated by the dashed lines. (b) Refractive index extracted from the in-depth scans of various irradiated pad detectors from the CiS16 campaign. The nominal refractive index $n(250\,\mathrm{K}) = 3.4681 \pm 0.0002$ is taken from [86]. All scans are performed with a bias voltage of 300 V.

A quantitative study of the refractive index is performed using the scaling factor, which is found by comparing the extracted device thicknesses in stage coordinates, i.e. uncorrected coordinates. The boundaries are extracted from fits towards the SPA corrected charge profile of all devices individually, with the fitting model described in the appendix A.3. The scaling factor is found by comparison with the non-irradiated device and the refractive index is then calculated from equation (4.4). This procedure is performed for all devices that do not show the double junction effect, because the double junction is found to dominate the ToT and CC profile and hinders the precise extraction of the device's boundaries. The results are summarised in figure 4.14b. All measured values are compatible with the nominal value of the non-irradiated device and no trend with the equivalent fluence is observed. The error bars are quite large, because the used method is only indirect, and measurement uncertainties propagate to yield the presented errors. In conclusion, it is found that potential changes of the refractive index due to irradiation are smaller than 5.5 % for equivalent fluences up to $3.32 \cdot 10^{14}\,\mathrm{cm}^{-2}$ and doses up to 186 Mrad.

5 Gain reduction in low gain avalanche detectors

In the following, silicon devices with intrinsic gain are investigated. The discussed diodes have the implantation $n^+/p^+/p/p^+$, where the additional p^+ layer at the top n^+ contact introduces a high field region that leads to charge multiplication. Originally, such devices were developed for low energy photon detection [147] and recent developments show that they are well suited for high precision timing applications with time resolutions in the order of few 10 ps [148]. Gain values of ten to twenty are commonly used, wherefore the devices are called low gain avalanche detectors (LGADs) to distinct them from other avalanche diodes such as silicon photo multipliers with gain values of several thousands [149]. LGADs are a selected technology for precision timing detectors at the phase II upgrade of the ATLAS [150] and the CMS [151] detector at the large hadron collider (LHC) at CERN. The gain originates from impact ionisation in the high field region at the top junction and is sensitive to several measurement parameters: the bias voltage [149], the temperature [152], and the excess charge carrier density [153]. The dependence on the excess charge carrier density is subject to this section. It is found that increasing excess charge carrier densities at the junction lead to a decreasing gain, which worsens the timing performance [43]. The mechanism is understood as a polarisation effect that arises from an electric field that the primary charge carriers build up together with secondary charge carriers. Figure 5.1a shows a sketch of the gain reduction mechanism. Electrons drift towards the top electrode and are multiplied at the junction. The created secondary electrons and holes drift towards the top and back side, respectively. Due to the opposite polarity of electrons and holes, an electric field is built up that is counter directed to the device's electric field. Following electrons find a lowered electric field at the junction and thus a reduced impact ionisation, which is observed as a lower gain.

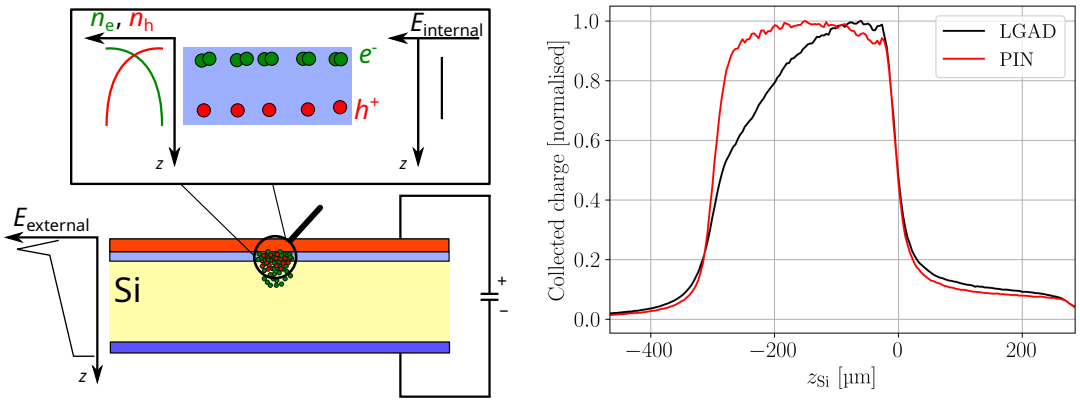

(a) **(b)**

Figure 5.1: (a) Visual explanation of the charge carrier density related gain reduction mechanism in an LGAD. $n_{e,h}$ refers to the density of electrons e^- and holes h^+. (b) Normalised charge collection profiles of the LGAD W5-D8-LGAD2 and the pad detector W5-J6-PIN2. The detectors are aligned so that the back side is at $z_{Si} = 0\,\mu m$. The gain reduction at the top side of the LGAD can be clearly seen. The bias voltage is 900 V.

The TPA-TCT is used to study the gain reduction mechanism in a single in-depth scan [45]. All measurements presented within this section were measured at a temperature of 20 °C and a relative humidity of $\approx 0\,\%$. Optical beam parameters of $w_0 = 1.3\,\mu m$ and $z_{R,Si} = 11.9\,\mu m$ were present, and the averaged current transients of 256 single acquisitions were recorded.

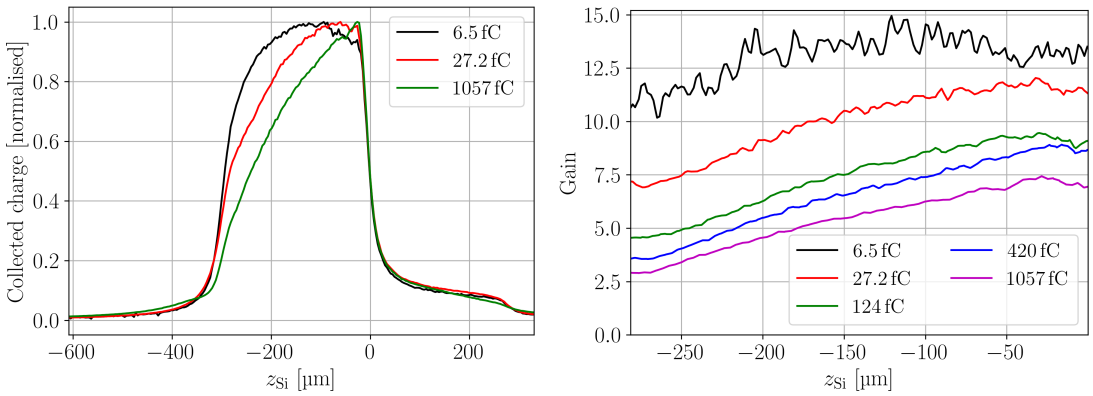

(a) **(b)**

Figure 5.2: Gain reduction mechanism observed in the W5-D8-LGAD2 LGAD by in-depth scans (a) and gain profiles (b) at different laser intensities. The laser intensity is given in units of the generated charge, which is extracted from measurements in a pad detector. The top side is located at $z_{Si} \approx -300\,\mu m$ and the coordinates in the z-axis of both plots match. The gain reduction becomes more pronounced when charge is generated inside or close to the top side junction. All measurements are performed with a bias voltage of 900 V.

The laser was operated at a pulse frequency of 200 Hz. Figure 5.1b shows the charge collection profile of an LGAD that yields the characteristic *shark fin* shape. The LGAD is $\approx 285\,\mu m$ thick and from run 8622. More details about it and its corresponding pad detector can be found in section 3.1. Less charge is collected in the LGAD when the excess charge is deposited directly inside or near the avalanche region. When the excess charge is generated further away from the top junction the collected charge (CC), i.e. gain increases. The recovery of gain is related to diffusion as explained in the following. When the excess charge is deposited inside the device it begins to drift and diffuse. The deeper the charge is deposited, the longer it drifts to the top side and the more time is available for diffusion. Diffusion seeks to equalise densities, which is why longer drift times lead to stronger broadening of the excess charge carrier density. This hypothesis is verified below via simulation in section 5.2.

Gain is defined as

$$G = \frac{Q_{\mathrm{LGAD}}}{Q_{\mathrm{PIN}}}\,, \tag{5.1}$$

with the CC of the LGAD Q_{LGAD} and the CC of the corresponding pad detector Q_{PIN}. Figure 5.2 shows in-depth scans (a) and gain profiles (b) of an LGAD for increasing deposited charge. Increasing deposited charge corresponds to increasing charge carrier densities. It can be seen that gain reduction is present for all used intensities and a constant gain value across the active volume is not reached for any of the used intensities. On the one hand, there should be a low intensity threshold, below which no gain reduction occurs. On the other hand, there should be an upper threshold above which the gain reduction is saturated, i.e. the gain should asymptomatically approach the value 1, which indicates that no gain is left. The continuous presence of gain reduction suggests that the gain strongly depends on the generated charge and shows that the understanding of the effect is of great importance, as it is most likely always present. Further, a low signal-to-noise ratio (SNR) is present for the lowest investigated intensity, which originates from the low

SNR in the measurement of the pad detector. From figure 5.2b it can be concluded that the gain always needs to be mentioned with respect to the generated charge and setup parameters, as suggested in [43]. Otherwise, absolute values of the gain become ambiguous, as they differ with the used intensity.

Figure 5.3 shows waveforms recorded at different deposition depths and laser intensities. The separation between primary and secondary charge carrier is clearly visible in the waveform from the back side. The primary carriers lead to the first part of the induced current, while the secondary carriers lead to the strong increase after about 2 ns. This separation is not possible for the waveforms recorded at the top side, as primary and secondary carriers simultaneously induce a current. When comparing the waveforms at different intensities in figure 5.3a and 5.3b, it can be seen that the lower intensity results in more similar amplitudes, which indicates that the integral over time is also more similar. Hence, the waveform at the top and back side comprises a more similar amount of charge than the waveforms from the higher intensity measurement. This represents a direct observation of the gain reduction mechanism.

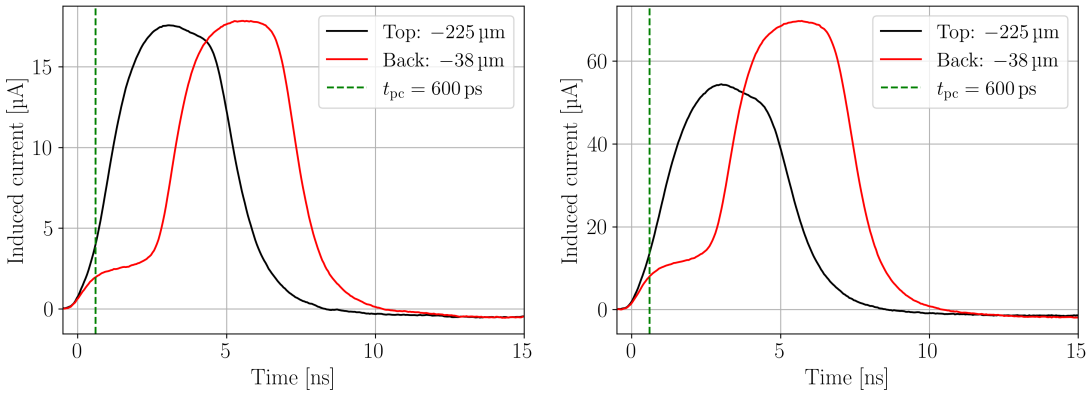

Figure 5.3: Waveforms recorded at the top and back side of the W5-D8-LGAD2 LGAD for $V_{bias} = 900$ V. Multiplication of primary electrons is visible in the waveform from the back side as a rapid increase in the current after about 2 ns. The drift of primary and secondary charge carriers overlaps in the waveform from the top. The generated charge is 6.5 fC (a) and 27.5 fC (b), which correspond to the pulse energy 90 pJ and 180 pJ, respectively. The prompt current time is indicated by the dashed line.

5.1 Investigation of the electric field

The prompt current (PC) method is used to investigate the electric field of an LGAD as a function of its device depth. Figure 5.4 shows the PC profile at different bias voltages, for a lower (a) and a higher (b) laser intensity. The laser intensities are selected so that potential electron-hole plasma has a negligible influence. The peak at the top side is a result of the multiplication layer. The peak height relative to the bulk height increases with the bias voltage, which is related to an increasing gain. Comparing the scans taken with lower (a) and higher (b) laser intensity shows that the peak height relative to the bulk height decreases with the laser intensity. A decreasing peak height is associated to a decreasing electric field, i.e. a decreasing gain. The dependence on the laser intensity

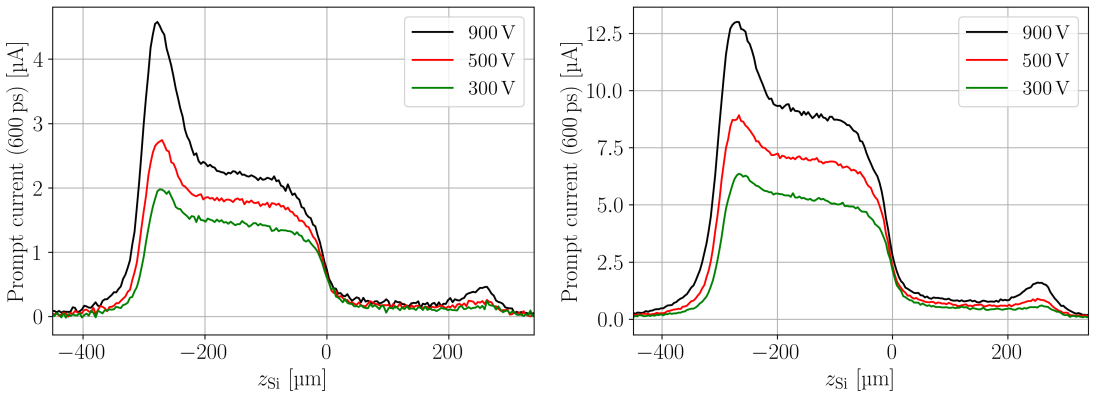

Figure 5.4: Prompt current profile of the W5-D8-LGAD2 LGAD for different bias voltages. The peak at $z_{Si} \approx -280\,\mu m$ corresponds to the multiplication layer at the top junction. The generated charge is 6.5 fC (a) and 27.5 fC (b).

is interpreted to be a result of the gain reduction mechanism, as lower laser intensities correspond to higher measured gains. The most striking feature in the PC profile is the peak from the multiplication layer. The thickness of this layer is in the order of 2 µm, but it appears much thicker in the scan. Reasons behind the thicker appearance are twofold. First, TPA-TCT offers a limited spatial resolution, which tends to round out edges and elongate thin features that are smaller than $\approx 2 \cdot z_{R,Si}$. Figure 5.5a shows a simulated convolution of a modelled electric field of an LGAD and the TPA-TCT charge generation for the measured beam parameters. The edges are rounded, the peak at the top side is lowered in height, and the peak width broadens by the convolution. Second, the excess charge carriers that are generated near the avalanche region increase the peak's width further. During the PC time t_{pc}, primary electrons in a region close to the multiplication layer get amplified and secondary charge carriers are created. These secondary carriers also contribute to the induced current, i.e. the PC. Longer t_{pc} increase the peak width, as well as the ratio between peak height and bulk height. Figure 5.5b shows the measured PC profile for various PC times. When the excess charge is generated in the vicinity of the multiplication layer, not only primary, but also secondary charge carriers contribute to the PC. The participation of the secondary carriers increases the PC and leads to a higher peak. Current transients previously shown in figure 5.3 visualise the simultaneous contribution of primary and secondary carrier, when looking at the transient taken at the top side (black curve). Longer t_{pc} allow even primary carriers further away from the multiplication region to be multiplied, so that their secondary carriers contribute to the PC as well. This broadens the peak in an asymmetric manner towards the bulk. Three processes contribute to the height of the peak: the saturation of drift velocity, the spatial resolution, and the contribution of secondary carriers. The prior two decrease and the latter increases the extracted peak height. The electric field in the avalanche region is expected to be $> 20\,V/\mu m$ [149], which is beyond saturation of the drift velocity. Hence, such high fields are not accessible for the PC method, due to a saturated induced current as explained in section 2.3.4. Further, the spatial resolution leads to a height reduction of thin structures that lower the measured peak height (see figure 5.5a). Contrary to the prior two effects, the additional induced current from the secondary carriers increases the peak height. It applies that longer t_{pc} lead to a higher additional contribution.

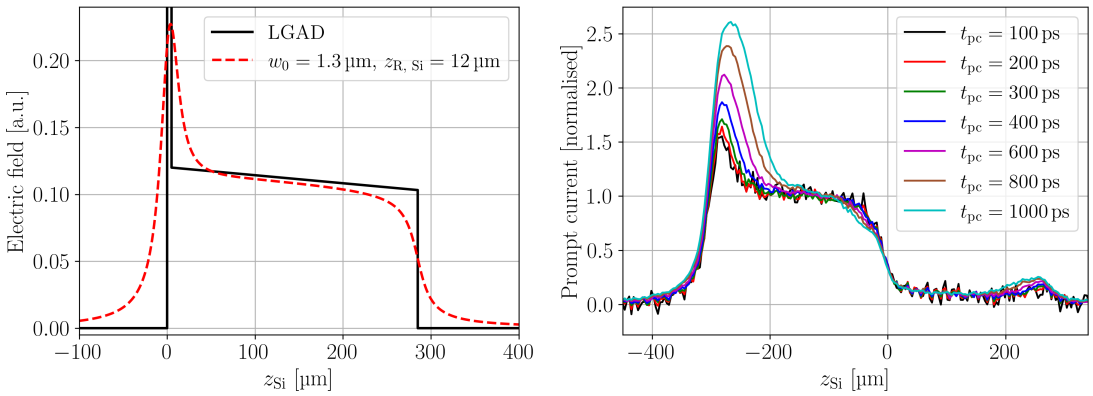

(a) **(b)**

Figure 5.5: (a) Convolution of the TPA-TCT charge profile with a modelled LGAD electric field. A gain of 11 is selected and 5 µm width of the multiplication layer is assumed. The peak of the modelled electric field reaches the value 1.32, wherefore the y-axis is cut off to maintain a reasonable scale. The convolution smears out the edges and broadens the peak. (b) Prompt current profiles of the W5-D8-LGAD2 LGAD for different prompt current times t_{pc}. The profiles are normalised with the prompt current in the bulk. The bias voltage is 900 V.

5.2 Influence of diffusion

In this section, the hypothesis that diffusion recovers part of the gain of LGADs is investigated. Only the diffusion of electrons need to be considered, as the primary holes drift towards the back side of the LGAD and play a minor role in the gain reduction. After deposition, the excess electron density $n_{TPA,e}$ experiences diffusion, which is described by the diffusion equation (2.16). The distribution broadens in all directions, which reduces its density. To simulate diffusion, a two-dimensional approach is made to exploit the rotation symmetry of $n_{TPA,e}$. Following equation (2.16), two-dimensional diffusion is described by

$$\frac{\partial}{\partial t} n_{TPA,e} = D_e \left(\frac{\partial^2}{\partial^2 r} + \frac{\partial^2}{\partial^2 z} \right) n_{TPA,e} \,. \tag{5.2}$$

The equation is numerically solved by discretisation of the time in time steps $\Delta t = 2.8\,ps$. $D_e \approx 36\,cm^2/s$ is used as the diffusion constant [58] and the beam parameters $w_0 = 1.3\,\mu m$ and $z_{R,Si} = 11.9\,\mu m$ are taken. The drift time of a given deposition depth is extracted from a measurement at low laser intensity $E_p \approx 85\,pJ$, to avoid any influence of electron-hole plasma. Absolute values of $n_{TPA,e}$ used in the modelling might differ from the actual values during the measurement, as no tuning to the measured charge values was performed. The potential relative difference in $n_{TPA,e}$ is not expected influence the broadening process, because diffusion is independent of the absolute value. Thus, potential absolute differences do not diminish the validity of the simulation.

Figure 5.6 shows the results of the simulated diffusion. The gain measured at different deposition depth is shown as a function of the central excess charge carrier density, without (a) and with (b) the diffusion model applied. The gain values are a mean of ≈ 2 µm around the corresponding deposition depth, and the error bars indicate the standard deviation of these values. The error on the central charge carrier density is derived from uncertainties

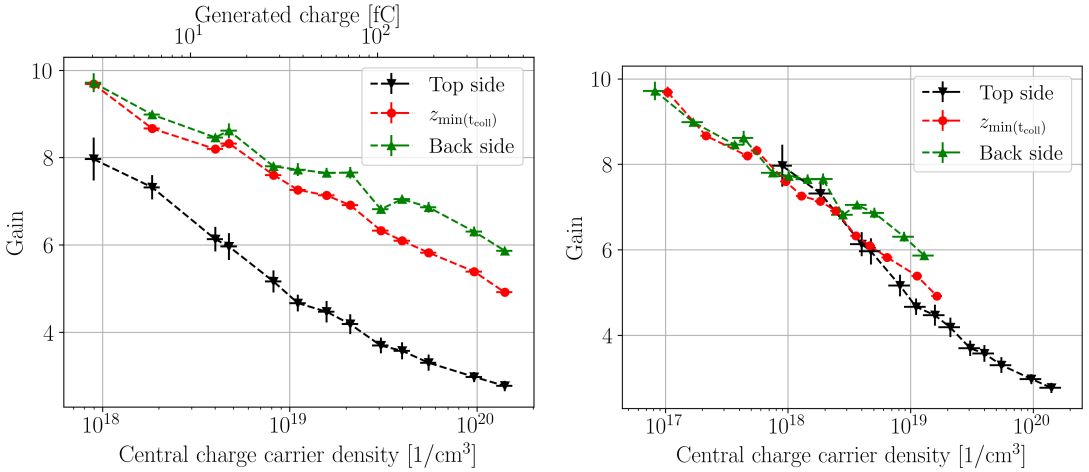

Figure 5.6: Gain as a function the central excess charge carrier density for different deposition depth without (a) and with (b) the diffusion correction in the W5-D8-LGAD2 LGAD. The diffusion correction accounts for the broadening of the deposited charge carrier density by diffusion during its drift to the top side junction. The generated charge is included in (a) as an x-axis. The bias voltage is 500 V.

in the pulse energy and the extracted drift time to about 10 % of its mean value. The consideration of diffusion shifts the gain curves according to their drift time towards lower charge carrier densities. It can be seen that the diffusion corrected gain curves are in much better agreement with each other, compared to the uncorrected gain curves. The good agreement is taken as a verification that diffusion is responsible for the observed deposition depth dependence in the TPA-TCT gain profiles shown in figure 5.2b. Further, the results strongly indicate that diffusion is responsible for the recovery of gain. At a certain lower and higher charge carrier density the gain should saturate at an upper and a lower gain limit value, respectively. This is not observed within the investigated range. The absence of the upper gain limit value means that the gain reduction is present in all TPA-TCT measurements.

5.3 Comparison to SPA-TCT and ^{90}Sr measurements

Gain reduction was observed before with SPA-TCT and ^{90}Sr measurements [43]. This section compares IR-TCT and ^{90}Sr β-particle results from [43] with the ones obtained by TPA-TCT. Additional red-TCT measurements are presented, to compare red-TCT, IR-TCT, TPA-TCT, and ^{90}Sr β-particle gain measurements. The ^{90}Sr setup described in section 3.3 is used and a description of the used SPA-TCT can be found in [43]. Beam parameters of the red- and IR-TCT are about 5 µm and 6 µm, respectively, and illumination is either applied from the top or back side. The focal plane for the SPA-TCT lasers is positioned at the middle of the DUT. Ionisation profiles of all four methods are sketched in figure 5.7a. It is visible how different the ionisation profiles for the methods are. Thus, a comparison of the charge carrier densities is complicated, as it is far from evident to extract the charge carrier density value that compares all methods in a meaningful way. To avoid these complications, the gain is shown as a function of the generated charge for all

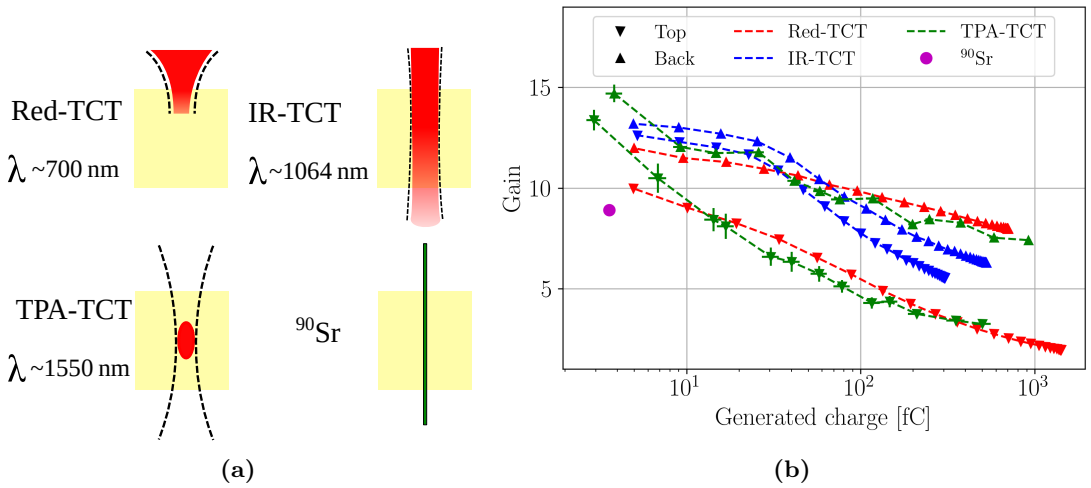

Figure 5.7: (a) Sketches of the ionisation profiles of red, IR, and TPA lasers and ^{90}Sr β-particles. (b) Gain versus the generated charge measured with different techniques. The W5-D8-LGAD2 LGAD is used with a bias voltage of 900 V. The generated charge is extracted from measurements of the corresponding pad detector.

methods in figure 5.7b. The generated charge is extracted from the measurements using the corresponding pad detector. All SPA-TCT measurements are performed with a fixed focus at the focal plane and the generated charge is varied by tuning the laser intensity. The ^{90}Sr measurement is performed with incident bombardment and the gain is extracted from the most probable value (MPV) of the CC. It can be seen that all methods show a decrease in gain with increasing charge generation, where the ^{90}Sr measurement yields the lowest gain for one minimum ionising particle (MIP) charge equivalent (3.6 fC). Further, both illumination configurations of the IR-TCT perform very similar. A slightly higher gain is measured using back side illumination, which might be related to beam depletion. For illumination from the back side more light is absorbed in the back side region and thus the generated charges might undergo more diffusion compared to charge generated by top side illumination. Thus, a slightly lower gain reduction is observed compared to illumination from the top side. The red-TCT measurement shows significant differences for illumination from the top or back side. When illumination is applied from the top, all the charge is generated inside or in the vicinity of the gain layer and the gain is minimal. In contrast, when illumination is applied from the back side, the charge carrier distribution drifts the whole active volume and is maximal broadened by diffusion, which lead to higher gain values. Only gain values for charge generation at the top and back side is shown for the TPA-TCT, because they give the minimum and maximum measured gain. Any deposition position between these boundaries yields a gain value between the two curves. The selected deposition depth show gain values similar to the red laser for a charge generation > 10 fC. This hints that the excess carrier densities of the two methods are comparable. However, the TPA-TCT has the potential to scan any deposition depth, while the red laser is limited to the surfaces. Further, it can be seen that none of the methods reaches saturation in the gain value. This highlights the relevance of the gain reduction mechanism, as it is present for all measurements and can not be avoided by the presented characterisation techniques.

6 Techniques for the investigation of segmented devices

This chapter discusses the application of the TPA-TCT on segmented devices. First, dedicated methods to extract the device thickness and to investigate the electric field of segmented devices are discussed, followed by an application of the developed methods to strip and monolithic detectors. The passive CMOS strip detector, HV-CMOS CCPD v3, RD50-MPW2, and the Monolith picoAD are discussed in this framework.

Segmented devices can come along with complex implantation profiles and electrode structures that can lead to laser beam clipping and reflection, similar to the effects discussed in sections 3.5.10 and 3.5.11. Artefacts due to clipping and reflection can be seen in figure 6.1, where the passive CMOS strip detector is used as an example. The layout of the device is shown in (a) and the collected charge (CC) measurement along the cross-section is shown in (b). For the measurement, one strip is read out and the two closest neighbours on both sides are grounded together with the bias ring. The DUT has a pitch of 75.5 µm and additional metallisations above the p-stop, which are a design approach to obtain a more gradual decrease of the electric field towards the edges. This additional metallisations lead to only $\approx 24\,\mu m$ of open silicon between the strip and p-stop metal that is available for light injection. The small open area makes this device well suited to study the influence of clipping. The device is fully depleted for the selected bias voltage, which is why all generated charge is expected to be collected. Triangular shapes of higher charge collection are observed in the CC profile, which are a result of laser beam clipping at the top side metals. The deeper the focal spot is moved inside the DUT, the larger is the opening cone of the laser at the top side. The increasing opening cone leads to clipping at the top side metallisations that introduces the observed triangular shape. Further, the back side of the device is metallised, which leads to reflection. Increased charge collection at $z_{Si} \approx -0.31\,mm$ is a result of the reflection, and it introduces charge collection beyond the active volume $z_{Si} \leq -0.31\,mm$. These artefacts complicate the interpretation of the

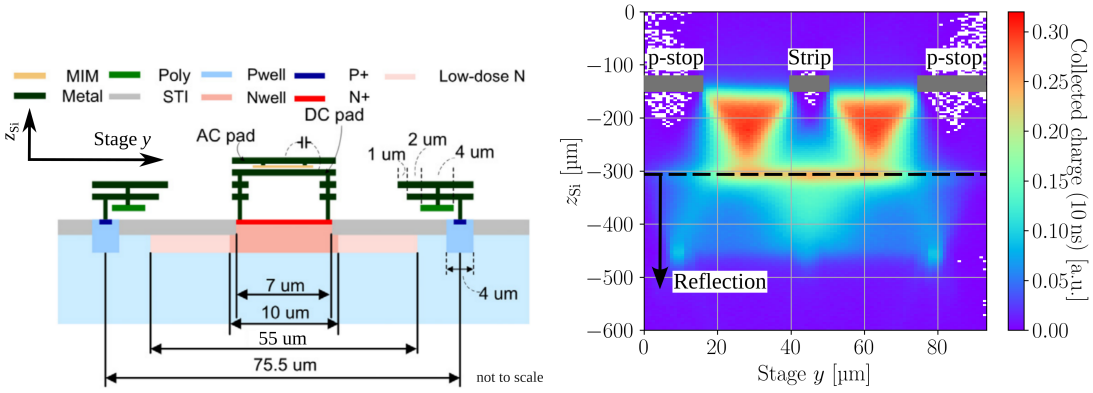

Figure 6.1: (a) Schematic design of the passive CMOS strip detector adapted from [46]. (b) Charge collection measurements in cross-section of the passive CMOS strip detector, with schematically drawn top side metallisations. The dashed black line indicates the position of the metallised back side. The triangular shaped inhomogeneity is caused by laser beam clipping at the top side metallisations and the increased charge collection at $z_{Si} \approx -0.31\,mm$ originates from reflection at the back side. The bias voltage is 100 V, which is above the full depletion voltage [24].

results and especially the extraction of the active thickness.

6.1 Extraction of the active thickness

In the following, a method to extract the active thickness under the presence of clipping and reflection is discussed. The top surface and then the back surface are found independently, by extracting the top surface from the CC and the back surface from the time over threshold (ToT) profile. Figure 6.2a shows the CC profile of the passive CMOS strip detector. It can be seen that clipping and reflection deform the CC. Clipping decreases the CC, starting at $z_{\mathrm{Si}} < -0.2\,\mathrm{mm}$, and reflection results in the peak at $z_{\mathrm{Si}} \approx -0.31\,\mathrm{mm}$. However, the rising edge of the CC is affected neither by clipping nor reflection, which is why the position of the top surface aligns with the top side half maximum. The top side half maximum is extracted by fitting the first part of the CC profile Q_{FP} using the function

$$Q_{\mathrm{FP}}(z) = C \cdot \arctan\left(\frac{z - z_{\mathrm{off}}}{z_{\mathrm{R}}}\right), \tag{6.1}$$

where C is a constant that accounts for the amplitude and z_{off} is the offset from the z-axis origin. A function to fit CC profiles is discussed in the appendix A.3 and the here presented equation (6.1) is a simplification of equation (A.5). Following the discussion of the ToT profile of section 3.5.12, the back side position aligns with the peak in the ToT profile shown in figure 6.2b. The ToT is presented for various voltages and the dashed lines in the figure indicate the extracted surface positions. A device thickness of 156 µm is found, which is in good agreement with the nominal thickness of 150 µm. Besides, the ToT can be used to investigate the depletion behaviour of the device. For a bias voltage of 20 V a steep increase close to the back side is observed in figure 6.2b, which indicates a longer collection time. Long collection times are a sign of diffusion and thus an incomplete depletion of the DUT.

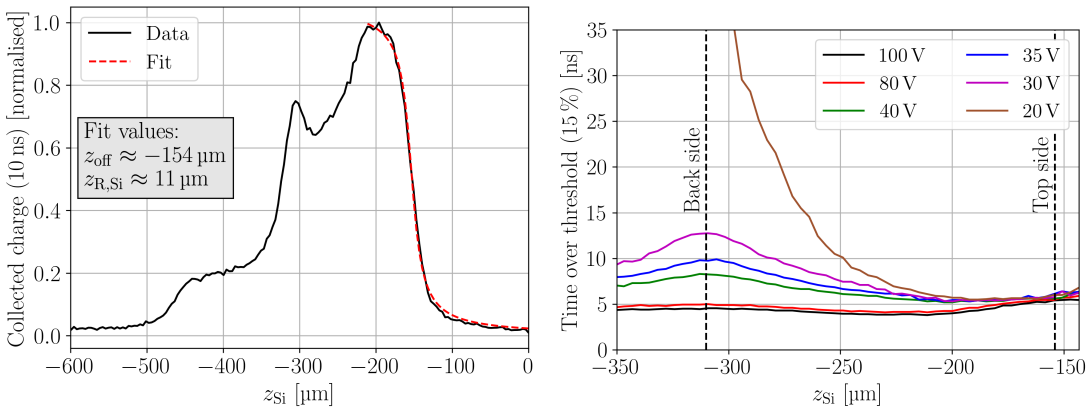

(a) **(b)**

Figure 6.2: Method to extract the device thickness in the presence of clipping and reflection. The position of the top surface is extracted from a fit towards the front part of the charge collection profile (a) and the back side position is found from the time over thresholds profile (b) as the maximum at the back side [24]. Note that the top side is at the right-hand side, which was chosen to match the z-axis in figure 6.1b.

6.2 The weighted prompt current method

The influence of beam clipping seen in the CC profile in figure 6.1b, propagates to all quantities that are intensity dependent. The prompt current (PC) is as well affected, as can be seen in figure 6.3a. Clipping leads to areas of increased PC at the top side between the p-stop and the strip metal, whereas reflection causes an increased PC close to the back side and the PC measured beyond the DUT boundaries. The intensity dependence of the PC can be mitigated by weighting the PC with the generated charge. This technique is in the following referred to as the weighted prompt current (WPC) method [24]. It is based on the rearranged Shockley-Ramo theorem of equation (2.18)

$$\frac{I_{\mathrm{m}}(t_{\mathrm{pc}}, x, y, z)}{Q_{\mathrm{coll}}(x, y, z)} \approx \frac{I(x, y, z)}{Q(x, y, z)} = (\mu_{\mathrm{e}} + \mu_{\mathrm{h}}) \vec{E}_{\mathrm{W}}(x, y, z) \vec{E}(x, y, z)\,, \tag{6.2}$$

where x, y, z indicate the position of excess charge carrier generation. I_{m} is the measured current and Q_{coll} the measured CC. Ideally, the generated charge Q is used for the WPC, but as it is experimentally not available, Q_{coll} is used as an approximation. The approximation becomes less satisfactory for highly irradiated devices, where significant charge loss might be present. The WPC method was developed to study the PC even under the presence of laser intensity varying effects like clipping, reflection, or fluctuations in the generated charge. As shown in equation (6.2), the WPC method yields the product of the weighting field E_{W} with the drift velocity μE, which is why conclusions on the electric field are only possible if E_{W} is known. For segmented devices with complex weighting field, the simulation with a suitable technology computer-aided design (TCAD) tool might be needed in order to calculate E_{W}.

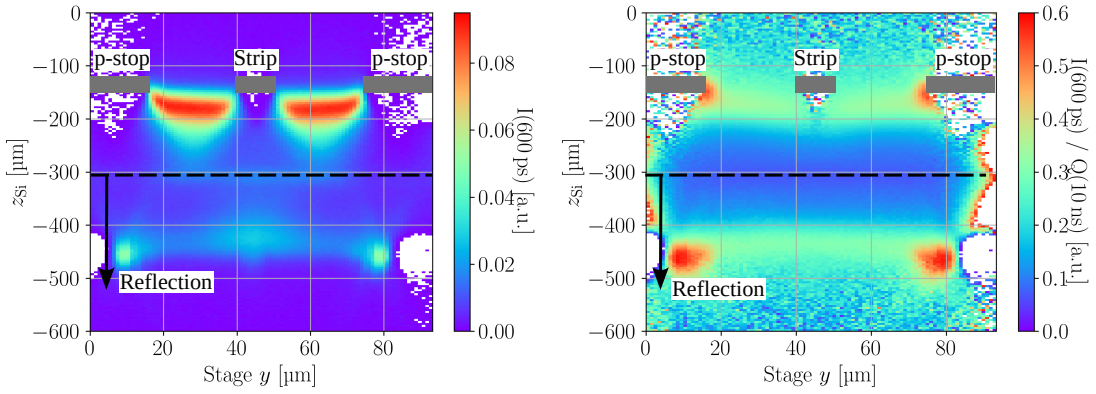

Figure 6.3: Prompt current (a) and weighted prompt current (b) measured in the passive CMOS strip detector. The top side metallisations are shown by grey boxes and the dashed black line indicates the position of the back side metal. Artefacts from clipping and reflection are observed in the prompt current, while the weighted prompt current mitigates those [24].

The WPC profile of the passive CMOS strip detector is shown in figure 6.3b. A much more homogeneous behaviour is found across the active volume compared to the PC in figure 6.3a and the maximum WPC is located at the edge of the p-stop. The artefacts of clipping and reflection are fully compensated by the weighting. Regions at the edges

at $y < 0.05\,\text{mm}$ and $y > 0.085\,\text{mm}$ appear white, because they have much higher WPC values that originate from a CC that is close to zero. When little to no charge is collected, the WPC amplifies such values, because it is proportional to $1/Q_{\text{coll}}$ and thus the colour scale needs to be limited. Further, the WPC reveals that the reflection contains a mirror image of the ordinary profile and in the mirror image regions directly below the top side metals are accessible. The mirror image will be discussed in detail below in section 6.3, while in the following the WPC is further investigated.

After demonstrating the WPC on a segmented device, the WPC method is investigated in more detail using a 300 µm thick p-type planar pad detector from the CiS16 campaign. Details about the DUT can be found in section 3.1.1. A pad detector is used to lower the complexity and simplify the disentanglement between device and method related effects. Pad detectors have a constant weighting field ($E_{\text{W,pad}} = 1/d$), wherefore the WPC is directly proportional to the drift velocity. The WPC profile can be seen in figure 6.4a for increasing bias voltages. The axis limits are selected to show only the active volume with the top side on the left and the back side on the right side. The shown absolute values of the WPC depend on the t_{pc}, but the relative evolution of the drift velocity and electric field is the same for reasonable t_{pc}. It can be seen how the WPC, i.e. the electric field, increases with the bias voltage. The depletion voltage is found from CV measurements as $V_{\text{dep}} = 14.2\,\text{V}$ and bias voltages below the depletion voltage yield electric fields that do not reach the back side of the DUT. Directly at the back side ($z_{\text{Si}} \approx 300\,\mu\text{m}$) a non-zero WPC is found even for $V_{\text{bias}} < V_{\text{dep}}$. This is caused by the back side implantation that builds up together with the bulk implant a built-in potential, which leads to a non-zero electric field. For zero bias voltage, the built-in potentials at the top junction and the back side implantation can be directly seen as a small WPC.

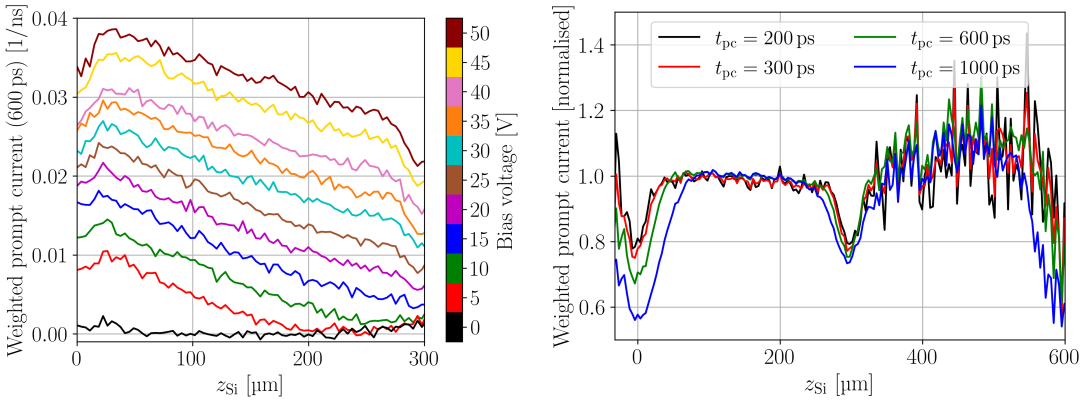

Figure 6.4: Weighted prompt current in the CiS16 25-DS-66 pad detector. (a) Different bias voltages below and above the full depletion are shown. Full depletion is reached for 14.2 V. (b) The influence of different prompt current times t_{pc} measured at $V_{\text{bias}} = 300\,\text{V}$. A valley is found at the top and back side boundary position. The valleys are caused by a less satisfactory approximation of the prompt current close to the surfaces.

Figure 6.4b shows normalised WPC profiles at a bias voltage of 300 V. The PC time t_{pc} is varied, and the axis limits are selected to show also the reflection region. Compared to the PC profile that was shown in section 3.5.12 in figure 3.19, the WPC of the reflection yields a comparable magnitude relative to the ordinary region. The SNR in the reflection region is much lower due to the lower intensity, hence the WPC becomes noisy. Increased

laser intensities would increase the SNR, but in order to mitigate the regime of plasma formation, higher intensities are avoided. All shown PC times yield a comparable profile within the bulk WPC, but the valleys at the boundaries show a dependence on t_{pc}. The valleys become deeper and extend further into the bulk for increasing t_{pc}, where the top side is stronger impacted than the back side. When charge carriers are generated near their corresponding collection electrode, they can be collected within t_{pc} and thus not contribute to the PC, i.e. a lower PC is measured. At the device's boundaries, the assumption to use the induced current at t_{pc} to approximate the current at injection can become invalid, when $t_{\mathrm{coll}} < t_{\mathrm{pc}}$ applies for some charge carriers. In the appendix A.7, the valleys are reproduced by a TCAD simulation, which verifies that the valleys are related to charge collection within the PC time. Differences between valleys at the top and at the back side originate from the different mobility of electrons and holes. Electrons have a higher mobility than holes, wherefore they are collected faster, which leads to a more pronounced valley at the top side. In general, shorter PC times minimise this effect, but t_{pc} has to be balanced off with the SNR. For the used readout electronics, PC times shorter than 200 ps are not feasible due to a too low SNR. In conclusion, the WPC is a powerful tool for the investigation of the DUT's electric field. Compared to the PC method, the influence of the absolute generated charge can be mitigated, which makes it especially suitable when clipping or reflection of the laser are present. Further, the WPC at the device boundaries has to be studied with care, because CC within t_{pc} impacts the PC.

6.3 The mirror technique

In the following, the mirror technique is further discussed. An application of the mirror technique was already shown in the reflection region of figure 6.3b. The principle of the mirror technique is sketched in figure 6.5. When the focal point is moved behind the active volume, it is reflected back inside the active volume and moves in opposite direction compared to the ordinary focal point. Thus, the reflection scans the active volume from the back towards the top side. Figure 6.6 shows an image of the passive CMOS strip detector taken with the IR microscope, with the focal plane at the top side (a) and the mirror image at the same position (b), i.e. the area below the top side metals is observed. The focal spot is deformed by the clipping at the top side metals and a diffraction pattern is visible. The pattern depends on the y-position, i.e. the position perpendicular to the top side metals. The volume of charge generation can be very different compared to the non-clipped volume and the mirror image needs to be interpreted with respect to a varied volume of charge generation. Further investigation of the mirror technique uses the Micron [154] 2328-11 p-type strip detector as an example. The strip detector has an active thickness of 300 µm and a pitch of 80 µm. The layout of the device is schematically shown in figure 6.7a and its CC profile is shown in figure 6.7b. For the measurement only one strip is read out and the two nearest neighbours on both sides are grounded. The back side of the DUT is fully metallised, wherefore part of the back side metal was etched to allow illumination from the back side. The CC profile is measured with illumination from the back side to avoid clipping at the top side metals. The influence of reflection at the strip metal can be seen as the region of maximum CC. A negative CC is observed in the region close or directly at the neighbouring strip, which is related to bipolar signals and a too short collection time. As before shown in figure 2.6a, bipolar signals occur when

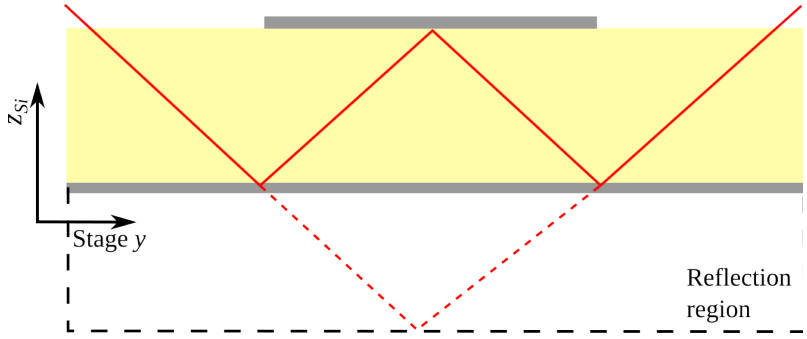

Figure 6.5: Schematic showing the exploitation of reflection at a metallised back side to probe below the top side metal using light injection from the top side. The metals are shown in grey, the solid red line represent the path of the outermost laser light rays, and the dashed red line indicates the focus in absence of the back side metal.

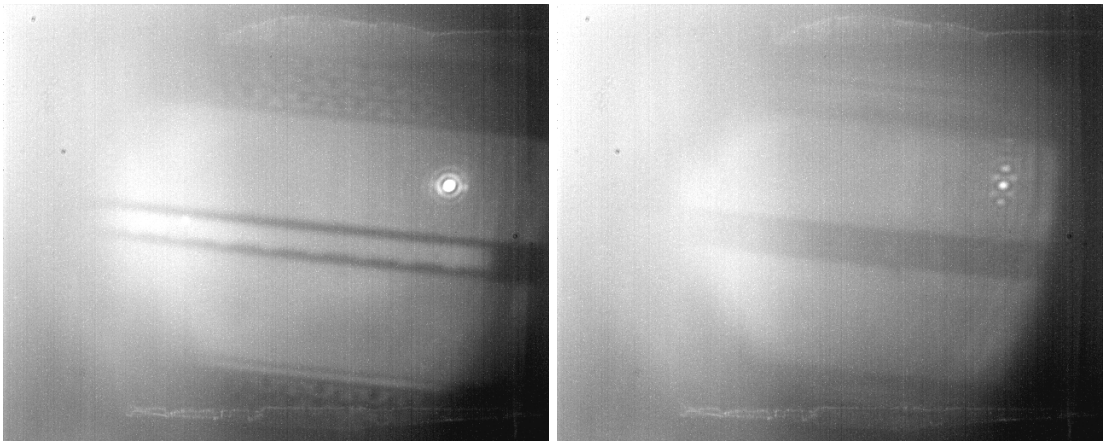

(a) **(b)**

Figure 6.6: Picture of the passive CMOS strip detector, recorded with the IR microscope. (a) The focal plane aligns with the top surface and the laser is between the strip metal and the p-stop. The laser's focal point is seen as a bright spot. (b) Mirror image at the same position. The focal plane is one device thickness behind the DUT and shows the top side metals from below. The focal point is positioned like sketched in figure 6.5. The laser spot is deformed due to clipping.

charge is collected by a neighbouring strip. For such current transients the integral of equation (3.1) is zero [74], but when the collection time is selected too short a negative CC occurs. From the CC profile, three regions can be distinguished: the region where only the readout strip collects charge, the region where the readout strip and the neighbouring strip collect charge simultaneously, and the region where only the neighbouring strip collects charge. The first corresponds to a CC of about 0.6 (and the region below the strip that is due to reflection ≈ 1.2), while the second leads to only partial collection of the generated charge, wherefore the CC under the presence of charge sharing is < 0.6. The region where only the neighbouring strip collects charge can be identified by a CC around zero.

Figure 6.8 shows the WPC measured in the 2328-11 strip detector. In (a) the illumination is applied from the back side through the etched metal and (b) shows the mirror image, which is obtained by illumination from the top side. For (b) a position in the DUT is selected where the back side metal is not etched. Note that the ordinate is counter directed in (b), because the mirror technique probes the volume in opposite direction from the back

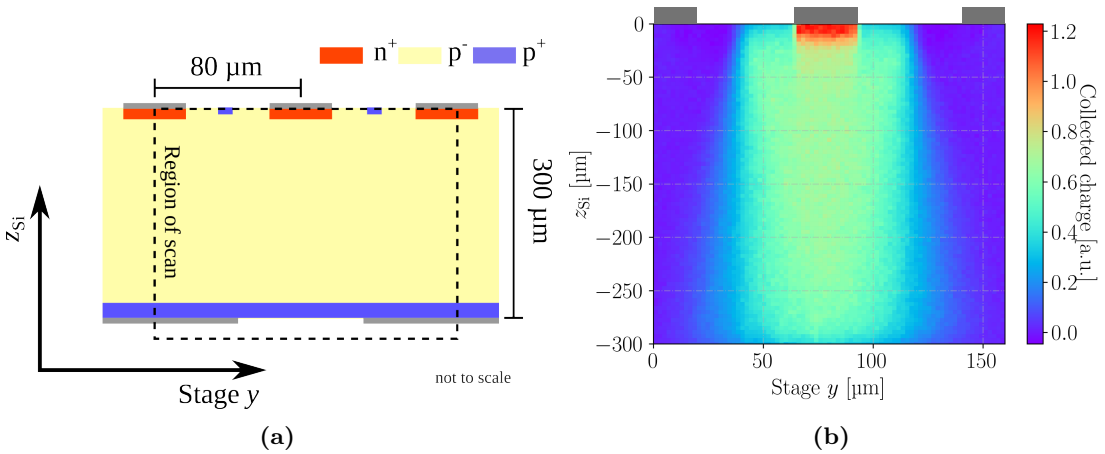

Figure 6.7: (a) Schematic implantation layout of the Micron strip detector. The strip metals are indicated in grey, the top side n-implants in red, and the back side p-implant in blue. Part of the back side metal is removed by etching, which is indicated by the discontinued grey rectangles at the back side. (b) Charge collection measurement of the Micron strip detector with illumination from the back side through the etched back side metal [24]. The axes are according to the coordinate system in (a) and the high charge collection below the readout strip is an artefact of reflection at the strip metal.

towards the top side. Comparing both figures allows drawing qualitative conclusions on the mirror technique. First, it can be seen that the same features appear in both figures at the same position. The maximum is found close to the top side junction, followed by a decrease towards the back side. The regions where no charge is collected, i.e. where the neighbouring strip collects the charge, appear non-coloured or irregularly coloured (e.g. for the values along $y = 150\,\mu\text{m}$). Second, the region around the top junction appears broadened in the mirror image compared to the ordinary image. This is an effect of the deformed focal spot that has less resolution along the y-axis as can be seen from the infrared image in figure 6.6b. Besides the deformation of the focal spot, the numerical aperture decreases due to clipping. To cope with the decreased numerical aperture, i.e. spatial resolution, a slightly larger z-range is used in figure 6.8b.

In conclusion, the mirror technique allows probing below top side metallisations, even when the illumination is applied from the top side. As clipping and reflection potentially occur, it is most powerful for intensity independent quantities like the WPC. The technique requires three-dimensional resolution and is not available for SPA-TCT. The spatial resolution decreases in the mirror image, because clipping influences the shape of the focal spot.

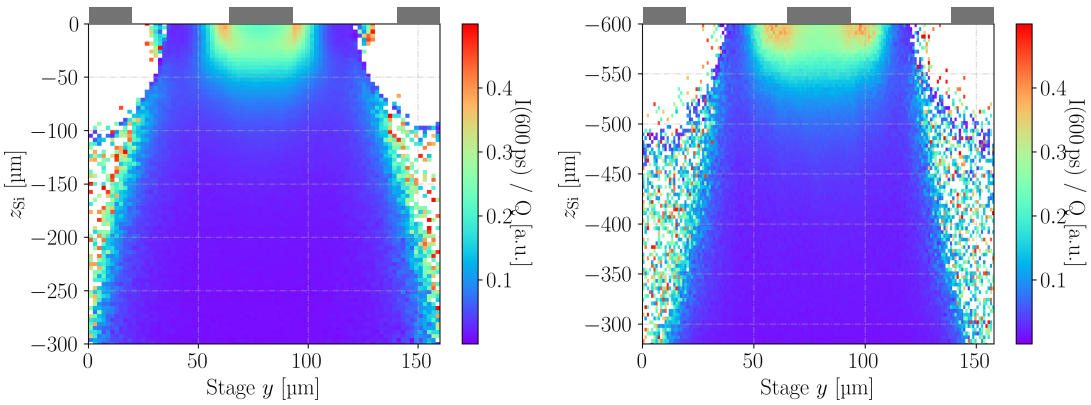

Figure 6.8: Comparison between the weighted prompt current measured with back side illumination (a) and the mirror image obtained with top side illumination (b) in the Micron strip detector [24]. The mirror image exploits the reflection at the metallised back side to obtain a measurement below the top side metal. Note that the ordinate in (b) is counter directed to the ordinate in (a), because the reflection scans the volume from the back towards the top side. The colour scales in both figures are the same and the axes are according to the reference system in figure 6.7a.

6.4 Application to monolithic detectors

Application of the above developed techniques was already demonstrated on pad and strip detectors. In this section, the methods are applied to the following monolithic devices: a high voltage complementary metal-oxide-semiconductor (HV-CMOS) [47], the RD50-MPW2 [48], and the Monolith picosecond avalanche detector (picoAD) [49]. First, the HV-CMOS is discussed, followed by a discussion of the RD50-MPW2, and the picoAD. Details about the devices are summarised in section 3.1.2. Monolithic detectors are a promising technology for future tracking and timing application. In contrast to the conventional hybrid technology, the front-end electronics are integrated in the sensing volume, hence the name monolithic. The costly step of bump bonding required for hybrid technologies to connect the front-end electronic to the sensing volume, is avoided and thus the fabrication cost for monolithic devices is lowered. The material budget and power consumption is decreased compared to hybrid devices, because the design can be produced much more compact and with a lower input capacitance. All these advantages come with the drawback of an increased device complexity.

6.4.1 HV-CMOS

The HV-CMOS is a sensor technology with the aim of low cost, radiation hard, and large area particle detection. It is manufactured with a 180 nm HV-CMOS process, which is a commercial process and offered by various foundries, which potentially lowers the production cost. The tested HV-CMOS is a capacitively coupled pixel detector version 3 (CCPD v3) and it was previously investigated in [155]. The DUT has a fairly deep n-implant (deep n-well) in a low-resistivity p-type bulk, and the device was fabricated especially for optical testing, meaning that NMOS and PMOS transistors are not embedded in the n-well. The active volume is buried approximately 50 µm deep inside silicon, is about 120 µm

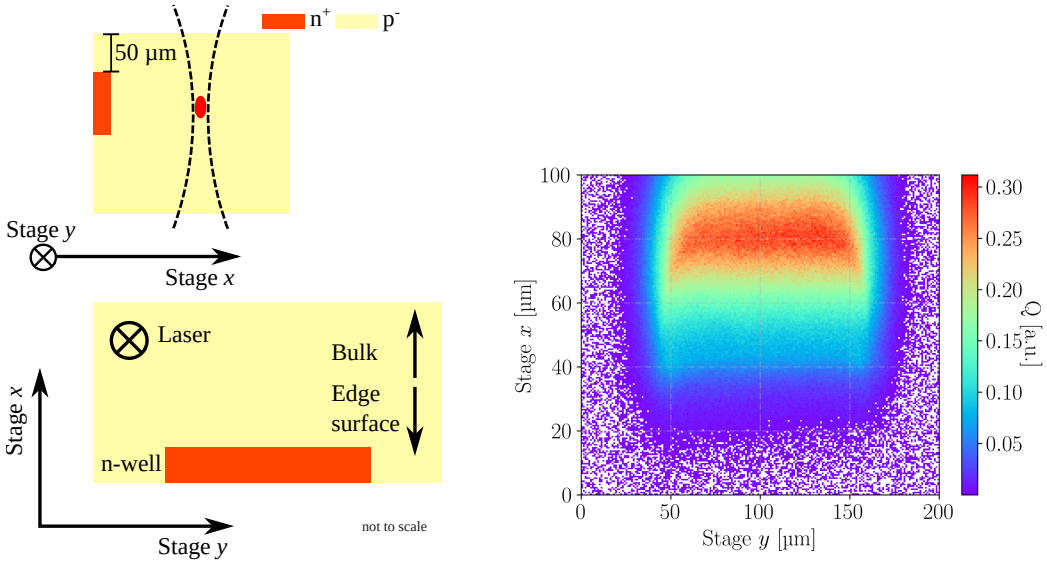

Figure 6.9: (a) Simplified sketched of the HV-CMOS CCPD v3. The red structure indicates the deep n-well and the p-type substrate is shown in light yellow. A side and a top view of the reference coordinate system for the device is shown in the upper and lower sketch, respectively. (b) Charge collection measurement of the HV-CMOS CCPD v3. The highest charge collection is observed in the bulk behind the deep n-well ($x < -30\,\mu m$). The deep n-well begins at about $x = 42\,\mu m$ and ends at $x = 52\,\mu m$. The charge collection profile is influenced by laser beam clipping at the edge surface and charge collected at $x < 42\,\mu m$ is associated to reflection. The bias voltage is 60 V.

wide, and it extends about 30 µm into the bulk. The design is schematically shown in figure 6.9a with a side and a top view, which includes a coordinate system that serves as a reference for the performed measurements. Illumination was applied from the edge in order to achieve a spatial resolution of about 2.4 µm and exploit the fact that the region of interest is positioned at the edge. For illumination from the edge, the x-coordinate corresponds to the device depth, compared to illumination from the top and back side, where the depth corresponds to the z-coordinate. The presented data for the HV-CMOS was taken in the framework of [13] and is reanalysed to apply the developed methods. The CC profile of a single pixel is presented in figure 6.9b for a bias voltage of 60 V, which corresponds to the usual operation voltage. The measurement was performed at room temperature ($\approx 25\,°C$), with the beam parameters $w_0 = 1.2\,\mu m$ and $z_{R,Si} = 10.2\,\mu m$. The averaged current transients of 256 single acquisition were recorded, and the laser was operated at a pulse frequency of 100 Hz. Inside the bulk, the highest CC is found, and the profile is in general inhomogeneous. Inhomogeneity towards the edge surface is caused by clipping at said surface. The laser beam is partially outside the device for positions close to or directly at the edge and thus less intensity contributes to the charge generation. Inhomogeneity in the bulk region is caused by charge generation in the non-depleted substrate. Charge generated in that region diffuses and only part of it reaches the depleted region to contribute to the induced current. Such signals are impacted by ballistic deficit, because their signal duration exceeds the CC time of 20 ns. Charge carriers generated within the depleted region have a collection time well below 10 ns and are not influenced by ballistic deficit. The deep n-well is not visible in the CC profile as it is overshadowed by clipping and reflection. It is found that the ToT profile is suitable in order to resolve the

deep n-well, because the ToT is intensity independent and thus not affected by a varying charge carrier generation. The ToT profile for a threshold of 50 % is shown in figure 6.10a, where the deep n-well is located at around $x = 40\,\mu\text{m}$ and appears as a bright region. Figure 6.10b shows a cut along the x-axis at $y = 105\,\mu\text{m}$ of the ToT profile. The influence of reflection at the edge surface is not mitigated by the ToT, wherefore the thickness of deep n-well appears at twice its nominal value of about $\approx 10\,\mu\text{m}$. Taking reflection into account, the position of the edge surface is found at $x = 42\,\mu\text{m}$, with the deep n-well located between $42\,\mu\text{m} < x < 52\,\mu\text{m}$. The active volume begins after the deep n-well and reaches $\approx 80\,\mu\text{m}$, resulting in a depleted region with $\approx 30\,\mu\text{m}$ thickness.

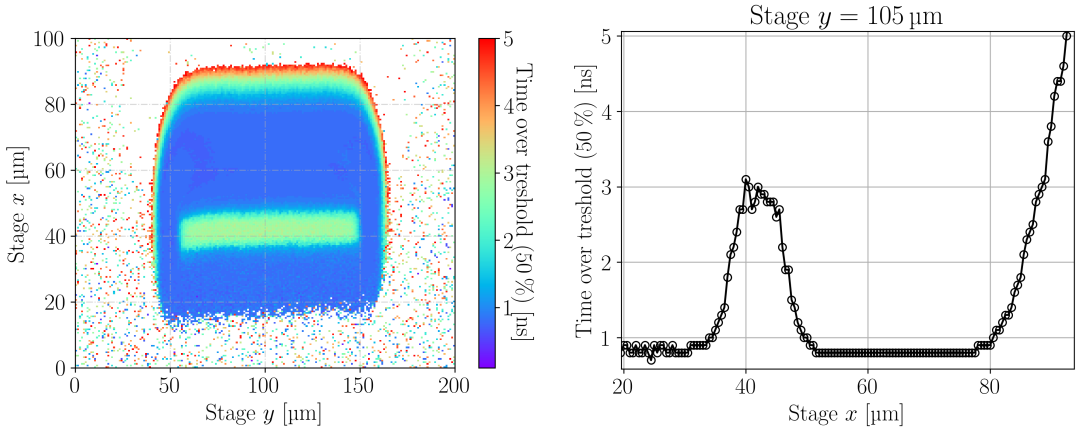

Figure 6.10: (a) Time over threshold profile of the HV-CMOS CCPD v3 for a threshold of 50 %. The coordinate systems are according to the reference system in figure 6.9a and the deep n-well is well resolved as a region with slightly higher ToT ($\approx 3\,\text{ns}$). The ToT profile is as well influenced by reflection at the edge surface. (b) Cut in the ToT profile along the x-axis for $y = 105\,\mu\text{m}$. The bias voltage is 60 V.

The influences of clipping and reflection propagate to the PC, which is depicted in figure 6.11a. It can be seen that the PC resolves the lateral edges of the deep n-well, but the highest PC is found, similar to the highest CC, in the bulk region. This gives the false impression that the electric field peaks in the bulk and not at the junction. The picture becomes more clear in the WPC that is shown in figure 6.11b. The WPC corrects for the loss in the generated charge and yields a picture of the electric field that agrees with the expectations. The maximum WPC is found at the edges of the deep n-well and the WPC is almost constant within the bulk, with an abrupt decrease at about $x = 80\,\mu\text{m}$. The abrupt decrease indicates the transition from the depleted to the non-depleted region and is related to the low electric field in the non-depleted region.

In conclusion, the HV-CMOS CCPD v3 was investigated using edge illumination. Reflection at the top side is found to difficult the extraction of the active volume of the device. The CC and PC profile are both influenced by clipping at the edge surface and the extraction of the deep n-well is not possible from these profiles. The deep n-well and the depletion region is extracted with the highest precision from the ToT profile and is also resolved by the WPC. Further, the WPC profile is in agreement with the expectations for the electric field, because the method compensates the influence of clipping.

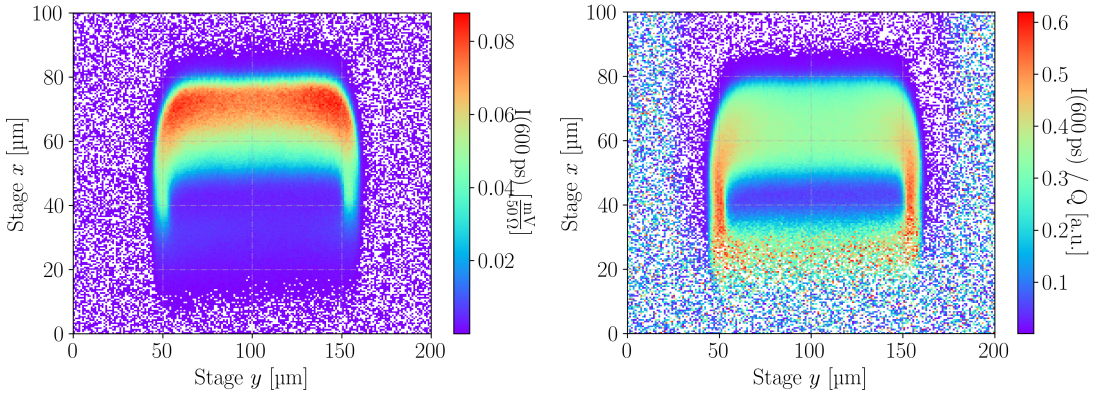

Figure 6.11: Prompt current (a) and weighted prompt current (b) profile of the HV-CMOS CCPD v3. The coordinate systems are according to the reference system in figure 6.9a. The artefacts of the collected charge (figure 6.9b) propagate to the prompt current, but the weighted prompt current is found to correct the influence of reflection and clipping properly. The weighted prompt current indicates the highest electric field at the edges of the deep n-well. The bias voltage in both figures is 60 V.

6.4.2 RD50-MPW2

The RD50-MPW2 is a depleted monolithic active pixel sensor (DMAPS), developed within the RD50 collaboration and the successor of the RD50-MPW1. It is fabricated in a 150 nm HV-CMOS process by LFoundry on multi-project wafers (MPW) [48]. The investigated device has a substrate resistivity of 1.9 kΩ cm and a device thickness of 280 µm. In-pixel measurements are conducted on $(60 \times 60)\,\mu\mathrm{m}^2$ single pixels of the 8×8 active pixel matrix. The signal acquisition can not be performed using the ordinary PCBs, like for pad detectors, because the front-end electronics require a more elaborate biasing scheme. Therefore, the Caribou system was used for the data acquisition [156]. All measurements were performed at room temperature ($\approx 25\,^{\circ}\mathrm{C}$). The laser was operated at a pulse frequency of 1 kHz and a pulse energy of 0.22 nJ. Beam parameters $w_0 = 1.3\,\mu\mathrm{m}$ and $z_{\mathrm{R,Si}} = 10.4\,\mu\mathrm{m}$ were present, and the averaged current transients of 128 single acquisition were recorded.

The system consists of a chip board that serves as a mount for the DUT, a control and readout (CaR) board, and a ZC 706 that serves as an evaluation board. Figure 6.12a shows the readout system mounted inside the TPA-TCT setup. The boards are stacked into each other, where the chip board is positioned below the objective and the CaR board interconnects the chip board with the evaluation board. An external computer is used to control the data acquisition and to configure the front-end electronics. In order to mount the system on the hexapod stage with mechanical integrity, a custom-made carbon holder is used. The top side of the chip is fully metallised and not accessible for light injection, which requires illumination from the back side of the chip. Analogue and digital transient signals can be obtained from the chip board, where the prior are used for the performed measurements. A CSA shapes the analogue signal in a way that the CC can be extracted as the signal amplitude V_{max}. Two different amplifier versions are available, which are referred to as AMP1 and AMP2. For the presented measurements, a pixel readout by the AMP2 is investigated. Figure 6.12b shows the CC obtained with back side illumination in a pixel. A single pixel is scanned with a step size of 1 µm. The focus is positioned

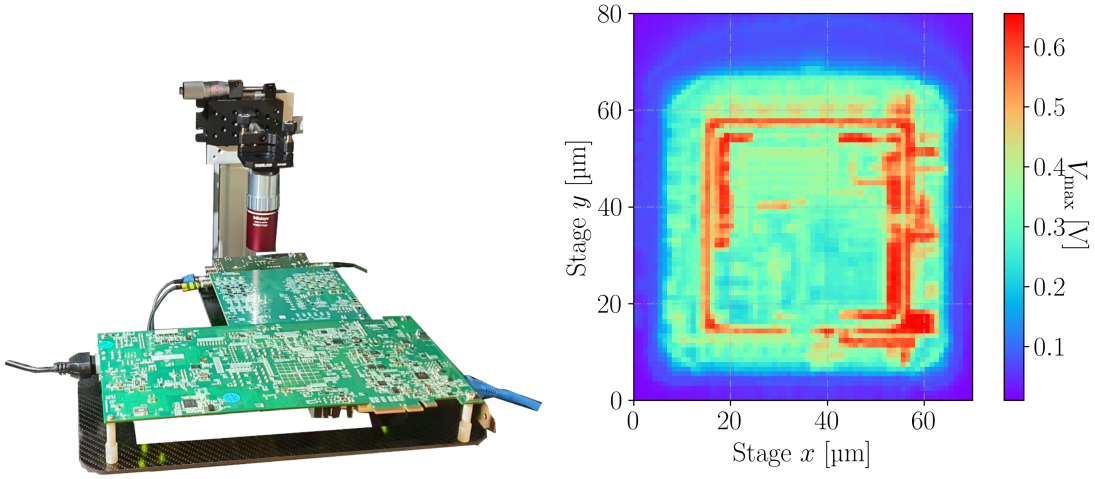

(a) **(b)**

Figure 6.12: (a) Caribou system mounted in the TPA-TCT setup for back side illumination. The chip board is below the objective and stacked into the CaR board, which is itself stacked into the ZC 706 evaluation board. The system is mounted on the hexapod via a custom-made carbon holder visible in black. (b) Profile of the collected charge measured in an RD50-MPW2 pixel with the amplifier AMP2. The profile is recorded with a step size of 1 µm in both direction for a fixed device depth. The focus is positioned close to the top side electronic. The illumination is performed from the back side and the maxima regions correspond to reflection at the lowest metal layer from the electronic. The bias voltage is 60 V.

close to the top side surface and the metallisations are found as regions of the increased charge collection, which is an artefact due to reflection. Exemplary waveforms for selected positions can be seen in figure 6.13a, aside the ToT (b), the peaking time (c), and the rise time (d) profile. The peaking time is the time at which the transient reaches its maximum. Shaping dominates the signal transients from the CSA, which leads to long signal times. The shaping is affected by the amount of CC, as can be seen from the comparison of the different waveforms. Higher CC corresponds to a higher slew rate and a longer signal time, and it introduces ringing, i.e. the side peak at ≈ 100 ns. The CSA shaping hinders the extraction of information about the charge carrier drift from the transients and thus time domain related methods like the WPC method can not be applied. Access to the induced current transient is needed to enable the full potential of the TCT. Therefore, the influence of reflection can not be compensated and is present in all observables. However, this data can be used to study the behaviour of the amplifier. As discussed above for figure 6.13a, the signal transient's shape is not always the same, but depends on the amount of generated charge.

Changing the deposition depth in the active volume helps to mitigate reflection or investigate the reflection in more detail. Figure 6.14 shows the CC of the same pixel for two deposition depths: (a) is recorded with the focus close to the back side and (b) is recorded with the focus in the mirror plane. The focal spot in 6.14a is moved far away from the metallisation so that artefacts from reflection are not visible, and the CC is homogeneous within the pixel's active volume. The CC is homogeneous in an area of about $(50 \times 50)\,\mu\text{m}^2$ and encircled by a decreasing CC at the edge. A lower electric field at the pixel edge might be the origin of the decrease. The pixel edges appear less sharp compared to figure 6.13,

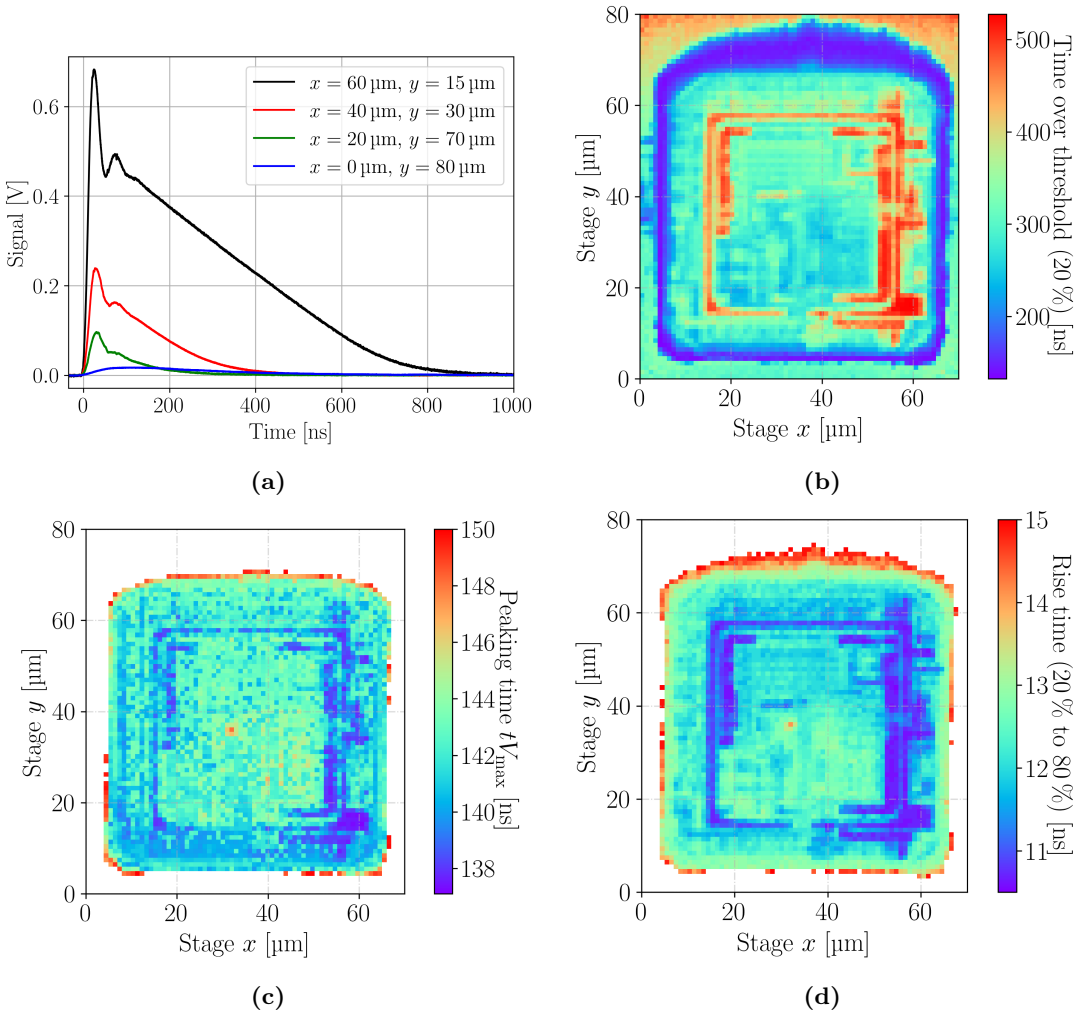

Figure 6.13: (a) Analogue signals measured in the RD50-MPW2 chip at different positions. The positions relate to the coordinate system used in the other figures. The shaping from the CSA prevents the extraction of information about the charge carrier drift. Areas of increased CC lead to variations in the ToT (b), peaking time tV_{max}, and rise time (d) profile. The bias voltage is 60 V.

because the change between high electric field to low electric field is more gradual at the back side and thus smoothens the CC profile. For figure 6.14b, the focal spot is positioned in the mirror plane (compare to figure 6.5) so that regions with high reflectivity correspond to high CC. Metallised regions are revealed in the CC profile, and it can be seen that the whole pixel is covered by metal with exception to a small area below the pixel centre. Performing such xy-scans at various depths would allow to obtain a three-dimensional profile of the pixel metals. SPA-TCT methods can not yield such xy-scans, because charge is generated everywhere along the propagation direction. Diffuse reflection at the metallisation would lead to charge generation aside the focal spot, which diminishes the xy-resolution. TPA-TCT is not sensitive to diffuse reflection, which is why spatial resolution along the x- and y-axis is maintained as demonstrated.

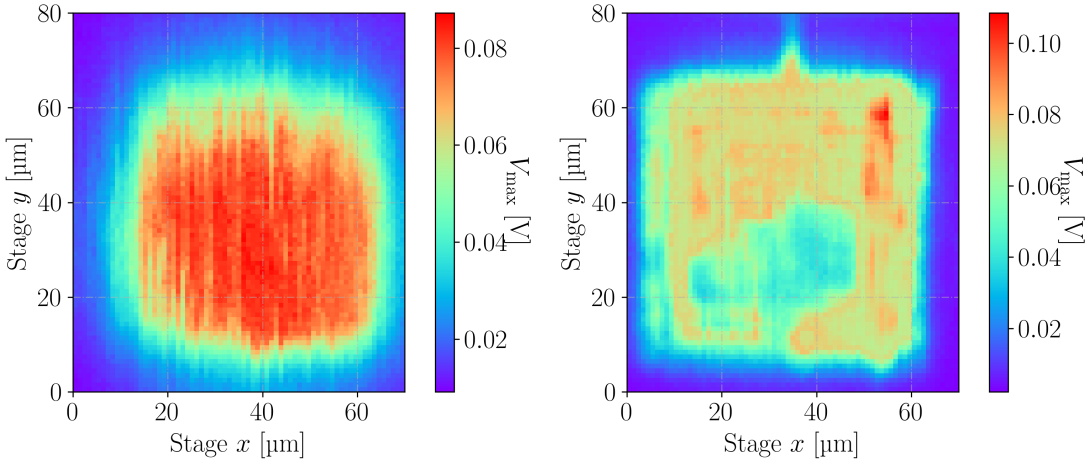

Figure 6.14: xy-scans of the RD50-MPW2 showing the collected charge for different focal plane positions: focal plane close to the back side (a) and focal plane in the mirror plane (b). Figure 6.5 shows the latter position schematically. The same pixel as in figure 6.12b is measured.

6.4.3 Monolith picoAD

The picoAD is a multi-junction monolithic silicon pixel detector developed within the Monolith project [157] and fabricated by IHP [158]. It is designed for timing applications and aims to combine the high spatial resolution and efficiency of pad detectors with the time resolution achieved by avalanche detectors. The device has a p-type bulk and is pixelated with hexagonal pixels that have a side length of 65 µm. The implant layout is schematically shown in figure 6.15a. Three distinct regions are present in the device: drift, gain, and absorption region. With a thickness of 10 µm, the drift region is the thickest, which is why most of the charge of a traversing ionising particle is deposited there. The gain layer is embedded between the drift and the absorption region and thus buried in the bulk. This design approach is similar to reach-through avalanche photodetectors [159] and deep-junction LGADs [160], and it allows a continuous implantation without segmentation for individual pixels. Hence, a ratio between active and total area, i.e. a fill-factor of 100 % is reached by design. Note that this is different to standard LGADs. Implantations are needed to isolate individual pixels of the standard LGAD, which lowers the fill-factor < 50 % [161]. The junction at the gain layer has a high electric field and introduces impact ionisation, i.e. charge multiplication. Charge multiplication is used to improve the timing capabilities of the device and time resolution up to 17 ps were reported [162]. The rear layer is the absorption region, and it is about 5 µm thick. As the device collects electrons at the top side and holes at the back side, electrons generated in the absorption region drift through the gain region and experience gain from the electron multiplication. Compared to electrons, the holes generated in the drift region traverse the gain region and experience hole multiplication. The electron multiplication is due to the higher ionisation rate more pronounced than the hole multiplication and thus the dominating gain mechanism.

A dedicated measurement campaign to investigate the picoAD using the TPA-TCT was performed in the summer of 2022. All measurements were performed at room temperature (≈ 25 °C), and the averaged current transients of 256 single acquisition were recorded. The

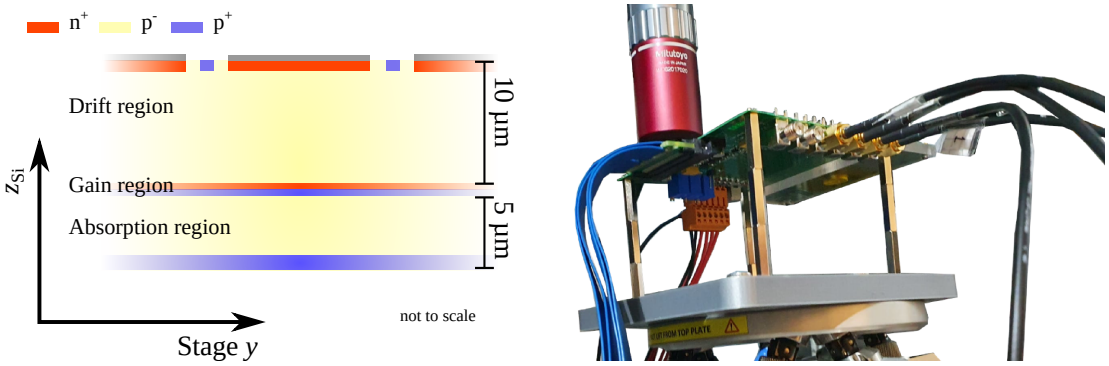

Figure 6.15: (a) Schematic implant layout of the picoAD after [49]. Not shown is the ≈ 200 µm thick support wafer below the active volume. (b) PicoAD on a carrier board mounted on the hexapod stage via a 3D-printed holder. The carrier board is flipped to illuminate the DUT from the back side.

laser was operated at a pulse frequency of 1 kHz and the beam parameters $w_0 = 1.3\,\mu m$ and $z_{R,Si} = 10.4\,\mu m$ were present. Figure 6.15b shows the DUT mounted below the objective in the TPA-TCT setup. The picoAD is glued to a carrier board that contains the readout electronics. For the measurement, the carrier board is mounted on a 3D-printed holder that is fixed to the hexapod. The DUT is metallised from the top side, which is why illumination is applied from the back side. The readout electronics have many operational parameters, which are configured using an external computer. For the presented measurements the readout electronics are configured so that the amplifier behaves as similar as possible to a transimpedance amplifier in order to study the charge carrier drift. It should be mentioned that the transfer function of the readout electronics is unknown and potential shaping might affect the current transients. Figure 6.16 shows measurements in a single pixel performed with increasing laser intensities. Exemplary current transients are shown in (a) and in-depth ToT and CC scans are shown in (b) and (c), respectively. The waveforms are recorded with the focal point at the middle depth of the active volume. It can be seen that increasing laser intensities lead to an increasing collection time. This is linked to the formation of electron-hole plasma, because the ToT increases along the full device depth and the increase is more pronounced when more charge is generated within the active volume (compare to the CC in (c)). This gives strong indication that electron-hole plasma is responsible for the longer collection time. It should be mentioned that all shown NDF angles correspond to less than one MIP of charge generation in a 300 µm thick pad detector. Thus, the generated charge is low compared to the operation regime used for other devices. The occurrence of electron-hole plasma at this low intensities might be related to the intrinsic gain of the DUT. Another possible explanation is that the formation of electron-hole plasma in such thin devices requires less dense charge carrier distributions. On the other hand, it is not excluded that the readout electronics behaves non-linear with the amount of generated charge. In this case, the effect could be solely related to the readout electronics.

In the following, the in-depth CC profile in figure 6.16c is further discussed with respect to the devices boundaries. The total active thickness is about 15 µm and hence thinner than twice the Rayleigh length ($z_{R,Si} = 10.4\,\mu m$). Hence, the volume of main charge carrier generation exceeds the device thickness. Figure 6.16c yields a FWHM of ≈ 35 µm, which

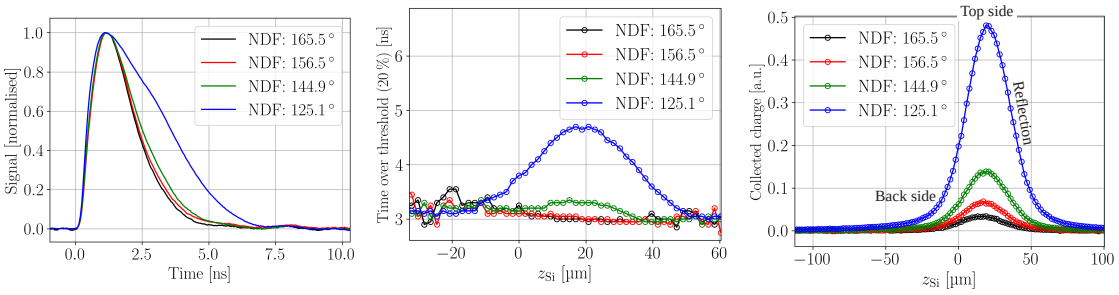

(a) (b) (c)

Figure 6.16: (a) Current transients for increasing charge generation (lower NDF corresponds to higher charge generation) recorded in the middle position of the picoAD. The collection time increases with increasing charge generation due to the formation of electron-hole plasma. In-depth ToT (b) and CC (c) scans of the picoAD for increasing charge generation. The latter figure contains notations about the positions of the DUT, which are motivated in the text. The bias voltage for the shown data is 110 V.

corresponds to more than twice the nominal device thickness. This is a result of reflection at the top side metallisation that mirrors the active volume and thus extends the FWHM. Hence, the FWHM can not reliably be used to extract the device thickness. However, as reflection increases the generated charge, the maximum of CC is linked to the top side position. The spatial resolution along the z-axis is not sufficient to extract the device's back side from the in-depth scan and only an approximate position is available. Using the nominal device thickness of 15 µm, it is found that the back side position is at $z_{Si} \approx 0$ µm in figure 6.16c.

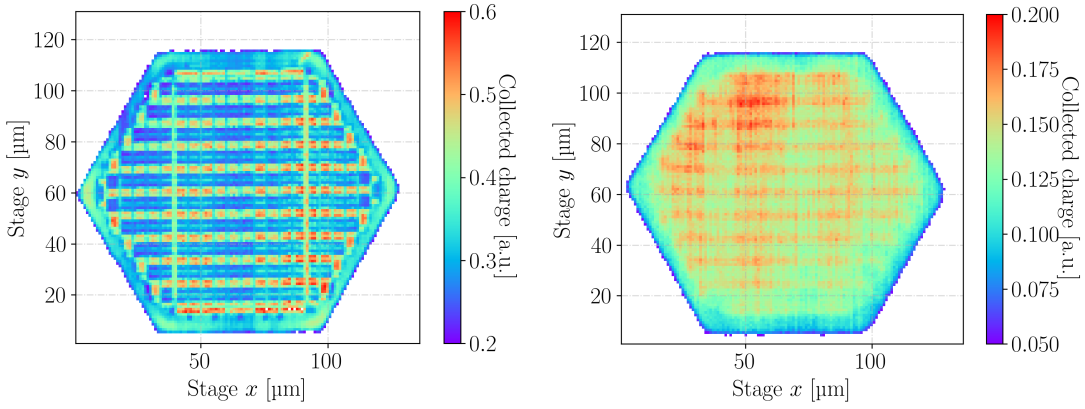

(a) (b)

Figure 6.17: xy-scan of the picoAD showing the collected charge for the focal plane close to the top side electronic (a) and close to the back side (b).

Figure 6.17 shows the CC in an xy-plane of a single pixel of the picoAD with the focal plane at the top side (a) and the focal plane at the back side (b). The NDF angle for the scans is 156.5° and the bias voltage is 110 V, which is well above the expected depletion voltage $V_{dep} \approx 85$ V. Reflection at the top side metallisation influences the CC profiles, as regions of reflection correspond to regions of increased CC. When the focus is at the top surface (figure 6.17a), reflection dominates the CC and leads to a structured pattern that reassembles the structure of the lowest metal layer of the picoAD. Individual pixels are isolated by a p-stop that is central in the region between individual pixels, i.e. the inter-

pixel region. A width of $\approx 10\,\mu m$ is measured for the inter-pixel region, where $\approx 2.5\,\mu m$ are accounted to the p-stop. The inter-pixel region encloses the pixel region and is visible as the outermost region in e.g. figure 6.17a. The region can be identified by the absence of the reflection related pattern. The DUT plane is slightly tilted with respect to the focal plane, which is visible in figure 6.17b as a gradient along the y-axis. In preparation of the scans, a tilt correction procedure was applied. However, as the scans take several hours tilt might was introduced over time due to an imperfect mechanical stability of the holder.

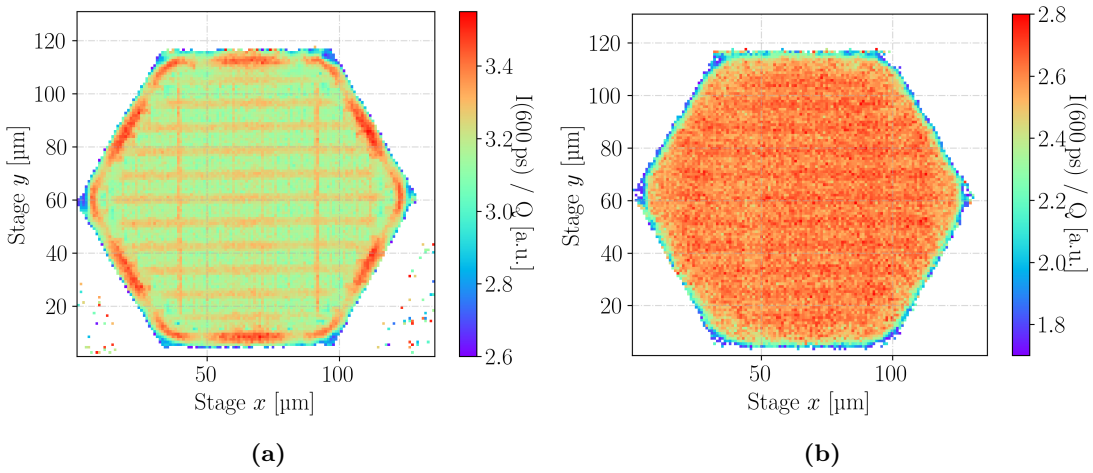

Figure 6.18: Weighted prompt current corresponding to the xy-scans in figure 6.17. The focal plane is at the top side (a) and at the back side (b).

The pitch-to-thickness ratio of the picoAD is comparable to a pad detector, which is why the weighting field is approximately $E_{\mathrm{W,pad}} = 1/d \approx E_{\mathrm{W,picoAD}}$ [163]. However, the weighting field diverges from a constant at the pixel edge [49] and shows similar to ordinary pixel detectors a high weighting field at the top side with a steep decrease towards the back side [164]. The WPC of an xy-scan is presented in figure 6.18. The focal plane, i.e. the main charge generation is positioned at the top (a) and back side (b). Compared to the CC profiles in figure 6.17, the influence of reflection is significantly compensated by the WPC. It is homogeneous in amplitude, which means that different CC leads to the same WPC. This suggests that the pattern might be related to the device itself and is not an artefact of the technique, i.e. the pattern might correspond to a region of increased electric field. At the top side's pixel edge a peak in the WPC is found (see figure 6.18a). The maximum at the edge is potentially an effect of the weighting field and not compulsory related to the electric field. However, TCAD simulations in [49] indicate that the electric field also peaks at the top side's pixel edge and thus contributes to the maximum in the WPC. Figure 6.18b shows a much more homogeneous WPC and does not show such maxima. This indicates that the electric field times the weighting field is more homogeneous at the back side. It should be mentioned that the WPC needs to be considered with care in devices with gain, because the generated charge is not equal to the CC. If the gain is the same for all positions, the WPC is only shifted towards lower absolute values and the relative values are not influenced.

The gain layer of the picoAD is intended to increase the timing capabilities of the device. Similar to LGADs, the gain is expected to be reduced for increasing excess charge carrier densities (compare to chapter 5). Only a device with gain was available for the presented

measurement, wherefore just the relative gain is studied. The relative gain is defined as

$$G_{\text{picoAD}} = V_{\text{max}}(110\,\text{V})/V_{\text{max}}(90\,\text{V})\,, \tag{6.3}$$

with the maximum signal amplitude V_{max}. Figure 6.19a shows the gain according to the given definition for different laser intensities as a function of the device depth, measured inside a single pixel. The x-axis is similar to figure 6.16c and can be used for orientation. It is found that the gain is the lowest for the highest laser intensity and has its minimum at the position where the CC has its maximum. Thus, the highest charge generation corresponds to a minimum gain, which is in agreement with the gain reduction mechanism. The order of intensities does not agree with the expectation, as the second-lowest intensity (red curve) has a lower gain than the third-lowest intensity (green curve). This might be a result of difficulties in the spatial alignment of the two scans, because in order to calculate the gain, two measurements at different bias voltages need to be performed and related in their absolute position. The latter is not a trivial task in such thin devices, as a clear identification of the boundaries is not possible, and it can only be assumed that the top surface corresponds to the maximum CC. Therefore, the WPC allows a more reliable conclusion, because it is measured within a single measurement. Figure 6.19b shows the WPC for different laser intensities as a function of the device depth. As all scans have the same weighting field, so that relative changes allow drawing conclusions on the electric field. In accordance with the gain measurements, the lowest electric field is found for the highest laser intensity. Further, the WPC curves are in the expected order, where the lowest two intensities (black and red curve) do not show a gain reduction, compared to the higher intensities (green and blue curve). The used laser intensities, i.e. the excess charge carrier densities are much lower compared to the ones used for the LGAD in chapter 5. This might be related to the higher ratio of charge generation volume to device thickness. In the picoAD the charge is generated all over the active volume, while the charge generation can be considered localised in the thick LGAD.

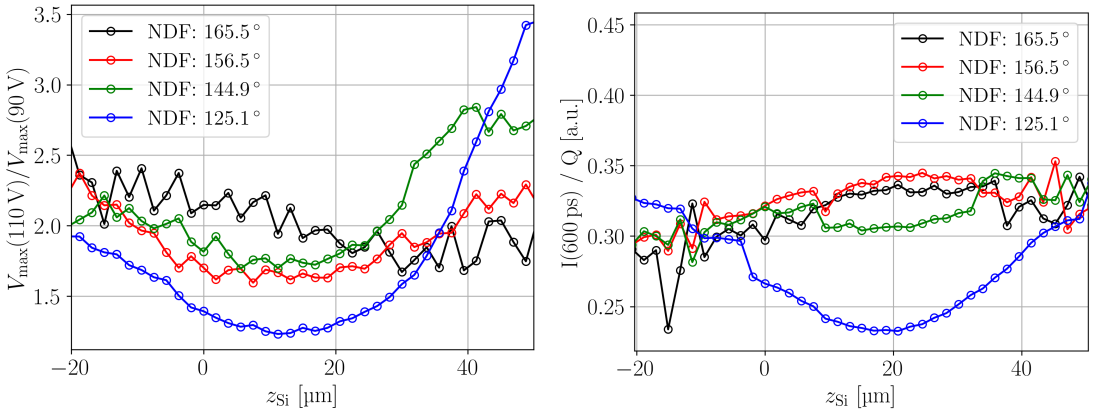

Figure 6.19: Gain reduction due to increasing excess charge density observed in the picoAD. In-depth scans performed at different laser intensities showing the maximum amplitude at 110 V divided by the maximum amplitude recorded at 90 V (a) and the WPC (b).

In summary, the TPA-TCT was used to perform high resolution xy-scans at different device depths. Thin active volumes (here $d_{\mathrm{picoAD}} = 15\,\mu\mathrm{m} < 2z_{\mathrm{R,Si}}$) result in difficulties to extract the device thickness and boundaries from in-depth scans. However, xy-scans from different deposition depths showed significant differences, which demonstrates that spatial resolution along the device depth is achieved. The precise xy-resolution can be used to investigate the device geometry and extract in-pixel and inter-pixel features. Further, the TPA-TCT allowed to investigate the WPC at different device depths, where findings from TCAD simulation about the weighting field and the electric field could be verified. Electron-hole induced plasma was stimulated for increasing laser intensities and the gain reduction mechanism was experimentally verified.

7 Feasibility of single event effect studies

This chapter highlights the potential of the TPA-TCT setup to investigate the electronics of an integrated chip. Previous to the detector characterisation, the TPA method was used to stimulate single event effects (SEEs) with three-dimensional resolution in electronic circuits [7]. TPA is used to mimic the localised charge deposition of an ionising particle, with sufficient spatial precision to investigate SEEs in micrometer-scale circuits. Laser based methods offer a low-cost alternative to X-ray machines and particle beams.

The feasibility of SEE investigation with the TPA-TCT setup is demonstrated using an RD53B chip from the preproduction as an example [50]. The RD53B chip is designed for application in the HL-LHC upgrade of the ATLAS and the CMS pixel detectors. The preproduction series is intended for testing, SEEs investigation, and bug fixing prior to the final design. To cope with the radiation hostile environment in the experiments, radiation and SEE tolerance is a mayor concern for the design. SEEs were observed in the digital logic and the clock and data recovery (CDR) circuit [165]. The lower analogue circuitry of an RD53B chip was subject to the performed campaign, and the campaign was carried out in cooperation with the RD53 collaboration. Here, the focus is set to measurements in the voltage-controlled oscillator that is part in the phase-locked loop. Measurements in various circuits of the analogue chip bottom were performed, which are not subject of the presented work. The aim of this section is the demonstration of the feasibility of such SEE measurements and further information about the full campaign can be found in [166].

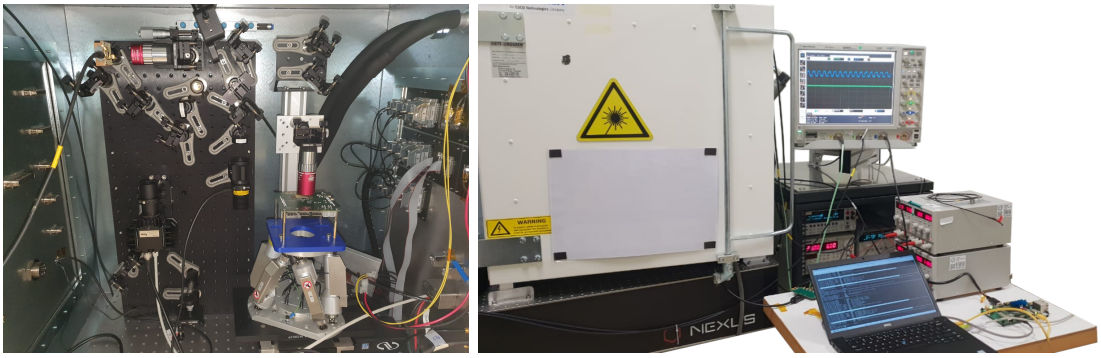

(a) **(b)**

Figure 7.1: Measurement setup for SEE studies of the RD53B chip in the TPA-TCT setup. (a) Insight into the Faraday cage with the DUT mounted on a custom-made 3D printed holder. (b) Data acquisition system in operation mode with the Faraday cage closed. The oscilloscope frame shows the periodic reference clock signal.

Figure 7.1 shows the measurement setup with the DUT mounted inside the TPA-TCT setup (a) and the used data acquisition infrastructure (b). The chip is investigated with illumination from the back side, because the top side is fully metallised. A custom-made holder was 3D-printed, to mount the RD53B chip into the setup. The low voltage is supplied to the chip by the low voltage supplies visible in the photo and the communication is handled using a laptop together with a field programmable gate array (FPGA). The FPGA provides a 640 MHz clock signal that is used as a reference for the chip's internal clock. Exemplary events can be seen in figure 7.2. The clock signals are shown in figure 7.2a with the chip clock in black and the reference clock in red. The half maxima of each clock cycle are determined independently and differences to the reference clock are normalised with the clock period and expressed as the phase difference in units of degree. Figure 7.2b

shows the phase difference versus time corresponding to the event. Right after the light injection, the chip clock skips a cycle, which leads to a jump in the phase difference. The phase difference starts to recover and the beginning of a damped oscillation is visible. The transient behaviour exceeds the recorded time, but from the following event it can be seen that the phase difference recovered to its initial value. All observed events were non-destructive. Figure 7.2c shows another example of a SEE where one full cycle is skipped and no damped oscillation is observed in the phase difference. The phase difference stays at a value of 360°, which corresponds to the delay of a full cycle.

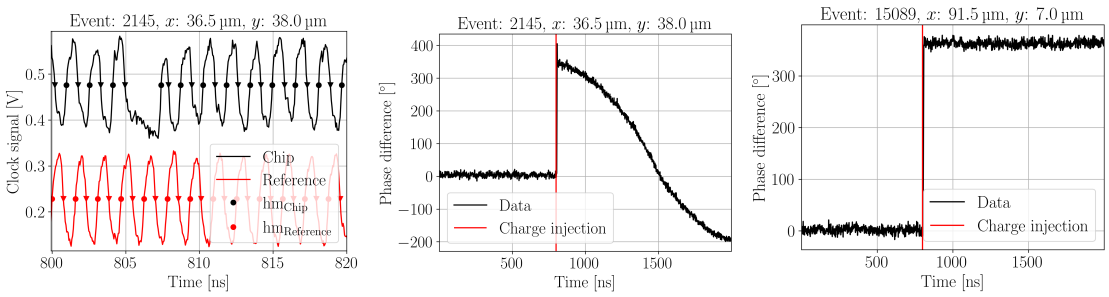

(a) **(b)** **(c)**

Figure 7.2: SEEs in the voltage-controlled oscillator. (a) The chip clock (black) and reference clock (red) signal. The half maxima are indicated by markers and used to calculate the phase difference between the two clocks. (b) Corresponding phase difference transient for the event shown in (a). The red line marks the time of light/charge injection and aligns with the deviating clock cycle at about 805 ns. The transient behaviour exceeds the recorded time. (c) A SEE leads to skip one full clock cycle. The coordinates in the figures title correspond to the *xy*-scan in figure 7.3.

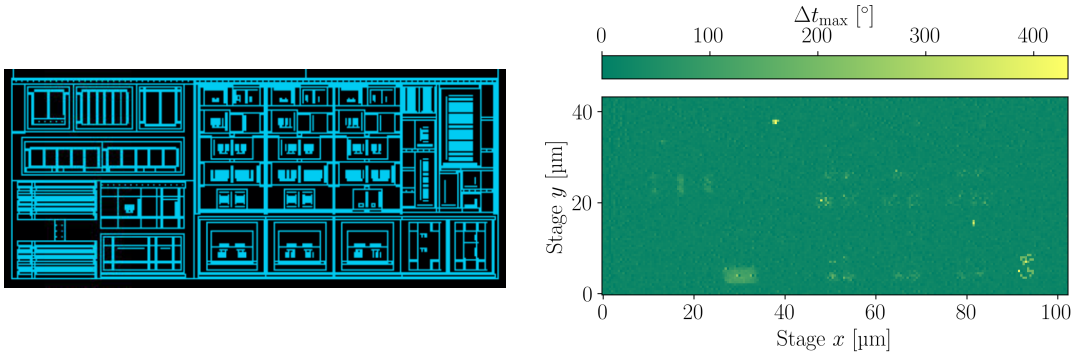

(a) **(b)**

Figure 7.3: Schematic of the voltage-controlled oscillator in the analogue chip bottom (a), next to a measured SEE *xy*-map (b). The maximum phase difference between the chip and reference clock is colour-coded. The laser pulse energy is 1.2 nJ, the laser repetition rate 5 Hz, and the step size 0.5 µm.

Light injection was performed for various *xy*-positions in a grid with a step size of 0.5 µm. The resulting SEE map can be seen in figure 7.3 where the schematic of the circuit (a) is shown next to the measured SEE map (b). The SEE map highlights the high spatial resolution and demonstrates the feasibility to investigate electronic circuits in the micrometer-scale with the present TPA-TCT setup.

8 Summary, conclusions, and outlook

In this work, the two photon absorption - transient current method (TPA-TCT) was investigated as a characterisation technique for silicon detectors. The main findings are summarised and concluded in the following, where studies concerning the fundamentals of the TPA-TCT are separately discussed from studies targeting the characterisation of concrete detector technologies. Finally, an outlook on the TPA-TCT setup and the TPA-TCT as a device characterisation technique is given.

Fundamentals of the TPA-TCT

First, basic properties of the setup were evaluated and adapted to reach satisfactory parameters. It was demonstrated that temperatures at the device under test in the range between −20 °C to 20 °C were reached with fluctuation below 0.1 °C and that the noise root-mean-square in single acquisitions could be reduced to the intrinsic amplifier noise of ≈ 3.3 mV. The laser stability was evaluated in long term measurements, where fluctuations in the deposited charge with a standard deviation of 7 % was measured. These fluctuations were related to instabilities in the temporal pulse structure of the laser, which is why a TPA reference is used as an energy monitor in order to correct such fluctuations. Using the TPA reference, the charge deposition could be corrected for the fluctuations up to a standard deviation of 2 %.

Second, the spatial resolution, the influence of the pulse energy, and the temperature dependence of the TPA charge generation were investigated. The spatial resolution of objectives with numerical apertures (NAs) of 0.5 and 0.7 were evaluated. Beam parameters of $w_0 = 1.3\,\mu\text{m}$ and $z_{\text{R,Si}} = 10\,\mu\text{m}$ were measured with the NA = 0.5 objective, while the NA = 0.7 objective achieves beam parameters of $w_0 = 0.9\,\mu\text{m}$ and $z_{\text{R,Si}} = 6\,\mu\text{m}$. Spherical aberration was observed for the NA = 0.7 objective for devices that exceed a thickness of ≈ 70 µm. Therefore, the NA = 0.5 objective was recommended for thicker devices in order to avoid spherical aberration. Increasing collection times were observed for increasing pulse energies, which was linked to the formation of electron-hole plasma. It was found that the plasma onset energy increases with bias voltages and the measured collection times were successfully described by the $E_{\text{p}}^{4/3}$-dependence that is predicted by the Tove-Seibt model. The temperature dependence of the TPA-TCT charge generation was investigated between −20 °C to 20 °C and a linear increase with temperature was observed. The increasing charge generation in the investigated temperature range was linked to an increasing absorption coefficient β_2. Furthermore, this work contributed to TCAD simulation of the TPA-TCT, where measurements in a pad detector were qualitatively reproduced.

Third, neutron, proton, and gamma irradiated pad detectors were systematically studied using the TPA-TCT. The main finding was the absence of a single photon absorption (SPA) background for gamma irradiated devices, contrary to irradiation with neutron or proton. For the latter it was found that the SPA background scales with the equivalent fluence, which indicates that it is in accordance with the non-ionising energy loss (NIEL) hypothesis. The functional relation was measured to be $14.3 \cdot 10^{-11}\,\text{cm}^{2\cdot 0.84}\text{fC/nJ} \cdot \Phi_{\text{eq}}^{0.84}$. Absence of the SPA background in gamma irradiated devices and the scaling of the SPA background with NIEL indicate that the occurrence of SPA is related to cluster damage. Differences in the prompt current profile between neutron and proton irradiated devices were observed for $\approx 7 \cdot 10^{15}\,\text{n}_{\text{eq}}/\text{cm}^2$. Both devices showed a double junction, but only the proton

irradiated device showed a space charge sign inversion (SCSI). This is especially interesting, because SCSI was so far not reported for float zone p-type detectors. Proton irradiation related SCSI could be relevant to p-type strip detectors as it potentially leads to a decreased charge collection efficiency (CCE) compared to similar neutron irradiated strip detectors. Methods to correct the influence of the additional SPA contribution were reviewed, and the waveform subtraction method was recommended for the general use. It was measured that the additional SPA contribution does not lead to a meaningful beam depletion in silicon devices up to fluences of at least $3.32 \cdot 10^{14}\,\mathrm{n_{eq}/cm^2}$, which is important in order to obtain comparable charge generation along the device depth of irradiated devices. Further, it was verified that the refractive index and the absorption coefficient β_2 are independent of the fluence up to at least $3.32 \cdot 10^{14}\,\mathrm{n_{eq}/cm^2}$. The latter was concluded by comparing the CCE measurements from the TPA-TCT setup with similar measurements in a ^{90}Sr setup. Within the CCE measurements of pad detectors, it was found that the TPA-TCT extends the available fluence range for CCE measurements beyond $3.32 \cdot 10^{14}\,\mathrm{n_{eq}/cm^2}$, which was not feasible with the ^{90}Sr setup. This is related to the higher signal-to-noise ratio achieved by the TPA-TCT. In general, it was demonstrated that the TPA-TCT produces meaningful results for irradiated devices and is a valuable addition to the present set of available characterisation methods.

Device characterisation

Pad detectors with and without gain, strip detectors, and monolithic detectors were investigated using the TPA-TCT. A decrease of charge multiplication was observed in a low gain avalanche detector (LGAD) for increasing excess charge carrier densities, i.e. laser intensities. This reduction of gain is currently subject to research efforts due to the relevance of LGADs to state-of-the-art and future timing detectors. Partial restoring of gain was observed and simulated for increasing diffusion of the excess electron density. A profound understanding of gain reduction is desirable, because it was observed for the whole available intensity range and is thus always present in the measurements. Gain reduction was as not only observed in the LGAD, but also in the Monolith picoAD, which is a monolithic timing detector. The TPA-TCT proves to be a valuable tool for the investigation of charge carrier density related phenomena, such as the gain reduction, because it offers a tunable charge carrier density and its three-dimensional spatial resolution allows to study such phenomena along the device depth.

Clipping and reflection were discussed in the context of pad and segmented detectors. Methods to extract detector quantities like the active thickness in the presence of clipping and reflection were introduced. Further, the weighted prompt current (WPC) method and the mirror technique were developed, which are methods dedicated to the investigation of segmented devices. The WPC is based on the prompt current (PC) method and designed to compensate intensity fluctuations, due to laser beam clipping, reflection, or laser instabilities. Similar to the PC method, it yields the product of the drift velocity and the weighting field, but in an intensity independent manner. The WPC was studied in detail in a pad detector, where valleys in the WPC at the device boundaries were observed. Charge collection within the PC time was found to be the origin of the valleys, which was confirmed by TCAD simulations. The mirror technique was developed to extend the application of top side illumination in segmented devices. It exploits the reflection at the DUT's back side in order to obtain access below top side metallisation. Here, the main application of the methods were strip detectors, because the region below the strip metal is otherwise not accessible by

top side illumination. The developed methods were applied to state-of-the-art monolithic detectors, namely the HV-CMOS CCPD v3, the RD50-MPW2, and the Monolith picoAD, and the feasibility of high resolution three-dimensional in-pixel scans with lateral resolution in the order of the beam waist $w_0 = 1.3\,\mu m$ was demonstrated. Finally, the potential of the TPA-TCT setup to investigate single event effects in micrometer-scale electronic circuits was proven. A campaign was conducted on the preproduction RD53B chip and the findings contributed to the latest RD53B design proposal.

To conclude, a profound understanding about the TPA-TCT as a device characterisation technique for non-irradiated and irradiated detectors was obtained during the efforts of this work and a contribution towards establishing the TPA-TCT in the framework of device characterisation techniques was made.

Outlook

Several future adaptations to the TPA-TCT setup are foreseen. A spatial light modulator will be implemented to counteract the effect of spherical aberration, which will extend the application range of the NA = 0.7 objective to device thicknesses beyond 70 µm. The NA = 0.7 objective provides beam parameters of $w_0 = 0.9\,\mu m$ and $z_{R,Si} = 6\,\mu m$, which increases the in-depth resolution by a factor of about two. Further, the implementation of a cryostat is foreseen to enable device characterisation with a three-dimensional resolution at cryogenic temperatures. Defect spectroscopy methods like the deep level transient spectroscopy (DLTS) or the thermal stimulated current (TSC) method in irradiated devices rely on cryogenic temperatures. The charge carrier generation needed within these techniques could be obtained by TPA in a confined volume to enable three-dimensional spatial resolution. This would be an improvement with respect to segmented devices, where high spatial resolution is desired to investigate single segments of the device, i.e. in-pixel measurements. Another application that was not explored in this work is the further development of TCAD simulation tools. The TPA-TCT could serve as a high precision tool to benchmark TCAD simulations and give spatially resolved input to such simulations. This would be especially interesting with respect to irradiated segmented devices that can not be studied with three-dimensional resolution in any other laser based technique.

A Appendix

A.1 Influence of readout electronics on the signal acquisition

This section contains a brief discussion on the influence of the readout electronics on the acquired signal, where especially the influence of the bandwidth, the sampling rate, and the transfer function are of interest. A more complete overview about the matter can be found in [74]. In the following, a transient current setup as described in section 3.5.1 is assumed. The readout chain consists of a computer, an amplifier, an oscilloscope, and the cables that connect all of these components. The goal of the readout electronics is to maximize the signal-to-noise (SNR) ratio while maintaining the highest possible signal fidelity. The computer is used for controlling the instruments, storing acquired data, and performing post-processing operations. Coaxial cables efficiently shield electromagnetic noise, which makes them suitable to interconnect the DUT with the high voltage supply and the amplifier. Cables in the order of 10 m are used to shift potential signal reflection outside the readout window of interest. Signal reflection might occur due to impedance mismatch at the amplifier input. The reflection becomes irrelevant to the signal, when they are delayed outside the recorded time window. Usually some 10 ns suffice for this purpose. The amplifier and the oscilloscope are the most delicate components with respect to the data acquisition. There are two types of amplifiers relevant to this work, transimpedance and charge sensitive amplifier (CSA). The prior is used to elevate the signal amplitude into a suitable voltage range, while preserving the temporal structure of the current transient. CSAs are used for precise charge measurements, where the charge is translated to the signal amplitude. Amplifiers need to be selected to increase the SNR, which is done by tailoring the bandwidth to allow as many signal frequencies as possible, while avoiding a maximum of the noise spectrum. The oscilloscope determines the re-trigger rate and the sampling rate of the readout. The re-trigger rate determines the frequency of the recorded acquisitions, which is for laser based TCT non-critical, because the re-trigger frequency is determined by the laser pulse rate that can be adapted to an adequate value. It should be mentioned that the re-trigger rate is very important to beam test experiments as oscilloscopes potentially introduce a significant dead time to the readout chain. Further, the oscilloscope has its own bandwidth limitations, but it is usually less delicate than the amplifier's bandwidth. Following the Nyquist-Shannon sampling theorem, the sampling rate needs to be at least twice the highest frequency present, in order to avoid distorted sampling, i.e. aliasing. Hence, the sampling rate defines the highest possible cut-off frequency.

In the following, a thought experiment is discussed, considering 150 µm thick pad detector at a bias voltage that saturated the drift velocity. Figure A.1a shows the modelled current transient of such a device. The input signal is shown in grey and a Gaussian distributed noise with a standard deviation of $\sigma = 50\,\mathrm{mV}$ is added to obtain the signal depicted in black. The red dots show the signal after it passed a 6th order band pass with a band between 10 kHz to 2 GHz. Figure A.1b shows the Fast Fourier transformation (FFT) of this signal, where the Gaussian noise becomes evident as the white spectrum, i.e. the constant background. It can be seen that the signal is dominantly composed out of low frequencies $< 1\,\mathrm{GHz}$ that are responsible for the peak in that region. Therefore, the setup bandwidth acceptance for 150 µm thick pad detector should not be below $< 1\,\mathrm{GHz}$. In the following, a measurement to get an idea of the frequency response of the readout electronics is described and performed. For the measurement the laser is turned off and a pad detector

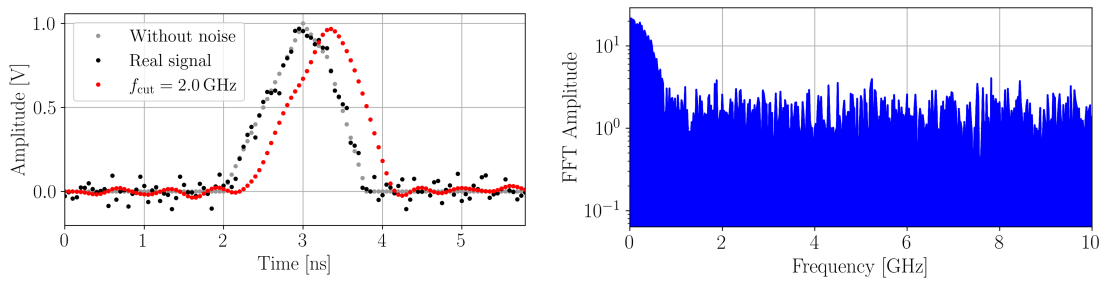

(a) **(b)**

Figure A.1: (a) Model of a transient current. The input signal is shown in grey and labelled *Without noise*. The black solid dots show the input signal superimposed with Gaussian distributed noise ($\sigma = 2\,\text{mV}$) and are labelled *Real signal*. The red dots show the *Real signal* after it was filtered by a bandpass with and lower cut of at 10 kHz and a higher cut off at 2 GHz. It is slightly shifted in time with respect to the other signals. (b) Fast Fourier transformed (FFT) of the *Real signal*. The Gaussian distributed noise leads to a white spectrum, i.e. equal contributions to all frequencies, while the input signal is predominant at frequencies below 1 GHz.

at zero bias voltage is mounted in the setup. In this configuration it is assumed that only noise is present in the current transient, which should be in good approximation white noise, i.e. all frequencies that are in accordance with the Nyquist-Shannon sampling theorem occur equally. Frequencies that are beyond the bandwidth of the setup should be damped by the readout electronics and thus have a lower amplitude in the FFT. Figure A.2a shows the result of the performed measurement. A knee at about 3 GHz is found, which is related to the oscilloscope, while the amplifier is responsible for the knee at about 1 GHz. The measurement hints that the frequency response of the setup is most likely suitable for measurements of devices with frequencies $\approx 1\,\text{GHz}$, i.e. 150 µm thick pad detectors. Such a measurement yields only first insights to the frequency response of the setup, but for a precise result measurements proposed in [167] would need to be performed. For timing detectors like thin gain detectors or three-dimensional segmented detectors (3D detectors) higher frequency components might are required, as the steep rising edges, which is exploited for the time resolution, is potentially composed of high frequencies beyond 2 GHz up to 6 GHz. Hence, for the investigation of timing detectors the readout electronics would need to be adapted to a suitable bandwidth and sampling rate. The frequency response of the electronic setup can be described in the time domain as a transfer function. The convolution between the input signal and output signal yield the measured signal. To investigate the influence of the transfer function of the used CIVIDEC C2HV [121] amplifier, a measurement in a pad detector was performed, once with the amplifier mounted and once without the amplifier mounted. For the latter, a bias-tee was used to protect the oscilloscope input from too high currents. Figure A.2b summarises the measurement, and it can be seen that both waveforms are in good agreement. From this measurement, the amplification factor can be determined by comparing the signal amplitudes and further it is found that the collected charge (CC) in both measurements agrees within $(1.0 \pm 0.9)\,\%$ difference. It is concluded that the transfer function of the used amplifier is negligible for such devices and hence no corrections need to be applied to the measurements. Details about transfer functions and means to determine it can be found in [167].

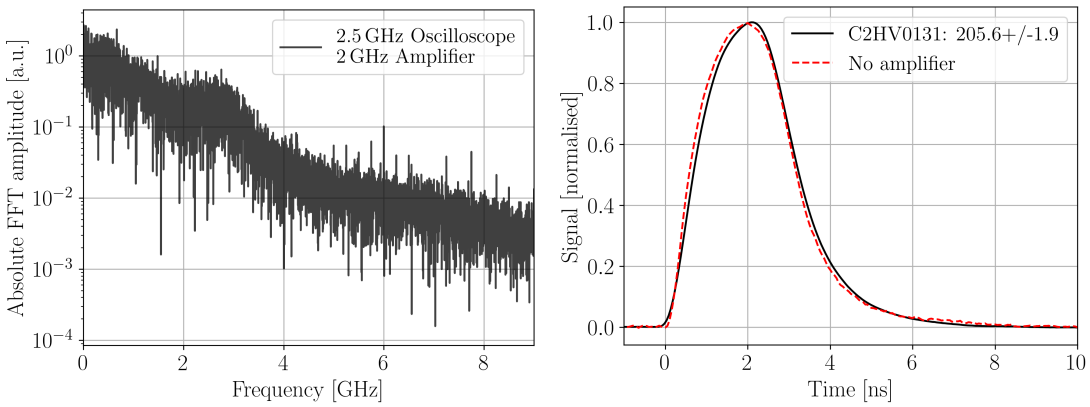

(a) **(b)**

Figure A.2: (a) FFT of noise recorded with the TPA-TCT setup. Information about the measurement is provided in the text. (b) Comparison between a current transient of a thick pad detector recorded with a CIVIDEC C2HV amplifier (black solid line) and a bias-tee (red dashed line). The collected charge is calculated from the integral of both waveforms and both agree within $(1.0 \pm 0.9)\,\%$ deviation. The error is propagated from the amplification factor stated in the figure's legend.

A.2 Tilt correction - A procedure to correct tilt between the DUT and the focal plane

To avoid tilt between the DUT and the focal plane, an alignment procedure, called tilt correction, was developed [13]. The procedure is visualised in figure A.3. In-depth scans are taken in a 3×3 grid across the DUT plane and the DUT surface is extracted as the first half maximum point in the CC profiles as shown in figure A.3a. Note that the here described procedure is exemplary performed using the CC profile to extract the top side position. It is as well applicable for any quantity that allows to extract the device top or back side. For example in cases where the charge collection profile is inhomogeneous, it might be more reasonable to extract a device boundary from the time over threshold profile or another intensity independent quantity instead. The extracted surface positions are fitted by a plane

$$z(x, y) = \tan(\alpha) \cdot x + \tan(\beta) \cdot y + C\,. \tag{A.1}$$

α is the angle between the x-axis and the focal plane, and β is the angle between the y-axis and the focal plane. C is the constant offset from the origin in z. An example of a surface fitted to the extracted DUT surface position is shown in figure A.3b. The compensation angle u and v, to correct the tilt of the y- and the x-axis, is found as

$$u = -\beta \tag{A.2}$$

$$v = \alpha\,. \tag{A.3}$$

The minus sign for u is a result of the axis definition in the hexapod. This method is found to correct tilt up to a residual tilt $< 0.03°$.

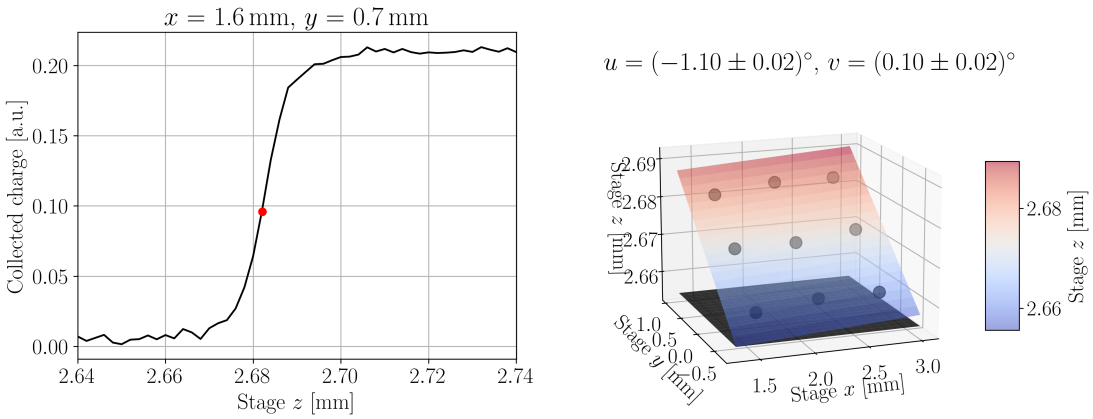

(a) **(b)**

Figure A.3: Tilt correction procedure. In-depth scans are taken at various xy-position and the position of the surface is extracted from the first half maximum point of the charge collection profile. An example is shown in (a). The xy-position of the scan is stated in the figure title. (b) A plane is fitted to the surface positions that are extracted from all in-depth scans. It can be seen that the DUT plane is tilted compared to the focal plane (black plane). The figure title shows the measured compensation angles that need to be applied in order to level the DUT plane. The z-positions are colour-coded.

A.3 Modelling of reflection

Reflection leads to signal beyond the boundaries of the DUT. It is usually present as a tail in the charge collection profile at deposition depth beyond the DUT's back surface. In the following, a model to describe such reflection in a charge profile is presented and discussed. The model underlies the assumption that the temporal width of the laser pulse is negligible, i.e. that the illumination is instantaneous. A fitting function to the CC of a pad detector with the active thickness d is derived in [42] to

$$\gamma = \frac{E_\mathrm{p}^2 \beta_2 \sqrt{\ln 2}}{2\tau\hbar\omega\pi^{3/2}\sqrt{\ln 4}} = \text{const.}\,, \tag{A.4}$$

$$N_\mathrm{TPA}(z) = \gamma \cdot \left[\arctan\left(\frac{d-z}{z_\mathrm{R}}\right) + \arctan\left(\frac{z}{z_\mathrm{R}}\right)\right]. \tag{A.5}$$

However, this fit function does not account for reflection at the back side surface. Such a reflection begins at $z = d$ and scans the active volume from the back to the front side, i.e. in opposite direction than the ordinary focal point. It depends quadratically on the reflectance R of the surface, as the charge generation by reflection scales quadratically with the reflected intensity. Hence, the reflection can be described by

$$N_\mathrm{R}(z) = R^2 \cdot N_\mathrm{TPA}(2d - z)\,. \tag{A.6}$$

Fitting both equations together leads to deviations near d, because the charge generation increases when the ordinary focal point overlaps with the reflected focal point, due to the quadratic relation between the light intensity and charge generation. This interaction leads to a maximum charge generation that is $2R$ times the charge collection. It is modelled

by

$$P(z) = 2R \cdot \hat{N}_{\mathrm{TPA}}(z) \cdot \hat{N}_{\mathrm{R}}(z) \cdot (N_{\mathrm{TPA}}(z) + N_{\mathrm{R}}(z)) \tag{A.7}$$
$$= 2R \cdot W(z) \cdot (N_{\mathrm{TPA}}(z) + N_{\mathrm{R}}(z)) \,, \tag{A.8}$$

with $W(z)$ being the product of the fitting function normalised by its maximum. The introduction of $W(z)$ weights the interaction so that the contribution is maximum when the overlap between the ordinary and the reflected focal point is the greatest. The interaction is not symmetric before and behind the back side surface, as motivated in figure A.4a. When the focal point is in front of a surface, it does not lead to a reflection. Only when the focal point is near or behind the surface, a contribution from reflection is observed. This behaviour is modelled with

$$S(z) = \frac{1}{2} \left(1 + \tanh\left(\epsilon \left(z + \delta - d\right)\right)\right) \,, \tag{A.9}$$

where ϵ and δ are free parameters that describe the steepness of the reflection onset and the onset position relative to the back side surface, respectively. When all above equations are combined, the fit function of the reflection model is obtained

$$N_{\mathrm{TPA,R}}(z) = (1 + S(z) \cdot W(z)) \cdot (N_{\mathrm{TPA}}(z) + N_{\mathrm{R}}(z)) \,. \tag{A.10}$$

Figure A.4b shows an exemplary application of this model with different corrections of the model switched on or off. The full model yields a satisfactory description of the data and quantities like the device thickness d, the Rayleigh length $z_{\mathrm{R,Si}}$, and the reflectance of the back side R can be extracted from the fit. Deviations from the data at $z = 2d$ may

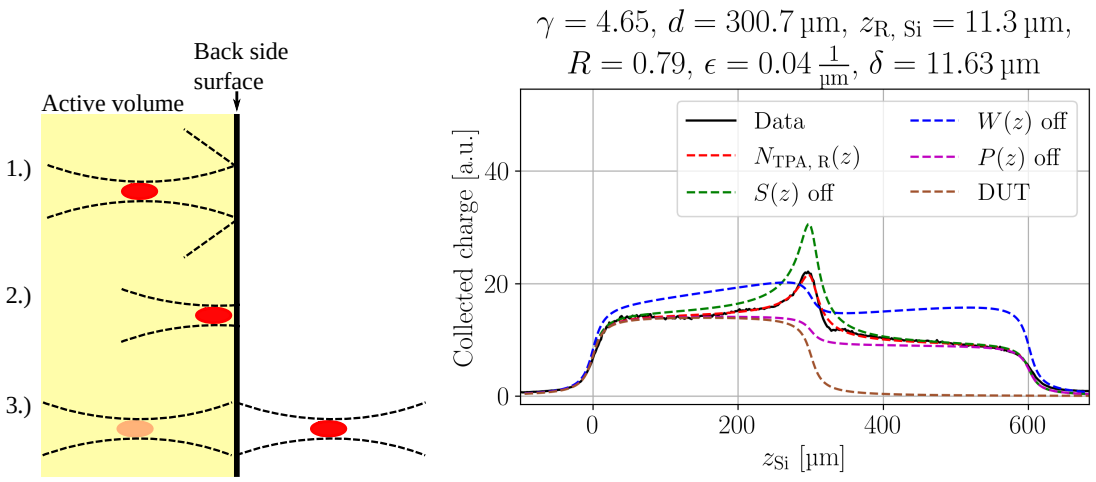

Figure A.4: (a) Sketch of reflection in TPA-TCT. 1.) In front of the surface the light is not reflected in a focused manner. 2.) The influence of reflection is already observed when the focal point is near the surface. 3.) When the focal point is positioned behind the back side, it is mirrored back into the active volume. (b) Application of the reflection model to a thick pad detector. The back side is metallised and causes a strong reflection peak at the back side. Fits with certain corrections turned on or off (see text) are included in the figure. The curve labelled DUT shows the extracted reflection corrected charge collection profile. The fitting parameters are given in the title of the figure.

occur due to the reflection of the reflection at the top surface, which is not considered in the model.

A.4 Median of the TPA-TCT excess charge

Naively, one expects that the position of the focal point represents the position of the dominating induced current contribution. In this picture, this means that when the focal point is positioned above or below the active volume, the current transient should be representative to charge generation right at the top or back side position, respectively. In this section it is shown that the naive picture is invalid near the boundaries. Figure A.5a shows the charge carrier density n_{TPA} integrated over the radial component along the z'-axis. The z'-axis is defined, in accordance with section 2.4.1, as the distance from the focal point. It can be seen that the charge is mainly generated in a small volume around the centre, which is the origin of the three-dimensional spatial resolution of the TPA-TCT. The median is calculated as the position, where the cumulative sum of the charge carrier density reaches 50 % of the total charge generated within the active volume. The distribution is symmetric around the focal point, which means that the median aligns with the focal point when it is central inside the active volume. However, if the distribution is not positioned central in the active volume of the DUT, the distribution might exceed the device's boundaries in a non-symmetrical manner and the median of the generated charge shifts away from the centre. This is especially relevant at the boundaries. When the focal point is positioned right at the top surface, only $z' \geq 0\,\mu\mathrm{m}$ generates charge in the active volume and the distribution is cut in half. The median of the resulting generated excess charge does not align with the focal point, but is shifted towards a $z' > 0\,\mu\mathrm{m}$.

Figure A.5b shows the evolution of the distance to the back side for the median in a 300 µm thick active volume for different positions of the focal point, compared to the naive expectation. Reflection of any kind is neglected and the charge carrier distribution of figure A.5a is used. Within the active volume the distance to the back side increases linear

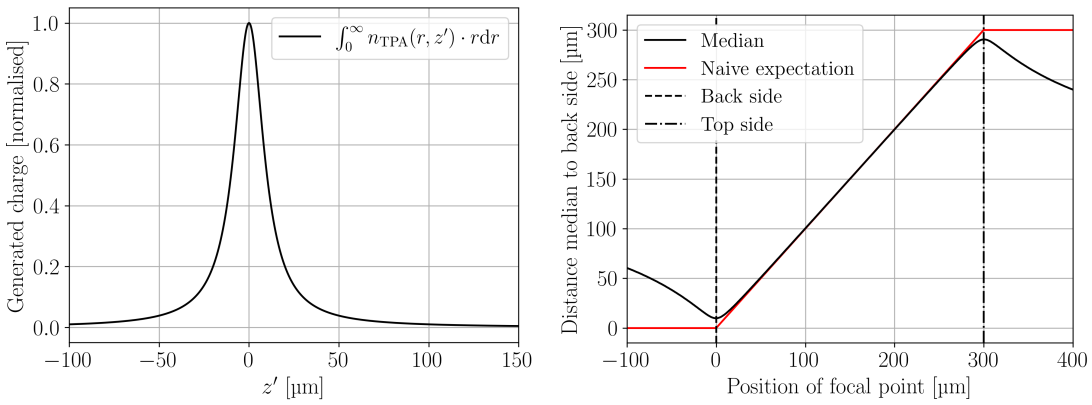

(a) **(b)**

Figure A.5: (a) TPA charge generation profile along the z'-axis for $w_0 = 1.3\,\mu\mathrm{m}$ and $z_{\mathrm{R,Si}} = 10\,\mu\mathrm{m}$. The profile is normalised to its maximum. (b) Calculated distance between the median of the TPA excess charge and the back side in a 300 µm thick active volume. The naive expectation is as well shown for comparison. The active volume's boundaries are indicated by the dashed and the dotted-dashed line.

with the focal point's position. Thus, the position of the focal point represents the position of the main contribution to the current transient, which is in accordance with the prior sketched naive picture. Near the boundaries the distance to the back side diverges from a linear relation and a minimum or maximum is found. The median of the TPA excess charge shifts away from the boundary, back into the active volume. A direct relation between the focal point's position and the main contribution to the induced current transient becomes invalid. The influence of this effect is especially relevant to the ToT, where it results in a decrease in the ToT in front of the top surface. An example of the ToT of a thick pad detector is shown in section 3.5.12 in figure 3.18. It can be seen that the distance of the median appears symmetric around the device boundary, but the symmetry ends for distances further away from the boundary.

A.5 Single photon absorption correction by intensity

Radiation damage can lead to a contribution of linear absorption in silicon. This absorption does not depend on the position of the focal point, but only the light intensity. It appears in an in-depth measurement as a constant offset and is therefore called SPA offset. Section 2.3.1 introduced three methods to correct this offset and this section focuses on the intensity method.

The additional linear absorption means that the SPA contribution in equation (2.19) can no longer be neglected. The light absorption, i.e. generation of excess charge carriers becomes a superposition of linear and quadratic absorption. Following [13], the induced current from such a measurement can be written as

$$I(t) = E_\mathrm{p} \cdot i_\mathrm{SPA}(t) + E_\mathrm{p}^2 \cdot i_\mathrm{TPA}(t)\,, \tag{A.11}$$

with the SPA and TPA contribution to the induced current i_SPA and i_TPA, respectively. The different dependence of the linear absorption and the quadratic absorption on the light intensity is exploited to obtain the SPA correction. The same measurement is performed twice at different intensities $E_{\mathrm{p},1}$ and $E_{\mathrm{p},2}$ to obtain $I_1(t)$ and $I_2(t)$. The values can be inserted in equation (A.11) and rearranged to

$$i_\mathrm{SPA} = \frac{E_{\mathrm{p},2}^2 I_1 - E_{\mathrm{p},1}^2 I_2}{E_{\mathrm{p},1} E_{\mathrm{p},2} (E_{\mathrm{p},2} - E_{\mathrm{p},1})}\,, \tag{A.12}$$

$$i_\mathrm{TPA} = \frac{E_{\mathrm{p},2} I_1 - E_{\mathrm{p},1} I_2}{E_{\mathrm{p},1} E_{\mathrm{p},2} (E_{\mathrm{p},1} - E_{\mathrm{p},2})}\,. \tag{A.13}$$

The quantities i_SPA and i_TPA are the pure SPA and TPA contribution to the induced current, respectively. Numerical instability is observed when the probing intensities $E_{\mathrm{p},1}$ and $E_{\mathrm{p},2}$ are too close together, as the subtraction of these intensities gives the denominator in the above equations.

A.6 Collection of current transients

This section contains selected current transients recorded during the measurements performed in the framework of this thesis. They could serve as a benchmark for simulation purposes. The figures captions contain information about the shown measurements. Current transients recorded in pad detectors at different bias voltages, different temperatures, and difference fluences are presented in figures A.6, A.7, and A.8, respectively.

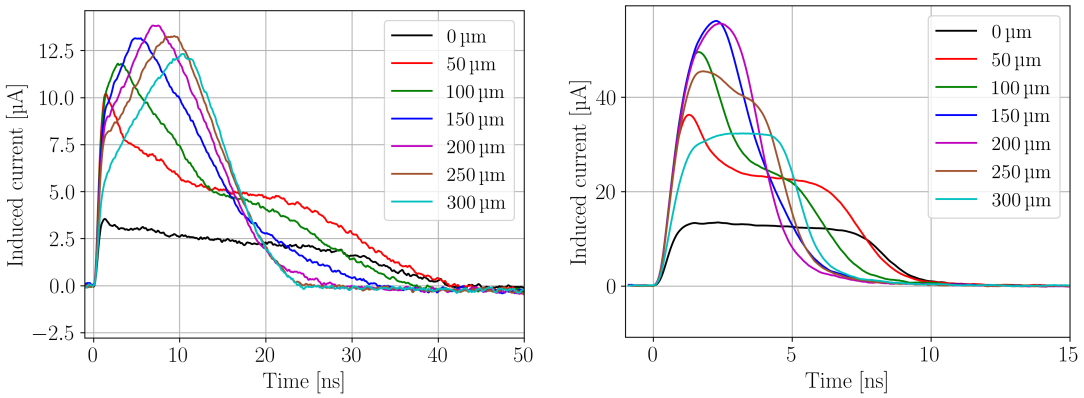

Figure A.6: Current transients recorded in the 25-DS-66 CiS pad detector with a bias voltage of 50 V (a) and 300 V (b). Positions in the legends refer to positions shown in figure 3.19, where 0 µm corresponds to the top side and 300 µm to the back side. The measurements were performed at 20 °C and 0 % relative humidity. The beam parameters were $w_0 = 1.2\,\mu\text{m}$ and $z_{\text{R,Si}} = 9.7\,\mu\text{m}$ and a pulse energy of $\approx 306\,\text{pJ}$ was used. The laser frequency was 1 kHz and the average of 256 single acquisitions was recorded.

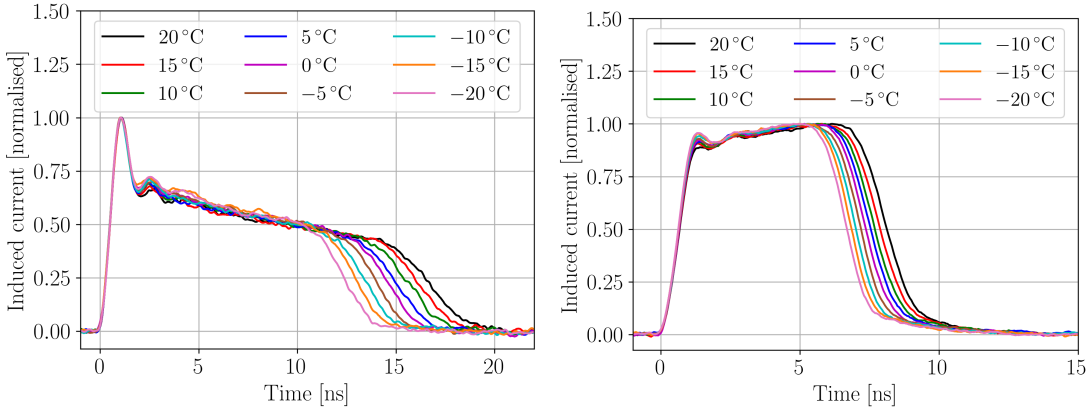

Figure A.7: Normalised current transients recorded at the top (a) and back side (b) of the WL-A63-PIN4 pad detector. The measurements were performed in the framework of section 3.5.9 at different temperatures and 0 % relative humidity. The beam parameters were $w_0 = 1.22\,\mu\text{m}$ and $z_{\text{R,Si}} = 10.6\,\mu\text{m}$ and a pulse energy of $\approx 200\,\text{pJ}$ was used. The laser frequency was 1 kHz and the average of 256 single acquisitions was recorded. The bias voltage was 100 V.

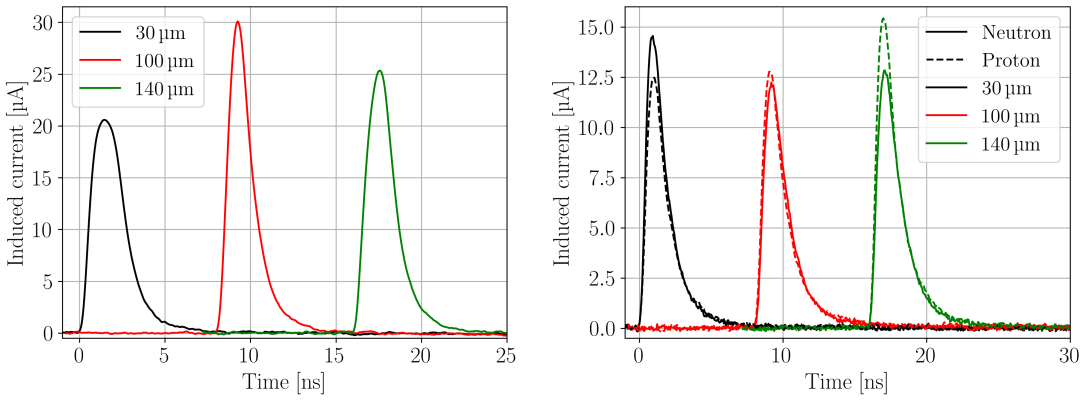

(a) **(b)**

Figure A.8: Current transients recorded in the non-irradiated 21-DS-79 (a), the neutron irradiated 21-DS-102, and the proton irradiated 21-DS-92 (b) CiS pad detector. The fluence of the neutron and proton irradiated device are $7.02 \cdot 10^{15}\,\mathrm{n/cm^2}$ and $1.17 \cdot 10^{16}\,\mathrm{p/cm^2}$, respectively. Positions in the legends refer to positions shown in figure 4.6, where 0 µm corresponds to the top side and 156 µm to the back side. The measurements were performed at −20 °C and 0 % relative humidity. The beam parameters were $w_0 = 1.2\,\mu\mathrm{m}$ and $z_{\mathrm{R,Si}} = 9.7\,\mu\mathrm{m}$ and a pulse energy of $\approx 200\,\mathrm{pJ}$ was used. The laser frequency was 200 Hz and the average of 256 single acquisitions was recorded. The bias voltage was 300 V.

A.7 Verification with TCAD simulation

In a collaborative effort, simulations with the TCAD tool Synopsis [168] were performed, where measurements from this work were used as an input to the simulations. A 290 µm thick pad detector was simulated, and the doping profile was based on the pad detector 7859 WL-A63-PIN4. For the simulation of the TPA charge carrier generation, a density following equation (2.34) is used. The beam parameters are $z_{\mathrm{R}} = 10.5\,\mu\mathrm{m}$ and $w_0 = 1.3\,\mu\mathrm{m}$. The simulated induced current was convoluted with the transfer function of the CIVIDEC C2HV amplifier to resemble measured current transients. Reflection at the back side interface was not considered for the simulation. The simulation is preliminary, wherefore the results are not compared to measurement data. Figure A.9 shows of the CC and time

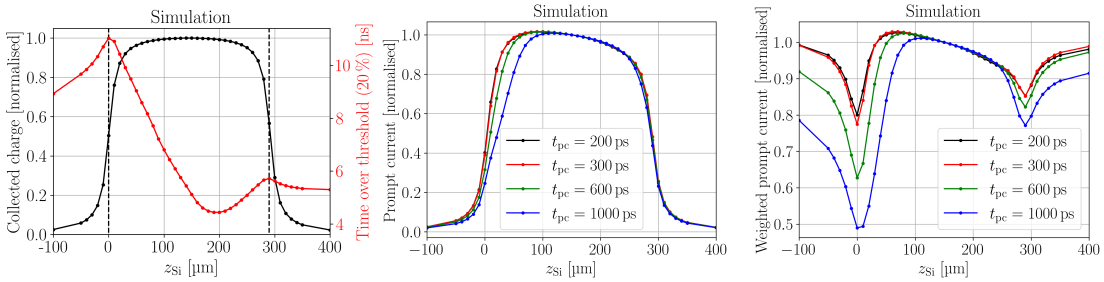

(a) **(b)** **(c)**

Figure A.9: TCAD simulation of a TPA-TCT in-depth measurement of a 290 µm thick pad detector. (a) Collected charge and time over threshold profile. The device boundaries are indicated by the dashed lines. (b) Prompt current for different prompt current times. (c) Weighted prompt current for different prompt current times.

over threshold profile (a), the prompt current (PC) (b) and the weighted prompt current (WPC) (c) that are extracted from simulated induced current transients. The latter two are calculated for different PC times to show the evolution with t_{pc}. The simulation can be compared to measurements presented within this work: CC and ToT to figure 3.18, the PC to figure 2.6b, and the WPC to figure 6.4b. It can be seen that all features of the measurements are well reproduced by the simulation. To be more specific, the box-like shape in the CC is found and the ToT shows two maxima and a minimum at the same position. The decrease in the ToT in front of the top side is as well reproduced, which supports the argumentation about the median of the excess charge of the appendix A.4. Further, the edge steepness in the PC decreases with the PC time, which is related to charge collection with in t_{pc} as discussed in section 6.2. Thus, the valleys at the device boundaries are found in the WPC, which is a result of the charge collection with in t_{pc}. The indicated symmetry in the WPC around the valleys is, similar as for the ToT, caused by the shifting median of the excess charge. Thus, the minima of the valley is linked to the position of the corresponding device boundary. All in all, the simulation confirms that the observed measurement features are well understood and shows that a profound understanding about the TPA-TCT was obtained within this work.

Acronyms

CaR Control and readout.

CB Conduction band.

CC Collected charge.

CCE Charge collection efficiency.

CCPD v3 Capacitively coupled pixel detector version 3.

CDR Clock and data recovery.

CMOS Complementary metal-oxide-semiconductor.

CSA Charge sensitive amplifier.

CV Capacitance voltage.

Cz Czochralski.

DLTS Deep level transient spectroscopy.

DMAPS Depleted monolithic active pixel sensor.

DUT Device under test.

Epi Epitaxial.

FCA Free carrier absorption.

FFT Fast Fourier transformation.

FPGA Field programmable gate array.

FWHM Full width at half maximum.

FZ Float zone.

GR Guard ring.

IBIC Ion beam induced charge.

IR Infrared.

IV Current voltage.

LGAD Low gain avalanche detector.

MCz Magnetic Czochralski.

MIP Minimum ionising particle.

MPV Most probable value.

NA Numerical aperture.

NDF Neutral density filter.

NIEL Non-ionising energy loss.

PC Prompt current.

PCB Printed circuit board.

picoAD Picosecond avalanche detector.

RMS Root-mean-square.

RT Rise time.

SCR Space charge region.

SCSI Space charge sign inversion.

SEE Single event effect.

SLM Spatial light modulator.

SNR Signal-to-noise ratio.

SPA Single photon absorption.

TCAD Technology computer-aided design.

TCT Transient current technique.

ToT Time over threshold.

TPA Two photon absorption.

TPA-TCT Two photon absorption – transient current technique.

TRIBIC Time resolved ion beam induced charge.

TSC Thermally stimulated current.

VB Valence band.

WPC Weighted prompt current.

Bibliography

[1] ECFA Detector R&D Roadmap Process Group. *The 2021 ECFA detector research and development roadmap*. Tech. rep. 2020. DOI: 10.17181/CERN.XDPL.W2EX.

[2] V. Eremin et al. "Development of transient current and charge techniques for the measurement of effective net concentration of ionized charges (N_{eff}) in the space charge region of p-n junction detectors." In: *Nucl. Instrum. Methods Phys. Res. A: Accel., Spectrom., Detect. Assoc. Equip.* (1996). DOI: 10.1016/0168-9002(95)01295-8.

[3] G. Kramberger et al. "Determination of effective trapping times for electrons and holes in irradiated silicon." In: *Nucl. Instrum. Methods Phys. Res. A: Accel., Spectrom., Detect. Assoc. Equip.* (2002). DOI: 10.1016/S0168-9002(01)01653-9.

[4] B. Dezillie et al. "Polarization of silicon detectors by minimum ionizing particles." In: *Nucl. Instrum. Methods Phys. Res. A: Accel., Spectrom., Detect. Assoc. Equip.* (2000). DOI: 10.1016/S0168-9002(00)00450-2.

[5] G. Kramberger et al. "Investigation of Irradiated Silicon Detectors by Edge-TCT." In: *IEEE Transactions on Nuclear Science* (2010). DOI: 10.1109/TNS.2010.2051957.

[6] J. S. Melinger et al. "Critical evaluation of the pulsed laser method for single event effects testing and fundamental studies." In: *IEEE Transactions on Nuclear Science* (1994). DOI: 10.1109/23.340618.

[7] D. McMorrow et al. "Subbandgap laser-induced single event effects: carrier generation via two-photon absorption." In: *IEEE Transactions on Nuclear Science* (2002). DOI: 10.1109/TNS.2002.805337.

[8] D. McMorrow et al. "Three-dimensional mapping of single-event effects using two photon absorption." In: *IEEE Transactions on Nuclear Science* (2003). DOI: 10.1109/TNS.2003.820742.

[9] M. Fernández García et al. "High resolution 3D characterization of silicon detectors using a Two Photon Absorption Transient Current Technique." In: *Nucl. Instrum. Methods Phys. Res. A: Accel., Spectrom., Detect. Assoc. Equip.* (2020). DOI: 10.1016/j.nima.2019.162865.

[10] M. Fernández García et al. "On the determination of the substrate effective doping concentration of irradiated HV-CMOS sensors using an edge-TCT technique based on the Two-Photon-Absorption process." In: *Journal of Instrumentation* (2017). DOI: 10.1088/1748-0221/12/01/C01038.

[11] F. R. Palomo et al. "Plasma effects in silicon detectors and the Two Photon Absorption Transient Current Technique." In: (2021). DOI: 10.1109/RADECS53308.2021.9954488.

[12] A. Almagro et al. "Fiber Laser System of 1550 nm Femtosecond Pulses with Configurable Properties for the Two-Photon Excitation of Transient Current in Semiconductor Detectors." In: *Applied Optics* (2022). DOI: 10.1364/AO.470780.

[13] M. Wiehe. "Development of a Two-Photon Absorption - TCT system and Study of Radiation Damage in Silicon Detectors." In: *Ph.D. thesis University of Freiburg* (2021). URL: https://cds.cern.ch/record/2795933.

[14] C. Manfredotti et al. "IBIC and IBIL microscopy applied to advanced semiconductor materials." In: *Nuc. Instrum. Methods Phys. Res. B: Beam Interactions with Materials and Atoms* (1998). DOI: 10.1016/S0168-583X(97)00829-X.

[15] D. Angell et al. "Charge collection ion microscopy: Imaging of defects in semiconductors with a positive ion microbeam." In: *Nuc. Instrum. Methods Phys. Res. B: Beam Interactions with Materials and Atoms* (1989). DOI: 10.1016/0168-583X(89)90424-2.

[16] G. Vizkelethy et al. "Investigation of the electronic properties of cadmium zinc telluride (CZT) detectors using a nuclear microprobe." In: *Nucl. Instrum. Methods Phys. Res. A: Accel., Spectrom., Detect. Assoc. Equip.* (2001). DOI: 10.1016/S0168-9002(00)00917-7.

[17] M. Jakšić et al. "Radiation damage microstructures in silicon and application in position sensitive charged particle detection." In: *Nuc. Instrum. Methods Phys. Res. B: Beam Interactions with Materials and Atoms* (2005). DOI: 10.1016/j.nimb.2005.01.107.

[18] M. Jakšić et al. "Ion Microbeam Studies of Charge Transport in Semiconductor Radiation Detectors With Three-Dimensional Structures: An Example of LGAD." In: *Frontiers in Physics* (2022). DOI: 10.3389/fphy.2022.877577.

[19] RD50 Collaboration. *Radiation hard semiconductor devices for very high luminosity colliders*. URL: https://rd50.web.cern.ch (visited on 2023-11-15).

[20] *AIDAinnova - Advancement and Innovation for Detectors and Accelerators*. URL: https://aidainnova.web.cern.ch (visited on 2023-11-15).

[21] *AIDAinnova milestones*. URL: https://aidainnova.web.cern.ch/milestones (visited on 2023-11-15).

[22] *AIDAinnova deliverables*. URL: https://aidainnova.web.cern.ch/deliverables (visited on 2023-11-15).

[23] A. Almagro-Ruiz et al. "Commissioning of a complete TPA-TCT system." In: (2023). DOI: 10.5281/zenodo.8027093.

[24] S. Pape et al. "Techniques for the Investigation of Segmented Sensors Using the Two Photon Absorption-Transient Current Technique." In: *Sensors* (2023). DOI: 10.3390/s23020962.

[25] I. Vila Álvarez et al. "TPA-TCT: A novel Transient Current Technique based on the Two Photon Absorption (TPA) process." In: *25th RD50 Workshop* (Nov. 20, 2014). URL: https://indico.cern.ch/event/334251/contributions/780782 (visited on 2023-11-15).

[26] R. Palomo Pinto et al. "Two Photon Absorption and carrier generation in semiconductors." In: *25th RD50 Workshop* (Nov. 20, 2014). URL: https://indico.cern.ch/event/334251/contributions/780784 (visited on 2023-11-15).

[27] M. Wiehe et al. "TPA-TCT – Two Photon Absorption - Transient Current Technique." In: *35th RD50 Workshop* (Nov. 20, 2019). URL: https://indico.cern.ch/event/855994/contributions/3637067 (visited on 2023-11-15).

[28] R. Palomo Pinto et al. "Plasma Effects in TCT-TPA." In: *35th RD50 Workshop* (Nov. 20, 2019). URL: https://indico.cern.ch/event/855994/contributions/3637059 (visited on 2023-11-15).

[29] M. Wiehe et al. "TPA-TCT – Two Photon Absorption - Transient Current Technique." In: *36th RD50 Workshop* (June 3, 2020). URL: https://indico.cern.ch/event/918298/contributions/3884789 (visited on 2023-11-15).

[30] P. Pérez-Millán et al. "1550 nm Femtosecond Fiber Laser System for the Two-Photon Excitation of Transient Currents in Semiconductor Detectors." In: *36th RD50 Workshop* (June 3, 2020). URL: https://indico.cern.ch/event/918298/contributions/3888761 (visited on 2023-11-15).

[31] M. Wiehe et al. "A table-top Two Photon Absorption - TCT system: Method and Setup." In: *38th RD50 Workshop* (June 23, 2021). URL: https://indico.cern.ch/event/1029124/contributions/4411338 (visited on 2023-11-15).

[32] S. Pape et al. "A table-top Two Photon Absorption - TCT system: experimental results." In: *38th RD50 Workshop* (June 23, 2021). URL: https://indico.cern.ch/event/1029124/contributions/4411336 (visited on 2023-11-15).

[33] S. Pape et al. "Gain suppression mechanism in LGADs and SEE studies in a RD53B chip measured with the TPA-TCT method." In: *39th RD50 Workshop* (Nov. 17, 2021). URL: https://indico.cern.ch/event/1074989/contributions/4601951 (visited on 2023-11-15).

[34] A. Almagro-Ruiz et al. "Towards an All-Fiber Femtosecond Laser System as Excitation Source in the Two-Photon Absorption - Transient Current Technique." In: *39th RD50 Workshop* (Nov. 17, 2021). URL: https://indico.cern.ch/event/1074989/contributions/4601935 (visited on 2023-11-15).

[35] S. Pape et al. "The gain reduction mechanism in Low Gain Avalanche Detectors investigated with the TPA-TCT." In: *40th RD50 Workshop* (June 23, 2022). URL: https://indico.cern.ch/event/1157463/contributions/4922748/ (visited on 2023-11-15).

[36] S. Pape et al. "Two Photon Absorption - Transient Current Technique: Techniques for the investigation of segmented sensors and the influence of temperature." In: *41st RD50 Workshop* (Nov. 30, 2022). URL: https://indico.cern.ch/event/1132520/contributions/5140040 (visited on 2023-11-15).

[37] S. Pape et al. "Two Photon Absorption - Transient Current Technique: Techniques for the investigation of segmented sensors and the influence of temperature." In: *42nd RD50 Workshop* (June 20, 2023). URL: https://indico.cern.ch/event/1270076/contributions/5450168 (visited on 2023-11-15).

[38] R. Geertsema et al. "Charge and temporal characterisation of silicon sensors using a two-photon absorption laser." In: *Journal of Instrumentation* (2022). DOI: 10.1088/1748-0221/17/02/P02023.

[39] G. Laštovička-Medin et al. "Femtosecond laser studies of the Single Event Effects in Low Gain Avalanche Detectors and PINs at ELI Beamlines." In: *Nucl. Instrum. Methods Phys. Res. A: Accel., Spectrom., Detect. Assoc. Equip.* (2022). DOI: 10.1016/j.nima.2022.167321.

[40] B. Hiti et al. "New TPA-TCT system at Jozef Stefan Institute (JSI)." In: *38th RD50 Workshop* (June 23, 2021). (Visited on 2023-11-15).

[41] E. Ejopu et al. "Solid-state sensor characterisation using Two-Photon Absorption (TPA) Technique." In: *42nd RD50 Workshop* (June 20, 2023). (Visited on 2023-11-15).

[42] M. Wiehe et al. "Development of a Tabletop Setup for the Transient Current Technique Using Two-Photon Absorption in Silicon Particle Detectors." In: *IEEE Transactions on Nuclear Science* (2021). DOI: 10.1109/TNS.2020.3044489.

[43] E. Currás, M. Fernández, and M. Moll. "Gain reduction mechanism observed in Low Gain Avalanche Diodes." In: *Nucl. Instrum. Methods Phys. Res. A: Accel., Spectrom., Detect. Assoc. Equip.* (2022). DOI: 10.1016/j.nima.2022.166530.

[44] G. Kramberger et al. "Gain dependence on free carrier concentration in LGADs." In: *Nucl. Instrum. Methods Phys. Res. A: Accel., Spectrom., Detect. Assoc. Equip.* (2023). DOI: 10.1016/j.nima.2022.167669.

[45] S. Pape et al. "First observation of the charge carrier density related gain reduction mechanism in LGADs with the Two Photon Absorption-Transient Current Technique." In: *Nucl. Instrum. Methods Phys. Res. A: Accel., Spectrom., Detect. Assoc. Equip.* (2022). DOI: 10.1016/j.nima.2022.167190.

[46] L. Diehl et al. "Characterization of passive CMOS strip sensors." In: *Nucl. Instrum. Methods Phys. Res. A: Accel., Spectrom., Detect. Assoc. Equip.* (2022). DOI: 10.1016/j.nima.2022.166671.

[47] I. Peric. "Active pixel sensors in high-voltage CMOS technologies for ATLAS." In: *Journal of Instrumentation* (2012). DOI: 10.1088/1748-0221/7/08/C08002.

[48] E. Vilella. "Development of high voltage-CMOS sensors within the CERN-RD50 collaboration." In: *Nucl. Instrum. Methods Phys. Res. A: Accel., Spectrom., Detect. Assoc. Equip.* (2022). DOI: 10.1016/j.nima.2022.166826.

[49] L. Paolozzi et al. "Picosecond Avalanche Detector — working principle and gain measurement with a proof-of-concept prototype." In: *Journal of Instrumentation* (2022). DOI: 10.1088/1748-0221/17/10/P10032.

[50] M. Garcia-Sciveres, F. Loddo, and J. Christiansen. *RD53B Manual*. Tech. rep. CERN, 2019. URL: http://cds.cern.ch/record/2665301.

[51] M. Grundmann. *The Physics of Semiconductors: An Introduction Including Nanophysics and Applications*. 3rd ed. Springer, 2016. DOI: 10.1007/978-3-319-23880-7.

[52] S. Sze and K. Ng. *Physics of Semiconductor Devices*. 3rd ed. Wiley, 2006. DOI: 10.1002/0470068329.

[53] R. Gross and A. Marx. *Festkörperphysik*. 4th ed. De Gruyter, 2022. DOI: 10.1515/9783110782394-201.

[54] National Institute of Standards and Technology, US. *The NIST Reference on Constants, Units, and Uncertainty*. URL: https://physics.nist.gov/cgi-bin/cuu/Value?asil (visited on 2023-11-15).

[55] V. Alex, S. Finkbeiner, and J. Weber. "Temperature dependence of the indirect energy gap in crystalline silicon." In: *Journal of Applied Physics* (1996). DOI: 10.1063/1.362447.

[56] D. Colella. "ALICE ITS 3: the first truly cylindrical inner tracker." In: *Journal of Instrumentation* (2022). DOI: 10.1088/1748-0221/17/09/C09018.

[57] M. Moll. "Radiation damage in silicon particle detectors. Microscopic defects and macroscopic properties." In: *Ph.D. thesis University of Hamburg* (1999). DOI: 10.3204/PUBDB-2016-02525.

[58] H. Kolanoski and N. Wermes. *Teilchendetektoren: Grundlagen und Anwendungen*. 1st ed. Springer Spektrum, 2016. DOI: 10.1007/978-3-662-45350-6.

[59] W. Lin. "Chapter 2 The Incorporation of Oxygen into Silicon Crystals." In: Semiconductors and Semimetals. 1994. DOI: 10.1016/S0080-8784(08)60245-8.

[60] S. Sze. *Semiconductor Devices: Physics and Technology*. 1st ed. Wiley, 1985. ISBN: 978-0-471-87424-9.

[61] J. Becker, E. Fretwurst, and R. Klanner. "Measurements of charge carrier mobilities and drift velocity saturation in bulk silicon of ⟨111⟩ and ⟨100⟩ crystal orientation at high electric fields." In: *Solid-State Electronics* (2011). DOI: 10.1016/j.sse.2010.10.009.

[62] F. Hartmann. *Evolution of Silicon Sensor Technology in Particle Physics*. 2nd ed. Springer Nature, 2017. DOI: 10.1007/978-3-319-64436-3.

[63] G. Lutz. *Semiconductor Radiation Detectors*. Springer, 2007. DOI: 10.1007/978-3-540-71679-2.

[64] A. Chilingarov. "Temperature dependence of the current generated in Si bulk." In: *Journal of Instrumentation* (2013). DOI: 10.1088/1748-0221/8/10/P10003.

[65] H. Bichsel. "A method to improve tracking and particle identification in TPCs and silicon detectors." In: *Nucl. Instrum. Methods Phys. Res. A: Accel., Spectrom., Detect. Assoc. Equip.* (2006). DOI: 10.1016/j.nima.2006.03.009.

[66] W. R. Leo. *Techniques for Nuclear and Particle Physics Experiments*. 2nd ed. Springer-Verlag, 1993. DOI: 10.1007/978-3-642-57920-2.

[67] R. L. Workman et al. "Review of Particle Physics." In: *PTEP* 2022 (2022). DOI: 10.1093/ptep/ptac097.

[68] T. Davidek and R. Leitner. *Parametrization of the muon response in the tile calorimeter*. Tech. rep. CERN, 1997. URL: http://cds.cern.ch/record/683578.

[69] M. Berger et al. "Stopping-Power & Range Tables for Electrons, Protons, and Helium Ions." In: (2017). URL: https://www.nist.gov/pml/data/star (visited on 2023-11-15).

[70] D. M. Caughey and R. E. Thomas. "Carrier mobilities in silicon empirically related to doping and field." In: *Proceedings of the IEEE* (1967). DOI: 10.1109/PROC.1967.6123.

[71] C. Jacoboni et al. "A review of some charge transport properties of silicon." In: *Solid-State Electronics* (1977). DOI: 10.1016/0038-1101(77)90054-5.

[72] W. Shockley. "Currents to Conductors Induced by a Moving Point Charge." In: *Journal of Applied Physics* 9 (1938). DOI: 10.1063/1.1710367.

[73] S. Ramo. "Currents Induced by Electron Motion." In: *Proceedings of the IRE* 27 (1939). DOI: 10.1109/JRPROC.1939.228757.

[74] H. Spieler. *Semiconductor Detector Systems*. 1st ed. Oxford University press, 2005. ISBN: 978-0-19-152365-6.

[75] H. Zhong. "Review of the Shockley-Ramo theorem and its application in semiconductor gamma-ray detectors." In: *Nucl. Instrum. Methods Phys. Res. A: Accel., Spectrom., Detect. Assoc. Equip.* (2001). DOI: 10.1016/S0168-9002(01)00223-6.

[76] W. Riegler. "An application of extensions of the Ramo-Shockley theorem to signals in silicon sensors." In: *Nucl. Instrum. Methods Phys. Res. A: Accel., Spectrom., Detect. Assoc. Equip.* (2019). DOI: 10.1016/j.nima.2019.06.056.

[77] V. Radeka. "Low-Noise Techniques in Detectors." In: *Annual Review of Nuclear and Particle Science* (1988). DOI: 10.1146/annurev.ns.38.120188.001245.

[78] R. Boyd. *Nonlinear optics*. 4th ed. Academic press, 2020. ISBN: 978-0-323-85057-5.

[79] M. Göpper-Mayer. "Über Elementarakte mit zwei Quantensprüngen." In: *Annalen der Physik* (1931). DOI: 10.1002/andp.19314010303.

[80] W. Kaiser and C. G. B. Garrett. "Two-Photon Excitation in CaF_2: Eu^{2+}." In: *Phys. Rev. Lett.* (1961). DOI: 10.1103/PhysRevLett.7.229.

[81] M. A. Green. "Improved silicon optical parameters at 25 °C, 295 K and 300 K including temperature coefficients." In: *Progress in Photovoltaics: Research and Applications* (2022). DOI: 10.1002/pip.3474.

[82] H. J. Eichler, J. Eichler, and O. Lux. *Lasers*. 1st ed. Springer Series in Optical Sciences, 2018. DOI: 10.1007/978-3-319-99895-4.

[83] I. Walmsley, L. Waxer, and C. Dorrer. "The role of dispersion in ultrafast optics." In: *Review of Scientific Instruments* (2001). DOI: 10.1063/1.1330575.

[84] A. D. Bristow, N. Rotenberg, and H. M. van Driel. "Two-photon absorption and Kerr coefficients of silicon for 850-2200nm." In: *Appl. Phys. Lett.* (2007). DOI: 10.1063/1.2737359.

[85] J. C. Sturm and C. M. Reaves. "Silicon temperature measurement by infrared absorption. Fundamental processes and doping effects." In: *IEEE Transactions on Electron Devices* (1992). DOI: 10.1109/16.108215.

[86] H. H. Li. "Refractive index of silicon and germanium and its wavelength and temperature derivatives." In: *Journal of Physical and Chemical Reference Data* (1980). DOI: 10.1063/1.555624.

[87] G. Lindström et al. "Radiation hard silicon detectors—developments by the RD48 (ROSE) collaboration." In: *Nucl. Instrum. Methods Phys. Res. A: Accel., Spectrom., Detect. Assoc. Equip.* (2001). DOI: 10.1016/S0168-9002(01)00560-5.

[88] M. Moll. "Displacement Damage in Silicon Detectors for High Energy Physics." In: *IEEE Transactions on Nuclear Science* (2018). DOI: 10.1109/TNS.2018.2819506.

[89] M. Huhtinen. "Simulation of non-ionising energy loss and defect formation in silicon." In: *Nucl. Instrum. Methods Phys. Res. A: Accel., Spectrom., Detect. Assoc. Equip.* (2002). DOI: 10.1016/S0168-9002(02)01227-5.

[90] A. Vasilescu and G. Lindström. *Displacement damage in silicon, on-line compilation*. 2000. URL: http://rd50.web.cern.ch/NIEL/default.html (visited on 2023-11-15).

[91] C. M. Davisson and R. D. Evans. "Gamma-Ray Absorption Coefficients." In: *Rev. Mod. Phys.* (1952). DOI: 10.1103/RevModPhys.24.79.

[92] J. H. Cahn. "Irradiation Damage in Germanium and Silicon due to Electrons and Gamma Rays." In: *Journal of Applied Physics* (2004). DOI: 10.1063/1.1735310.

[93] M. Moll et al. “Comparison of defects produced by fast neutrons and 60Co-gammas in high-resistivity silicon detectors using deep-level transient spectroscopy.” In: *Nucl. Instrum. Methods Phys. Res. A: Accel., Spectrom., Detect. Assoc. Equip.* (1997). DOI: 10.1016/S0168-9002(97)00003-X.

[94] P. M. Mooney et al. “Defect energy levels in boron-doped silicon irradiated with 1-MeV electrons.” In: *Phys. Rev. B* (1977). DOI: 10.1103/PhysRevB.15.3836.

[95] R. Wunstorf. “Systematische Untersuchungen zur Strahlenresistenz von Silizium-Detektoren für die Verwendung in Hochenergiephysik-Experimenten.” In: *Ph.D. thesis University of Hamburg* (1992). URL: https://bib-pubdb1.desy.de/record/153817.

[96] W. Shockley and W. T. Read. “Statistics of the Recombinations of Holes and Electrons.” In: *Phys. Rev.* (1952). DOI: 10.1103/PhysRev.87.835.

[97] R. N. Hall. “Electron-Hole Recombination in Germanium.” In: *Phys. Rev.* (1952). DOI: 10.1103/PhysRev.87.387.

[98] R. Wunstorf et al. “Radiation damage of silicon detectors by monoenergetic neutrons and electrons.” In: *Nuclear Physics B - Proceedings Supplements* (1991). DOI: 10.1016/0920-5632(91)90065-M.

[99] E. Fretwurst et al. “Radiation damage studies on MCz and standard and oxygen enriched epitaxial silicon devices.” In: *Nucl. Instrum. Methods Phys. Res. A: Accel., Spectrom., Detect. Assoc. Equip.* (2007). DOI: 10.1016/j.nima.2007.08.194.

[100] I. Pintilie et al. “Close to midgap trapping level in ^{60}Co gamma irradiated silicon detectors.” In: *Applied Physics Letters* (2002). DOI: 10.1063/1.1490397.

[101] J. Lange et al. “Charge collection studies of proton-irradiated n- and p-type epitaxial silicon detectors.” In: *Nucl. Instrum. Methods Phys. Res. A: Accel., Spectrom., Detect. Assoc. Equip.* (2010). DOI: 10.1016/j.nima.2009.11.082.

[102] Z. Li et al. “Gamma radiation induced space charge sign inversion and re-inversion in p-type MCZ Si detectors and in proton-irradiated n-type MCZ Si detectors.” In: *Nucl. Instrum. Methods Phys. Res. A: Accel., Spectrom., Detect. Assoc. Equip.* (2005). DOI: 10.1016/j.nima.2005.06.003.

[103] R. Wunstorf et al. “Investigations of donor and acceptor removal and long term annealing in silicon with different boron/phosphorus ratios.” In: *Nucl. Instrum. Methods Phys. Res. A: Accel., Spectrom., Detect. Assoc. Equip.* (1996). DOI: 10.1016/0168-9002(96)00217-3.

[104] M. Moll. “Acceptor removal - Displacement damage effects involving the shallow acceptor doping of p-type silicon devices.” In: *Proceedings of Science* (2020). DOI: 10.22323/1.373.0027.

[105] E. Curras Rivera et al. “Gain layer degradation study after neutron and proton irradiations in Low Gain Avalanche Diodes.” In: (2023). DOI: 10.48550/arXiv.2306.11760.

[106] V. Eremin, E. Verbitskaya, and Z. Li. “The origin of double peak electric field distribution in heavily irradiated silicon detectors.” In: *Nucl. Instrum. Methods Phys. Res. A: Accel., Spectrom., Detect. Assoc. Equip.* (2002). DOI: 10.1016/S0168-9002(01)01642-4.

[107] G. Kramberger et al. "Effective trapping time of electrons and holes in different silicon materials irradiated with neutrons, protons and pions." In: *Nucl. Instrum. Methods Phys. Res. A: Accel., Spectrom., Detect. Assoc. Equip.* (2002). DOI: 10.1016/S0168-9002(01)01263-3.

[108] Z. Li and H. W. Kraner. "Fast neutron radiation damage effects on high resistivity silicon junction detectors." In: *J. Electron. Mater* (1992). DOI: 10.1007/BF02655599.

[109] H. Y. Fan and A. K. Ramdas. "Infrared Absorption and Photoconductivity in Irradiated Silicon." In: *Journal of Applied Physics* (2004). DOI: 10.1063/1.1735282.

[110] E. Fretwurst et al. "Study of the V_2^0 state in neutron-irradiated silicon using photon-absorption measurements." In: *Nucl. Instrum. Methods Phys. Res. A: Accel., Spectrom., Detect. Assoc. Equip.* (2023). DOI: 10.1016/j.nima.2023.168353.

[111] R. Klanner et al. "Study of the band-gap energy of radiation-damaged silicon." In: *New Journal of Physics* (2022). DOI: 10.1088/1367-2630/ac7db3.

[112] K. F. Heidemann. "Complex-refractive-index profiles of 4 MeV Ge ion-irradiation damage in silicon." In: *Philosophical Magazine B* (1981). DOI: 10.1080/01418638108222583.

[113] O. Krasel et al. "Measurement of trapping time constants in proton-irradiated silicon pad detectors." In: *IEEE Transactions on Nuclear Science* (2004). DOI: 10.1109/TNS.2004.839096.

[114] *CiS Forschungsinstitut für Mikrosensorik GmbH, Erfurt, Germany.* URL: https://www.cismst.de/ (visited on 2023-11-15).

[115] *Jožef Stefan Institute, Ljubljana, Slovenia.* URL: https://www.ijs.si/ijsw/JSI (visited on 2023-11-15).

[116] *PS-IRRAD Proton Facility, CERN, Switzerland.* URL: https://ps-irrad.web.cern.ch/ps-irrad (visited on 2023-11-15).

[117] *Ruđer Bošković Institute, Zagreb, Croatia.* URL: https://www.irb.hr/eng (visited on 2023-11-15).

[118] *Peter Huber Kältemaschinenbau SE, Offenburg, Germany.* URL: https://www.huber-online.com (visited on 2023-11-15).

[119] S. Otero Ugobono. "Characterisation and Optimisation of Radiation-Tolerant Silicon Sensors with Intrinsic Gain." In: *Ph.D. thesis University of Santiago de Compostela* (2018). URL: https://cds.cern.ch/record/2649130.

[120] N. Pacifico. "Radiation damage study on innovative silicon sensors for the CMS tracker upgrade." In: *Ph.D. thesis University of Bari* (2011). URL: https://cds.cern.ch/record/2130663.

[121] *CIVIDEC Instrumentation GmbH, Vienna, Austria.* URL: https://cividec.at/index.php (visited on 2023-11-15).

[122] E. Curras Rivera. "Advanced silicon sensors for future collider experiments." In: *Ph.D. thesis University of Cantabria* (2017). URL: https://cds.cern.ch/record/2291517.

[123] *FYLA S.L., Valencia, Spain.* URL: https://fyla.com (visited on 2023-11-15).

[124] *Instituto de Física de Cantabria, Santander, Spain.* URL: https://ifca.unican.es (visited on 2023-11-15).

[125] *CERN, Geneva, Switzerland*. URL: https://home.cern (visited on 2023-11-15).

[126] *LabVIEW, National Instruments, Austin, US*. URL: https://www.ni.com/en-us/shop/product/labview.html (visited on 2023-11-15).

[127] *Laird Thermal Systems, Durham, US*. URL: https://lairdthermal.com/ (visited on 2023-11-15).

[128] *Thorlabs, Inc., Newton, US*. URL: https://www.thorlabs.com (visited on 2023-11-15).

[129] M. Gu. *Advanced optical imaging theory*. 1st ed. 2000. DOI: 10.1007/978-3-540-48471-4.

[130] C. Maurer et al. "What spatial light modulators can do for optical microscopy." In: *Laser & Photonics Reviews* (2011). DOI: 10.1002/lpor.200900047.

[131] N. Matsumoto et al. "Correction of depth-induced spherical aberration for deep observation using two-photon excitation fluorescence microscopy with spatial light modulator." In: *Biomed. Opt. Express* (2015). DOI: 10.1364/BOE.6.002575.

[132] G. Kontenis et al. "Dynamic aberration correction via spatial light modulator (SLM) for femtosecond direct laser writing: towards spherical voxels." In: *Opt. Express* (2020). DOI: 10.1364/OE.397006.

[133] M. Moll, E. Fretwurst, and G. Lindström. "Leakage current of hadron irradiated silicon detectors - material dependence." In: *Nucl. Instrum. Methods Phys. Res. A: Accel., Spectrom., Detect. Assoc. Equip.* (1999). DOI: 10.1016/S0168-9002(98)01475-2.

[134] J. Becker et al. "Impact of plasma effects on the performance of silicon sensors at an X-ray FEL." In: *Nucl. Instrum. Methods Phys. Res. A: Accel., Spectrom., Detect. Assoc. Equip.* (2010). DOI: 10.1016/j.nima.2010.01.082.

[135] P. A. Tove and W. Seibt. "Plasma effects in semiconductor detectors." In: *Nucl. Instrum. Methods* (1967). DOI: 10.1016/0029-554X(67)90012-2.

[136] M. Beresna, M. Gecevičius, and P. G. Kazansky. "Ultrafast laser direct writing and nanostructuring in transparent materials." In: *Advances in Optics and Photonics* (2014). DOI: 10.1364/AOP.6.000293.

[137] O. Tokel et al. "In-chip microstructures and photonic devices fabricated by nonlinear laser lithography deep inside silicon." In: *Nature photonics* (2017). DOI: 10.1038/s41566-017-0004-4.

[138] Y. P. Varshni. "Temperature dependence of the energy gap in semiconductors." In: *Physica* (1967). DOI: 10.1016/0031-8914(67)90062-6.

[139] J. Bardeen and W. Shockley. "Deformation Potentials and Mobilities in Non-Polar Crystals." In: *Phys. Rev.* (1950). DOI: 10.1103/PhysRev.80.72.

[140] M. A. Green. "Self-consistent optical parameters of intrinsic silicon at 300K including temperature coefficients." In: *Solar Energy Materials and Solar Cells* (2008). DOI: 10.1016/j.solmat.2008.06.009.

[141] G. F. Sinclair et al. "Temperature Dependence of the Kerr Nonlinearity and Two-Photon Absorption in a Silicon Waveguide at 1.55 μm." In: *Phys. Rev. Applied* (2019). DOI: 10.1103/PhysRevApplied.11.044084.

[142] S. Pape et al. "Influence of temperature on measurements of the Two Photon Absorption - Transient Current Technique in silicon planar detectors using a 1550 nm femtosecond fibre laser." In: *Nucl. Instrum. Methods Phys. Res. A: Accel., Spectrom., Detect. Assoc. Equip.* (2023). DOI: 10.1016/j.nima.2023.168387.

[143] S. Pape et al. "Characterisation of irradiated and non-irradiated silicon sensors with a table-top two photon absorption TCT system." In: *Journal of Instrumentation* (2022). DOI: 10.1088/1748-0221/17/08/c08011.

[144] V. A. J. van Lint, R. E. Leadon, and J. F. Colwell. "Energy Dependence of Displacement Effects in Semiconductors." In: *IEEE Transactions on Nuclear Science* (1972). DOI: 10.1109/TNS.1972.4326830.

[145] I. Mandić et al. "Observation of full charge collection efficiency in heavily irradiated n+p strip detectors irradiated up to 3×1015neq/cm2." In: *Nucl. Instrum. Methods Phys. Res. A: Accel., Spectrom., Detect. Assoc. Equip.* (2010). DOI: 10.1016/j.nima.2009.08.004.

[146] T. Davidek and R. Leitner. *Parametrization of the Muon Response in the Tile Calorimeter*. Tech. rep. 1997. URL: https://cds.cern.ch/record/683578.

[147] J. Conradi. "The distribution of gains in uniformly multiplying avalanche photodiodes: Experimental." In: *IEEE Transactions on Electron Devices* (1972). DOI: 10.1109/T-ED.1972.17486.

[148] H. F. W. Sadrozinski et al. "Ultra-fast silicon detectors (UFSD)." In: *Nucl. Instrum. Methods Phys. Res. A: Accel., Spectrom., Detect. Assoc. Equip.* (2016). DOI: 10.1016/j.nima.2016.03.093.

[149] G. Pellegrini et al. "Technology developments and first measurements of Low Gain Avalanche Detectors (LGAD) for high energy physics applications." In: *Nucl. Instrum. Methods Phys. Res. A: Accel., Spectrom., Detect. Assoc. Equip.* (2014). DOI: 10.1016/j.nima.2014.06.008.

[150] M. P. Casado. "A High-Granularity Timing Detector for the ATLAS Phase-II upgrade." In: *Nucl. Instrum. Methods Phys. Res. A: Accel., Spectrom., Detect. Assoc. Equip.* (2022). DOI: https://doi.org/10.1016/j.nima.2022.166628.

[151] M. Ferrero. "The CMS MTD Endcap Timing Layer: Precision timing with Low Gain Avalanche Diodes." In: *Nucl. Instrum. Methods Phys. Res. A: Accel., Spectrom., Detect. Assoc. Equip.* (2022). DOI: https://doi.org/10.1016/j.nima.2022.166627.

[152] R. Mulargia et al. "Temperature dependence of the response of ultra fast silicon detectors." In: *Journal of Instrumentation* 11 (2016). DOI: 10.1088/1748-0221/11/12/c12013.

[153] C. P. Allier et al. "Comparative study of silicon detectors." In: *IEEE Transactions on Nuclear Science* (1998). DOI: 10.1109/23.682451.

[154] *Micron Semiconductor Ltd, West Sussex, UK*. Micron Technologies, Inc. URL: https://www.micron.com (visited on 2023-11-15).

[155] M. Fernández García et al. "High-resolution three-dimensional imaging of a depleted CMOS sensor using an edge Transient Current Technique based on the Two-Photon Absorption process (TPA-eTCT)." In: *Nucl. Instrum. Methods Phys. Res. A: Accel., Spectrom., Detect. Assoc. Equip.* (2017).

[156] T. Vanat. "Caribou — A versatile data acquisition system." In: *Proceedings of Science* (2020). DOI: 10.22323/1.370.0100.

[157] *MONOLITH - Monolithic Multi-Junction Picosecond Avalanche Detector for future physics experiments and applications.* URL: https://doi.org/10.3030/884447 (visited on 2023-11-15).

[158] *Leibniz Institute for High Performance Microelectronics, Frankfurt (Oder), Germany.* URL: https://www.ihp-microelectronics.com (visited on 2023-11-15).

[159] H. W. Ruegg. "An optimized avalanche photodiode." In: *IEEE Transactions on Electron Devices* (1967). DOI: 10.1109/T-ED.1967.15937.

[160] S. M. Mazza. *Deep Junction LGAD: a new approach to high granularity LGAD.* Tech. rep. 2020. URL: https://cds.cern.ch/record/2718225/files/AIDA-2020-SLIDE-2020-016.pdf.

[161] N. Moffat and R. Bates. "Simulation of the small pixel effect contributing to a low fill factor for pixellated Low Gain Avalanche Detectors (LGAD)." In: *Nucl. Instrum. Methods Phys. Res. A: Accel., Spectrom., Detect. Assoc. Equip.* (2021). DOI: https://doi.org/10.1016/j.nima.2021.165746.

[162] G. Iacobucci et al. "Testbeam results of the Picosecond Avalanche Detector proof-of-concept prototype." In: *Journal of Instrumentation* (2022). DOI: 10.1088/1748-0221/17/10/P10040.

[163] G. Iacobucci, L. Paolozzi, and P. Valerio. "Monolithic Picosecond Silicon Pixel Sensors for Future Physics: Experiments and Applications." In: *IEEE Instrumentation & Measurement Magazine* (2021). DOI: 10.1109/MIM.2021.9620045.

[164] W. Riegler and G. Aglieri Rinella. "Point charge potential and weighting field of a pixel or pad in a plane condenser." In: *Nucl. Instrum. Methods Phys. Res. A: Accel., Spectrom., Detect. Assoc. Equip.* (2014). DOI: 10.1016/j.nima.2014.08.044.

[165] J. Lalic et al. "Single event effects on the RD53B pixel chip digital logic and on-chip CDR." In: *Journal of Instrumentation* (2022). DOI: 10.1088/1748-0221/17/05/C05001.

[166] J. Lalic. "Single Event Effect mitigation techniques, testing and verification of the RD53 chips." EP-ESE Electronics Seminars. 2023. URL: https://indico.cern.ch/event/1267936.

[167] C. Scharf and R. Klanner. "Determination of the electronics transfer function for current transient measurements." In: *Nucl. Instrum. Methods Phys. Res. A: Accel., Spectrom., Detect. Assoc. Equip.* (2015). DOI: 10.1016/j.nima.2014.12.016.

[168] *Synopsys TCAD, Sunnyvale, US.* URL: https://www.synopsys.com/ (visited on 2023-11-15).

Acknowledgment

This work was performed within the framework of the RD50 Collaboration and has been sponsored by the Wolfgang Gentner Program of the German Federal Ministry of Education and Research (grant no. 13E18CHA).

First of all, I want to thank my supervisor Michael Moll, who introduced me to the topic and mentored me throughout my Ph.D. Thank you for your continuous support, the tremendous input you gave to this work, and the excellent TCAD simulation. Further, I like to thank Prof. Dr. Kröninger for giving me the opportunity to write my thesis in his group, the formal supervision, and the input during our regular meetings. I am thankful to Iván Vila Álvarez for the many fruitful discussions in our TPA meetings and that he agreed to be the second referee to this thesis.

I thank Marcos Fernández García and Moritz Wiehe for the excellent introduction to the setup and the software. Thank you for always finding the time to discuss the interesting results we measured. Thanks to Esteban Currás for the discussions about the gain reduction in LGADs and the SPA-TCT measurement in that matter. I need to thank Rogelio Palomo Pinto for the idea of the MPW2 campaign, for providing the DUT, and for input to the theory of TPA. Thank you to Raúl Montero for the input concerning the optical setup. I am thankful to Ruddy Constanzi for the support with all the special requests concerning the TPA-TCT setup.

I am thankful to the SSD team for the friendly and cheerful working environment. Special thanks to Yana Gurimskaya, Anja Himmerlich, Vendula Subert, Niels Sorgenfrei and Veronika Kraus. I want to thank Vagelis Gkougkousis for joining my office during the last months and the many interesting discussions about readout electronics. Thanks to Veronique Wedlake and Stephanie Krause for helping me with all bureaucratic matters.

A lot of people contributed to the various campaigns performed during this work. Thank you to Jens Weingarten and Marta Baselga for providing the passive CMOS strip detector. Thanks to the Monolith group and especially Yana Gurimskaya and Matteo Milanesio for providing the picoAD sample and helping with the measurements. I am grateful for the provided RD53B preproduction chips and input concerning the SEE measurements from the RD53 group and especially Jelena Lalic. I thank Johannes Wüthrich for the insights into cold wafer-wafer bonded devices.

I want to thank the *KDW* for the motivation during my studies. Thanks to Stefan Grisard for correction reading and offering me an office place during my stays in Dortmund.

I wish to thank my family and especially my parents for their support.
Finally, I thank Rilana Reichhardt for everything.

Zur Person:

_____ _____
Name, Vorname geboren am/ in

_____
Matrikelnummer

Belehrung:

Die Abgabe einer eidesstattlichen Versicherung ist eine nach §§ 156, 161 Strafgesetzbuch (StGB) strafbewehrte Bestätigung der Richtigkeit einer Erklärung. Die Abgabe einer falschen oder unvollständigen Versicherung an Eides statt ist strafbar.

Wer vorsätzlich eine falsche Versicherung an Eides statt abgibt, kann mit einer Freiheitsstrafe bis zu drei Jahren oder mit Geldstrafe bestraft werden, § 156 StGB. Die fahrlässige Abgabe einer falschen Versicherung an Eides statt kann mit einer Freiheitsstrafe bis zu einem Jahr oder Geldstrafe bestraft werden, § 161 StGB.

Die oben stehende Belehrung habe ich zur Kenntnis genommen:

_____ _____
Ort, Datum Unterschrift

Eidesstattliche Versicherung

In Kenntnis der Bedeutung einer eidesstattlichen Versicherung und der Strafbarkeit der Abgabe einer falschen eidesstattlichen Versicherung versichere ich hiermit an Eides statt, dass ich die vorliegende Dissertation mit dem Titel

_____
_____
_____

selbstständig und ohne unzulässige fremde Hilfe angefertigt habe. Ich habe keine anderen als die angegebenen Quellen benutzt sowie wörtliche und sinngemäße Zitate kenntlich gemacht.

_____ _____
Ort, Datum Unterschrift